Anisotropy, multivalency and flexibility-induced effects in colloidal systems

Verweij, R.W.

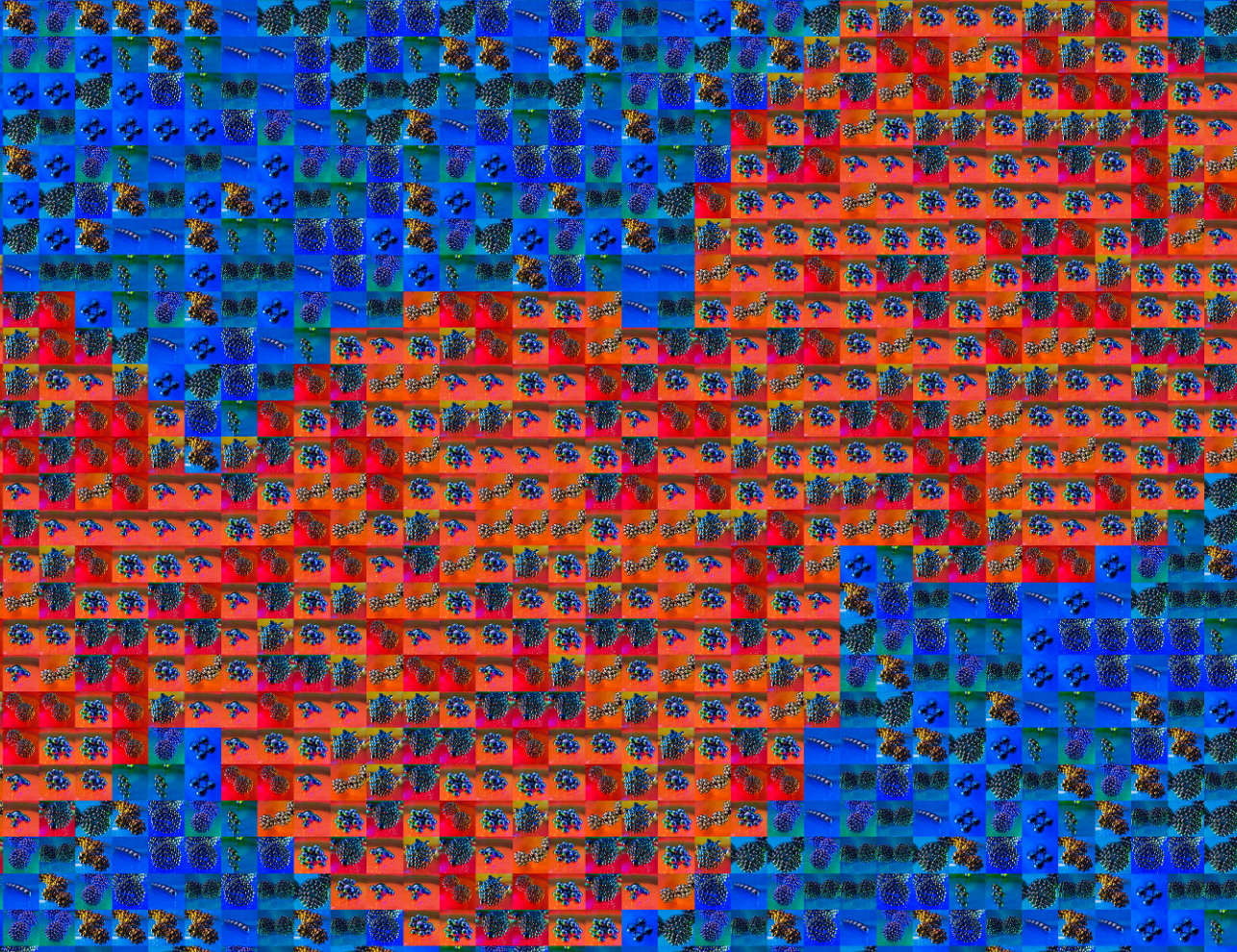

Anisotropy, multivalency and flexibility-induced effects in colloidal systems

Ruben W. Verweij

Anisotropy, multivalency and flexibility-induced effects in colloidal systems

Proefschrift

ter verkrijging van
de graad van doctor aan de Universiteit Leiden,
op gezag van rector magnificus prof.dr.ir. H. Bijl,
volgens besluit van het college voor promoties
te verdedigen op donderdag 27 mei 2021
klokke 11:15 uur

door

Ruben Wiñana Verweij
(geboren Van der Weij)

geboren te Heemskerk
in 1992

Promotores:	Dr. D.J. Kraft
	Prof. dr. M.L. Van Hecke
Promotiecommissie:	Prof. dr. A. Donev (New York University, USA)
	Prof. dr. W.K. Kegel (Utrecht University, NL)
	Prof. dr. ir. I.K. Voets (Eindhoven University, NL)
	Prof. dr. E.R. Eliel
	Prof. dr. T. Schmidt

Casimir PhD series, Delft-Leiden 2021-07
ISBN 978-90-8593-473-8

The work described in this thesis was supported by the European Research Council (ERC) under the European Union's Horizon 2020 research and innovation program (grant agreement no. 758383).

The cover shows a schematic depiction of a flexible colloidal chain. It consists of pictures of scale models of the various colloidal structures that are studied in this work. These scale models are also shown at the start of the relevant chapters. The scale models were assembled out of millimeter-sized magnetic beads.

The
dedication
of this thesis
is split
seven ways:
to mama Dees,
to opa Peter,
to oma Luck,
to Mark,
to W. Appelman,
to R.J. Kooman,
and to you,
if you have
read
this thesis
until the
very
end.

Contents

1 Introduction

What do clouds, whipped cream, milk, photographic film, cheese, smoke and marshmallows have in common with each other? One possible answer to that question is that these are all examples of colloidal dispersions. In general, a colloidal dispersion is a phase-separated mixture in which the dispersed phase has a typical size of approximately one nanometer up to a few micron. In addition to their abundance in everyday live, colloids are extensively studied in materials science,[1–4] the food industry,[5] for pharmaceutical purposes[6–9] and for their fundamental properties,[10–16] among other applications. In this work, we focus on one class of colloidal dispersions, in which the dispersed phase consist of mostly solid particles that are micron-sized, which from now on we call colloids or colloidal particles.

The typical size of colloidal particles sets them apart for two reasons: first, it is large enough for colloids to be observed using conventional light microscopy techniques. This is in stark contrast to, for example, molecular systems, which have length scales below a nanometer, or biological proteins, which can be tens of nanometers in size. Direct experimental measurements of dynamic properties in (bio)molecular systems are challenging because they require single-molecule measurement techniques with high spatial and temporal resolution. Instead, colloidal particles have been widely used as model systems for (macro)molecular structures,[17–19] because their behavior can be captured by simpler experimental techniques. Secondly, their size is small enough so that they are sensitive to thermal fluctuations, which makes them suitable as model systems for their smaller counterparts.

The properties of colloids that we will investigate here can be roughly divided into two topics: first, interactions between the colloidal particles and their environment. These include electrostatic interactions between a particle and a substrate or the hydrodynamic properties of different types of colloidal particles. Second, we study inter-particle interactions, such as the self-assembly of colloidal particles into larger structures. For both topics, it is important to know some fundamental properties of colloid science, which we will now briefly introduce.

Colloidal interactions

There is a large variety of interactions that can take place between colloidal particles and between colloids and their environment. Examples include electrostatic,[20,21] Van der Waals,[20,22] depletion,[23,24] magnetic,[25,26] hydrophobic/hydrophilic,[27,28] critical Casimir[29,30] or hydrodynamic interactions,[31–37] and many more. We will discuss some of the interactions that are relevant to the current work in this section.

Generally speaking, these interactions can be classified as either attractive or re-

pulsive and as either specific or nonspecific. For use in practical applications, it is of vital importance that the colloids are stable,[38] which means that the particles remain dispersed in the medium and do not form undesired aggregates. To this end, nonspecific attractive interactions need to be balanced by repulsive interactions.

Nonspecific attractive forces that tend to destabilize colloids are typically Van der Waals, or dispersion forces, which are attractive forces that arise from the interactions between instantaneous multipoles of the atoms and molecules that constitute the particles.[20,22] These interactions strongly depend on the distance r between colloids and decay as $1/r^6$.

Another example of nonspecific attractive forces are electrostatic interactions between surfaces of opposite charge, when attraction between the two surfaces is undesired, as is often the case between colloidal particles and the container walls, for example. In ionic solutions, electrical double layers are formed around charged surfaces, which consist roughly of a layer of adsorbed ions at the colloid surface and a diffuse layer of counterions further away from the surface.[20,39] Interactions between double layers of surfaces that carry opposite charges lead to an attractive force between them. Naturally, electrostatic interactions can also be used to encode (desired) specific repulsive interactions between colloids. In that case, the colloids are functionalized in such a way that their surface charge is nonzero and of the same sign. Like-charge repulsion between their electrical double layers then leads to colloidal stability, if this repulsion is greater than the nonspecific attractive forces acting on the particles.

A second important example of repulsive interactions between colloidal particles are entropic repulsive forces.[40] To that end, polymer chains are grafted on the surface of colloidal particles at a sufficient area density.[41,42] When two polymer coated particles approach each other, the polymer layers start to overlap. Because of excluded volume interactions between the polymer strands, the configurational entropy of the polymers is reduced: they have less room to move. This loss of configurational entropy results in an effective entropic repulsive force between the particles.[42] This method of entropic stabilization is also known as steric stabilization.

On the other hand, it is often desirable to form aggregates of colloidal particles that have specific properties, such as the desired size or shape. To enable the formation of specific clusters of colloidal particles, attractive interactions have to be used that act only between specific sets of particles. Examples include the electrostatic attraction of oppositely charged surfaces that was already discussed, depletion interactions,[23,24] magnetic interactions,[25,26] critical Casimir interactions,[29,30] or hydrophobic interactions.[27,28] Specifically, hydrophobic interactions are of interested in the context of this work, as these are responsible for the formation of the lipid bilayers[43–46] that form an integral part of the colloidal model systems presented here. Hydrophobic interactions cause dispersed objects that are nonpolar to maximize their contact with other hydrophobic surfaces, in order to minimize their contact with the surrounding aqueous medium. The exact origin of these interactions is not fully understood, but most likely originates from entropic effects, caused by the disruption of hydrogen

bond formation between water molecules by the hydrophobic moieties.[47]

Self-assembly

Having discussed some examples of possible attractive and repulsive interactions between colloidal particles, we are interested in studying how the interactions between colloidal building blocks can be used for bottom-up assembly of larger structures and materials. Such a bottom-up assembly process, where interactions between colloidal particles lead to the formation of specific structures without additional external input, is known as colloidal self-assembly.[3,4,28,48–58] Colloidal self-assembly has been used to fabricate a large variety of different structures that can have specific desired properties, such as specific crystal lattices that have photonic band gaps[1,2,59,60] or biomimetic materials that can be used as model systems for biological systems.[61–65]

Self-assembly requires specific interactions that can be provided by specialized molecules that can act as linkers between the colloids. For example, by using synthetically produced deoxyribonucleic acid (DNA) strands, DNA linkers can be fabricated. To understand how this works, we now briefly discuss the structure of the DNA double helix. The double helix structure of DNA is depicted schematically in Figure 1.1a. It consists of two sugar phosphate backbones that support a sequence of nucleobases. There are four nucleobases which each bind specifically only to one of the other bases, forming a base pair via hydrogen bonding: adenine (A) binds to thymine (T) and cytosine (C) binds to guanine (G). The complementary strands run in opposite directions, so that the 5'-end of one strand aligns with the 3'-end of the other. Figure 1.1b shows an electron microscopy image of a bundle of DNA strands, where the pitch of the DNA double helix structure is clearly visible.

By synthesizing two DNA strands that are complementary except for a few base pairs at the end, a double-stranded DNA linker is formed after hybridization, that contains a single-stranded overhang, or sticky end. As depicted in Figure 1.1c, by using two of these DNA linkers with complementary sticky ends, the linkers specifically bind with each other via Watson-Crick base paring. Because of the high specificity of DNA hybridization, these DNA strands can act as an "intelligent glue" between the micron-sized colloidal particles. As shown in Figure 1.1d, DNA linkers can for instance be employed to induce the crystallization of colloidal particles, which can be controlled by changing the temperature around the melting temperature of the sticky end.[69] DNA linkers have been employed in a large number of self-assembly studies[4,69–76] where a great variety of colloidal objects and materials with great potential for interesting applications were fabricated.

Apart from inter-particle interactions, there are two other important kinetic effects that are instrumental in self-assembly processes. First, in general, a colloidal system used for self-assembly starts in a state that is not in thermal equilibrium. Then, the free energy of the system is reduced during self-assembly, until either a local or a global minimum in the free energy of the system is reached. This can cause problems if the system can not transition from a certain local minimum in the free energy

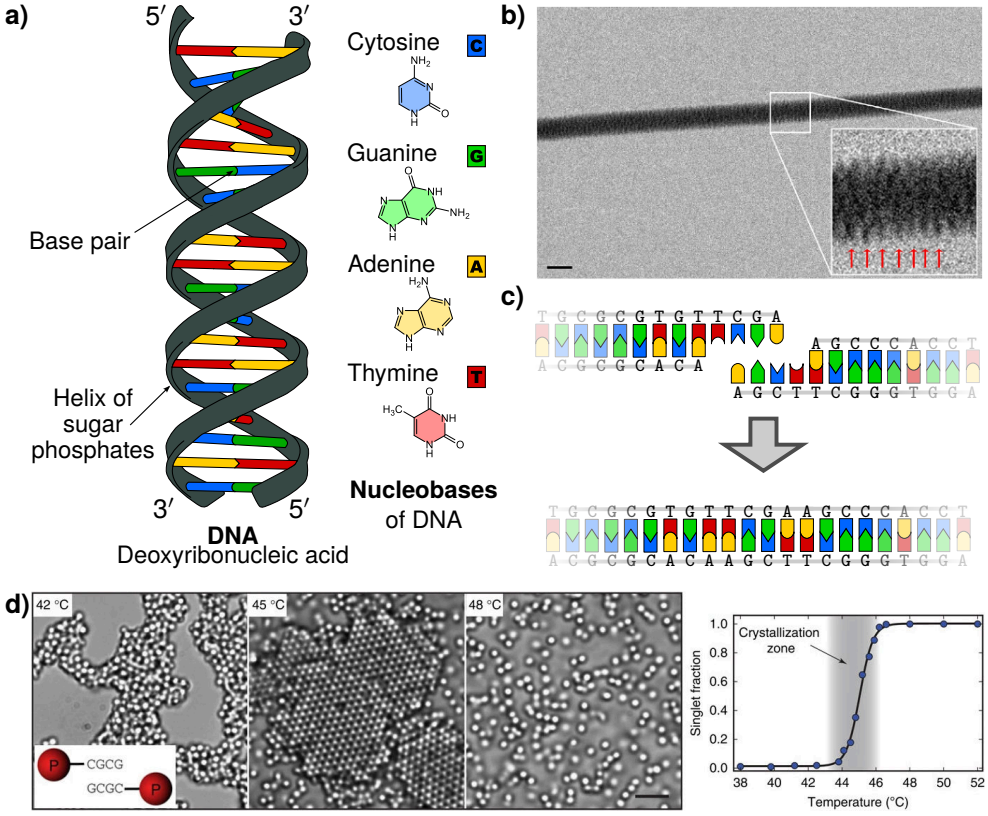

Figure 1.1: **Structure of DNA and crystallization of DNA coated colloids. a)** Schematic depiction of the DNA double helix and its base pairs: cytosine (C), guanine (G), adenine (A) and thymine (T). The two complementary strands run in opposite directions, so that the 5′-end of one strands aligns with the 3′-end of the other. **b)** Electron microscopy (EM) image of λ-DNA fibers. The inset zooms in on a part of the fiber, the red arrows indicate the 2.7 nm pitch of the double helix. Scale bar is 20 nm. **c)** Example of the hybridization of two complementary DNA sticky ends, consisting of four base pairs. The sequence is taken from the human hemoglobin α-subunit gene. **d)** Brightfield images showing the morphologies of amorphous (left, 42 °C), crystalline (middle, 45 °C) and unbound (right, 48 °C) assemblies of DNA-coated 1 µm colloids. Scale bar is 5 µm. Inset: schematic illustration of DNA-coated particles. The DNA is grafted to the particle surfaces. The particles are functionalized with DNA linkers that have CGCG (palindrome) sticky ends. Right: singlet particle fraction (unbound particles) of DNA-coated colloids as a function of temperature. The temperature window over which particle crystallization occurs is shaded. *Attribution: a) Reprinted (adapted) with permission from Gentile et al.*[66] *Copyright 2012 American Chemical Society. b) Adapted from "Difference DNA RNA" by Sponk*[67] *(CC BY-SA 3.0), via Wikimedia Commons. c) Adapted from "Ligation" by Ball*[68] *(CC0 1.0), via Wikimedia Commons. d) Adapted from Wang et al.*[69] *(CC BY 4.0).*

to the desired global minimal free energy state. In that case, the system is said to be kinetically arrested.[77] Various solutions have been proposed to overcome these kind of equilibration issues, such as by thermally annealing the system,[78,79] using directional interactions for greater control over the self-assembly pathway[51,53,80–83] or by using structures that are reconfigurable after they have formed.[57,58,84,85]

The second kinetic factor that determines the success of self-assembly is related to the typical range of the attractive interactions. By its definition, in colloidal self-assembly, interactions are local and therefore, typically short-ranged. This means that the rate at which particles approach each other close enough for them to interact has a large effect on the rate of the self-assembly process.[86,87] In the absence of external forces, mixing is typically a purely passive process, driven by the random diffusion or Brownian motion of the particles. Therefore, the diffusive properties of the constituents and their hydrodynamic interactions are of key importance to self-assembly processes as well.[36]

Brownian motion

The Brownian motion of colloidal particles is a central focus of this work. Brownian motion, which was first observed by the botanist Robert Brown in 1827, is well described by the (translated) words of Jean-Baptiste Perrin:[19] *"...all the particles situated in the liquid, instead of assuming a regular movement of fall or ascent, according to their density, are, on the contrary, animated with a perfectly irregular movement. They go and come, stop, start again, mount, descend, remount again, without in the least tending toward immobility."* We can make sense of this chaotic process by considering the first and second order moments of the particle displacements $\Delta \boldsymbol{r}(t+\tau)$ between a time t and a time $t+\tau$ later, where τ is the lag time between displacements. The first moment, $\langle \Delta \boldsymbol{r}(t+\tau) \rangle$ is equal to zero, which states that the average position of particles experiencing Brownian motion does not change in time. The amount of motion of the particles can instead be characterized by the second moment of particle displacements, or the mean squared displacement (MSD), which is equal to

$$\langle (\Delta \boldsymbol{r}(t+\tau))^2 \rangle = 2dD\tau, \tag{1.1}$$

with d the number of dimensions. D is the diffusion coefficient which characterizes the mobility of the particles. Einstein[17] and others[18,92] showed how this diffusion coefficient is related to the thermodynamic properties of the fluid and the size of the particle. For a spherical particle, the diffusion coefficient can be calculated using the Stokes-Einstein relation:[17,93]

$$D_{\text{sph.}} = \frac{k_B T}{6\pi\eta R_{\text{sph.}}}, \tag{1.2}$$

where k_B is the Boltzmann constant, used to describe the average thermal energy of each degree of freedom in a thermodynamic system, which equals $\frac{1}{2}k_B T$. The absolute temperature of the system is given by T, η is the viscosity of the medium and $R_{\text{sph.}}$ is the radius of the sphere.

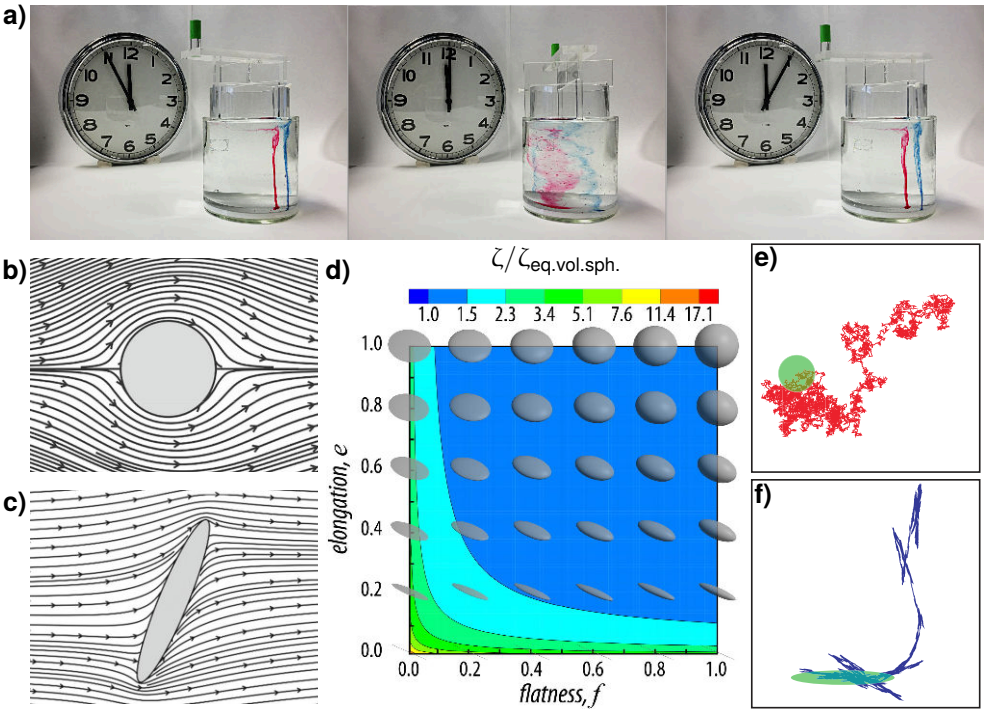

Figure 1.2: **Low Reynolds number hydrodynamics. a)** Left: Dye is injected in a viscous fluid (low Re) between two cilinders. Center: Rotating the fluid in one direction mixes the dyes and the fluid. Right: After the same amount of turns in the opposite direction, the dyes return to their approximate initial position. **b)** Streamlines of the 3D flow field around a 6:1 prolate spheroid in the equatorial plane, obtained by integration of the full Navier-Stokes equations at $Re = 1$ for an attack angle of 90 deg (the angle between the flow direction and the long axis). **c)** Streamlines for the same spheroid as in panel b, but now in the meridional plane for an attack angle of 67.5 deg. **d)** The ratio between the drag coefficient ζ of ellipsoids and the drag coefficient $\zeta_{\text{eq.vol.sph.}}$ of a sphere of the same volume as the ellipsoid shows marked size effects as function of flatness and elongation. **e)** Simulation of a 2D random walk for a sphere with diffusion coefficients $D_a = D_b = 0.5$. **f)** Same as in panel e, but for an ellipsoid with $D_a = 0.99$, $D_b = 0.01$. The total diffusion coefficient $D = (D_a + D_b) = 1.0$ is the same for both particles in panels e and f. Trajectories are shown during the time it takes an ellipsoid to rotate 1 rad. During this time, the behavior of the sphere (self-similar isotropic random walk) is very different from the ellipsoid (quasi 1D diffusion along the long axis). At longer times, the coarse-grained trajectories of both shapes correspond to an isotropic random walk. *Attribution: a) Adapted from "Time reversible flow demonstration" by Ved1123 [88] (CC BY-SA 4.0), via Wikimedia Commons. b+c) Reprinted by permission from Springer Nature: Andersson and Jiang, [89] copyright Springer Nature 2019. d) Reprinted from Bagheri and Bonadonna, [90] with permission from Elsevier. e+f) From Han et al. [91] Reprinted with permission from AAAS.*

Because of their small size, colloidal particles behave very differently in fluids compared to larger objects. A striking example is shown in Figure 1.2a, where two dyes are injected into a viscous fluid that is sandwiched between two cilinders. By rotating the cilinders with respect to each other, the fluid is sheared and the dyes and fluid mix, as shown in the center panel of Figure 1.2a. Amazingly, by rotating the cilinders by the same amount but in the opposite direction, the dyes return to their original position, as shown in the last panel of Figure 1.2a. The dyes are only slightly more spread out compared to their original position, which is caused by diffusion of the dye molecules in the intermediate time. Apart from this, the behavior of the dye particles in the viscous fluid shows time-reversal symmetry.

This behavior, which is not limited to "viscous" fluids, can be characterized by the Reynolds number Re, which is defined as[31]

$$Re = \frac{\rho_p u L_p}{\eta}, \tag{1.3}$$

with ρ_p the mass density of the particle, u the velocity of the particle with respect to the fluid, L_p the typical dimension of the particle (e.g. the radius in case the particle is spherical) and η the viscosity of the fluid. Reynolds numbers can be roughly characterized as high ($Re \gtrapprox 10^3$) or low ($Re \lessapprox 10$). A high Reynolds number is what we are typically used to in everyday live: for a human swimming in water*, $Re \approx 10^6$. In the high Reynolds number regime, flows are turbulent and the motion no longer has time-reversal symmetry: that means that if the swimmer moves their arms and legs in a symmetric back-and-forth motion, they can propel themselves. Conversely, at low Reynolds numbers, there is time-reversal symmetry. That means that a human swimming in peanut butter* ($Re \approx 4$) has to perform asymmetric forward and backward strokes, or they will be stuck in the same position indefinitely. The same holds true for colloidal particles: for micron-sized silica particles in water, the Reynolds number $Re \ll 1$. Fluid flows around the particle are therefore not turbulent, but laminar, as shown in Figure 1.2b for a circular cross section of a colloidal particle.

In addition to spherical particles, the Brownian motion at low Reynolds number of colloids of various shapes have been studied. These include ellipsoids,[91,95,96] boomerangs[14,97,98] and clusters.[12,13] These studies have revealed that shape affects the diffusive motion at short timescales. For example, it can be seen that the flow field around a circular cross section of an ellipsoid (Figure 1.2b) is very different from the flow field around a different cross section in the meridional plane,[89] as shown in Figure 1.2c. Moreover, as shown in Figure 1.2d, the drag coefficient ζ is also greatly affected by the shape of the particle. For a drag coefficient $\zeta = k_B T / D_T$, with D_T the translational diffusion coefficient, it was found that anisotropic particles typically have a higher drag coefficient compared to spheres of the same volume.[90]

*Here, $\rho_p = 1000\,\mathrm{kgm^{-3}}$, $u = 1\,\mathrm{ms^{-1}}$, $L_p = 1\,\mathrm{m}$ and $\eta = 0.001\,\mathrm{Pa\,s}$ for water and $\eta = 250\,\mathrm{Pa\,s}$ for peanut butter.[94] It is possible that the swimming speed will be lower in peanut butter, which will lower the Reynolds number further.

The drag coefficient of anisotropic particles is typically different along different particle symmetry axes. By comparing a random walk of a spherical particle in Figure 1.2e to that of an ellipsoidal particle in Figure 1.2f, it becomes apparent that they show very different trajectories.[91] While the sphere performs a self-similar isotropic random walk, the ellipsoid performs a quasi one-dimensional random walk in the direction of its long axis. Therefore, for particles of anisotropic shape at short timescales, Equation 1.1 can be generalized as follows

$$\langle X_i(t+\tau)\, X_j(t+\tau)\rangle = 2D_{ij}\tau, \tag{1.4}$$

where $X_i(t+\tau)$ is a generalized displacement corresponding to one of the degrees of freedom labeled by i (i.e. translational, rotational, ...) and D_{ij} is the element of a generalized diffusion tensor which relates the mobility of particle displacements corresponding to the degrees of freedom i and j. Diagonal elements of $\boldsymbol{D}$ where $i = j$ describe properties such as the translational diffusivity and the rotational diffusivity. Additionally, different diffusive modes can be coupled, e.g. helical particles rotate as they translate and vice versa.[99] These modes are described by the off-diagonal elements where $i \neq j$.

In general, the diffusion tensor $\boldsymbol{D}$ depends on the shape and size of the particle studied. Similarly to what is known for spherical particles, displacements of anisotropic particles are typically larger in directions that correspond to smaller hydrodynamic drag.[12–14,16,91,97] Therefore, the ellipsoid in Figure 1.2f primarily diffuses along its long axis at shorter timescales than the rotational diffusion time. The rotational diffusion time characterizes the time it takes for the particle to rotate 1 rad. At longer timescales, the influence of particle shape decreases, as the shape effects are averaged out because of rotational diffusion.[91]

While the Brownian motion of rigid particles has been extensively studied, little is known about the diffusive properties of flexible particles, that change their shape as they diffuse. This question is highly relevant, because many (macro)molecular systems found in nature display segmental flexibility. For most of these, reconfigurability also affect the biological function of the compound.[100–104] For such flexible structures, the diffusion tensor D_{ij} contains terms related to these internal deformation modes.[105–108] In turn, this shows that couplings between deformation modes and other degrees of freedom, such as translational or rotational diffusivity, are possible. The study of the diffusive properties of flexible structures is the main subject of Chapters 5–7.

Colloid-supported lipid bilayers

The study of the diffusivity of flexible colloidal structures was made possible by the development of DNA linker-functionalized colloid-supported lipid bilayers[110–112] (CSLBs). CSLBs are used in a diverse range of research areas and applications,[113] which range from drug delivery,[7–9,114–117] to bio-sensing applications[15,118] and more fundamental studies on lipid phase separation.[64,65] Of special interest to this work

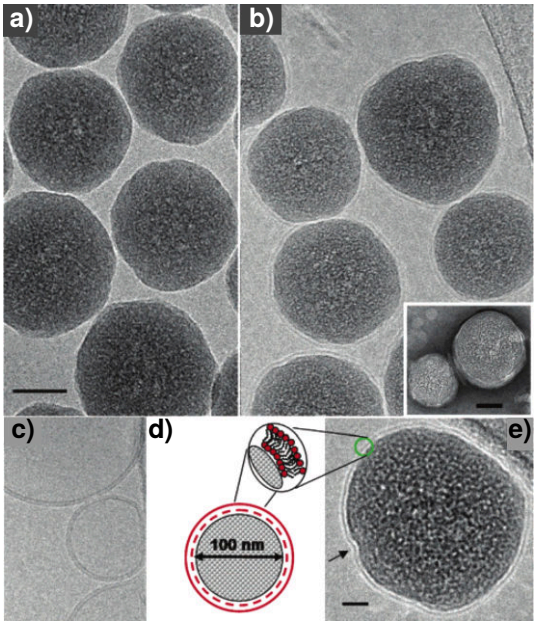

Figure 1.3: **Cryo-EM images of colloid-supported lipid bilayers (CSLBs). a)** 110 nm silica nanoparticles. The scale bar is 50 nm, the same magnification is used in panels b and c. **b)** Bilayer-functionalized silica nanoparticles formed by the rupture and spreading of liposomes. Inset: CSLBs imaged using a negative staining method. Scale bar is 50 nm. **c)** Several liposomes, the polar head groups of the two lipid layers are visible (darker rings). **d)** Schematic of a nanoparticle surrounded by a lipid bilayer. **e)** The bilayer is in close contact with the particle surface. Scale bar is 20 nm. *Attribution: Reprinted (adapted) with permission from Mornet et al.* [109] *Copyright 2004 American Chemical Society.*

are self-assembly applications.[85,110–112] Various properties of CSLBs are discussed extensively in Chapters 3–7.

CSLBs consist of solid colloidal particles surrounded by a fluid lipid bilayer. In Figure 1.3a, cryo-EM images of colloidal nanoparticles are shown, which can be functionalized with a lipid bilayer, as can be seen from Figure 1.3b. The bilayer is formed by the adhesion and rupture of small liposomes (shown in Figure 1.3c) on the particle surface. As depicted graphically in Figure 1.3d and shown in the cryo-EM image in Figure 1.3e, the bilayer is in close contact with the particle surface and follows its overall shape. Therefore, the particles act as a scaffold for the lipid bilayer. The shape of the particle in turn sets the shape of the lipid bilayer.[85] Interestingly, DNA linkers that are functionalized with a hydrophobic end group, or anchor, can be inserted into the bilayer surrounding the particle, via hydrophobic interactions between the lipids and anchor. Because of the fluidity of the bilayer, these linkers can freely surf over the particle.[110–112] Then, by functionalizing two sets of particles with two different DNA linkers with complementary sticky ends, self-assembled clusters of CSLBs can be formed that are bonded by the DNA linkers. But because the DNA linkers can diffuse over the particle surface, the particles in the cluster can also move with respect to one another, while remaining permanently bonded.

CSLBs surrounded by fluid membranes with surface-mobile binding groups are of great interest to a wide range of applications and fundamental problems. The flexible bonds that are provided by CSLBs open the door to answering numerous fundamental questions where flexibility plays a role, such as the study of the relation

between internal deformation modes and Brownian motion. In addition, their reconfigurability should allow for easier relaxation of self-assembled structures towards thermal equilibrium. This will enable the study of structural flexibility and its impact on phase behavior, such as in lattices that have a specific crystal structure or other sought after properties.[57,58,119,120] Furthermore, CSLBs, because of their lipid bilayer, can be thought of as biomimetic particles and are therefore of interest to model membrane and cell biology studies,[61–65] smart drug delivery[7–9,114–117] and bio-sensing applications.[15,118] Lastly, they may be used as building blocks in the fabrication of nano- to micron-sized robotic devices.[121–125]

Outline of this thesis

In this thesis, we study the impact of particle shape anisotropy, multivalent interactions and flexibility on systems of colloidal particles. This thesis is structured as follows:

In **Chapter 2**, we study the behavior of colloidal dimer particles that diffuse above a planar wall. Our results highlight the rich dynamics that nonspherical particles exhibit in the proximity of walls and can aid in developing quantitative frameworks for the dynamics of arbitrarily-shaped particles in confinement.

Having studied rigid anisotropic particles in Chapter 2, in the next chapters we extend this to anisotropic particles that have internal deformation modes. In Chapters 3–4, we study the fundamental properties of DNA-functionalized CSLBs, which form the basic building blocks of anisotropic colloids with flexible bonds. This, in turn, enables the study of flexibility on their conformational and diffusive properties in Chapters 5–7.

Specifically, in **Chapter 3**, we have studied colloidal systems that have internal degrees of freedom that allow for shape changes: CSLBs. We show how to optimize their functionalization, in order to obtain particles suitable for self-assembly experiments, which requires well-stabilized colloids with a homogeneous bilayer that is fully fluid.

Then, in **Chapter 4**, we have studied the multivalent interactions between DNA linker-functionalized CSLBs that can form flexible bonds. We characterize how linker depletion effects[84,126] could be used to limit the valency of self-assembled clusters made of CSLBs.

By taking advantage of the ability to limit the valency of clusters of CSLBs using low DNA linker concentrations, in **Chapter 5**, we have formed flexibly-linked colloidal chains of three CSLBs. We have measured the full diffusion tensor of these flexible trimers and have found marked flexibility-induced effects.

Based on these results, in **Chapter 6**, we study the conformational and diffusive behavior of flexibly-linked colloidal chains of three to six CSLBs. There, we find that the behavior of these chains can be described using results from polymer theory.

Because of their unique topology, in **Chapter 7**, we have assembled flexible rings of four and six CSLBs. We have quantified the differences between flexible chains, loops and domino lattices. Our findings could have implications for the flexibility of

floppy colloidal materials.

Finally, in the last chapter, we provide a short outlook on how to synthesize flexibly-linked particles with directional interactions. Our work demonstrates the rich dynamics and possibilities for applications of reconfigurable colloidal systems.

2 Heights and orientations of colloidal dumbbells near a wall

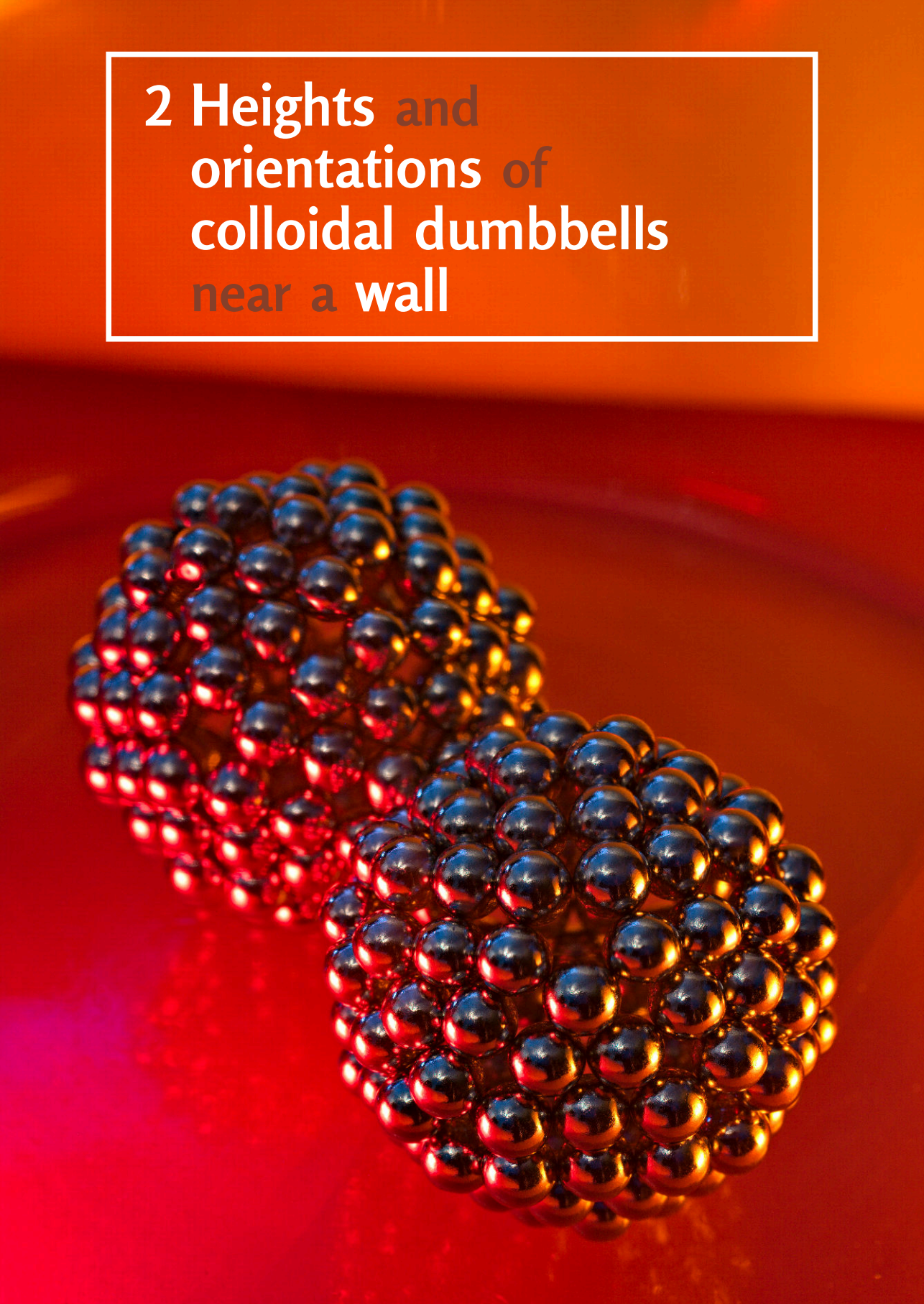

Geometric confinement strongly influences the behavior of microparticles in liquid environments. However, to date, nonspherical particle behaviors close to confining boundaries, even as simple as planar walls, remain largely unexplored. Here, we measure the height distribution and orientation of colloidal dumbbells above walls by means of digital in-line holographic microscopy. We find that while larger dumbbells are oriented almost parallel to the wall, smaller dumbbells of the same material are surprisingly oriented at preferred angles. We determine the total height-dependent force acting on the dumbbells by considering gravitational effects and electrostatic particle-wall interactions. Our modeling reveals that at specific heights both net forces and torques on the dumbbells are simultaneously below the thermal force and energy, respectively, which makes the observed orientations possible. Our results highlight the rich near-wall dynamics of nonspherical particles, and can further contribute to the development of quantitative frameworks for arbitrarily-shaped microparticle dynamics in confinement.

2.1 Introduction

The behavior of micron-sized colloidal particles under confinement has been a subject of intensive research in engineering, materials science, and soft matter physics.[10] Such particles often serve as model systems for understanding the effects of confinement on microscale processes, e.g. structure formation and rheology, offering quantitative insights into the behavior of biological systems.[127–129] This understanding is further desirable for various applications where confinement dictates the dynamics, ranging from improving microfluidic transport in lab-on-a-chip devices,[130] growing low-defect photonic crystals[1] and tuning pattern formation for materials design.[131–133]

Confinement can strongly affect hydrodynamic and electrostatic (self-)interactions. These effects depend on particle-wall separation as well as particle size and shape.[134] Yet, the majority of research has focused on the behavior of spherical particles, both from a theoretical and experimental standpoint. This includes the behavior of single spheres close to a planar wall,[32,135–142] between two walls[143–146] and microchannels.[147,148] Going beyond single particle dynamics, the collective behavior of sphere clusters and dense suspensions has also been examined close to,[37,149] as well as in between walls,[150] microchannels[151,152] and confining droplets.[153]

However, microparticles involved in biological processes and industrial applica-

tions typically depart from the ideal spherical shape. Since the motion of nonspherical particles is different from that of spherical ones,[13,31,91,154,155] there is a need to study the effect of confinement on nonspherical particles[156] to gain proper understanding of both naturally occurring and technologically relevant systems. For nonspherical colloids, dynamics have typically been measured far from walls.[13] Despite predictions for axisymmetric particles[157] and simulated studies for arbitrary shapes,[158,159] the effect of particle-wall separation remains experimentally unexplored. Yet, the interplay between shape anisotropy and wall separation ought to be examined as well, to develop accurate model systems for molecular matter.

To date, a plethora of techniques has been employed for colloidal studies, including optical microscopy,[160] optical tweezers,[144,161–163] light scattering,[164–167] evanescent wave dynamic light scattering (EWDLS),[143,149,168–171] total internal reflection microscopy (TIRM),[139,172,173] TIRM combined with optical tweezers,[174] holographic microscopy,[175,176] and holographic optical tweezers.[37] Each of these techniques has its own strengths and weaknesses, especially when it comes to measuring anisotropic particle dynamics near walls with high spatiotemporal resolution in three dimensions. For example, optical microscopy is a straightforward technique, yet lacks sensitivity to out-of-plane motion. Confocal microscopy on the other hand provides accurate three-dimensional measurements, but is relatively slow when recording image stacks and additionally requires refractive index matching and fluorescent labeling. Optical tweezers confine particle motion and hence hinder long-term three-dimensional measurements, while light scattering determines ensemble properties and is thus difficult to interpret in the case of anisotropic particles.[177] TIRM is an elaborate technique that provides high resolution, though its range is limited to the near-wall regime, typically less than 400 nm from the wall.[139,172–174]

To overcome the above limitations, holographic microscopy may be employed instead, as it records both position and shape[178] with high resolution,[176] also in the out-of-plane direction. In addition, it is even capable of resolving weakly-scattering objects as used in biology[175,179–181] without the need for fluorescent labeling.[182] Moreover, while measurements are typically performed using lasers, a cost-effective holographic microscopy setup can also be constructed using an LED mounted on an existing microscope.[181] As a downside, analyzing holographic measurements may be computationally expensive which, if desired, can be compensated by implementation of a neural network[183] at the expense of some accuracy loss.

In this chapter, we measure colloidal dumbbell dynamics above a planar wall, a simple model system that enables the study of the effects of shape anisotropy on confined dynamics. We accurately probe how the particle orientation is affected by the presence of the wall, and specifically, the particle-wall separation by means of digital in-line holographic microscopy. We find that smaller dumbbells are oriented at nonzero angles with respect to the wall, while in contrast, larger dumbbells of the same material are oriented mostly parallel to the wall. In all cases, we were able to identify the relation between particle orientation and particle-wall separation. We further compare our experimental findings to a minimal model for the dumbbell that

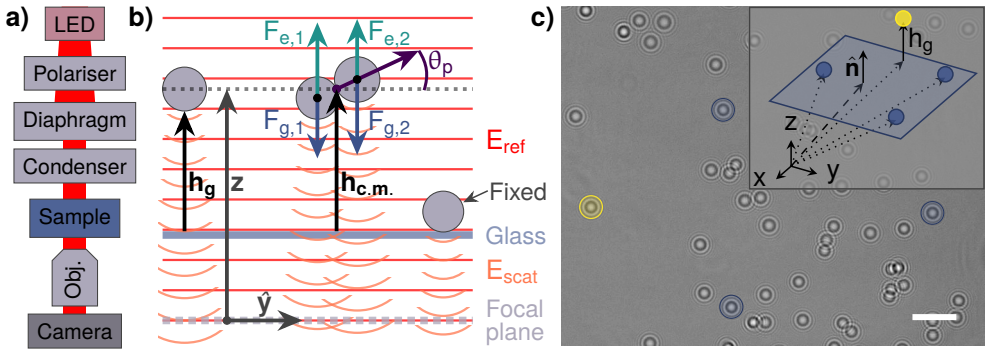

Figure 2.1: **Measuring particle-wall separation with in-line holographic microscopy (HM). a)** Schematic representation of the light path of our setup. **b)** Holograms are formed by the interference of the reference field E_{ref} with the scattered field E_{scat}. We are interested in the gap height h_g (or equivalently the center of mass (c.m.) height $h_{\text{c.m.}}$) with respect to a planar glass wall. **c)** We determine the position of the wall by fitting a plane to the positions of at least three particles fixed on the wall (blue). The gap height h_g between a diffusing particle (yellow) and the wall is the distance between the particle's measured position and its position projected on the plane along $\hat{n}$.

combines gravitational and electrostatic dumbbell-wall interactions. We find that, despite its simplicity, the model provides qualitative insight into our observations. Our results highlight the importance of wall effects on anisotropic particle motion, and may ultimately contribute to the development of a quantitative framework for the dynamics of particles with arbitrary shapes in confinement, not fully established at present in the literature.

2.2 Methods

2.2.1 Materials

We used spherical silica particles* of diameter (1.10 ± 0.04) µm (size polydispersity (PD) 3.7 %) prepared following the method of Zhang et al.[184] Briefly, 0.5 mL tetraethyl orthosilicate (TEOS) diluted with 2 mL ethanol was added to a mixture of 50 mL ethanol and 10 mL ammonia (25 %). The mixture was stirred magnetically for 2 h. The seed particles were grown to the desired size by adding 5 mL TEOS diluted with 20 mL ethanol during 2 h using a peristaltic pump. The dispersion was stirred overnight and washed by centrifuging and redispersing in ethanol three times. We obtained their diameter and PD from transmission electron micrographs using ImageJ,[185] by fitting particle diameters with the software's builtin functions.

In addition, we used (2.10 ± 0.06) µm diameter (PD 2.8 %) spherical silica particles

*The 1.1 µm spherical silica particles and the TEM images were provided by Dr. Samia Ouhajji.

purchased from Microparticles GmbH. In all experiments, dumbbell particles are naturally occurring aggregates of two spherical particles. All solutions were prepared with fresh ultra-pure Milli-Q water (Milli-Q Gradient A10, 18.2 MΩ cm resistivity). Glass cover slips were purchased from VWR and were used as received.

2.2.2 Holographic setup

We employed a digital inline holographic microscopy (DIHM) setup based on existing examples.[181] Our setup made use of an inverted microscope (Nikon Ti-E) equipped with a 60× oil immersion objective (NA = 1.4). To generate a scatter pattern, we used a 660 nm light-emitting diode (LED) source (Thorlabs M660L4) at its maximum power (3120 mW, using a Thorlabs LEDD1B LED driver), mounted on the lamphouse port of the microscope instead of the standard brightfield lamp (see Figure 2.1a for a schematic). Prior to each measurement, we performed a Köhler illumination procedure in brightfield mode to align the diaphragm and condenser. Additionally, we employed a linear polarizer on top of the condenser to improve the quality of the holograms by enforcing a specific polarization direction.

2.2.3 Sample preparation and measurement details

Spherical silica particles of either 1.1 or 2.1 μm diameter were spin coated from ethanol at dilute concentration onto the glass cover slips, which fixated their position. The cover slips were then placed at the base of the sample holder, serving as the walls relative to which particle motion was measured. The fixated-to-the-wall spheres served as reference points for determining the position of said wall (see also Figure 2.1b and 2.1c as well as the discussion in Section 2.2.5). Afterwards, an aqueous dispersion of particles of the same size was added in the sample holder, which was subsequently entirely filled with water and covered at the top with a glass cover slip to prevent drift. The dispersion contained single spheres as well as small fractions of dumbbell particles that consisted of two touching spheres, see also Figure 2.1b for an illustration. The motion of all particles above the wall was recorded at a frame rate of 19 fps for at least 6 minutes.

2.2.4 Analysis of holograms

For all measurements, the recorded holographic microscopy images were corrected with background as well as darkfield images to minimize errors stemming from interfering impurities along the optical train. Then, for each measurement, the particle of interest was selected manually and a circular crop around its hologram was taken, see also Figure 2.2 Plot 4a, to reduce the amount of pixels considered during model fitting, thereby increasing computational efficiency. From the holograms, we determine the three-dimensional position, (x, y, z), the radius, R, and refractive index, n, of the spheres and dumbbells as described in subsections 2.2.4 and 2.2.4, respectively.

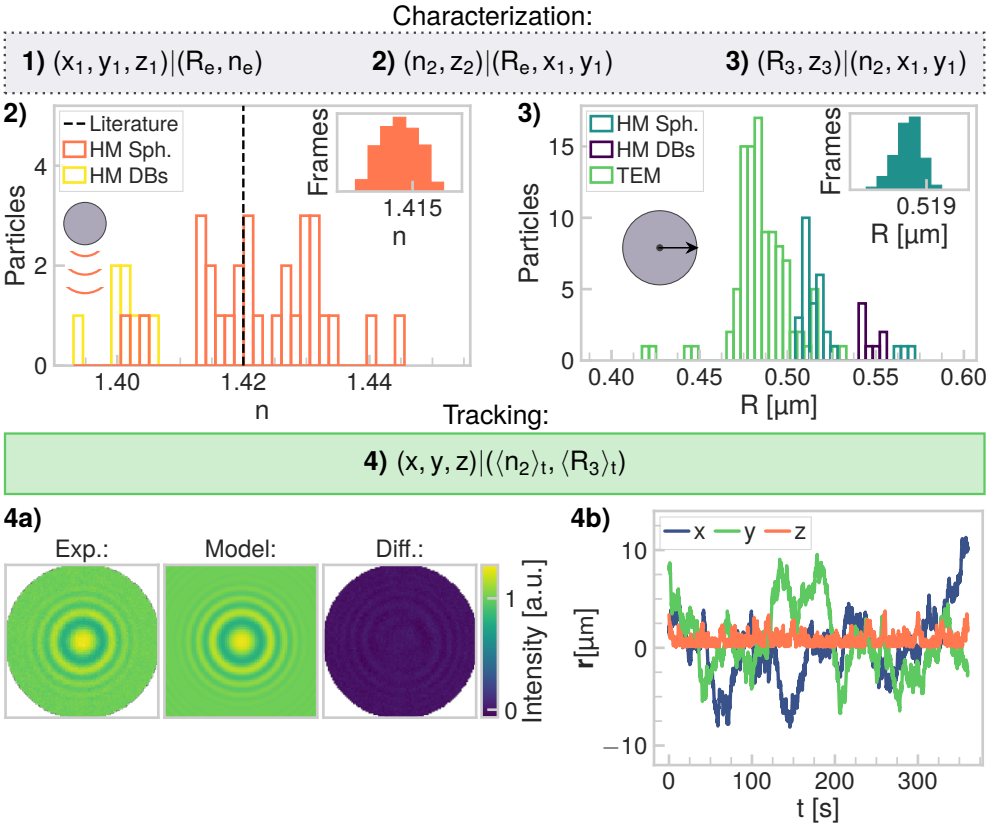

Figure 2.2: **Tracking particle positions with HM.** The 3D position of the particles in time is fitted in four steps: the first three are characterization steps, in which we find the approximate 3D position (fitting step 1) as well as appropriate guesses for the refractive index n (fitting step 2) and radius R (fitting step 3). In the fourth step, we use these positions and the average n and R values to determine the 3D position accurately (fitting step 4). All steps are explained in detail in Section 2.2.4. **Plot 2)** Average n obtained from fitting step 2 for both spheres and dumbbells, the inset shows a distribution from a single measurement. **Plot 3)** Average R obtained from fitting step 3 for both spheres and dumbbells, the inset shows a distribution from a single measurement. For comparison, we show particle radii measured using TEM. **Plot 4a)** Comparison of an experimental image, the fitted model and the residual for a sphere, the low values of which indicate the good agreement between experimental data and model. **Plot 4b)** Final 3D position in time for an $R = 0.55\,\mu\text{m}$ sphere, as obtained in fitting step 4.

Spherical particles

To fit the experimental data, we performed least-squares fits of a model based on Mie scattering theory[175] using the Python package HoloPy[186] (see Figure 2.2 Plot 4a as an example). The 3D position of the particles in time was fitted in four steps, as depicted in Figure 2.2: the first three are characterization steps to find the approximate 3D position (fitting step 1) as well as appropriate guesses for the refractive index n (fitting step 2) and the radius R (fitting step 3). In the fourth step, we used these positions and the average values of the radius and refractive index to determine the 3D position accurately (fitting step 4). We will now discuss these steps in detail. The subscripts correspond to the fitting step in which each parameter was determined.

Fitting step 1) For each frame, we determined the rough particle position (x_1, y_1, z_1), using reasonable estimates for the radius R_e and refractive index n_e.

Fitting step 2) For the current frame, we determined z_2 and characterized the particle refractive index n_2, while keeping the (x_1, y_1) position and the estimated radius R_e fixed. Example distributions and average values of the refractive indices obtained in this fitting step are shown in Figure 2.2 Plot 2.

Fitting step 3) Whilst keeping the (x_1, y_1) position and the estimated refractive index n_2 fixed, we fitted z_3 and the radius R_3. Example distributions and average values of the radii obtained in this fitting step are shown in Figure 2.2 Plot 3.

Fitting step 4) Once the initial positions (x_1, y_1, z_3) and particle properties (n_2, R_3) were determined for all frames, we calculated the time averaged over all frames properties ($\langle n_2 \rangle_t$, $\langle R_3 \rangle_t$). Lastly, we performed a least-squares fit for each frame allowing (x, y, z) to vary, keeping ($n = \langle n_2 \rangle$, $R = \langle R_3 \rangle$) fixed (Figure 2.2 Plot 4b).

Following this procedure, we minimized unwanted correlations between (z, R, n) that can arise when allowing all parameters to vary at once during the fit. For every frame, save the initial one, we used the values of the previous frame as starting guesses to speed up the (convergence of the) analysis.

Dumbbell particles

The steps followed to obtain particle properties and positions of the dumbbells were analogous to those of the single spheres, only modified to additionally account for determining the dumbbell orientations. The scattering pattern of the dumbbell, calculated using the T matrix (or null-field) method,[187] was modeled using the Python package HoloPy.[186] We used three characterization fitting steps to find the approximate 3D position and orientation (fitting step 1) as well as appropriate guesses for refractive indices $n^{(A)}$, $n^{(B)}$ (fitting step 2) and the radii $R^{(A)}$, $R^{(B)}$ (fitting step 3). $R^{(A)}$, $R^{(B)}$ are the radii of the respective 'A' and 'B' spheres of the dumbbell with refractive indices $n^{(A)}$, $n^{(B)}$. In the fourth and final step, we used these positions, orientations and the average values of the radii and refractive indices to determine the 3D position and orientation accurately (fitting step 4). We will now discuss these steps in detail. The subscripts correspond to the fitting step in which each parameter was determined.

Fitting step 1) In this first step, we determined (x_1, y_1, z_1, α_1, β_1, γ_1) of the center

of mass (c.m.), with ($R_e^{(A)}$, $n_e^{(A)}$, $R_e^{(B)}$, $n_e^{(B)}$) set to reasonable estimates. Here, (α, β, γ) correspond to the three Euler angles using the ZYZ-convention, while (x, y, z) denote the c.m. positions and, again, numbered subscripts the fitting step in which the parameter was obtained.

Fitting step 2) We determined the refractive indices and z-position ($n_2^{(A)}$, $n_2^{(B)}$, z_2) while keeping the parameters (x_1, y_1, α_1, β_1, γ_1, $R_e^{(A)}$, $R_e^{(B)}$) fixed.

Fitting step 3) Radii and z-position ($R_3^{(A)}$, $R_3^{(B)}$, z_3) were fitted while (x_1, y_1, α_1, β_1, γ_1, $n_2^{(A)}$, $n_2^{(B)}$) were kept constant.

Fitting step 4) After determining the initial positions (x_1, y_1, z_3), orientations (α_1, β_1, γ_1) and particle properties ($n_2^{(A)}$, $n_2^{(B)}$, $R_3^{(A)}$, $R_3^{(B)}$) for all frames, we calculated the time averaged properties ($n^{(A)} = \langle n_2^{(A)} \rangle_t$, $n^{(B)} = \langle n_2^{(B)} \rangle_t$, $R^{(A)} = \langle R_3^{(A)} \rangle_t$, $R^{(B)} = \langle R_3^{(B)} \rangle_t$) over all frames. Then, we performed a least-squares fit for each frame again, where we allowed (x, y, z, α, β, γ) to vary, keeping ($R^{(A)}$, $R^{(B)}$, $n^{(A)}$, $n^{(B)}$) fixed.

Following this procedure, we minimize unwanted correlations between (α, β, γ, z, $R^{(A)}$, $R^{(B)}$, $n^{(A)}$, $n^{(B)}$) that can arise when allowing all parameters to vary at the same time. For every frame, save the initial one, we used the values of the previous frame as starting guesses to speed up the analysis. On that note, we additionally restricted the differences in rotation angles between subsequent frames to be smaller than 90 deg. Finally, we used the open-source TrackPy implementation[188] of the Crocker-Grier algorithm[189] to link the individual sphere positions between frames into continuous trajectories, ensuring a correct and consistent orientation of the dumbbell. Because we assign specific labels to both particles in the first frame of the video, we can distinguish the particles, and in turn, between positive and negative orientations, throughout the video.

2.2.5 Particle-plane separation

The position and orientation of the wall was accurately determined from the three-dimensional positions of at least three spin coated spheres that were irreversibly fixed to the wall. This served two purposes: first, to speed up the fit of the mobile particles under study by providing a reliable lower bound on their axial position, and second, to accurately determine their height from the wall. A reference point on the plane $\mathbf{r}_p = (0, 0, z_p)$ and a normal vector $\mathbf{n}_p$ (see the inset of Figure 2.1c) were determined for all the fixed particles for each frame. Using $\mathbf{r}_p$ and $\mathbf{n}_p$, the particle-plane separation along the normal vector $\mathbf{n}_p$ was determined for the mobile spheres (see also Figure 2.3) from $\mathbf{n}_p \cdot (\mathbf{r} - \mathbf{r}_p) - R$, with $\mathbf{r}$ and R the position and radius of the sphere, respectively. For the dumbbells, particle-plane separation was determined using the same procedure as the individual spheres; both the c.m. height, $h_{\text{c.m.}} = \mathbf{n}_p \cdot (\mathbf{r}_{c.m.} - \mathbf{r}_p)$, above the wall is reported, as well as gap heights of both the lower and upper sphere. Note that since the orientation of the dumbbell can flip, the lower (or upper) sphere is not necessarily always the same physical particle.

2.2.6 Sphere height distribution

To model the height distributions of the spherical particles above the wall in Section 2.3.1, we used a model that combines electrostatic and gravitational effects[39,134] to calculate the total height-dependent force $F(h_{\text{c.m.}})$ in the z direction (see also schematic in Figure 2.1b):

$$F(h_{\text{c.m.}}) = F_e(h_{\text{c.m.}}) + F_g \tag{2.1}$$

$$F_e(h_{\text{c.m.}}) = 64\pi\epsilon\kappa R \left(\frac{k_B T}{e}\right)^2 \tanh\left(\frac{e\Psi_w}{4k_B T}\right) \tanh\left(\frac{e\Psi_p}{4k_B T}\right) e^{-\kappa h_{\text{c.m.}}} \tag{2.2}$$

$$F_g = -\frac{4}{3}\pi R^3 \left(\rho_p - \rho_f\right) g \tag{2.3}$$

with $h_{\text{c.m.}}$ the height of the center of the sphere, $F_e(h_{\text{c.m.}})$ the force due to overlapping electric double layers of the particle and the wall, F_g the gravitational force, ϵ the dielectric permittivity of water, k_B the Boltzmann constant, $T = 300\,\text{K}$ the temperature, e the elemental charge, Ψ_p and Ψ_w the Stern potentials of the particle and wall respectively, $\rho_p \approx 2.0\,\text{g cm}^{-3}$ the particle density, ρ_f the density of water, g the gravitational acceleration and κ^{-1} the Debye length. Based on the pH of our solution (pH≈5.5), we find that the solution ionic strength is approximately $I = 10^{-5.5} = 3 \times 10^{-6}\,\text{M}$. Therefore, the Debye length is expected to be $\kappa^{-1}(\text{nm}) = 0.304/\sqrt{I(M)} = 175\,\text{nm}$,[20] in good agreement with the fit values of 100 to 230 nm that we obtained by fitting Equations 2.7 and 2.11 to the experimental data for both sphere and dumbbell particles, respectively. We neglected van der Waals interactions; we used the Derjaguin approximations for F_e. For the electrostatic potential, we used the Debye-Hückel approximation,

$$\Psi(r) = \Psi_s \frac{R}{r} \exp\big(-\kappa(r - R)\big), \tag{2.4}$$

with $\Psi(r)$ the electrostatic potential at a distance r from the center of the particle and Ψ_s the Stern potential. By setting $\Psi(r = 1/\kappa)$ equal to the here measured zeta potential of the spherical particles, see values in Section 2.3.1, we calculated an approximate value for the Stern potential. This we subsequently used as a starting value for the least-squares fit of the model to our experimental height distributions. For the wall, we converted the zeta potential value of $-55\,\text{mV}$[190] to an approximate Stern potential using Equation 2.4. For ρ_p and Ψ_p we used $\pm 2\sigma$ bounds; we fixed Ψ_w to the calculated value as discussed above, and put no restrictions on κ.

To calculate the expected height distribution, we first obtained the electrostatic and gravitational potential energy, $\phi_e(h_{\text{c.m.}})$ and $\phi_g(h_{\text{c.m.}})$, respectively, from the force,

$$\phi_e(h_{\text{c.m.}}) = F_e(h_{\text{c.m.}})/\kappa \tag{2.5}$$

$$\phi_g(h_{\text{c.m.}}) = -F_g h_{\text{c.m.}}, \tag{2.6}$$

which we then used to derive the appropriate Boltzmann distribution,

$$p(h_{\text{c.m.}}) = A \exp\left(-\frac{\phi_e(h_{\text{c.m.}}) + \phi_g(h_{\text{c.m.}})}{k_B T}\right), \tag{2.7}$$

up to a normalization constant A.[134]

2.2.7 Sphere near-wall diffusion

To test the validity of our measuring approach and the accuracy of our extracted gap heights above the wall, we sought to compare our measurements to theoretical predictions. To this end, and since well established predictions exist for spheres alone, we determined the translational diffusion coefficient for our sphere measurements as function of gap height. To calculate the translational diffusion coefficient with gap height in Section 2.3.1, we proceeded as follows: instead of binning particle trajectories in time leading to bins with large height variations, we split all trajectories into shorter trajectories for which the gap height stayed within a certain height range, typically binning the total height range in bins of 0.30 μm and 0.12 μm for the 1.1 and 2.1 μm spheres, respectively. For each height bin, the in-plane mean squared displacement (MSD, $\langle \Delta r^2 \rangle$) was calculated. The in-plane translational diffusion coefficient D and its error (standard deviation), was obtained from the first data point, typically an average of at least 300 measurements, of the MSD corresponding to a lagtime Δt of 0.053 s using $\langle \Delta r^2 \rangle = 4D\Delta t$.

2.2.8 Modeling forces and torques on the dumbbell

To elucidate dumbbell behaviors above the wall presented in Section 2.3.3, we extended the sphere model of Section 2.2.6 to our dumbbells. To this end, we approximated the gravitational and electrostatic forces acting on a dumbbell, by assuming that the spheres which comprise the dumbbell interact with the wall individually, as though the other is not present. That is, we use the expressions from Equations 2.1–2.3 on each sphere, see Section 2.3.4 for the results. This approximation ignores the distortion of the electrostatic double layer caused by the presence of the other sphere, but allows us to derive predictions efficiently. We discuss the consequences of this approximation in Section 2.3.4. The total force and torque acting on the dumbbell c.m. are thus given by:

$$F_{DB} = F(h_1) + F(h_2) \tag{2.8}$$

$$T_{DB} = ((\mathbf{r}_1 - \mathbf{r}_{c.m.}) \times F(h_1)\mathbf{e}_z + (\mathbf{r}_2 - \mathbf{r}_{c.m.}) \times F(h_2)\mathbf{e}_z) \cdot \mathbf{e}_x \tag{2.9}$$

with h_i, $\mathbf{r}_i$ the height and position of sphere i, θ_p the angle between the long axis of the dumbbell and the wall and $\mathbf{e}_j$ the unit vector along the $j \in [x, y, z]$ axis (see Figure 2.1b for a schematic).

From the force expressions acting on the individual spheres of the dumbbell, we

calculated the corresponding potential energy:

$$\phi_{DB}(h_{\text{c.m.}}, \theta_p) = -2F_g h_{\text{c.m.}} + \frac{2F_e(h_{\text{c.m.}})}{\kappa} \cosh\Big(\kappa R \sin\theta_p\Big). \tag{2.10}$$

Equation 2.10 assumes both spheres to have the same radius, see Equation 2.17 for a general expression for dumbbells made of spheres of unequal radii. This potential can be differentiated with respect to the $h_{\text{c.m.}}$ to obtain the force and to θ_p to obtain the torque. We subsequently used the potential to derive the appropriate height distribution for the dumbbell c.m. $p_{DB}(h_{\text{c.m.}}, \theta_p)$ up to a normalization constant,

$$p_{DB}(h_{\text{c.m.}}, \theta_p) \propto K \exp\left[-\frac{\phi_{DB}(h_{\text{c.m.}}, \theta_p)}{k_B T}\right] \tag{2.11}$$

$$p_{DB}(h_{\text{c.m.}}) \propto \int_{-\frac{\pi}{2}}^{\frac{\pi}{2}} d\theta_p \cos(\theta_p) K \exp\left[-\frac{\phi_{DB}(h_{\text{c.m.}}, \theta_p)}{k_B T}\right], \tag{2.12}$$

$$p_{DB}(\theta_p) \propto \int_{R}^{h_{max}} dh_{\text{c.m.}} K \exp\left[-\frac{\phi_{DB}(h_{\text{c.m.}}, \theta_p)}{k_B T}\right], \tag{2.13}$$

where we evaluated Equation 2.12 by numeric integration over all possible plane angles θ_p, and Equation 2.13 by numeric integration over all possible heights $h_{\text{c.m.}}$; h_{max} was set to 5 µm. K represents the particle-wall hard-core interaction potential contribution to the Boltzmann weight: $K = 1$ if both spheres of the dumbbell are above the wall; otherwise $K = 0$. We have calculated the probability as function of the lowest dumbbell gap height (i.e., the separation between the wall and the bottom of the lower sphere of the dumbbell) by substituting $h_{\text{c.m.}} = h_{g,l} + R + R\sin\theta_p$ in Equation 2.12. Equivalently, for the upper gap height, we substituted $h_{\text{c.m.}} = h_{g,u} + R - R\sin\theta_p$ in Equation 2.12 to derive its distribution.

Modeling dumbbells of differently sized spheres

Next, we derive the electrostatic and gravitational forces on a dumbbell of two unequally sized spheres of radii $R = R_1, R_2$ and use it to calculate the potential energy and probability density function in terms of c.m. height $h_{\text{c.m.}}$ and plane angle θ_p. The force $F(R, h)$ on one of the spheres is given by Equation 2.1. The net force $F_{DB}(R_1, R_2, h_{\text{c.m.}}, \theta_p)$ is then given by

$$F_{DB} = F(R_1, h_1) + F(R_2, h_2), \tag{2.14}$$

$$h_1 = h_{\text{c.m.}} + \frac{R_2^3(R_1 + R_2)\sin\theta_p}{R_1^3 + R_2^3} \tag{2.15}$$

$$h_2 = h_1 - (R_1 + R_2)\sin\theta_p \tag{2.16}$$

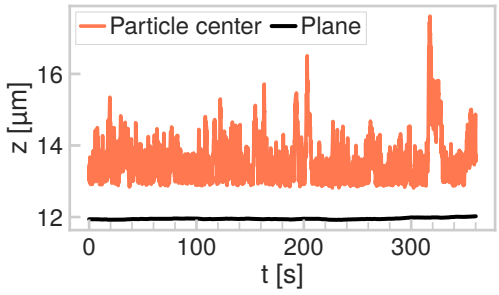

Figure 2.3: **Sphere-wall gap height.** The z positions of a spherical particle diffusing above a wall, as well as that of the plane (directly below the particle) obtained from the positions of three spheres fixed on the wall, are plotted in time. Using the plane z position, the gap height h_g between the diffusive particle and wall is determined.

Equation 2.14 can be integrated to give the potential energy $\phi_{DB}(R_1, R_2, h_{\text{c.m.}}, \theta_p)$

$$\phi_{DB} = \phi_{DB,g} + \phi_{DB,e} \tag{2.17}$$

$$\phi_{DB,g} = -\Big(F_g(R_1)h_1 + F_g(R_2)h_2\Big) \tag{2.18}$$

$$\phi_{DB,e} = \frac{B(R_1)}{\kappa}\exp\left[-\kappa h_1\right] + \frac{B(R_2)}{\kappa}\exp\left[-\kappa h_2\right]. \tag{2.19}$$

This potential can be derived with respect to the $h_{\text{c.m.}}$ to obtain the force and to θ_p to obtain the torque. We subsequently used the potential to derive the appropriate height distribution for the dumbbell c.m. $p_{DB}(R_1, R_2, h_{\text{c.m.}}, \theta_p)$ up to a normalization constant,

$$p_{DB}(R_1, R_2, h_{\text{c.m.}}, \theta_p) \propto K \exp\left[-\frac{\phi_{DB}}{k_B T}\right]. \tag{2.20}$$

K represents the particle-wall hard-core interaction potential contribution to the Boltzmann weight: $K = 1$ if both spheres of the dumbbell are above the wall; otherwise $K = 0$.

2.3 Results and Discussion

2.3.1 Characterization, height distribution and diffusion of spherical particles above a substrate

First, we measured the sphere dynamics above a planar wall both to assess the sensitivity of our LED-based in-line holographic microscopy setup, as well as to verify our new method of using fixed particles to accurately locate the position of the wall. Indeed, despite the simplicity of our setup, we find an excellent agreement between the measured holograms and the Mie scattering-based model, see Figure 2.2 Plot 4a for a direct comparison that additionally shows the residual between data and model. Moreover, in steps 2 and 3 of Figure 2.2 we show the refractive indices and particle radii that we obtained during characterization, respectively. Both parameters agree with expectations: the refractive index, $n_{\text{silica}} = (1.42 \pm 0.02)$ agrees with the value provided by the supplier (1.42) and at the same time the radius of the particles ((0.51 ± 0.03) μm) follows our TEM results ((0.48 ± 0.03) μm).

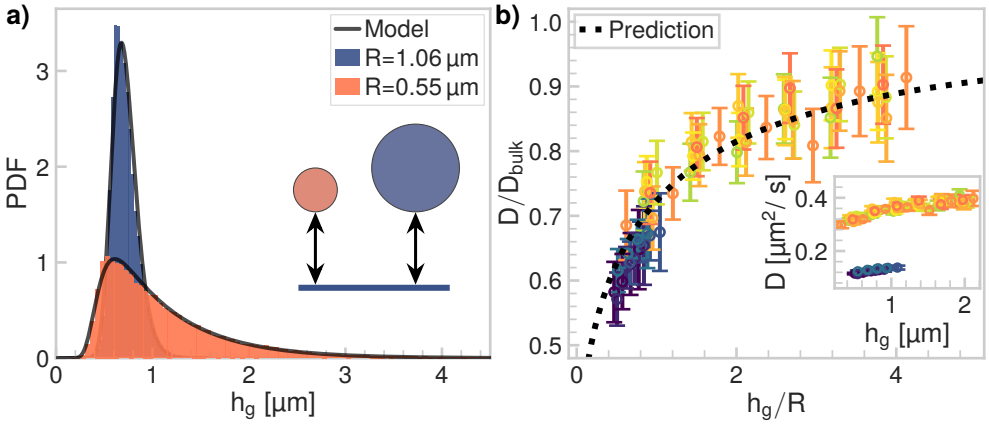

Figure 2.4: **Sphere-wall gap height and translational diffusion above a planar wall. a)** Experimental sphere-wall gap height distributions together with a fit with the model from Wu and Bevan [134] which combines gravitational and electrostatic effects for 1.1 µm (orange, fit parameters $\rho_p = 2.1\,\mathrm{g\,cm^{-3}}$, $1/\kappa = 107\,\mathrm{nm}$, $\zeta_p = -41\,\mathrm{mV}$) and 2.1 µm (blue, fit parameters $\rho_p = 2.2\,\mathrm{g\,cm^{-3}}$, $1/\kappa = 207\,\mathrm{nm}$, $\zeta_p = -52\,\mathrm{mV}$) spheres. **b)** Normalized translational near-wall in plane diffusion coefficient of 1.1 µm (light) and 2.1 µm (dark) spheres as function of normalized gap height. Error bars denote standard deviations. Experimental data are plotted against the theoretical prediction that follows from Ketzetzi et al. [191] Inset shows the non-normalized diffusion coefficient values for both sphere sizes with gap height.

For high precision measurements, careful consideration should be given to the determination of both the position and local orientation of the wall, from which the gap height can be derived, as walls in experiments may be tilted. Here, we achieved such precision (see Figure 2.3), by using at least three fixed particles that define a plane and by subsequently obtaining the position of the diffusing particle relative to said plane. Note that the position and orientation of the plane is fitted accurately to the positions of the bottom of the fixed particles, since our method also measures the radii of the fixed particles at the same time.

In Figure 2.4a, we report the distribution of gap heights between the diffusing spheres of two different sizes and the wall. We find that the height distributions can faithfully be described using established methods that combine a barometric height distribution with electrostatic interactions (see also Section 2.2.6 and Wu and Bevan [134]). In comparison, the height distributions of the 1.1 µm and 2.1 µm spheres feature qualitatively different behaviors. As expected, the smaller spheres probe a wider range of gap heights, while the axial motion of the larger spheres is more confined. However, we note that the median gap height of the larger spheres is slightly greater than that of the smaller ones, which is in line with the higher surface charge that we measured for these particles using laser doppler micro-electrophoresis.

The corresponding zeta potentials are (-35 ± 6) mV and (-54 ± 7) mV for the 1.1 and 2.1 μm batches, respectively. The excellent agreement that we obtained between the prediction and our experiment for different particle parameters further verifies the sensitivity of our setup. We conclude that our method of localizing the plane, and thereby the wall, using fixed control particles allows for high precision measurements of colloidal systems near walls.

Finally, to further evaluate our method, we determined the height-dependent translational diffusivity of the spheres, presented in Figure 2.4b. Additionally, in the same figure, we compared our data to the theoretical prediction for translational diffusion with wall gap height of Ketzetzi et al.,[191] which covers the entire separation range from the far-field regime captured by Faxén[192] and the near-wall regime captured by lubrication theory.[138] We find that both particle sizes follow the prediction within error, with small random variations between individual measurements, which demonstrates that we can accurately determine the diffusion constant across the whole range of here accessible sphere-wall gap heights.

2.3.2 Dumbbell height distribution above the wall

Having established the validity of our setup and method, we proceeded to study the near-wall behavior of our colloidal dumbbells. These dumbbells were formed by random aggregation of two individual spheres caused by Van der Waals attraction; we expect that the spheres do not roll with respect to each other. Analogously to the spheres, we measured the three-dimensional position of dumbbells of two sizes (long axis 2.2 and 4.2 μm respectively), formed either by two 1.1 μm or two 2.1 μm spheres. We first checked the quality of our hologram analysis in Figure 2.5a and b, where the good agreement between the model and our experimental images is shown. In this model, the free parameters are the c.m. position, the dumbbell orientation, the radii, and the refractive indices of the two touching spheres comprising the dumbbell. We note that the obtained values agreed with the single spheres results (Figure 2.2 step 2 and 3).

Figure 2.5c shows the positions of the 1.1 μm spheres comprising the dumbbell (dumbbell long axis 2.2 μm) as function of time, revealing that one of the spheres is positioned higher than the other in relation to the wall. Moreover, it clearly shows that twice during the duration of our 8 min measurement, the spheres drastically changed positions, i.e. a flipping between upper and lower spheres occurred. Based on the estimated rotational diffusion time $\tau_r = 8\pi\eta R_{\text{eff}}^3/(k_B T) \approx 2\,\text{s}$ (with viscosity $\eta = 8.9 \times 10^{-4}\,\text{Pa s}$ and the radius of a sphere of volume equal to the dumbbell $R_{\text{eff}} = (2R^3)^{1/3} \approx 0.69\,\mu\text{m}$), this flipping should have been observed more frequently if it were a purely diffusive process, faraway from the wall. For the larger dumbbells in Figure 2.5e, which move further from the wall, we observe despite their larger size ($\tau_r \approx 13\,\text{s}$), frequent flipping between the upper and lower spheres.

By fitting the c.m. height distribution of the dumbbell in Figure 2.5d and f using Equation 2.12 (solid black line), we conclude that our simple model for a dumbbell particle near a wall describes the experimental height distribution very well. Further-

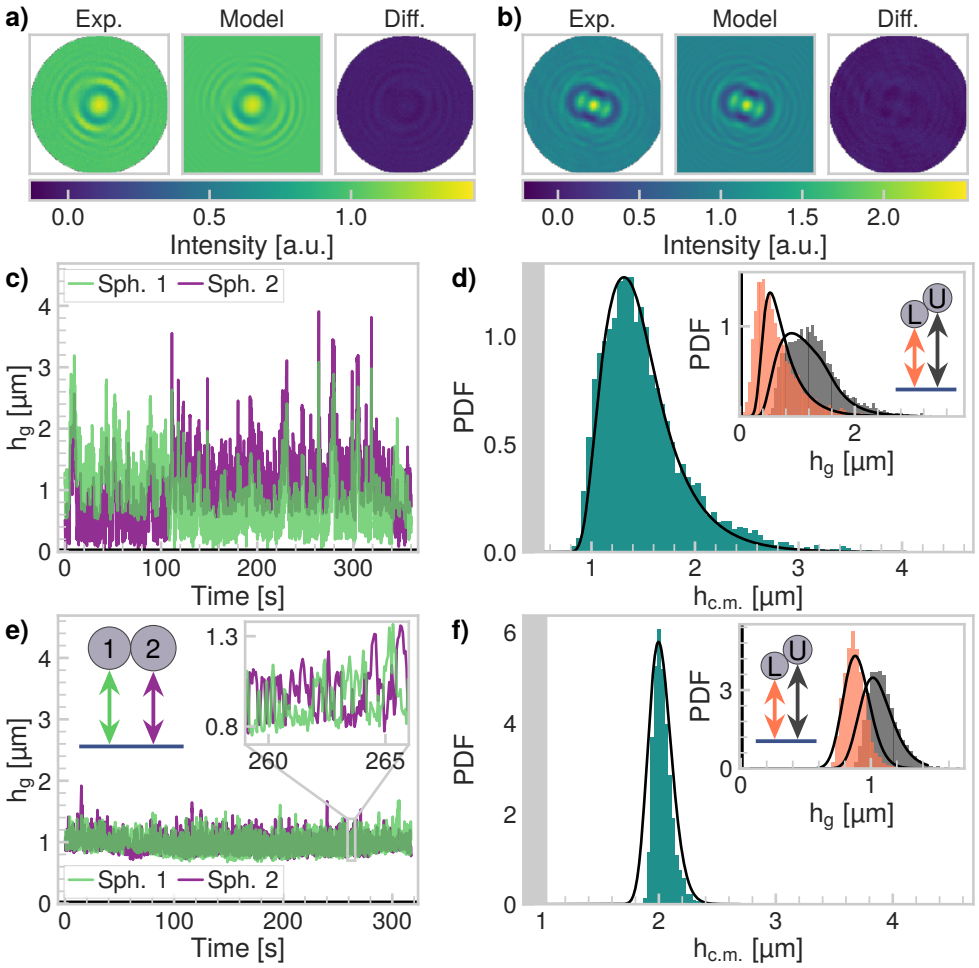

Figure 2.5: **Height distributions of colloidal dumbbells above a planar wall. a)** Comparison of an experimental image, the fitted model and the residual for a 2.2 μm dumbbell and **b)** for a 4.2 μm dumbbell. The low values of the residuals in a and b indicate the excellent agreement between data and model. **c)** Gap heights for the two 1.1 μm spheres that form the dumbbell as function of time. **d)** Center of mass (c.m.) dumbbell height distributions (same particle as in b), with the corresponding gap heights of the lower (L) and upper (U) spheres as inset. Solid lines indicate the theoretical prediction of Equation 2.12 (fit parameters $\rho_p = 2.0\,\mathrm{g\,cm^{-3}}$, $1/\kappa = 103\,\mathrm{nm}$, $\zeta_p = -30\,\mathrm{mV}$). **e)** Gap heights for the two touching 2.1 μm spheres that form the dumbbell as function of time. The inset zooms in on a short sequence of the measurement to indicate the frequent flipping of the dumbbell. **f)** Center of mass (c.m.) dumbbell height distributions (same particle as in e), with the corresponding dumbbell gap heights of the lower (L) and upper (U) spheres as inset. Solid lines indicate the theoretical prediction of Equation 2.12 (fit parameters $\rho_p = 2.1\,\mathrm{g\,cm^{-3}}$, $1/\kappa = 228\,\mathrm{nm}$, $\zeta_p = -61\,\mathrm{mV}$).

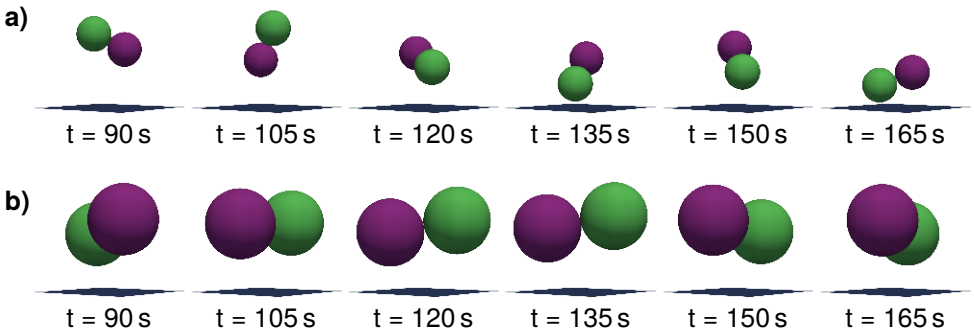

Figure 2.6: **Dumbbell orientation and height as function of time. a)** Schematics based on the experimentally tracked positions of a 2.2 μm dumbbell at random times, showing out of plane rotations in addition to height variations. **b)** Schematics based on the experimentally tracked positions of a 4.2 μm dumbbell at the same times as in panel a, showing significantly fewer out of plane rotations compared to the smaller dumbbell of panel a.

more, the fit parameters we have obtained from this fit agree with the single sphere fit parameters from the height distribution in Figure 2.4a. Additionally, we calculate the height distribution of the dumbbell gap heights of the lower (L) and upper (U) spheres, as shown in the inset of Figure 2.5d and f. Compared to the theoretical prediction from Equation 2.12, we observe a slight shift towards smaller heights for the lower and, conversely, greater heights for the upper sphere in the experiments. This may indicate that to fully describe the experimental data, higher order effects need to be taken into account, such as the distortion of the electric double layer of one sphere by the presence of the other sphere and the wall. These effects become more pronounced when the dumbbells are closer to the wall, as can be seen when comparing panels d and f from Figure 2.5.

2.3.3 Dumbbell orientation with respect to the wall

The stable and significant differences in sphere positions of Figure 2.5c, already indicated that these dumbbells are oriented at an angle relative to the wall. On the other hand, for larger dumbbells of the same material, the spheres being approximately at the same height at all times in Figure 2.5e suggested a roughly parallel orientation with the wall. We verify our observations in Figure 2.6a and 2.6b, where we visualize orientations that the dumbbells assumed during the measurements at 15 s intervals. Indeed, from the snapshots we clearly see that, while flipping between lower and upper sphere did occur, the height above as well as orientation with respect to the wall remained relatively constant for the larger dumbbell (Figure 2.6b). Conversely, the smaller dumbbell featured a richer behavior that includes notable changes in height, orientation, as well as flipping between which of the two spheres is the lowest (Figure 2.6a).

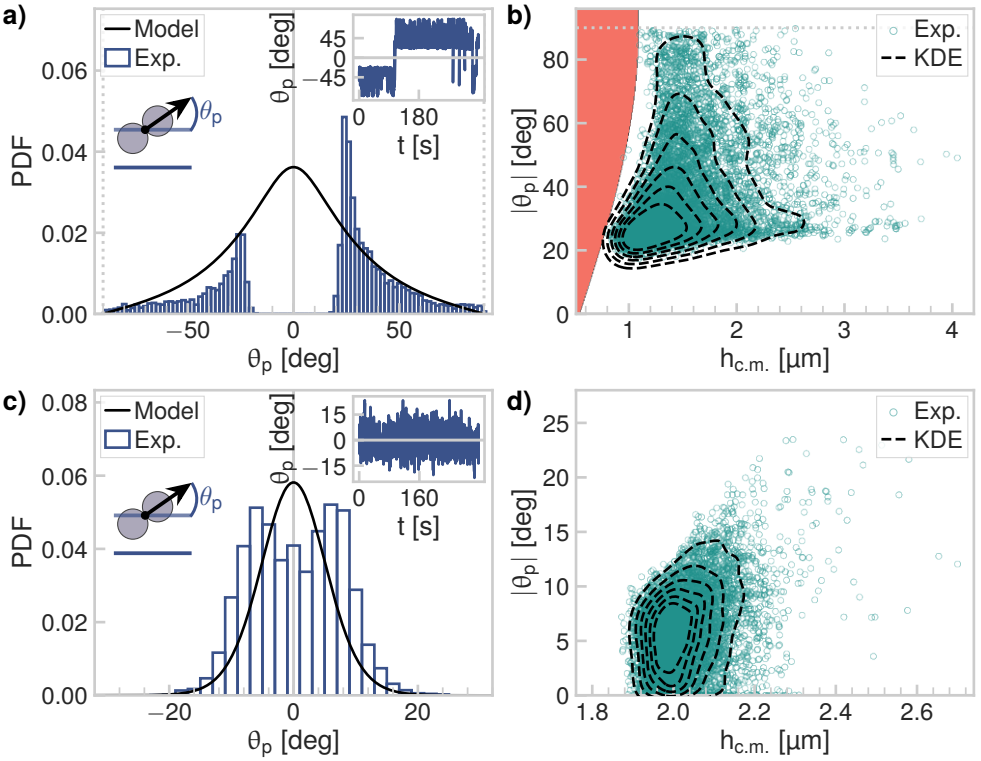

Figure 2.7: **Dumbbell orientation with respect to the planar wall as function of height. a)** Distribution of plane angles for a 2.2 µm dumbbell. The difference in peak heights is due to the respective length of the parts of the measurement where the dumbbell assumed a negative or positive orientation (see inset). We distinguish negative from positive orientations as outlined in Section 2.2.4. The solid line indicates the expected distribution based on Equation 2.13 (same parameters as in Figure 2.5d). The inset shows the plane angle in time. **b)** Plane angle with c.m. height for the 2.2 µm dumbbell. The red area indicates geometrically forbidden configurations. **c)** Distribution of plane angles for a 4.2 µm dumbbell. The solid line indicates the expected distribution based on Equation 2.13 (same parameters as in Figure 2.5f). The inset shows the plane angle in time. **d)** Plane angle with c.m. height for the 4.2 µm dumbbell. In panel c and f, the dashed lines are a contour plot of the kernel density estimation, corresponding to 12.5 %, 25 %, 37.5 %, 50 %, 62.5 % and 75 % of the data.

In what follows, we further quantify our observations, by calculating the angle, θ_p, between the long dumbbell axis and wall (see schematic of Figure 2.7a). Strikingly, we observe in Figure 2.7a a double-peaked structure not predicted by our model: we find no parallel orientations with respect to the wall for the 2.2 μm dumbbell. Instead, the dumbbell is more likely to be oriented at an angle between 25 and 56 deg (median 32 deg) with the wall. In separate brightfield microscopy measurements, we verified that dumbbells of this size and material indeed show frequent out-of-plane rotations. The preferred range of orientations is robust, and persists even when the dumbbell flips, i.e. when the lower sphere becomes the upper sphere. The difference in peak heights in Figure 2.7b is due to the respective length of the parts of the measurement where the dumbbell assumed a negative or positive orientation. Such preferred orientations are surprising, since an angle distribution centered around zero degrees is naively expected in view of the effects of buoyancy and electrostatics, see the expected distribution depicted by the solid line in Figure 2.7a and 2.7c.

Examining the larger and hence heavier 4.2 μm dumbbells in Figure 2.7c, we notice that these indeed have assumed mostly flat orientations with the wall, with the most probable angles ranging between 2.2 and 9.6 deg (median 6 deg). However, the double-peak structure in the angle probability density function that we observed for the smaller dumbbells persists to some degree even for these larger particles, indicating that the increased gravitational force leads to a suppression of the interaction which causes the dumbbells to adopt a nonparallel orientation. We hypothesize that the observed angle distributions for both dumbbell sizes stem from a higher-order electrostatic effect not accounted for in our theory. However, we cannot exclude a more subtle interplay of other effects, such as buoyancy and hydrodynamics.

Naturally, the question arises whether changes in height relate to changes in dumbbell orientation. To test for this, we plot the measured angles as function of center of mass height. We find that for the smaller dumbbells, there is a clear preference for lower angles at low heights in Figure 2.7b, the preference for which disappears with height. That is, further from the wall, the dumbbells may adopt a wider range of orientations. For the larger dumbbell, we also find a narrower distribution of angles at lower heights in Figure 2.7d. However, we note that both angle and height distributions are considerably narrower compared to those that correspond to the smaller dumbbell. At the same time, the particle-wall separation distance is typically greater than that of the smaller dumbbell: while the smaller dumbbell moves closely to the wall (see also the red area in Figure 2.7b which indicates geometrically forbidden configurations caused by particle-wall overlap), the larger dumbbell does not come into close contact with the wall.

2.3.4 Theoretical considerations for preferred dumbbell orientations

To gain insight into the preferred orientations and minimal angle measured in Section 2.3.3, we extended the gravity and electrostatics model for a sphere above the wall (Equations 2.1–2.3) to the dumbbell. Briefly, Equations 2.8–2.9 model the dumbbell

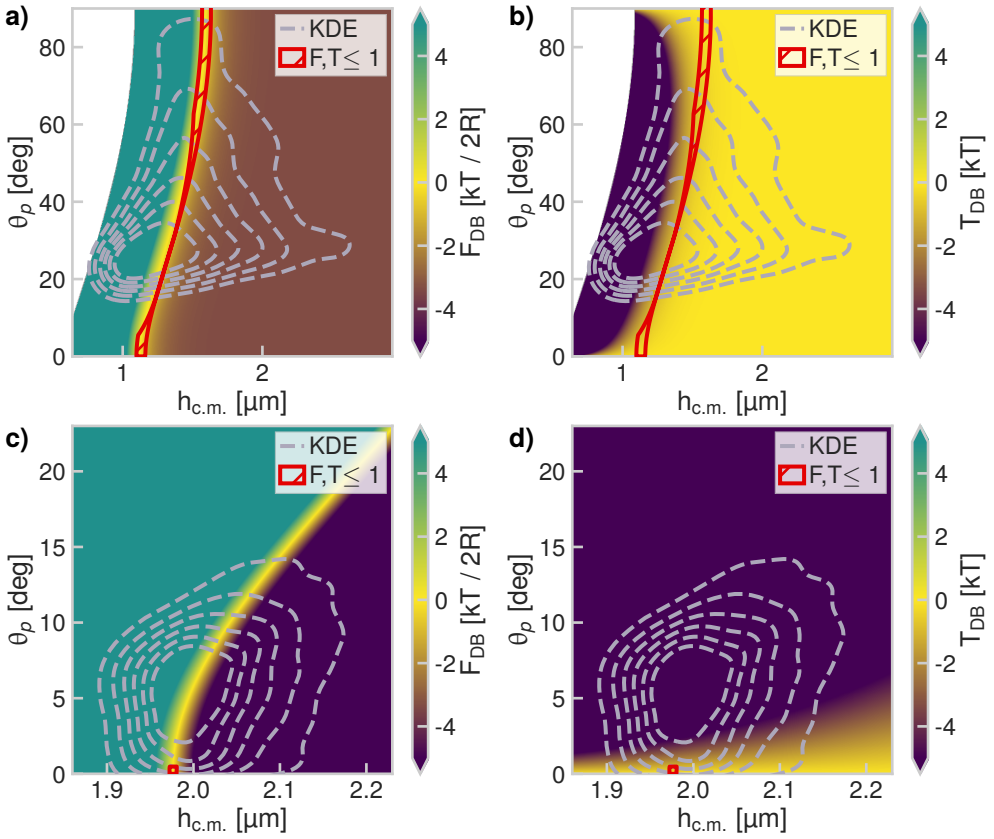

Figure 2.8: **Force and torque acting on a dumbbell by balancing electrostatics and gravity. a)** The force as function of θ_p and $h_{\mathrm{c.m.}}$ for the 2.2 µm dumbbell. For all orientations, there is a height range for which the net force is zero. **b)** The torque as function of θ_p and $h_{\mathrm{c.m.}}$ for the 2.2 µm dumbbell. **c)** The force as function of θ_p and $h_{\mathrm{c.m.}}$ for the 4.2 µm dumbbell. The area where the net force is zero is smaller compared to the smaller dumbbell in panel a. **d)** The torque as function of θ_p and $h_{\mathrm{c.m.}}$ for the 4.2 µm dumbbell. For the same range of angles as in panel b, the torque on the larger dumbbell is considerably higher than the thermal energy for the majority of angles, causing the dumbbell to adopt a flat orientation with respect to the wall. In all panels, the red lines indicate regions where both the force and torque are simultaneously small compared to the thermal energy, indicating a possibility of observing the dumbbell at those heights and orientations. Values outside the indicated range of the colorbars are clipped to visualize the low force and torque region relevant to the experiments, while white regions represent sterically forbidden combinations of height and angle. Dashed lines are a contour plot of the kernel density estimation of the experimental data (see Figure 2.7).

as two connected (but otherwise non-interacting) spheres, by balancing electrostatic and gravitational forces. This approximation ignores the distortion of the electrostatic double layer caused by the presence of the other sphere, but allowed us to probe the origin of the dumbbell orientation described in Section 2.3.3, by examining whether the combined effects of electrostatics and gravity would result in zero force and torque solutions as function of plane angle and height above the wall.

By applying the reduced model of Section 2.2.8 to the experimental data, we reach a number of interesting conclusions in Figure 2.8, where we plot the results from the model. Figure 2.8a shows that the net force on the 2.2 μm dumbbell vanishes for a range of heights and orientations. That is, for each given orientation there exists a narrow distribution of heights where the force balance is zero. As expected for a particle with a larger mass, for the 4.2 μm dumbbell in Figure 2.8c the range of heights where the net force vanishes is considerably narrower compared to the 2.2 μm dumbbell of Figure 2.8a. To answer whether such configurations are expected to be stable, one must additionally consider the possibility of a reorienting torque stemming from the combined effect of gravity and electrostatics acting on the dumbbell. We expect that the interplay between the magnitude of this reorienting torque and a random torque, stemming from thermal fluctuations, causes changes in the dumbbell orientations with respect to the wall. In the case of a reorienting torque that is large in comparison to the random torque ($\approx 1\ k_BT$), we expect a mostly parallel orientation with respect to the wall. In contrast, for a reorienting torque that is small compared to the random torque, we expect largely fluctuating orientations. In what follows, we examine the presence and magnitude of the reorienting torque.

Interestingly, for the smaller 2.2 μm dumbbells, a regime arises where both net forces and reorienting torques are simultaneously below the thermal force and energy, respectively, for certain combinations of dumbbell-wall separations and nonzero plane angles (as indicated by the red lines in Figure 2.8a and b). The presence of such a regime that spans throughout state space suggests that the large variations of the angle as found in Figure 2.7 (evidenced also in the dashed lines of Figure 2.8a and b) are expected. This is further corroborated by the angle probability plot that follows from our model in Figure 2.9a for heights relevant to our experiment. For the largest dumbbells, our minimal modeling (Figure 2.8c-d and Figure 2.9b) agrees well with the almost parallel orientations observed in the experiments (Figure 2.7d), which mostly fall within the high reorienting torque regime (see dashed line in Figure 2.8c).

Our minimal dumbbell model also sheds light on the relation between height and orientation observed in Figure 2.7b and d, indicated also by the dashed lines in Figure 2.9. Although the agreement is not fully quantitative, the model shown in Figure 2.9a and b predicts an increase in the most probable angle with greater heights, similar to our experiments. Moreover, the height and orientation combinations that the dumbbells experimentally adopt most often coincide with the zero net force regime (and equivalently nonzero probabilities in Figure 2.9a and b) for both dumbbell sizes, as evidenced by the overlap between the experimental data and the areas of higher probability.

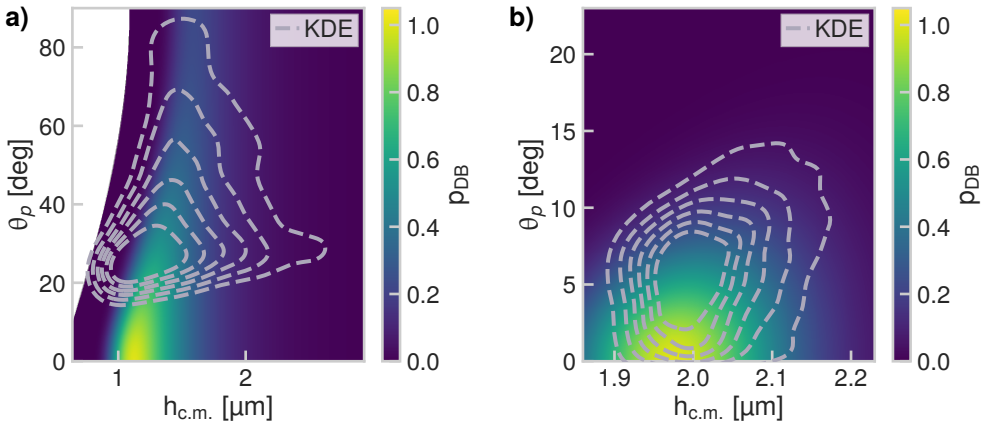

Figure 2.9: **Dumbbell PDF as function of height and orientation by balancing electrostatics and gravity. a)** The probability of observing a combination of θ_p and $h_{\text{c.m.}}$ for the 2.2 µm dumbbell, as predicted by Equation 2.11 and measured in the experiments (dashed line). **b)** The probability of observing a combination of θ_p and $h_{\text{c.m.}}$ for the 4.2 µm dumbbell. White regions represent sterically forbidden combinations of height and angle. Dashed lines are a contour plot of the kernel density estimation of the experimental data (see Figure 2.7).

Finally, we notice that the range of experimentally observed angles for the 2.2 µm dumbbells does not fully coincide with the range of angles that fall within the low force and torque regime from the model. For torques below the thermal energy, the model also allows for angles below 17 deg, which we did not observe here for these dumbbells. We note that the discrepancy between our model and experiment does not stem from a difference in size between the two spheres in the dumbbell. As can be seen in Figure 2.10 and Figure 2.11 where we additionally account for (an experimentally relevant) 5 % dispersity in the sphere sizes, the most probable heights are only slightly shifted towards greater values. The individual contributions of the gravitational and electrostatic potential to the net potential energy are shown in the first and second column, respectively, in Figure 2.10 (dumbbells of the same volume as the 2.2 µm dumbbells) and Figure 2.11 (dumbbells of the same volume as the 4.2 µm dumbbells). It is clear that the electrostatic potential is not negligible compared to the gravitational potential, therefore, the height from the surface is greatly influenced by electrostatic repulsion despite the relatively short Debye length (on the order of 150 nm). We have calculated two experimentally relevant size dispersities: an experimentally relevant 5 % size dispersity and a highly anisotropic dumbbell (snowman particle) for which $R_2 \approx 2R_1$. We have chosen the R_1, R_2 in such a way that the total mass of the dumbbell is the same as the $R_1 = R_2 = R$ case. As a convention, positive angles denote the orientation where the sphere of the smaller radius R_1 is higher than the sphere of the larger radius R_2, as given in Equations 2.15–2.16.

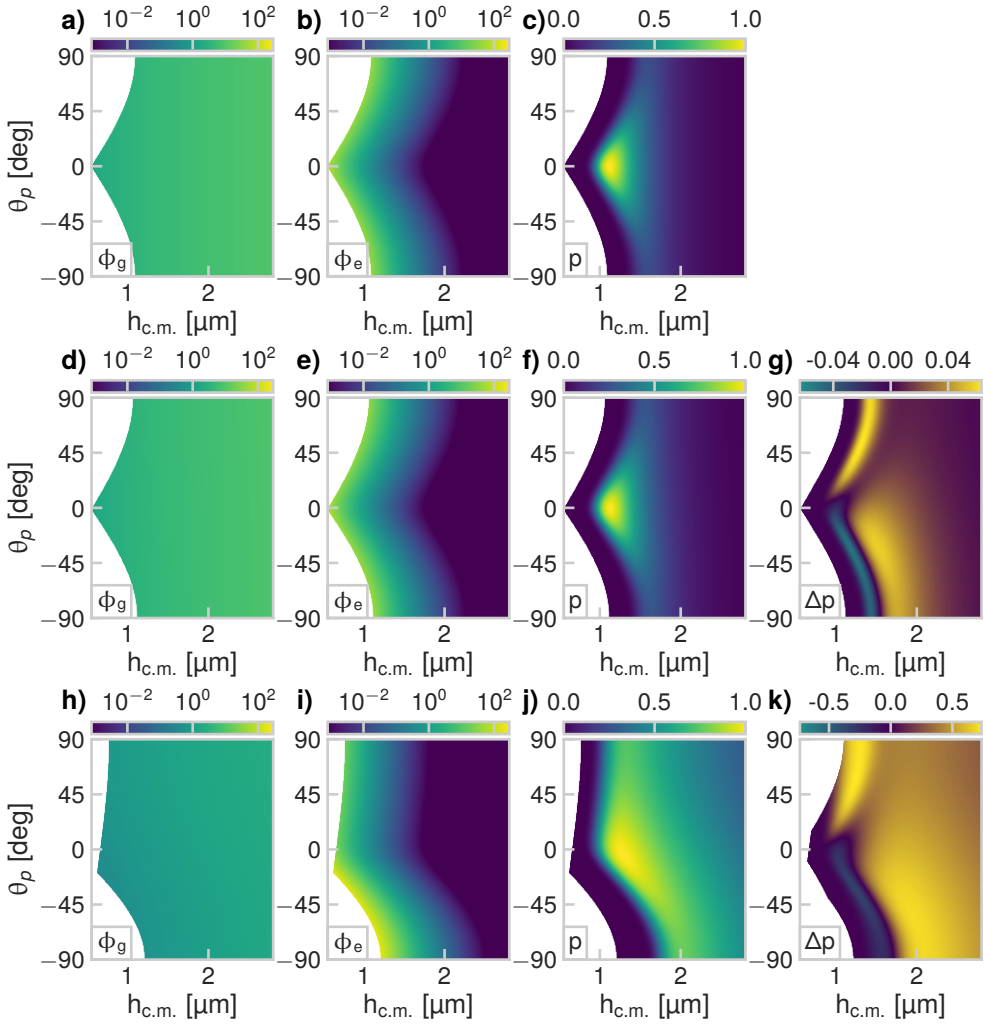

Figure 2.10: **Effect of sphere size dispersity on dumbbell plane height and orientation probability density** for dumbbells of the same volume as the 2.2 µm dumbbells ($R = 0.54\,\mu m$). All gravitational and electrostatic potentials were calculated according to Equation 2.18 and Equation 2.19, respectively, and given in units of k_BT. All probabilities were calculated according to Equation 2.20. **a)** Gravitational potential for $R_1 = R_2 = R$. **b)** Electrostatic potential for $R_1 = R_2 = R$. **c)** PDF for $R_1 = R_2 = R$. **d)** Gravitational potential for $R_1 = 0.975R, R_2 = 1.024R$. **e)** Electrostatic potential for $R_1 = 0.975R, R_2 = 1.024R$. **f)** PDF for $R_1 = 0.975R, R_2 = 1.024R$. **g)** Probability difference $\Delta p = p(0.975R, 1.024R) - p(R, R)$. **h)** Gravitational potential for $R_1 = 0.605R, R_2 = 1.212R$. **i)** Electrostatic potential for $R_1 = 0.605R, R_2 = 1.212R$. **j)** PDF for $R_1 = 0.605R, R_2 = 1.212R$. **k)** Probability difference $\Delta p = p(0.605R, 1.212R) - p(R, R)$.

Compared to the case where both spheres are equal, increasing the size dispersity between the two spheres has two effects: firstly, the distribution around $\theta_p = 0$ is no longer symmetric, as shown in Figure 2.10 and Figure 2.11d-k. Secondly, a larger range of both angles and c.m. heights become accessible. However, the overall dumbbell behavior that the model yields remains the same with or without polydispersity in the sphere size. We hypothesize that the discrepancy between our minimal model and the experimental data may be resolved by considering higher-order electrostatic effects. However, higher-order effects, together with the possibility of dynamic charge redistribution in the double layers which may be relevant here, cannot be described by a simple analytical model.

2.4 Summary and Conclusions

We have measured the height of colloidal particles relative to planar walls with high precision by means of holographic microscopy. The position of the wall was tracked in time by following the position of spheres fixed on its surface, thereby allowing for an accurate measurement of the location and orientation of the plane and wall. For spheres, the obtained height distributions and diffusivities as function of height agree with well known theoretical predictions. More importantly, we studied the height distributions and orientations of colloidal dumbbells relative to walls. We found that smaller dumbbells assume nonparallel orientations with the wall and further examined the connection between orientation and particle-wall separation. Conversely, we found that larger dumbbells of the same material were always oriented almost parallel to the wall.

We showed that, despite its simplicity, a minimal model accounting for gravity and electrostatics not only faithfully describes the dumbbell height distribution, but also predicts stable configurations for a large range of orientations and dumbbell-wall separations. However, our model predicts a larger range of stable orientations than was found in our experiment, indicating that refinements that account for higher-order electrostatic effects may need to be considered. We thus hope that our findings will encourage further investigations of near-wall particle dynamics. Our results highlight the rich dynamics that nonspherical particles exhibit in the proximity of walls and can aid in developing quantitative frameworks for arbitrarily-shaped particle dynamics in confinement.

Acknowledgments

This chapter is based on the following publication:

Height distribution and orientation of colloidal dumbbells near a wall.
R.W. Verweij*, S. Ketzetzi*, J. de Graaf and D.J. Kraft
Phys. Rev. E, 102, 062608 (2020). doi:10.1103/PhysRevE.102.062608

*These authors contributed equally.

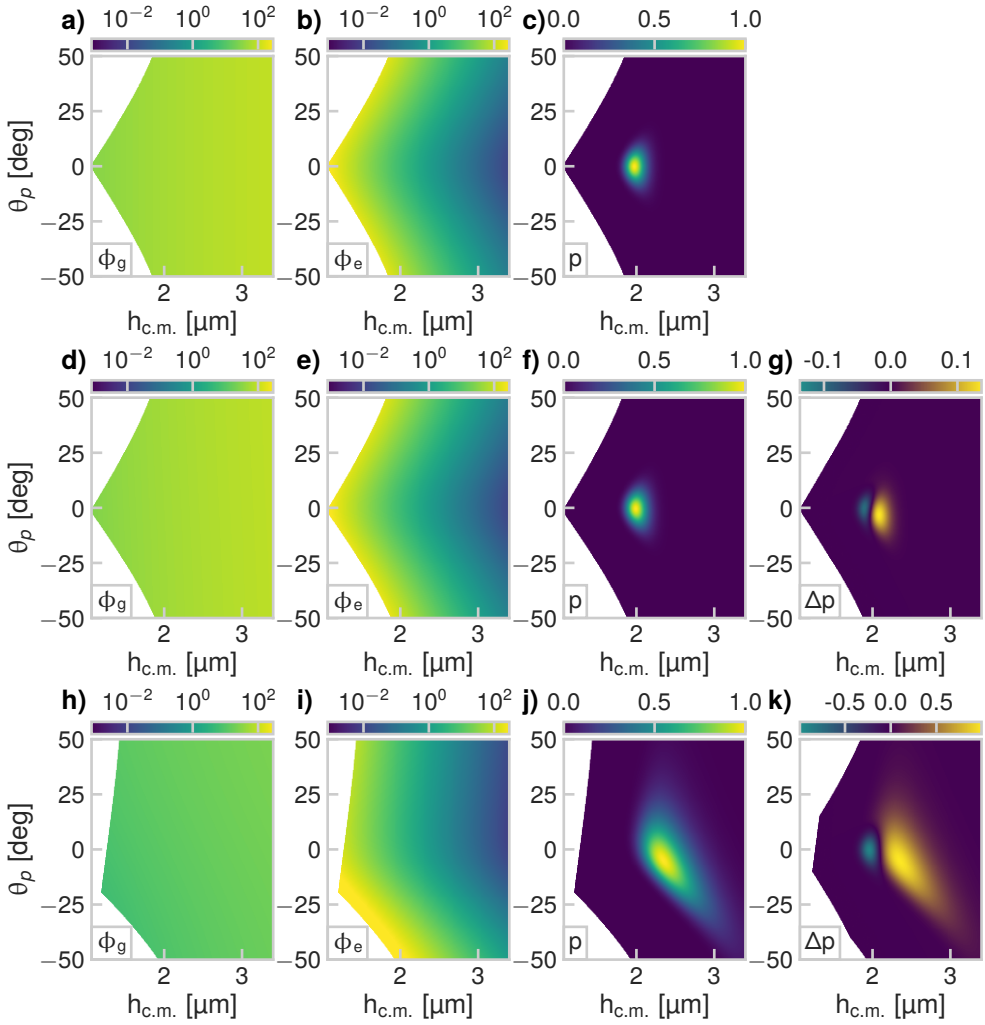

Figure 2.11: **Effect of sphere size dispersity on dumbbell plane height and orientation probability density** for dumbbells of the same volume as the 4.2 µm dumbbells ($R = 1.04\,\mu m$). All gravitational and electrostatic potentials were calculated according to Equation 2.18 and Equation 2.19, respectively, and given in units of k_BT. All probabilities were calculated according to Equation 2.20. **a)** Gravitational potential for $R_1 = R_2 = R$. **b)** Electrostatic potential for $R_1 = R_2 = R$. **c)** PDF for $R_1 = R_2 = R$. **d)** Gravitational potential for $R_1 = 0.975R, R_2 = 1.024R$. **e)** Electrostatic potential for $R_1 = 0.975R, R_2 = 1.024R$. **f)** PDF for $R_1 = 0.975R, R_2 = 1.024R$. **g)** Probability difference $\Delta p = p(0.975R, 1.024R) - p(R, R)$. **h)** Gravitational potential for $R_1 = 0.605R, R_2 = 1.212R$. **i)** Electrostatic potential for $R_1 = 0.605R, R_2 = 1.212R$. **j)** PDF for $R_1 = 0.605R, R_2 = 1.212R$. **k)** Probability difference $\Delta p = p(0.605R, 1.212R) - p(R, R)$.

We gratefully acknowledge Samia Ouhajji for providing the 1.1 μm silica spheres. We thank Sarah Smolders for exploratory experiments, and Nikos Oikonomeas for exploratory experiments and useful discussions on analyzing digital holograms. J.d.G. thanks NWO for funding through Start-Up Grant 740.018.013 and through association with the EU-FET project NANOPHLOW (766972) within Horizon 2020. This project was funded by the European Research Council (ERC) under the European Union's Horizon 2020 research and innovation program (grant agreement no. 758383).

3 Colloid-supported lipid bilayers for self-assembly

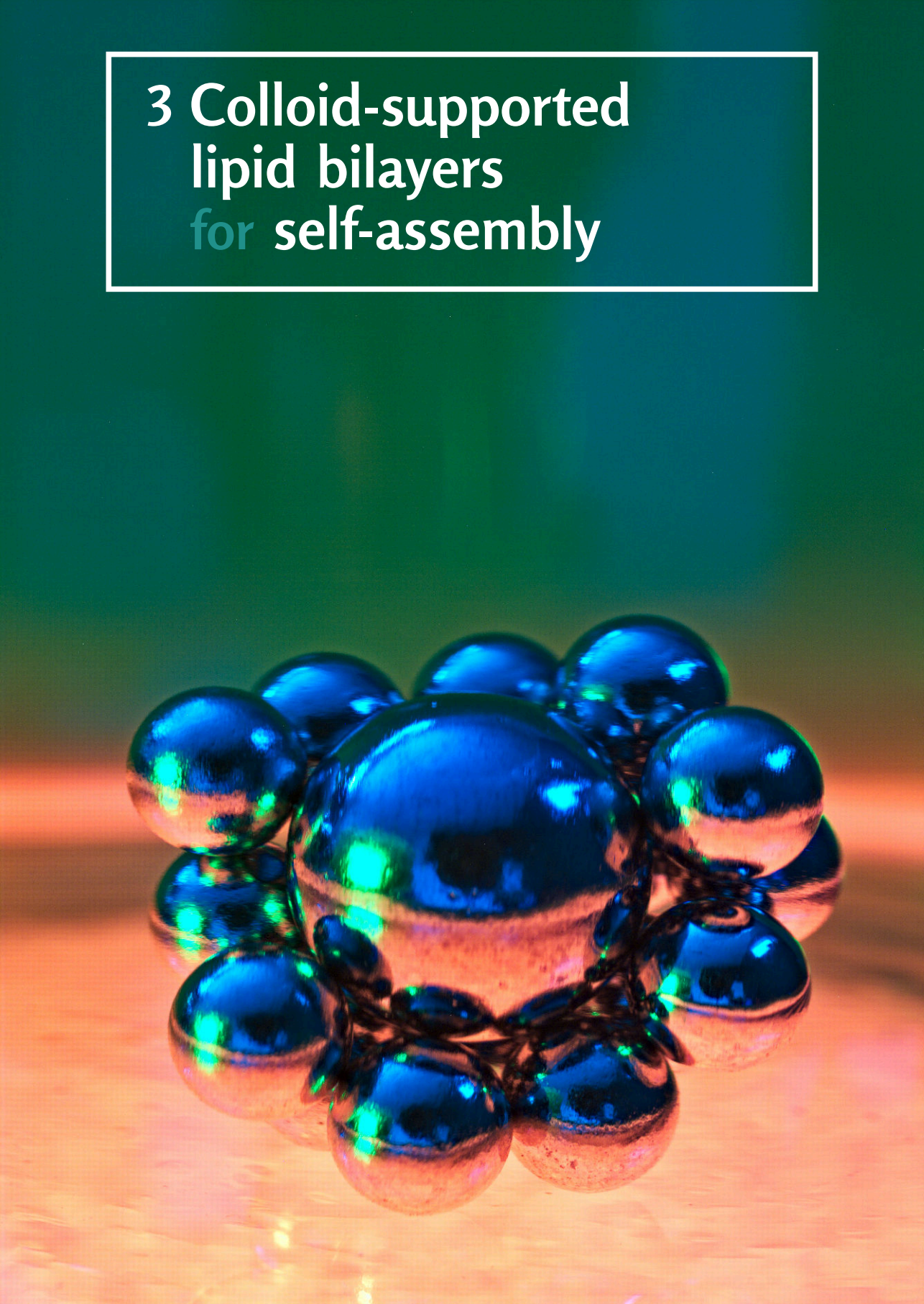

The use of colloid-supported lipid bilayers (CSLBs) has recently been extended to create colloidal joints, that enable the assembly of structures with internal degrees of flexibility. Additionally, CSLBs were used to study lipid membranes on curved and closed geometries. These novel applications of CSLBs rely on previously unappreciated properties: the simultaneous fluidity of the bilayer, lateral mobility of inserted (linker) molecules and colloidal stability. Here we characterize every step in the manufacturing of CSLBs in view of these requirements using confocal microscopy and fluorescence recovery after photobleaching (FRAP). Specifically, we have studied the influence of different particle properties (roughness, surface charge, chemical composition, polymer coating) on the quality and mobility of the supported bilayer. We find that the insertion of lipopolymers in the bilayer can affect its homogeneity and fluidity. We improve the colloidal stability by inserting lipopolymers or double-stranded inert DNA constructs into the bilayer. We include surface-mobile DNA linkers and use FRAP to characterize their lateral mobility both in their freely-diffusive and bonded state. Finally, we demonstrate the self-assembly of flexibly linked structures from the CSLBs modified with surface-mobile DNA linkers. Our work offers a collection of experimental tools for working with CSLBs in applications ranging from controlled bottom-up self-assembly to model membrane studies.

3.1 Introduction

Colloid-supported lipid bilayers (CSLBs) are used in a diverse range of research areas and applications,[113] from drug delivery,[7–9,114–117] bio-sensing,[15,118] membrane manipulation[193] and cell biology[61–63] to fundamental studies on lipid phase separation[64,65] and self-assembly.[85,110–112] The presence of a lipid bilayer around nano- or micrometer-sized solid particles or droplets provides biomimetic properties and a platform for further functionalization. One intriguing recent example used DNA-based linkers to functionalize the lipid bilayer, thereby enabling self-assembly of the underlying colloidal particles or droplets into flexible structures.[84,85,110–112,194] Within such a structure, the colloidal elements can move over each other's surface while remaining strongly and specifically bonded. This new type of bonding enables fundamental studies on structures with internal degrees of flexibility, such as the self-assembly of novel crystal phases and their phase transitions.[57,58,119,120] Furthermore,

these complex colloids have great potential for smart drug delivery techniques,[9] photonic bandgap materials[59,60] and wet computing.[195]

CSLBs are particularly suitable and versatile building blocks for the assembly of floppy structures, because they combine the best qualities of free standing bilayers (vesicles) and colloids. Vesicles, upon applications of linkers,[55] can connect into flexible structures, but are unstable to small disturbances, heterogeneous in size and easily deformable. Colloidal particles are available in diverse materials and with a variety of stable shapes, and can be assembled after functionalization with surface-bound DNA linkers.[69,80] However, the obtained structures are often rigid due to the immobility of the linking groups on the particles' surface and are non-equilibrium structures due to a "hit-and-stick" aggregation process.[77,196] Emulsions coated with lipid monolayers and DNA linkers that are mobile on the droplet interface posses both interaction specificity and bond flexibility.[56,84,194] Therefore, they assemble into flexible structures in a controlled fashion, but their shape is limited to spheres and they deform upon binding. Conversely, CSLBs consist of colloidal particles which provide a stable support for the lipid bilayer that is tunable in shape, size and material. The range of shapes for colloidal particles comprises, among others, spheres, cubes, rods, and (a)symmetric dumbbell particles, and their sizes range from hundreds of nanometers to several micrometers. They can be produced reliably with a narrow size distribution and are commercially available. Additionally, CSLBs feature a lipid bilayer on the surface of the colloids which creates a liquid film for molecules, such as DNA linkers, to freely move in. This allows for binding particles specifically, and yet non-rigidly, making the assembly of floppy structures possible.[56,85,110–112]

To obtain flexible instead of rigid structures, it is vital that the linker molecules which are inserted into the lipid bilayer are free to move over the surface of the CSLBs. Their lateral mobility relies on the fluidity and homogeneity of the bilayer, which in turn depend on the linker concentration[85] and lipid composition. The lipids need to be in the fluid state under experimental conditions, and this may be impeded by bilayer-surface interactions. Similarly, the success of experiments studying the phase separation of lipid bilayers on anisotropic colloidal supports relies on the fluidity and homogeneity of the bilayer.[64,65] Finally, controlling the self-assembly pathway through DNA linkers with complementary sticky ends implies that all other nonspecific interactions need to be suppressed. In other words, CSLBs need to have sufficient colloidal stability. To the best of our knowledge, these requirements of membrane homogeneity and fluidity plus colloidal stability have not been studied simultaneously. However, they are of key importance for using CSLBs in self-assembly and model membrane studies, while possibly having wider implications for all other applications.

Here, we carefully characterize every stage in the preparation of CSLBs specifically related to these three properties. First, we study the effect of the material properties of the colloidal particles and the use of polymers on the membrane fluidity and homogeneity. Then, we investigate the influence of lipopolymers and inert double-stranded DNA on the colloidal stability of the CSLBs. Subsequently, we in-

clude double-stranded DNA-based linkers connected to hydrophobic anchors and characterize their diffusion in the bilayer. Finally, we show that when using the optimal experimental parameters determined by this study, CSLBs self-assemble into flexibly-linked structures that are freely-jointed.

3.2 Experimental methods

3.2.1 Reagents

Chemicals

The lipids 1-palmitoyl-2-oleoyl-sn-glycero-3-phosphocholine (POPC) and (Δ9-Cis)-1,2-dioleoyl-sn-glycero-3-phosphocholine (DOPC), the fluorescently-labeled lipids L-α-Phosphatidylethanolamine-N-(DOPE lissamine rhodamine B sulfonyl) and 23-(dipyrromethene boron difluoride)-24-norcholesterol (TopFluor®-Cholesterol) and the lipopolymers 1,2-dioleoyl-sn-glycero-3-phosphoethanolamine-N-[methoxy(polyethylene glycol)-2000] (DOPE-PEG(2000)) and equivalently, DOPE-PEG(3000) and DOPE-PEG(5000) were purchased from Avanti Polar Lipids. 4-(2-hydroxyethyl)-1-piperazineethanesulfonic acid (HEPES, ≥99.5 %) and calcium chloride ($CaCl_2$, Calciumchlorid Dihydrat, ≥99 %) were purchased from Carl Roth. Sodium chloride (NaCl, extra pure), hydrogen peroxide (H_2O_2, 35 %w/w), acrylamide (98.5 %, extra pure), N,N,N′,N′-tetramethylethylenediamine (TEMED, 99 %), ammonium persulfate (APS, 98 %), sodium hydroxide (NaOH, 98.5 %) and sodium azide (NaN_3, 99 %, extra pure) were purchased from Acros Organics. Hellmanex™ III, ammonium hydroxide (NH_4OH, 28-30 %w/w), 3-(trimethoxysilyl)propyl methacrylate (TPM, 98 %), Pluronic®F-127, dipotassium phosphate (K_2HPO_4, ≥99 %), ethanol (≥99.8 %), sodium dodecyl sulfate (SDS, ≥98.5 %), polyvinylpyrrolidone (PVP, average Mw 40 000), itaconic acid (≥99 %), 3-aminopropyltriethoxysilane (99 %) and acetic acid (99.8 %) were purchased from Sigma-Aldrich. Magnesium chloride ($MgCl_2$, for analysis) was purchased from Merck. All solutions were prepared with Milli-Q water (Milli-Q Gradient A10).

Buffers

HEPES buffer type 1 was made with 115 mM NaCl, 1.2 mM $CaCl_2$, 1.2 mM $MgCl_2$, 2.4 mM K_2HPO_4 and 20 mM HEPES. HEPES buffer type 2 consisted of 10 mM HEPES, 40 mM NaCl, 2 mM $CaCl_2$ and 3 mM NaN_3. HEPES buffer type 3 consisted of 10 mM HEPES, 40 mM NaCl and 3 mM NaN_3. The buffers were prepared by mixing all reagents in the appropriate amounts in fresh Milli-Q water. After mixing, the pH was adjusted to 7.4 using NaOH.

Particles

Commercial silica spheres ((2.06 ± 0.05) μm, (2.12 ± 0.06) μm and (7.00 ± 0.29) μm) were synthesized by Microparticles GmbH, using a Stöber method where tetraethoxysilane (TEOS) reacts with water and bases in an ethanolic solution (sol-gel process). Commercial polystyrene particles ((2.0 ± 0.3) μm) were obtained from Sigma

Aldrich. Hematite cubic particles ((1.76 ± 0.08) μm) were made following the protocol of Sugimoto and Sakata [197] and coated according to Rossi et al. [24] Polystyrene-3--(Trimethoxysilyl)propyl methacrylate (Polystyrene-TPM) particles ((1.24 ± 0.04) μm) with varying asperity were synthesized and coated with silica following the protocol of Meester and Kraft. [198] TPM particles ((2.03 ± 0.06) μm) were made following the protocol of Van der Wel et al. [199] TPM particles functionalized with carboxyl groups ((2.71 ± 0.14) μm), or amino groups ((2.14 ± 0.07) μm) were prepared by synthesizing according to Van der Wel et al. [199] and then functionalizing according to Doherty and Kraft. [200] Briefly, amine or carboxylic acid groups were incorporated onto the TPM surface by addition of either 3-aminopropyltriethoxysilane or itaconic acid, respectively, during the emulsification stage. Polystyrene particles with carboxyl groups ((1.99 ± 0.15) μm) were synthesized according to Appel et al. [201] Polystyrene-TPM particles of spherical, symmetric and asymmetric dumbbell shape were made and coated with silica following the protocols reported in Rinaldin et al. [64]

DNA oligonucleotides

All DNA strands were synthesized as single-stranded DNA, purified using reverse phase high-performance liquid chromatography (HPLC-RP) and checked using matrix-assisted laser desorption/ionization time-of-flight mass spectrometry (Maldi-TOF MS) by Kaneka Eurogentec S.A. We used double-stranded inert DNA for steric stabilization and double-stranded DNA linkers with a sticky end for binding. Both types of DNA have a hydrophobic anchor (double stearyl/double cholesterol for linker and double cholesterol for inert DNA) connected to a short carbon chain which is then connected to the oligonucleotide. The linkers are additionally functionalized with a fluorescent dye. All strands, including all functionalizations, are listed in Table A.1. These DNA strands were hybridized by mixing the single strands in a 1:1 molar ratio in HEPES buffer type 3. The solution was then heated in an oven to 90 °C for 30 min, after which the oven was turned off and the solution was allowed to cool down slowly overnight in the closed oven. From now on, for the strands given in Table A.1, we label strand CH-10-H as "10 nm Inert DNA", strand CH-20-I as "20 nm Inert DNA", strand CH-20-H-A as "20 nm Linker A", strand CH-20-H-B as "20 nm Linker A'", strand DS-H-A as "30 nm Linker A" and, finally, we label strand DS-H-B as "30 nm Linker A'". The linkers "A" have a single-stranded sticky end (indicated by cursive text in Table A.1) that is complementary to the single-stranded end of linkers "A'".

3.2.2 Preparation of CSLBs

Typically, CSLBs were made by spontaneous spreading and fusion of small unilamellar vesicles (SUVs) on the particle surface. An SUV dispersion prepared via either extrusion or sonication was mixed with the particles, allowing a bilayer to spread on the surface for at least one hour. Subsequently, the CSLBs were washed to remove excess SUVs. We observed no substantial differences in the obtained CSLBs between the two methods presented here.

CSLB preparation: method 1

500 µg of a mixture of DOPE-Rhodamine (0.2 mole%) and varying amounts of POPC and PEGylated lipids was dried by two hours of vacuum desiccation and then re-suspended to a 2 g L^{-1} dispersion with HEPES buffer type 1. The solution was vortexed for 15 min to produce multilamellar vesicles. Then, the vesicle dispersion was extruded 21 times with a mini extruder (Avanti Polar Lipids) equipped with two 250 µL gas-tight syringes (Hamilton), two drain discs and one nucleopore track-etch membrane (Whatman). The pore size of the membrane was 0.05 or 0.1 µm for experiments with DOPE-PEG(2000) and DOPE-PEG(3000-5000), respectively. The as-prepared 50 µL of SUVs were added to 1 mL of 0.05 %w/v of particles dispersed in HEPES buffer 1. The particles were gently rotated for 1 h. The resulting dispersion was centrifuged at 419 rcf for 1 min and the supernatant replaced with HEPES buffer type 1 to remove any SUVs present in the dispersion.

This method was used for all experiments regarding the influence of particle material, surface roughness and the effect of polymer insertion on the spreading and mobility of the lipid bilayer.

CSLB preparation: method 2

Typically, a lipid mixture consisting of 98.9 mol % DOPC, 1 mol % DOPE-PEG(2000) and 0.1 mol % DOPE-Rhodamine or TopFluor-Cholesterol in chloroform was dried overnight in a glass vial covered with aluminum foil under vacuum desiccation. We investigated different PEGylated lipid lengths and molar ratios. After drying, 1 mL HEPES buffer type 2 or 3 was added to reach a concentration of 2 g L^{-1}. The dispersion was vortexed for 30 min, after which it became turbid. It was then transferred to a plastic test tube and ultrasonicated using a tip sonicator (Branson Sonifier SFX150) set to 30 % of its maximum amplitude for a total time of 30 min using a pulsed sequence (18 s on/42 s off, total on time 9 min) on ice to prevent heating. The SUV dispersion was then centrifuged for 45 min at 2029 rcf to sediment larger vesicles and titania particles originating from the tip.[44] 200 µL SUVs were taken from the top to isolate the smallest vesicles.

17 µL of 0.5 g L^{-1} SUVs in HEPES buffer 2 or 3 were mixed with 35 µL 0.5 %w/v of particles in Milli-Q water, leading to a surface ratio of SUVs:particles of 8:1. The dispersion was gently rotated for 1 h. The particles were centrifuged at 43 rcf for 2 min and the supernatant was replaced with HEPES buffer type 2 or 3 to remove any remaining free SUVs from the dispersion. Alternatively, the particles were allowed to sediment by gravity for 30 min instead of centrifuging and the supernatant was replaced.

This method was used for all experiments regarding the colloidal stability of CSLBs, the mobility of inserted DNA and the mobility of self-assembled CSLB clusters.

3.2.3 Coating CSLBs with DNA for self-assembly

After the particles were coated with a lipid bilayer using method 2, various amounts of inert and/or linker DNA were added and the dispersion was gently rotated for 1 h.

To remove any remaining free DNA strands in solution, the particles were washed by centrifugation for 2 min at 43 rcf, or alternatively, by sedimentation by gravity for 30 min, and the supernatant was replaced three times by HEPES buffer type 2 or 3.

We characterize the amount of dsDNA that we add as a surface density σ_{DNA}, which we define as follows:

$$\sigma_{\mathrm{DNA}} = \frac{N_{\mathrm{DNA}}}{A_{\mathrm{CSLB}}}, \tag{3.1}$$

where N_{DNA} is the total number of dsDNA strands and A_{CSLB} is the total surface area of the CSLBs. The total number of dsDNA strands and particles were estimated from the reported stock concentrations. In this calculation, we assume that all the added dsDNA strands are distributed homogeneously over all particles and that no dsDNA remains in solution. We typically used $\sigma_{\mathrm{DNA}} = 320\,\mu\mathrm{m}^{-2}$ dsDNA linkers to obtain flexible structures.

Particle clusters were formed by mixing two particle types coated with complementary DNA linkers in a 1:1 number ratio in a round metal sample holder equipped with a polyacrylamide-coated glass cover slip (see Van Der Wel et al.[202] for details). The polyacrylamide coating keeps the particles from sticking to the glass surface, allowing them to cluster via diffusion limited aggregation.

3.2.4 Sample characterization

The samples were imaged with an inverted confocal microscope (Nikon Ti-E) equipped with a Nikon A1R confocal scanhead with galvano and resonant scanning mirrors. A $100\times$ oil immersion objective (NA = 1.49) was used. A 561 nm laser was employed to excite the Lissamine Rhodamine dye, a 488 nm laser was used to excite the TopFluor-Cholesterol dye. The excitation light passed through a quarter wave plate to prevent polarization of the dyes. 500-550 nm and 565-625 nm filters were used to separate the emitted light from the TopFluor and the Rhodamine dyes, respectively.

The charge of the particles in Milli-Q water was determined via zeta potential measurements using a Malvern Zetasizer Nano ZS.

3.2.5 Fluorescence recovery after photobleaching (FRAP)

We used fluorescence recovery after photobleaching (FRAP) to check the mobility of the lipids in a CSLB. A circular area of the fluorescent sample was bleached, the recovery signal was collected and normalized as

$$I_{\mathrm{corr}}(t) = \frac{I(t)}{I(t=0)I_{\mathrm{ref}}(t)}\ , \tag{3.2}$$

where $I_{\mathrm{corr}}(t)$ is the measured intensity $I(t)$ normalized with respect to the intensity just before bleaching $I(t=0)$ and corrected for bleaching through measurement of the intensity of a non-bleached reference area, $I_{\mathrm{ref}}(t)$. Additionally, we subtracted the background signal from I and I_{ref}. We found that the signal can be fitted using the

following expression:

$$I_{\text{corr}}(t) = A\left(1 - \exp\left[-\frac{t - t_0}{\tau}\right]\right) \tag{3.3}$$

where A is the extent of the recovery, $t - t_0$ is the time elapsed since the beginning of the recovery process and τ the recovery time.

While there is a simple relation linking τ to D for circular bleaching areas on planar surfaces,[203] we are not aware of a similar expression for a spherical surface that is partly bleached from the side, as is the case in our experiments. Therefore, we quantify the lateral mobility in terms of the recovery time τ only.

All FRAP experiments on silica particles were performed using 7 µm particles, unless stated otherwise. To measure the lateral mobility of DNA linkers using FRAP, no fluorescently-labeled lipids were used and instead, we used a high linker DNA concentration ($\sigma_{\text{DNA}} = 3 \times 10^5\ \mu\text{m}^{-2}$) that provided a sufficiently bright fluorescent signal.

3.2.6 Particle stability analysis

To estimate the colloidal stability of particles, we rotated the particles (0.4 %w/w) in a test tube for at least 1 h, thereby allowing them to aggregate. We then immobilized some of the clusters on a glass substrate, allowing us to take a "snapshot" of the cluster distribution at that time. Particles were located in brightfield microscopy images of these sedimented, semi-dilute (volume fraction $\phi \approx 0.001$) samples. The cluster sizes were determined by using the `bandpass`, `locate` and `cluster` functions from TrackPy.[188] Erroneously tracked positions were corrected manually. The separation distance below which particles are considered to be part of a cluster was chosen to be $2.2R$, where R is the particle radius. This can lead to a small overestimation of the number of clusters when particles are close together but have not irreversibly aggregated. We defined the fraction of single particles f_{single} as the number of detected clusters with a size of 1 (i.e. single particles) divided by the total number of individual particles. The error on this fraction was estimated as the standard deviation of the average cluster size divided by the square root of the total number of particles. For each measurement, we analyzed between 150 to 4000 individual particles.

3.2.7 Trimer flexibility analysis

We have analyzed three linearly-connected CSLBs that were functionalized with inert dsDNA and linker dsDNA. To quantify the mobility of the self-assembled trimers, we tracked the position of the three individual particles in brightfield movies as a function of time and calculated the opening angle θ between them. For tracking and calculating θ, we used a custom algorithm that is depicted in Figure 3.1.

First, the user selects the particles of interest from the first frame (see Figure 3.1a). This increases the computational efficiency of tracking because it reduces the number of tracked features and allows for cropping of all frames. We then iterate over all

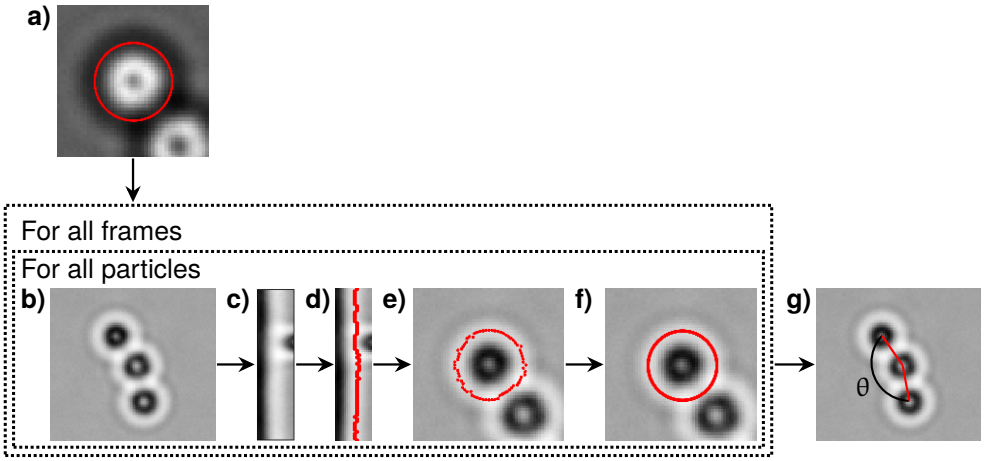

Figure 3.1: **The algorithm used for tracking particles** in brightfield movies, depicted graphically. **a)** The user selects the particles that need to be tracked from the first frame using a Matplotlib [204] interface. **b)** The current frame is inverted so that the dark ring around features becomes bright. **c)** The frame is interpolated and converted to polar coordinates with the current provisional particle position at the origin. **d)** For each row (corresponds to each polar angle), the position with the maximum intensity is found (for intensities higher than a set threshold). **e)** The coordinates that were found are then converted to the original Cartesian coordinates. **f)** A circle is fit to the coordinates using a least-squares method. **g)** The opening angle between the three particles is determined, whilst keeping the particle order the same for all frames.

frames to identify the positions of the selected particles. Each current frame is inverted, so that all particles have a ring of high intensity around them (see Figure 3.1b). The frame is converted to polar coordinates with the current provisional particle position at the origin (see Figure 3.1c), where the provisional position is the one that the user selected for the first frame and the previous tracked position for all subsequent frames. For each row (each polar angle), the position of maximum intensity is found (see Figure 3.1d) and these coordinates are then converted back to the original Cartesian coordinate system of the frame (see Figure 3.1e). A circle is fitted to these coordinates using a least-squares method (see Figure 3.1f). After all three particles are found in this frame, the opening angle between them is determined using simple trigonometry (see Figure 3.1g). From the opening angles of all the frames, we calculated the mean squared displacement of the angle (MSAD) or, equivalently, the "joint flexibility", [85] which we label as J.

We analyzed the free energy of trimers as function of opening angle using two methods: first, by converting the histogram to the free energy using Boltzmann weighing and second, using a maximum-likelihood estimation method of angular displacements. [202,205] We confirmed that both methods agreed and show only the result of

the maximum-likelihood method, because it allows us to estimate the error in our measurement. We now describe these methods in detail.

Trimer free energy: Boltzmann weighing

We obtained a histogram of opening angles between 60 deg to 300 deg with a bin width of 3 deg. We then mirrored and averaged the data around 180 deg and converted this to a probability density function. From the probability density function we determined the free energy using Boltzmann weighing,

$$\frac{F}{k_B T} = -\ln p + \frac{F_0}{k_B T}, \tag{3.4}$$

where F is the free energy, k_B is the Boltzmann constant, T is the temperature, p is the probability density and F_0 is a constant offset to the free energy, which we chose at a reference point (180 deg) so that the free energy is equal to zero there.

Trimer free energy: maximum-likelihood estimation

While the Boltzmann weighing method is very straightforward, it gives no information about the experimental error. To estimate the error, we used an analysis that is based on a maximum-likelihood method in which particle displacements are modeled,[202,205] which we adapted for our experimental system. We used (angular) displacements because for Brownian particles they are uncorrelated in time, in contrast to positions, or values of the opening angle. This means that using this method, we can obtain reliable results even for a limited number of particles.[206]

To summarize, we followed the method outlined in subsection 3.4.2 of Van der Wel:[205] we find the maximum-likelihood estimate of the local force field $F(\theta)$ by using a model for the transition probability P:

$$P(\theta_1, t+\tau|\theta_0, t) = (4\pi D\tau)^{-1/2} \exp\left(-\frac{(\Delta\theta - \beta D F(\theta)\tau)^2}{4\pi D\tau}\right) \tag{3.5}$$

where θ_0 is the opening angle at a time t and θ_1 is the angle at a later time $t+\tau$, τ is the time between measurements, D is the diffusion coefficient determined from the mean squared displacement, $\Delta\theta = \theta_1 - \theta_0$ and β is the Boltzmann constant times the temperature. A Bayesian method was used to find the maximum-likelihood estimate by using emcee[207] and the error was determined as the standard deviation of the chain of Markov Chain Monte Carlo (MCMC) samples. We determined the free energy up to an arbitrary choice of a reference energy by numerical integration of this force. This free energy was then mirrored around 180 deg and averaged to determine the free energy between 60 deg and 180 deg. We observed a boundary effect inherent to the analysis for angles smaller than 60 deg+$\sqrt{2J\tau}$ (where J is the joint flexibility) leading to a slight overestimation of the free energy for those angles.

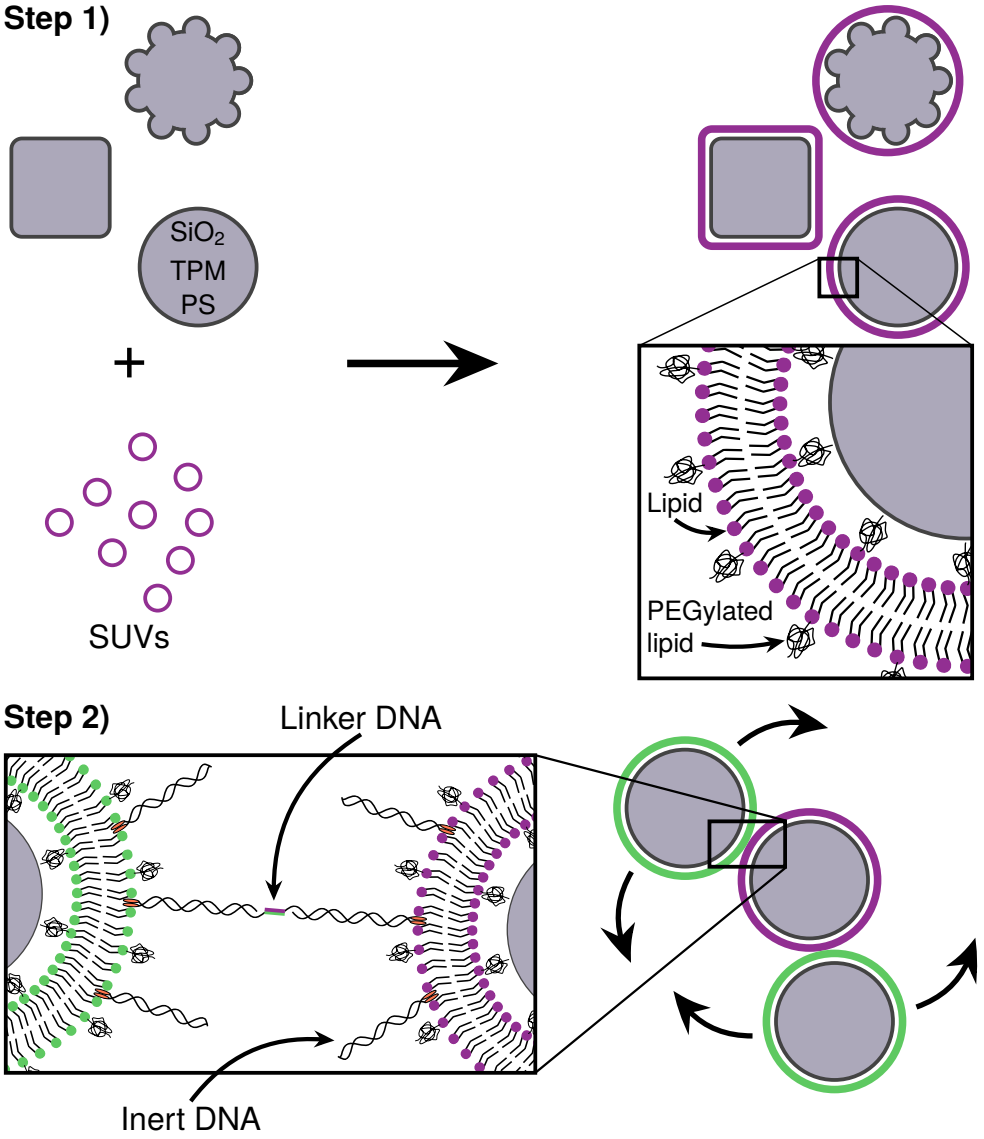

Figure 3.2: **Overview of the experimental system.** Not to scale. **Step 1)** Micrometer-sized colloidal particles are coated with a lipid bilayer by adding small unilamellar vesicles (SUVs) that rupture and spread on the particle surface. We varied the composition of the lipids, as well as the material and shape of the particles. **Step 2)** DNA linkers with hydrophobic anchors can be added to make particles that are functionalized with DNA with complementary sticky ends. When the lipid bilayer is fluid, the linkers can diffuse over the particle surface and therefore also the linked particles can slide over each other.

3.3 Results and Discussion

We will now characterize every step in the formation of CSLBs. In the first section of the results we study the homogeneity and mobility of the lipid bilayer on colloidal particles made from different materials, and therefore various surface functionalities and degrees of roughness. Furthermore, we investigate the effect of PEGylated lipids on the homogeneity and mobility of the lipid bilayer and their use as steric stabilizers to prevent nonspecific aggregation.

Having found conditions that yield colloidal particles with a homogeneous and mobile bilayer, we subsequently introduce double-stranded DNA connected to a hydrophobic anchor into the bilayer, as shown in Figure 3.2.2. We employ DNA constructs both with and without single-stranded sticky ends, to investigate their use in DNA-mediated binding and their effect on colloidal stability, respectively. Finally, we demonstrate that CSLBs can be used for self-assembly by employing DNA linkers with complementary single-stranded sequences. We use FRAP to measure the lateral mobility of DNA linkers on the particle surface inside and outside the bond area. In this way, we show that they are mobile if the bilayer is fluid and that, in this case, the particles can freely roll over each other's surfaces when bonded.

3.3.1 Lipid bilayer coating of colloidal particles

To use CSLBs in self-assembly studies or as model membrane systems, it is critical that a homogeneous and fluid bilayer forms on the colloidal particles. This implies successful assembly of both leaflets of the bilayer and lateral mobility of the lipids, and hence proteins, linkers, and larger lipid domains, in the membrane. The formation of lipid bilayers on solid supports can be achieved by deposition of SUVs under physiological conditions, as shown in Figure 3.2.1. A combination of electrostatic and Van der Waals forces lead to spreading and fusion of the liposomes on the surface of the supports.[43,45,208,209] Between the surface of the support and the bilayer a thin layer of water remains, allowing the lipids to laterally diffuse in the absence of other motion-restricting forces. Previous studies on planar SLBs reported that there are many factors which can prevent homogeneity and mobility of the bilayer.[210] These factors are related to the surface that is coated (its surface charge, chemical composition and roughness), the aqueous medium (pH and ionic strength), the SUVs (composition, charge, size, transition temperature) and the temperature at which the lipid coating happens.[45,46] Here we will study how some of these factors, that are inherent to the use of solid particles, influence the formation of supported lipid bilayers on colloidal substrates.

Influence of the chemical properties of the particle surface

The available variety of colloids with anisotropic shapes makes them attractive for self-assembly and model membrane studies. Current synthetic procedures tailored to obtain different shapes, however, typically rely on the use of specific materials and therefore yield colloids with different surface properties. We have selected

Table 3.1: Classification of bilayer spreading and mobility based on the material and the surface charge of the colloidal substrates. All Zeta potential measurements were performed in Milli-Q water at room temperature.

Material	Zeta pot. [mV]	Homogeneous	Fluid
Silica spheres (Stöber, Microparticles GmbH)	−56 ± 6	**yes**	**yes**
Hematite cubic particles[197]	+39 ± 5	no	no
Silica-coated hematite cubic particles[24]	−32 ± 6	**yes**	**yes**
Polystyrene (PS) spheres (Sigma Aldrich)	−38 ± 2	no	no
PS spheres with carboxyl groups[201]	−43 ± 1	no	no
Silica-coated PS-TPM anisotropic particles[64]	−33 ± 1	**yes**	**yes**
TPM spheres[199]	−42 ± 1	**yes**	no
TPM spheres with carboxyl groups[200]	−46 ± 1	no	no
TPM spheres with amino groups[200]	−12 ± 4	no	no

a range of particles of different shapes and commonly used materials to test for membrane homogeneity and mobility after coating with SUVs. In particular, we tested silica spheres prepared by a sol-gel method, commercially available polystyrene spheres, polystyrene spheres with carboxyl groups made using a surfactant-free dispersion polymerization method,[201] 3-(trimethoxysilyl)propyl methacrylate (TPM) spheres,[199] TPM spheres functionalized with carboxyl and amino groups,[200] silica-coated polystyrene-TPM spheres and symmetric and asymmetric dumbbells;[64] as well as hematite cubes[197] and silica-coated hematite particles.[24] Silica-coated polystyrene-TPM dumbbells and hematite cubes were obtained by depositing a silica layer following the Stöber method.[211]

After coating, we visually inspect the lipid-coated particles using confocal microscopy and consider bilayers to be homogeneous if more than 50% of the particles do not show defects in the bilayer. We characterize the bilayer fluidity by measuring the mobility of the fluorescently-labeled lipids on the colloid surface using FRAP. After bleaching, we observe the recovery of the fluorescence intensity due to the diffusion of the dyed lipids in and out of the bleached area. We consider the lipids and thus the bilayer to be mobile if the intensity signal recovers homogeneously in the bleached area, otherwise we consider them to be (partially) pinned to the surface.

Our first observation was that only particles that possess a silica surface exhibited homogeneous and mobile bilayers (Table 3.1). We did not succeed in coating colloids made from polystyrene or hematite with a homogeneous bilayer. However, once such substrates were first coated with a silica shell, the bilayer was found to be both homogeneous and mobile. Unexpectedly, particles made from an organosilica compound (TPM) whose surfaces are similar to silica[199] only showed homogeneous, but not mobile bilayers. Since silica, TPM and polystyrene colloids were all negatively

charged, we conclude that the chemical composition of the substrate and not only the surface charge plays a fundamental role in the homogeneity and fluidity of the bilayer. These results agree with previous experiments on planar SLBs, in which silica-based surfaces were found to be one of the most reliable supports for homogeneous and mobile lipid bilayers.[45]

Since colloidal particles are often functionalized with different groups on the surface, we furthermore have characterized the bilayer on particles equipped with surface groups commonly used in colloidal science (Table 3.1). While TPM particles with an unmodified silica-like surface showed homogeneous bilayers, we found that functionalization with negatively charged carboxyl or positively charged amino group prevented spreading and fusion of the lipid vesicles. Likewise, functionalization of polystyrene spheres with carboxyl groups did not enhance the homogeneity of the lipid bilayer. A previous study on planar SLBs reported that the spreading of SUVs depends on the combination of the molecular ions in the buffer and the type and density of surface charge.[212] While amino-functionalized surfaces are hence expected to disrupt the spreading of SUVs in the presence of the negatively charged HEPES molecules of the buffer, the observation of inhomogenous bilayers on carboxyl-functionalized surfaces can likely be allocated to an insufficiently dense surface coverage. We conclude that similar to planar SLBs, the homogeneity and fluidity of the bilayer of CSLBs is dependent on a complex interplay of the chemical and physical properties of the lipids and the particle's surface.

Influence of particle curvature differences

Another factor that may influence the successful formation of a homogeneous and mobile bilayer is the variation in curvature of the colloidal substrate, which may hinder spreading and fusion of SUVs. Curvature differences can originate from the overall anisotropic shape of the particles or from surface roughness. As discussed before, we found that particles with a comparably slowly varying curvature, such as hematite cubes or symmetric and asymmetric dumbbells (see Table 3.1), had a fluid and homogeneous bilayer after coating, if they featured a silica surface clean of any polymer residues from synthesis. Particles with rough surfaces, however, have a much higher and frequent variation in curvature. To investigate the effect of large curvature differences, we prepared two batches of polystyrene particles which only differed in their surface roughness and coated them with a silica layer following a Stöber method.[198] In Figure 3.3 we show that particles with some roughness (b) can be homogeneously coated with a bilayer (a) while particles with very rough surfaces (e) show an inhomogeneous bilayer (d). FRAP experiments confirmed that the bilayer on the "smooth" surface is not only homogeneous, but also mobile, as shown by the recovery in Figure 3.3c. On the contrary, the inhomogeneous bilayer on the rough particle is immobile as indicated by the non-recovering intensity signal in Figure 3.3f. We conclude that the roughness of the surface plays an important role in both bilayer homogeneity and mobility.

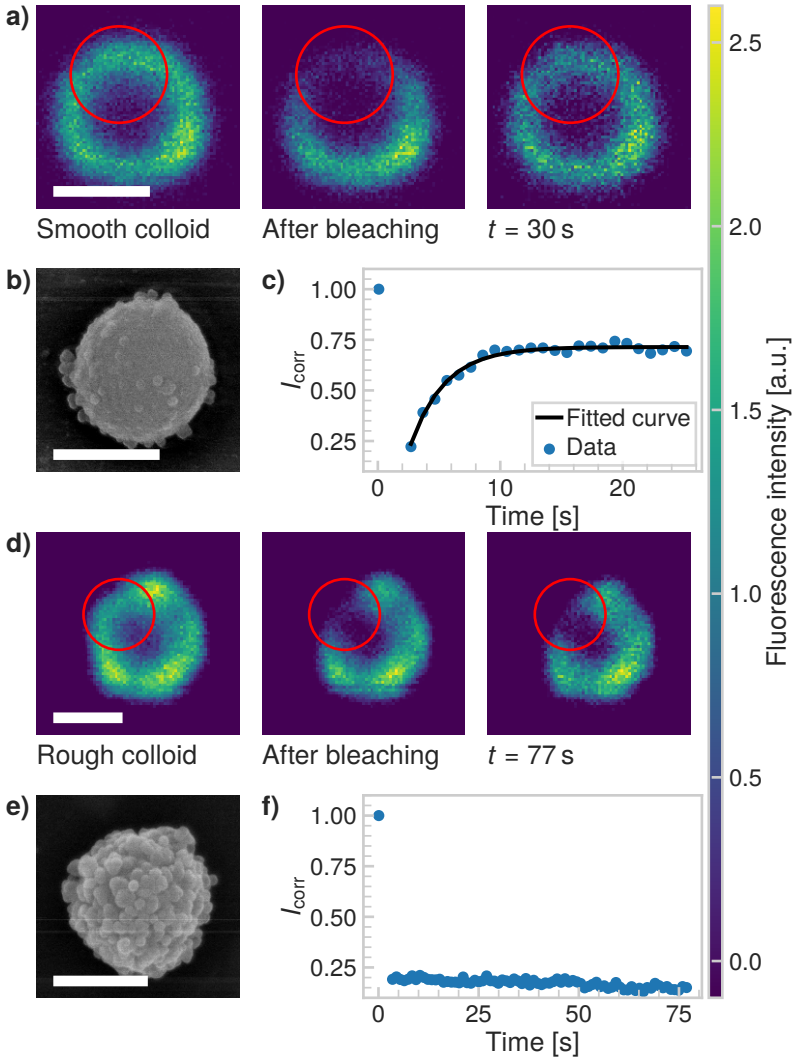

Figure 3.3: **Effect of surface roughness on lipid bilayer formation.** Sequence of a FRAP experiment before bleaching, just after bleaching and after 30s and 77s for the **a)** smooth and **d)** rough particle, respectively. Scanning electron microscopy images (SEM) images of **b)** a smooth and **e)** rough polystyrene-TPM particle coated with silica. On the right, the fluorescence intensity as a function of time and an exponential fit of the data for the **c)** smooth and **f)** rough particle are shown. The fluorescence recovery of the bilayer on the smooth particle shows that the bilayer is fluid, in contrast to the rough particle which does not show a recovery of the fluorescence. Scale bars are 1 μm.

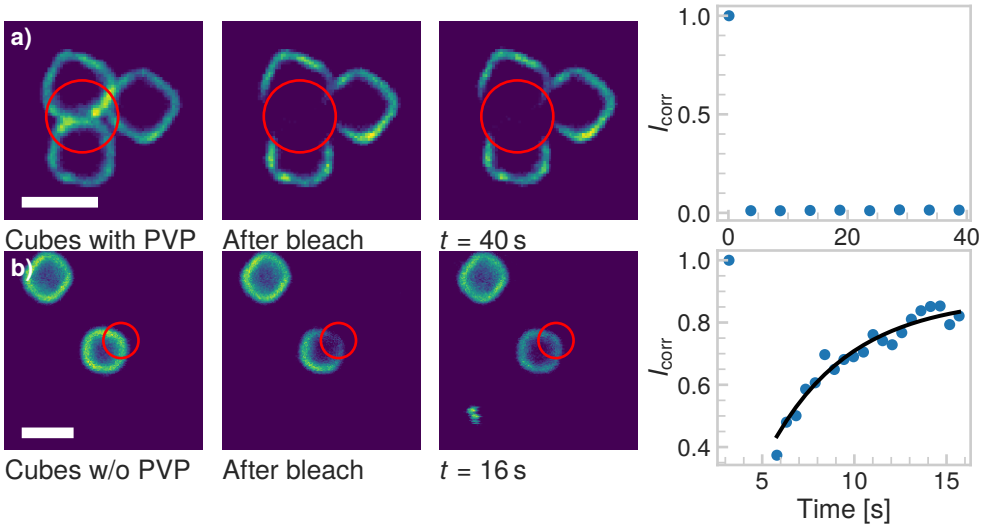

Figure 3.4: **Effect of PVP on CSLB formation.** FRAP experiment on a group of three cubes with **a)** and without **b)** PVP. Only the sample without PVP shows recovery of the signal in the bleached area. Scale bars are 2 μm.

Influence of free and grafted polymers

Polymers or surfactants are often employed to stabilize colloidal particles in solution,[213–215] but may influence the formation and mobility of the bilayer in CSLBs. Here, we test how the presence of, for example, leftover polymers from particle synthesis, affects the bilayer. We compare a sample of silica-coated hematite cubes with and without PVP, a polymer commonly used in colloidal syntheses and conservation. To remove the PVP from the surface after synthesis, we calcinated the colloids at 500 °C for 2h. Figure 3.4 shows that cubes with PVP (Figure 3.4a) posses an inhomogeneous bilayer and the ones without it feature a bilayer that homogeneously covers the surface (Figure 3.4b). As expected for Stöber silica surfaces, the bilayer on the colloids for which the PVP was removed is also mobile, as indicated by the recovery of the fluorescence intensity.

Moreover, the presence of polymers may not only affect the bilayer's properties, but also the incorporation of functional groups such as DNA linkers into it. We tested this by preparing CSLBs with fluorescently-labeled DNA linkers connected to double cholesterol anchors and then transferring an aliquot of this dispersion to a HEPES solution containing 5% w/w of Pluronic F-127, a polymer that is commonly used for the stabilization of colloidal particles. While the fluorescent signal of the CSLBs with and without F-127 were initially equal, already 15 minutes after mixing we observed less dsDNA fluorescence on the CSLBs with F-127 compared to particles without it. After 1 h, the fluorescence intensity of the CSLBs with F-127 was comparable to that of control particles not coated with linker dsDNA (Figure 3.5a-d). We therefore conclude

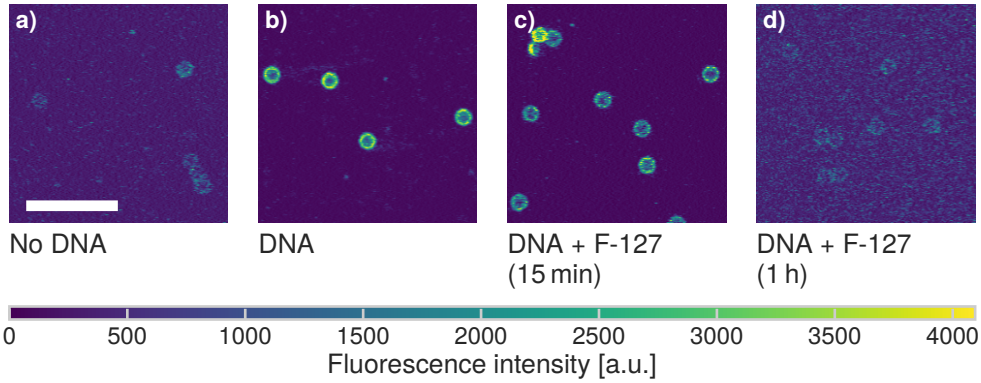

Figure 3.5: **Influence of F127 in linker inclusion. a)** Control image of the fluorescence of the undyed CSLBs. **b)** Fluorescence intensity of CSLBs coated with 20 nm linker dsDNA. **c)** The same sample as in panel b, but imaged 15 min after dispersion in 5 % F-127 solution. The fluorescence on the particles was found to be significantly less homogeneous than in panel b. **f)** The same sample as in panel b, but imaged 1 h after dispersion in 5 % F-127 solution. The fluorescence intensity is comparable to the uncoated control in panel a so we conclude that all dsDNA has been removed from the bilayer by F-127. Scale bar is 10 μm.

that F-127 removed the cholesterol-anchored linker DNA from the bilayer, in line with recent experiments on emulsion droplets coated with mobile DNA linkers.[216]

Influence of PEGylated lipids on bilayer homogeneity and mobility

The presence of polymers in SLBs is not always detrimental, but may even improve bilayer mobility. Previous studies on planar SLBs showed that membranes can be supported by polymers covalently bound to lipids, constructs also known as lipopolymer tethers.[217–221] Since lipopolymer tethers increase the thickness of the water layer between the solid support and the bilayer,[217–219] they are thought to reduce the friction between the substrate and the bilayer, allowing for higher diffusivity of lipid molecules and linkers.

Inspired by this, we study how a specific lipopolymer tether affects the spreading and the fluidity of the bilayer in CSLBs. We used the lipopolymer DOPE-PEG, a phospholipid with a covalently-bound PEG molecule. We employed PEGylated lipids with three different molecular weights: 2000, 3000 and 5000 g mol^{-1} in varying concentrations. It is important to note that PEGylated lipids were introduced in the system during the SUV formation by mixing them with the other lipids. This means that once the bilayer is formed, they are present in both leaflets.

We report in Figure 3.6a-b the effect of varying concentration and molecular weight of the lipopolymers on the spreading and the mobility of the bilayer. In the absence of PEGylated lipids, the bilayer on the CSLBs was observed to be fluid. At increased

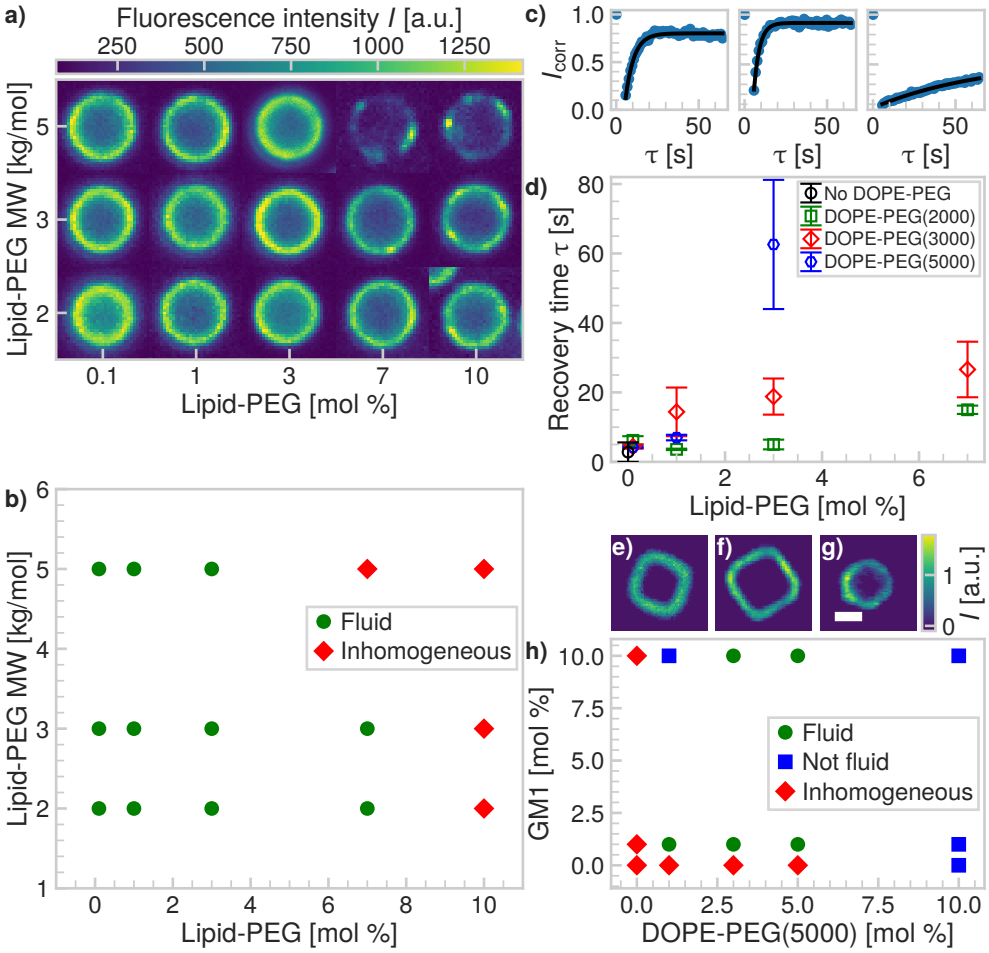

Figure 3.6: **Effect of PEGylated lipids on CSLB formation and fluidity. a)** Colormap of the intensity of the bilayer of spherical CSLBs ordered by increasing molecular weight and concentration of PEGylated lipids. The images are taken in the equatorial plane. **b)** Phase diagram of the state of the bilayer for varying molecular weight and concentration of PEGylated lipids. **c)** Intensity recovery curves as a function of time from FRAP experiments of, from left to right, CSLBs without PEGylated lipids, with 1 mol % DOPE-PEG(2000) and 3 mol % DOPE-PEG(5000). **d)** Plot of the recovery time after FRAP depending on molar concentration and size of the PEGylated lipids. Colormap of a fluorescent image of a cubic bilayer made with **e)** 1 mol % GM1 and 3 mol % DOPE-PEG(5000), **f)** 1 mol % GM1 and 10 mol % DOPE-PEG(5000), **g)** no GM1 or DOPE-PEG(5000). Scale bar 1.5 µm. **h)** Phase diagram of spreading and fluidity of the bilayer on cubic silica shells depending on GM1 and PEGylated lipids.

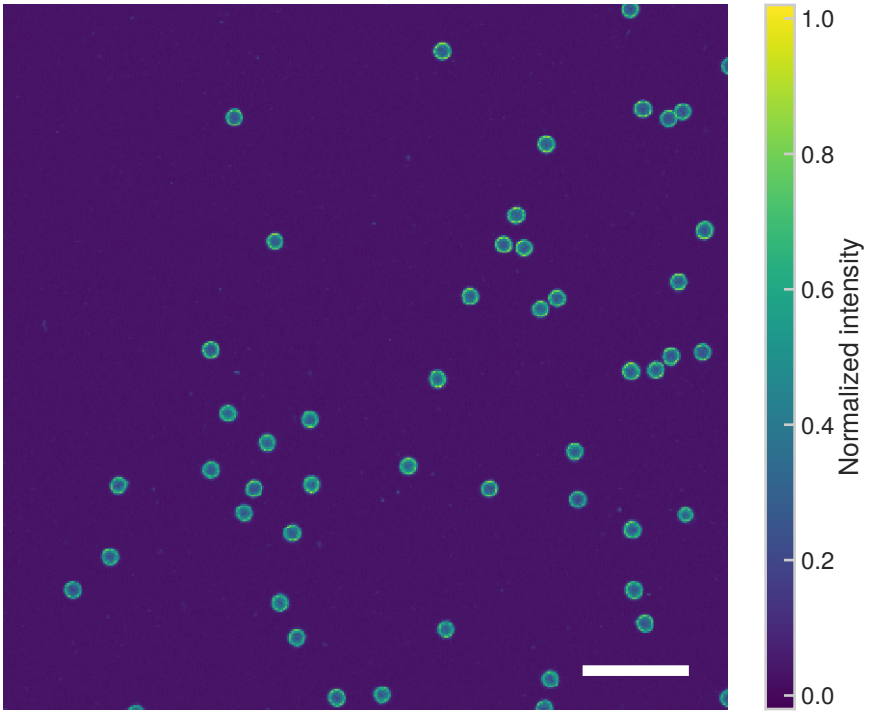

Figure 3.7: **Overview picture showing the homogeneity of the lipid bilayer** for CSLBs containing 1 mol % DOPE-PEG(2000). The scale bar is 15 µm.

concentrations of DOPE-PEG, the bilayer became inhomogeneous, which indicates insufficient spreading and fusion of the SUVs. This effect appeared at lower molar fractions for lipopolymers with higher molecular weights of the DOPE-PEG. For completeness, we note that a small fraction of particles in samples that are labeled as inhomogeneously coated do exhibit a homogeneous, but nevertheless immobile, bilayer. We believe that the reason for the observed inhomogeneity is twofold. On the one hand, higher concentrations of lipopolymers lead to an increased steric stabilization, that prevents fusion of the SUVs and hinders the van der Waals interactions between the SUVs and the substrate that aid spreading. On the other hand, PEGylated lipids in the brush state increase the bending rigidity of the SUV membrane, thereby preventing rupture and spreading on the surface.[222]

For fluid membranes, we quantified the mobility of the lipids by calculating the recovery time from FRAP experiments, which is the time it takes a bleached area to recover its fluorescence intensity. We find that the diffusion of the lipids is faster for PEGylated lipids with a lower molecular weight and increases with decreasing amount of the lipopolymers, see Figure 3.6c-d. This latter result agrees with a study performed on planar supported lipid bilayers.[217] In the presence of lipopolymers,

we find the shortest recovery time ((3.20 ± 0.02) s), e.g. highest diffusivity, for 1 mol % of DOPE-PEG(2000). For this concentration and type of lipopolymer, the resulting bilayer is also homogeneous, as shown in Figure 3.7. The decrease of the diffusion coefficient with the amount of lipopolymer indicates that the PEGylated lipids are pinned to the surface and in this way hinder the mobility of the other lipids.

We emphasize that the mobility of supported lipid bilayers in presence of polymers is dependent on many factors and one may not extend our results to other types of polymers, lipid bilayers or physiological environments.[221] The complex interplay between polymers and the chemical properties of the colloidal surface can lead to surprising results. For example, and in contrast to what we reported above, we found that a homogeneous bilayer on cubic silica particles could only be obtained by using both PEGylated lipids (DOPE-PEG(5000)) and a negatively charged lipid (GM1). Interestingly, at high concentrations of PEGylated lipids, the bilayer is very homogeneous but not mobile (Figure 3.6h). This is in contrast to silica spheres coated with the same concentrations of lipopolymers and only zwitterionic lipids, which do not possess a homogeneous bilayer, see Figure 3.6a. We indicated this state in which the bilayer is homogeneous, but not fluid, with blue squares in Figure 3.6h. A possible origin of this unusual behavior could be the different porosity, surface chemistry and charge of the silica cubes[211] compared to the silica spheres (Table 3.1).

3.3.2 Stabilizing CSLBs against nonspecific aggregation

To build specific colloidal structures from the bottom up, careful control over the interactions between the particles is required. On the one hand, specific attractive interactions may be employed to control which particles interact. This specific binding can be achieved by using dsDNA linkers with complementary sticky ends.[74,85,110] On the other hand, the particles need to be prevented from binding to each other nonspecifically: that is, not via dsDNA linker interactions but via other attractive forces that act indiscriminately between all particles, such as Van der Waals forces. In other words, it is crucial to be able to control the colloidal stability of the CSLBs.[49]

In our experiments, stabilization by repulsive electrostatic interactions is not a feasible approach. Namely, surface charges are screened by the counterions in the HEPES buffer, which is necessary to allow the complementary DNA sticky ends to bind.[74] The ionic strength of the buffer must be higher than at least 50 mM for clusters to form via DNA-mediated attractions.[223] At these salt concentrations, even the bare silica particles are no longer stabilized by their negatively charged surface groups. Indeed, we found that both the bare silica particles and the silica particles coated with a lipid bilayer aggregated in all buffers, as was previously observed.[224] The fraction of single particles determined from light microscopy images was $f_{\text{single}} = 0.67 \pm 0.10$ for uncoated silica particles after one hour of mixing in the buffer, while they were previously stable in deionized water. We therefore explored different ways to sterically stabilize the particles using higher concentrations of PEGylated lipids, SDS and inert dsDNA strands.

Stabilization using SDS

SDS is a surfactant with amphiphilic properties, consisting of a polar headgroup and a hydrocarbon tail, that has been shown to stabilize emulsion droplets coated with lipid monolayers.[56] Inspired by these findings, we added SDS to the CSLBs after bilayer coating to increase their stability. However, in contrast to lipid coated emulsion droplets we found no significant increase in stability when we varied the SDS concentration between 0 mM to 1 mM. In fact, the highest concentration of 1 mM led to a decrease in particle stability from $f_{\text{single}} = 0.67$ without SDS to $f_{\text{single}} = 0.45$ at 1 mM. This is likely caused by the disruptive effect that SDS can have on lipid bilayers. In a study[225] on large unilamellar vesicles (LUVs) made from POPC, it was found that SDS can completely solubilize the vesicles above concentrations of 2 mM. While this concentration is higher than the concentrations that we used here, we already observed some damage to the bilayer. The resulting inhomogeneous coating may allow nonspecific "sticking" on patches that are not covered with a lipid bilayer and this leads to a subsequent decrease in overall colloidal stability.

Stabilization using PEGylated lipids

In contrast to SDS, PEGylated lipids can provide colloidal stability through steric repulsion between the PEG moieties while also being easily integrated into the bilayer through their lipid tails.[213–215] To test their use for colloidal stabilization, we coated the particles with SUVs that contain a small fraction of the following PEGylated lipids: DOPE-PEG(2000), DOPE-PEG(3000) and DOPE-PEG(5000). Since we include these lipopolymers during SUV preparation, they are part of both the inner and outer leaflet, as depicted in Figure 3.2.1. At low concentrations, we observed no significant change in the stability of the particles upon an increase in the concentration of PEGylated lipids. For example, for DOPE-PEG(2000) stability remained constant below 5 mol % as shown in Figure 3.8a. For concentrations between 1 mol % and 7 mol % for DOPE-PEG(2000), 1 mol % and 6.8 mol % for DOPE-PEG(3000) and 2 mol % and 2.7 mol % for DOPE-PEG(5000), the average fraction of unclustered particles lay between $f_{\text{single}} = 0.5$ and $f_{\text{single}} = 0.77$, with no clear trend observed for different polymer lengths or concentrations. For all measurements, we verified that the spreading of the SUVs was successful. We believe that the stability of the particles did not improve significantly because at these concentrations, the grafted PEG was in the mushroom state instead of the brush state, and therefore not sufficient to provide steric stability.[226,227] Therefore, we increased the concentration of DOPE-PEG(2000) above 7 mol %. Indeed, as shown in Figure 3.8, the colloidal stability increases above this concentration, likely due to a transition from the mushroom to the brush state, as was shown[228] for similar lipopolymers (DSPE-PEG(2000)) around 8 mol %.

While the colloidal stability can be improved by increasing the concentration of PEGylated lipids, the bilayer is not fluid at the required concentrations, which can be seen by comparing Figure 3.8a to Figure 3.6b. Therefore, embedded DNA linkers will also not be mobile in the bilayer and it is not possible to form reconfigurable structures from CSLBs stabilized by PEGylated lipids only.

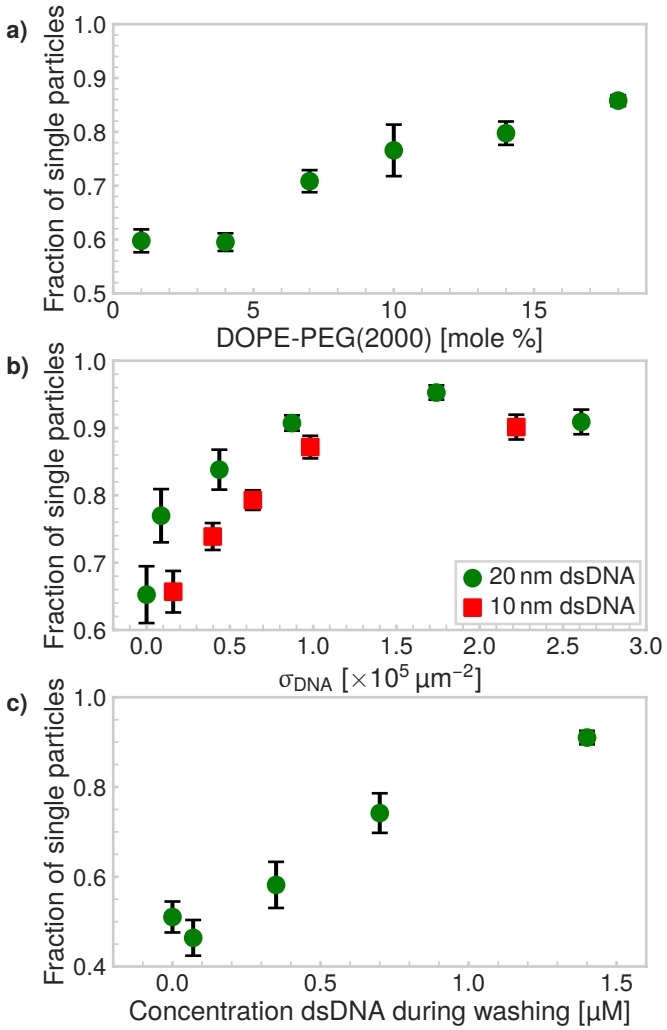

Figure 3.8: **Steric stabilization of CSLBs. a)** Higher concentrations of DOPE-PEG(2000) lead to a higher fraction of single particles in the absence of linker DNA. Stability is shown after one washing cycle of 2 min at 43 rcf and overnight rotation. We hypothesize that above 8 mol %, the packing density of PEG on the surface of the membrane is high enough for the PEG to be in the brush state, making it more effective as a steric stabilizer. **b)** Increasing the number of dsDNA strands on the particle surface increases the particle's stability for two different lengths of inert dsDNA (10 nm and 20 nm). **c)** Centrifugation and redispersion with a solution containing dsDNA affects the fraction of single particles. After centrifuging particles that were initially stable ($f_{\text{single}} = 0.95$, $\sigma_{\text{DNA}} = 1.7 \times 10^5\ \mu\text{m}^{-2}$ dsDNA) 3× at 43 rcf for 2 min, we observed nonspecific aggregation ($f_{\text{single}} = 0.51$) in the absence of dsDNA strands in solution while increasing the concentration of dsDNA (20 nm) in the washing solution could preserve stability.

Stabilization using inert dsDNA

Since PEGylated lipids cannot be used to provide steric stability, because they reduce the fluidity of the membrane, we explored an alternative route to stabilize the CSLBs. Inspired by numerical findings that inert double stranded DNA (dsDNA) can also act as a steric stabilizer via excluded volume interactions between DNA strands on different particles,[229] we employed dsDNA strands with a double-cholesterol anchor at one end, in order to functionalize the CSLBs with these DNA linkers via hydrophobic insertion of the cholesterol into the bilayer,[111] as schematically depicted in Figure 3.2.2.

We varied the surface concentration σ_{DNA} (as defined in Equation 3.1) of two inert dsDNA strands with different lengths and measured its effect on the particle stability, which is shown in Figure 3.8b. The stability was determined after the particles were coated with dsDNA and rotated for one hour. For both the 10 nm dsDNA and the 20 nm dsDNA, we found that increasing the number of grafted dsDNA strands per particle led to an increase in particle stability from $f_{\mathrm{single}} = 0.68$ without dsDNA to $f_{\mathrm{single}} = 0.90$ to 0.95 above $\sigma_{\mathrm{DNA}} = 2 \times 10^5\ \mu\mathrm{m}^{-2}$. We found that the 20 nm dsDNA is slightly more efficient as a steric stabilizer than the 10 nm dsDNA, as can be seen in Figure 3.8b. This is expected, because for the longer DNA, excluded volume interactions between particles start to become important already at larger particle separations than for the shorter DNA. Additionally, excluded volume interactions between DNA strands on the same particle force the DNA to extend outwards already at lower concentrations for the longer DNA strands as compared to the shorter DNA strands. Therefore, the repulsion between the particles also has a longer range, leading to better colloidal stability. However, at concentrations above $\sigma_{\mathrm{DNA}} = 2 \times 10^5\ \mu\mathrm{m}^{-2}$, the difference between the 10 nm and 20 nm dsDNA is less pronounced, because the particles are so densely coated that adding longer or more DNA strands will not stabilize the particles any further.

To use these particles in self-assembly studies, specific interactions need to be present as well, which we here induce by adding dsDNA *linkers*, that is, dsDNA strands with a sticky end and double cholesterol anchors. After the particles are functionalized, any excess linker DNA left in the solvent needs to be removed to reduce unwanted aggregation or saturation of the complementary functionalized particles. To remove excess linker DNA, we washed and redispersed the particles in buffer solution three times and measured the particle stability afterwards. Unexpectedly, it decreased from $f_{\mathrm{single}} = 0.95$ before washing to $f_{\mathrm{single}} = 0.51$ after washing. To detect whether the partial removal of the stabilizing inert dsDNA during washing had caused this aggregation, we washed the particles in a HEPES buffer that contained various concentrations of inert dsDNA. As shown in Figure 3.8c, increasing the concentration of dsDNA in the washing solution led to an increase in particle stability after washing, therefore confirming our hypothesis. Including 1.4 μM of inert DNA in the washing solution allowed us to preserve the particle stability ($f_{\mathrm{single}} = 0.91$).

However, washing the particles with such high concentrations of dsDNA proved

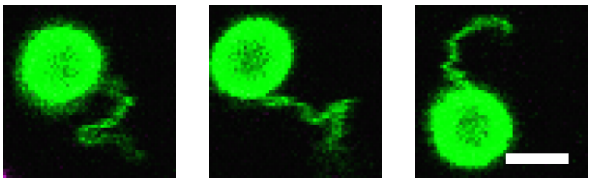

Figure 3.9: **Formation of membrane tubes** at high DNA coating concentrations, shown for three different particles. The scale bar is 2 μm. The tube lengths are comparable to the particle size (2 μm) and the tubes are very floppy. Note that the brightness was increased to show the tubes and as a result the particles are oversaturated.

detrimental to the bilayer and led to the formation of membrane tubes between 1 μm to 3 μm long (see Figure 3.9). These membrane tubes are highly curved surfaces that are only formed under specific conditions, for example a difference in spontaneous curvature between the inner and the outer membrane leaflets.[230] In the present case, since dsDNA is only added after the formation of the bilayer, it is consequently only present in the outer leaflet and hence induces a difference in spontaneous curvature, which in turn causes the formation of tubes. If the DNA would be present on both leaflets, no tube formation is expected. We tested this by mixing the dsDNA with the SUVs before coating the particles, but found no fluorescence signal on the particles' surface, implying the absence of a bilayer coating. We believe that the dsDNA sterically stabilizes the SUVs and prevents spreading and fusion of SUVs on the particle surface.

To summarize, we found that inert double-stranded DNA can impart colloidal stability to the CSLBs. The asymmetric distribution of the DNA constructs over the membrane leaflets causes the formation of membrane tubes at high coating concentrations above approximately 1×10^5 μm^{-2}, but this is currently unavoidable if colloidal stability needs to be preserved during repeated washing cycles.

3.3.3 Linker functionalization for self-assembly

To be able to employ CSLBs in self-assembly experiments, we induce specific attractive interactions by using two sets of dsDNA linkers with complementary single-stranded sticky ends that can form bonds via hybridization. We use two hydrophobic anchors (either cholesterol or stearyl) per dsDNA complex to insert the dsDNA linker into the outer leaflet (see Figure 3.2.2), while at the same time adding inert dsDNA strands for steric stabilization. We use double hydrophobic anchors because dsDNA with a single hydrophobic anchor is less strongly confined to the bilayer.[111] The dsDNA is attached to the double hydrophobic anchor with a tetraethylene glycol (TEG) or hexaethylene glycol (HEG) spacer to allow it to swivel with respect to the anchor. We label the dsDNA linkers with a fluorescent dye to image them using confocal microscopy. Table A.1 contains more details on the DNA strands that we have used here.

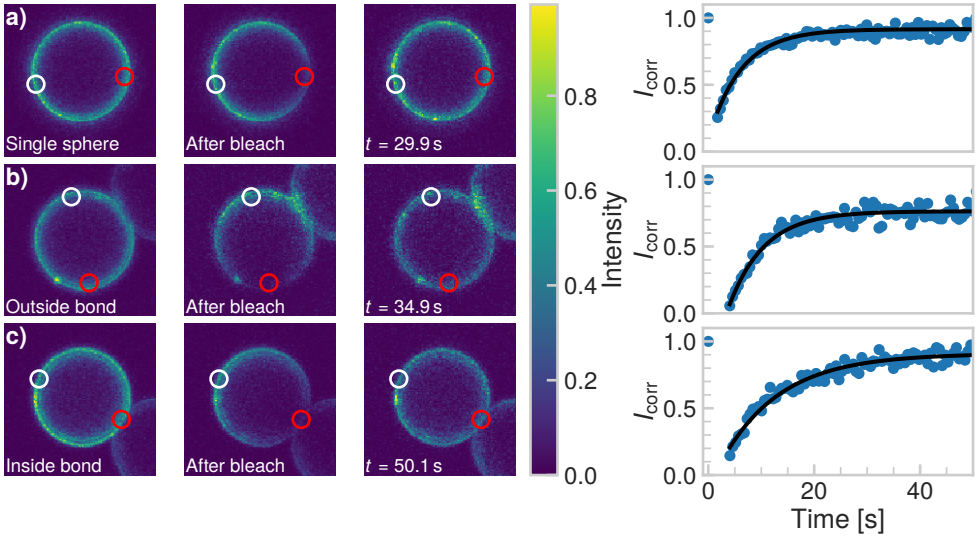

Figure 3.10: **DNA linker mobility on CSLBs.** Three representative FRAP experiments are shown that probe the mobility of DNA linkers on the surface of a 7 µm CSLB. In the intensity plots, a red circle indicates the bleached area and a white circle shows the reference area. For all experiments, the DNA linkers are mobile. **a)** FRAP on a single sphere. We measured an average recovery time of (8 ± 2) s (16 different particles). **b)** FRAP on a sphere in a cluster, taken outside the bond area. We measured an average recovery time of (6 ± 2) s (15 different clusters). Within the error, this is the same as the recovery time of single particles in panel a. **c)** FRAP on a sphere in a cluster, inside the bond area. We measured recovery times of 5 s to 62 s with an average recovery time of (17 ± 16) s (12 different clusters). This is longer than the recovery times we measured outside the bond area in panels a and b, which indicates that the diffusion is slower in the bond area. However, the spread in recovery times was also larger for bleached areas inside the bond area.

Previous experiments[85] have shown that several interesting structures, such as flexible colloidal polymers and molecules, can be obtained via self-assembly of CSLBs. In order to form these reconfigurable structures, not only the lipids in the bilayer should be mobile but also the grafted linker DNA should be mobile on the surface of the membrane. We can quantify the mobility of dsDNA on the surface of the bilayer by measuring the FRAP of fluorescently-labeled DNA. Note that for these experiments we did not employ fluorescent lipids. For a successful recovery after bleaching of the DNA linkers in the binding patch between two particles, two requirements need to be fulfilled: the DNA linkers outside of the binding patch have to be mobile and the bleached linkers inside the binding patch have to be able to unbind, to allow unbleached linkers to diffuse into the binding patch. We have calculated the melting temperature of the sticky end using an approximate formula[231] and find a melting

temperature T_m = 30.4 °C, meaning that at 25 °C the probability for the sticky end to form a duplex is $P(25\,°C) = 0.68$ based on melting temperature considerations only. Therefore, the sticky ends continuously bind and unbind in our experiments, making fluorescence recovery possible, while the sheer number of linkers in the patch area keeps the particles always bound.

We confirmed the mobility of linker DNA on the particle surface using FRAP experiments, shown in Figure 3.10. Note that the whole cluster is immobilized on the (non-passivated) glass coverslip to enable FRAP on these micrometer-sized particles. Therefore these clusters do not show translational diffusion or cluster flexibility. In Figure 3.10a, a representative FRAP experiment on a single sphere is shown. We measured an average recovery time of (8 ± 2) s from independent measurements on 16 different particles. Outside the bond area (Figure 3.10b), we measured an average recovery time of (6 ± 2) s from independent measurements on 15 different clusters. Within the error, the diffusion of DNA outside of the bond area is the same as on free particles, as expected. Inside the bond area (Figure 3.10c), we measured recovery times of 5 s to 62 s with an average recovery time of (17 ± 16) s from independent measurements on 12 different clusters. This is longer than the recovery times we measured outside the bond area and on single particles, which indicates the diffusion is slower in the bond area. However, the recovery time inside the bond area varied greatly between different clusters, indicating that diffusion rates into and out of the bond area can vary between different particles. A likely cause is the spread in the DNA concentration between individual particles in a batch. Higher DNA concentrations imply a higher concentration of bonded linkers in the bond area. This will sterically hinder the diffusion of unbonded linkers inside the patch area and will thus lead to longer recovery times. Furthermore, we hypothesize that the linker concentration in the patch area slowly increases as a function of time after binding, so that the recovery time depends on the time that has elapsed after the formation of the cluster, which we did not control. In summary, we have shown here that the dsDNA linkers are mobile on each part of the (un)bound particle, which is a prerequisite for creating flexibly linked clusters.

3.3.4 Mobility of self-assembled structures

The mobility of individual dsDNA linkers on the surface does not necessarily imply that bonded clusters of DNA-functionalized CSLBs are also reconfigurable. For example, for emulsion droplets functionalized with DNA linkers, the large linker patch that is formed between particles can slow down the motion when the supporting fluid is inhomogeneous[216] and colloidal joints lose their flexibility with an increasing concentration of dsDNA linkers in the bond area.[85]

To measure the flexibility of larger structures, we assembled CSLBs with complementary dsDNA linkers and imaged chains of three CSLBs, so called trimers, over time. We extracted the position of the individual particles and the opening angle θ (see inset Figure 3.11a) for all frames and calculated the mean squared angular displacement (MSAD) to characterize the flexibility.[85] To investigate the influence of

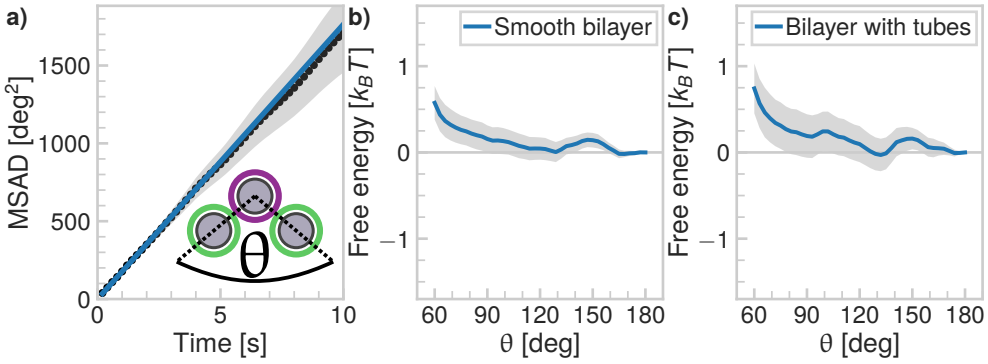

Figure 3.11: **Mobility of self-assembled trimers. a)** Mean squared angular displacement (MSAD) of the opening angle θ for a mobile trimer. The MSAD is linear and we find a joint flexibility $J = (176 \pm 12)\,\mathrm{deg}^2/\mathrm{s}$ ($J = (184 \pm 101)\,\mathrm{deg}^2/\mathrm{s}$ when averaging over all experiments). **b, c)** Free energy as function of opening angle θ for particles with **b)** smooth bilayers and **c)** bilayers that have membrane tubes. The grey shaded area marks one standard deviation confidence interval. We analyzed 53 clusters with smooth bilayers and 18 clusters with membrane tubes. In both cases, we find no preference for specific opening angles within the experimental error, meaning that the particles are freely-jointed. Note that the slight repulsion at small angles is caused by boundary effects inherent to our analysis method.

the membrane homogeneity on the structural flexibility, we compared trimers assembled from CSLBs with homogeneous, fluid bilayers to trimers with bilayers that had spontaneously formed membrane tubes. In the following, we will only show the free energy landscape for θ from 60 deg to 180 deg due to the symmetry of a trimer.

For trimers made from CSLBs with smooth lipid bilayers, we found that the particles ($R = 1.06\,\mu\mathrm{m}$) move with respect to each other over the full angular range. We analyzed the opening angle θ for 53 different clusters by tracking the individual particles and calculating θ for all frames (see inset Figure 3.11a). The average value of the flexibility of the trimers is $J = (184 \pm 101)\,\mathrm{deg}^2/\mathrm{s}$ (or $(0.03 \pm 0.02)\,\mu\mathrm{m}^2\,\mathrm{s}^{-1}$) and agrees well with previous experiments.[85] The spread in the flexibility that we observe is likely caused by the spread in dsDNA linker density on the particles. We then determined the free energy using the maximum-likelihood estimation of angular displacements method (see Section 3.2.7), as shown in Figure 3.11b. We found no preference in the opening angle that is significant with respect to the thermal energy k_BT, indicating that the surface is smooth enough to allow the particles to move over one another without restrictions. We observed a boundary effect inherent to the analysis for angles smaller than $60\,\mathrm{deg} + \sqrt{2J\tau} \approx 69\,\mathrm{deg}$ (where J is the joint flexibility) leading to a slight overestimation of the free energy for those angles. In previous experiments, we observed a small preference, namely a $0.9K_BT$ difference in the free energy, for opening angles around 140 deg.[85] We do not find the same

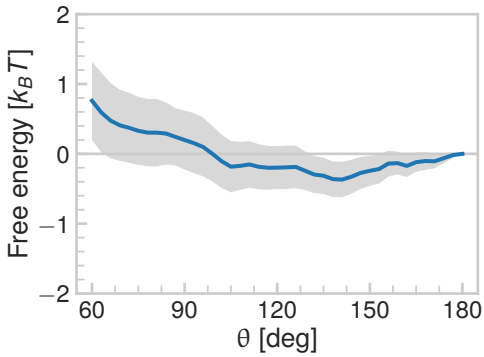

Figure 3.12: **Previous results reanalyzed using a maximum-likelihood method.** In Chakraborty et al.,[85] we measured a preferred angle of 140 deg with a magnitude of roughly 0.9 k_BT. When we analyze this data using the angular displacement method outlined in this work, we see that the observed preference is within the experimental error, as indicated by the shaded gray area.

preference in angle for the experiments presented here. When reanalyzing the data from Chakraborty et al.[85] using our maximum-likelihood method, we noted that the observed free energy difference is within the experimental error (see Figure 3.12) and therefore we conclude that there is no preference in opening angle. This is also in line with recent experiments on flexibly linked emulsion droplets, which are freely-jointed like the CSLBs we present here.[194]

To test the robustness of this structural flexibility in the presence of membrane inhomogeneities, we prepared particles with a large number of membrane tubes by washing with inert dsDNA. As shown in Figure 3.11c, this did not alter the flexibility of the clusters: they still explore the full angular range and do not show a significant preferred opening angle, similar to the particles coated with a smooth membrane. Surprisingly, this means that particles stabilized by dsDNA can in principle be used for self-assembly studies, despite the fact that the high concentration of dsDNA causes membrane tubes to form, because the tubes do not significantly alter the relative motion of bonded particles.

3.4 Summary and Conclusions

We investigated various factors in the preparation protocol of colloid-supported lipid bilayers (CSLBs) in view of their emerging use in self-assembly and model membrane studies. Specifically, we focused on realizing a homogeneous and fluid bilayer, while achieving colloidal stability and functionalization with DNA linkers at the same time.

Similar to what has been reported for flat supported lipid bilayers, we found that the quality of the lipid bilayer on colloidal particles critically depends on the material of the particle's surface. The bilayer was not fluid on particles made from polystyrene (with or without carboxyl groups), hematite and TPM particles (with or without carboxyl or amino groups). Colloids featuring a silica surface, on the other hand, were able to host a fluid and homogeneous bilayer, at least in the absence of any polymer residues from the synthesis. We furthermore observed that the variation in the substrate curvature does not affect the bilayer formation if it is sufficiently gentle, while excessive surface roughness can hinder the spreading and fusion of SUVs.

Use of PEGylated lipids in the bilayer increased the colloidal stability, but affected

the bilayer homogeneity and mobility negatively. Addition of the amphiphilic surfactant SDS led to a disintegration of the bilayer. A better way to provide colloidal stability is by steric stabilization by excluded volume effects through the insertion of double-stranded inert DNA. Increasing the concentration of dsDNA leads to an increase in colloidal stability.

Finally, we demonstrated that these CSLBs can be functionalized with surface-mobile DNA linkers and assembled them into flexible structures of freely-jointed particles. We found that local bilayer inhomogeneities in the form of membrane tubes do not affect the free energy landscape of the connected particles.

CSLBs with fluid, homogeneous membranes and surface-mobile binding groups have great promise in a wide range of applications and fundamental studies. The fact that the bonded particles can flexibly move with respect to each other opens the door to overcoming equilibration issues, as previously encountered in hit-and-stick processes.[196] Moreover, it allows for the assembly of structures with internal deformation modes. This enables the study of the impact of structural flexibility on the phase behavior, such as the formation of crystals with new lattices or properties[57,58,119,120] and the experimental realization of information elements for wet computing.[195] CSLBs with increased membrane fluidity also mimic biological membranes much more closely, which may be advantageous for model membrane and cell biology studies,[61–65] smart drug delivery[9,116,117] and bio-sensing applications.[15,118]

Acknowledgments

This chapter is based on the following publication:

Colloid-supported lipid bilayers for self-assembly.
M. Rinaldin*, R.W. Verweij*, I. Chakraborty, and D.J. Kraft
Soft Matter, 15, 1345-1360 (2019). doi:10.1039/C8SM01661E

We thank Rachel Doherty and Vera Meester for help with the colloidal syntheses and electron microscopy imaging. We are grateful to Piermarco Fonda and Luca Giomi for useful discussions. This work was supported by the Netherlands Organization for Scientific Research (NWO/OCW), as part of the Frontiers of Nanoscience program and VENI grant 680-47-431. This project has received funding from the European Research Council (ERC) under the European Union's Horizon 2020 research and innovation program (grant agreement no. 758383).

*These authors contributed equally.

4 Linker-mediated interactions among colloid-supported lipid bilayers

In biological systems, adhesion is commonly mediated by multivalent interactions of multiple ligands and receptors, for example in the attachment of viruses to host cells and in cell signaling processes. Additionally, multivalent interactions are a promising way to control the self-assembly of synthetic materials, for example in colloidal systems. Here, we have used optical tweezers to directly probe the binding probability of DNA-decorated colloid-supported lipid bilayers as function of DNA linker concentration and valency. We have quantified the effect of linker depletion, where binding multiple 'guest' particles to the same 'host' particle that has a fixed linker concentration leads to a decrease in the binding probability. Using these results, we predict the dependence of the expected valency in self-assembly experiments on the linker concentration and compare this to preliminary experimental data. Beyond applications for colloidal self-assembly processes, our findings could have implications for multivalent interactions found in biological systems, such as in cell-signaling and drug-delivery systems.

4.1 Introduction

In biological systems, attractive interactions are commonly mediated by multiple ligands and receptors that have a specific affinity for each other, for example in the attachment of viruses to the membrane of host cells.[232] Moreover, these multivalent interactions also play a large role in cell signaling processes.[233–235] While the individual interactions between ligands and receptors are often weak, the number of formed bonds amplifies the overall adhesive strength, leading to large bonding energies with a high affinity for the target structures.[235] A complete understanding of these multivalent interactions could lead to significant advances in targeted drug delivery, where fine-grained control over the type of cells a drug acts on is called for.[7–9,114–117] In drug-delivery systems, both nanoparticle- and microparticle-based systems are used. While both classes of particles have useful applications, significant advantages of microparticles over nanoparticles are their higher loading capacity,[7] their lower biotoxicity because of their inability to cross biological membranes[6,8,115] and simpler production and characterization methods. Therefore, microparticle-based drug delivery systems show great promise to provide new therapies to a wide range of diseases.[7,8]

Beyond biological and medical applications, multivalent interactions are a promising route to providing full control over self-assembly processes in material science,

for example by using microparticles functionalized with DNA linkers.[4,70–76] There, the specificity of the Watson-Crick base paring has been used to synthetically construct pieces of single-stranded DNA that specifically hybridize with each other and therefore can act as an "intelligent glue" between the micron-sized colloidal particles. These developments triggered efforts to employ DNA-coated colloids as building blocks for materials with highly sought after properties, such as photonic bandgaps.[71]

Theoretical and experimental studies on multivalent interactions in systems of DNA-coated colloids have revealed their great potential for applications and their rich behavior, in which entropic effects were found to play a dominant role.[50,73,75,236–240] Namely, the entropic contributions of the DNA linkers to the free energy were found to be of similar magnitude as the hybridization free energy of a pair of sticky ends.[73] Entropic contributions to the free energy of the system can stem, for example, from the reduction in the configurational entropy of the linkers upon binding,[73,237,240] from entropic repulsion between linkers (and/or surfaces) because of excluded volume interactions,[73,229,240] from the combinatorial entropy gain originating from the possible combinations of forming bonds between a given number of linkers,[73,229] or from the loss in configurational entropy when surface-mobile linkers are confined to the contact area between two bound particles.[240] Additionally, the distribution of DNA linkers on the surface was shown to lead to large variations in binding strength.[73] The interactions between DNA-coated colloids were found to be further modifiable by, for example, changing the ionic strength of the solution, or by including inert DNA strands that alter only the repulsive part of the free energy.[236] These examples are not fully comprehensive, but serve to illustrate both the complexity and the rich potential of DNA-mediated interactions.

Typically, because of the combination of the high binding strength, narrow melting temperature range and slow binding kinetics[50] of DNA-mediated interactions, most DNA-coated colloids were found to kinetically arrest into amorphous structures, except if patchy particles were used[2] or by employing high coating densities of short DNA linkers consisting of a few basepairs.[241] Another proposed way to overcome the effects of kinetic arrest is to employ colloidal particles where the DNA linkers can freely diffuse on the particle surface, using colloid-supported lipid bilayers[85,110,112,242] (CSLBs). CSLBs consist of solid colloidal particles that are coated with a fluid lipid bilayer, into which DNA linkers with a hydrophobic anchor can be inserted. Because of the fluidity of the bilayer, the DNA linkers can surf over the particle[110,112] and the resulting self-assembled structures can rearrange with respect to each other,[85,242] thereby overcoming equilibration issues caused by kinetic arrest.

While, as discussed, the interactions between DNA-coated colloids containing grafted DNA linkers have been extensively studied, less is known about the effect of mobile DNA linkers. Experimentally, their binding probability as function of temperature was characterized[110] and broad association/dissociation transitions were found for a range of DNA concentrations. In theoretical studies, it was shown that it should be possible to control the valency, i.e. the number of binding partners, of colloids

with mobile linkers by tuning the amount of nonspecific repulsion.[229] Another theoretical work found that when the rate at which bonds are formed is low with respect to the particle diffusion coefficient, the average valency can be controlled.[243] Linker depletion effects, that also lead to a slow down of the self-assembly process, were observed in the adhesion of nanoparticles to lipid membranes[126] and in systems of DNA linker-functionalized emulsion droplets.[84] These results taken together demonstrate that by using colloidal particles decorated with mobile DNA linkers, precise control over the valency of the particles, and therefore over the formed structures, should be within reach.

Here, we study linker depletion effects in a system of CSLBs as a means to control the average valency in self-assembly experiments. First, we measure the binding probability of CSLBs as function of DNA concentration. In addition, we asses the effect of the sequential assembly of particles onto a central particle. In this way, we experimentally quantify the effect of nonspecific repulsion, specific attraction and linker depletion effects. We provide an outlook of possible applications of our findings to colloidal self-assembly. Beyond that, our findings could have implications for multivalent interactions found in biological systems, such as in cell-signaling and drug-delivery systems.

4.2 Materials and Methods

4.2.1 Particle coating

Colloid-supported lipid bilayers (CSLBs) were prepared as described in previous work,[85,110,112,242,244] specifically, we followed a similar procedure as in chapters 3 and 5. First, we prepared small unilamellar vesicles (SUVs) consisting of 98.9 mol % of the unsaturated phospholipid DOPC ((Δ9-Cis)-1,2-dioleoyl-sn-glycero-3-phosphocholine), 1 mol % of the lipopolymer DOPE-PEG(2000) (1,2-dioleoyl-sn-glycero-3-phosphoethanolamine-N-[methoxy-(polyethylene glycol)-2000]) and 0.1 mol % of the dyed lipids TopFluor-Cholesterol (3-(dipyrrometheneboron difluoride)-24-norcholesterol) or alternatively, DOPE-Rhodamine (1,2-dioleoyl-sn-glycero-3-phosphoethanolamine N-(lissamine rhodamine B sulfonyl)), where we matched the fluorescent dyes of the lipids and linker DNA. Specifically, we used 77 μL of DOPC (25 g L^{-1}), 7.3 μL of DOPE-PEG(2000) (10 g L^{-1}) and 3.4 μL of the fluorescent lipids (1 g L^{-1}). The lipids in chloroform were mixed and dried in a vacuum desiccator for 2 h in a glass vial. Then, 4 mL of a buffer at pH 7.4 containing 50 mM sodium chloride (NaCl) and 10 mM 4-(2-Hydroxyethyl)-1-piperazineethanesulfonic acid (HEPES) was added. The dispersion was mixed using a vortex mixer for 45 min. SUVs were prepared using an Avanti Mini Extruder by extruding the dispersion 21× through a 50 nm pore-size polycarbonate membrane supported by two filter supports.

Next, the (2.12 ± 0.06) μm silica particles obtained from MicroParticles GmbH were washed in water. The particles were coated with a fluid lipid bilayer by deposition and rupture of SUVs by mixing 200 μL of the 50 mM HEPES buffer, 23 μL of the SUVs and 100 μL of the silica particles (0.05 %w/w). This mixture was rotated for

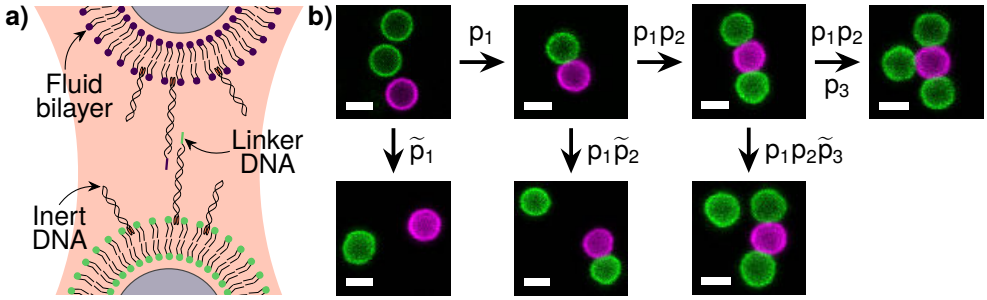

Figure 4.1: **Experimental system. a)** Two CSLBs decorated with complementary linker DNA are brought into close proximity using optical tweezers to facilitate DNA-mediated binding. In addition to linker DNA, we have added inert DNA that does not have a sticky end but provides additional steric repulsion and therefore improves colloidal stability. The fluid lipid bilayer allows the DNA to diffuse on the surface of the particles. **b)** After releasing the trap, the particles can either bind or not. We show confocal images of all tested cases with their associated probabilities p_n and negated probabilities $\widetilde{p}_n$. In this way, we performed a sequence of Bernoulli trials until a valency n of up to three bonded particles to the central particle (here, in purple) was reached. We waited for at least 5 min between consecutive trials and discarded the cluster when a trial was unsuccessful. Scale bars are 2 μm.

30 min. Afterwards, the mixture was washed once in HEPES buffer solution in order to remove excess SUVs.

We added double-stranded DNA (of respectively strands DS-H-A and DS-H-B, see Table A.1) with an 11 base pair long sticky end and a double stearyl anchor, which inserts itself into the bilayer via hydrophobic interactions, as shown Figure 4.1a. The sticky end of strand DS-H-A is complementary to the sticky end of strand DS-H-B, which allows them to act as linkers. For additional steric stabilization without adding additional linkers, we have added double-stranded inert DNA with a double stearyl anchor (strand DS-H-I in Table A.1). The length of the inert DNA is approximately 20 nm and the linker DNA length is 30 nm. We tested various concentrations of both inert and linker DNA. All DNA solutions were prepared using a buffer of pH 7.4, containing 200 mM NaCl and 10 mM HEPES, which we call the 200 mM HEPES buffer. Buffers and DNA solutions were freshly prepared in the same week as the experiment, to prevent degradation of the hybridized DNA that happens over time. After adding the required amounts of DNA to the particles, the mixture was rotated for 1 h. Then, it was washed three times in 200 mM HEPES buffer. For imaging, we used a metal sample holder containing a polyacrylamide (PAA) coated cover glass.[244] Confocal microscopy images of the coated particles are shown in Figure 4.1b. All solutions were prepared with ultra pure Milli-Q water (Milli-Q Gradient A10).

4.2.2 Microscopy and binding experiments

Imaging was performed using an inverted confocal microscope (Nikon Eclipse Ti-E) equipped with a Nikon A1R confocal scanhead with galvano and resonant scanning mirrors. A 60× water immersion objective (NA=1.2) was used. 488 and 561 nm lasers were used to excite, respectively, the TopFluor and Rhodamine dyes. Laser emission passed through a quarter wave plate to avoid polarization of the dyes and the emitted light was separated by using 500 − 550 nm and 565 − 625 nm filters.

We used optical tweezers to probe the binding probabilities. Briefly, we employed a homemade optical setup consisting of a highly focused trapping laser manufactured by Laser QUANTUM (1064 nm wavelength). The laser beam entered the confocal microscope through the fluorescent port, after first passing through a beam expander and a near-infrared shortpass filter. The same objective was used for imaging and to focus the trapping laser beam. During the trapping, the quarter wave plate was removed from the light path. The temperature of the sample was controlled using a water-cooled sample stage set at 20 °C.

We are interested in testing the binding probability as function of valency n, or the total number of binding partners, as depicted in Figure 4.1b. To probe the binding probability, two complementary particles were trapped using a trap strength of 75 to 150 mW for 30 s. The trapping strength was determined empirically, by testing the power that was just enough to lift a particle from the substrate. We then multiplied the obtained value by a factor of two and repeated this procedure of calibrating the trapping strength for each set of experiments. After 30 s of trapping two particles, the trap was released. If particles remained bonded, we tested whether they were indeed permanently bound by gently pulling on one of the particles using the optical tweezers. We then counted all pairs of particles that were either bound or not. After waiting for at least 5 min, we repeated the experiment by trying to add another particle, while ensuring that enough time had passed after binding for the binding patch of bonded linker DNA to fully develop. This was repeated until the particles would either not bind, or a valency $n = 3$ was reached, as depicted in Figure 4.1b. In this way, we performed a sequence of Bernoulli trials using the same cluster, which implies that the amount of DNA on the central particle is expected to be the same for the different trials, allowing for a direct comparison of the binding probabilities as function of valency.

4.2.3 Self-assembly experiments

In addition to the optical tweezers experiments, we have performed self-assembly experiments, in which two sets of CSLBs functionalized with complementary DNA linkers were mixed at a high number ratio of 'host' to 'guest' particles of 1:30. This high number ratio drives the self-assembly process towards the formation of clusters,[85] as opposed to other structures such as chains and fractal aggregates. The particles were mixed in the 200 mM HEPES buffer and put into a metal sample holder containing a PAA coated cover glass[244] at a particle concentration of approximately 2×10^{-4} % w/v.

The effective particle area density in the experiment was larger, because the particles were confined to the substrate by sedimentation. Then, the distribution of clusters was counted at several instances in time, where we recorded the number of clusters per valency, the number of nonspecific aggregates and the number of clusters that we could not ascribe a valency to, such as chains or fractal aggregates. For each measurement, at least 100 clusters were counted. The average valency we report here was determined after at least 24 h of mixing. After that time, we found that the average valency did not increase further.

4.2.4 Data analysis

The experimental binding probabilities p_n were determined from the number of bound and unbound particles by calculating a binomial proportion confidence interval, specifically, the Wilson score interval,[245]

$$p_n \pm \sigma_n = \frac{N_B + \frac{1}{2}z^2}{N_T + z^2} \pm \frac{z}{N_T + z^2}\sqrt{\frac{N_B\, N_U}{N_T} + \frac{z^2}{4}}, \tag{4.1}$$

where n is the valency, σ_n the estimated error on p_n, N_T the total number of particles tested, N_B is the number of trials that resulted in bonded particles, N_U is the number of trials where bonding failed and $z = 1$ such that we report one standard deviation. Fits to the experimental data were performed using a standard least-squares method as implemented in the Python package `lmfit`[246] and we report one standard deviation calculated using the `conf_interval` function.

4.3 Results and Discussion

4.3.1 DNA-mediated interactions between CSLBs

We experimentally probe the binding probability of DNA-functionalized colloid-supported lipid bilayers[85,110,112,242] (CSLBs). The CSLBs consist of spherical colloidal silica particles, that are surrounded by a fluid lipid bilayer. DNA linkers with complementary sticky ends are inserted into the bilayer using a hydrophobic anchor. The particles are self-assembled by hybridization of the DNA sticky ends, which provide strong and specific interactions. A fraction of the DNA strands, which we call inert DNA strands, do not contain a sticky end and therefore only contribute to the repulsive part of the interaction between two CSLBs. The resulting particle assemblies can rearrange with respect to each other, because the DNA linkers can diffuse on the fluid lipid bilayer that surrounds the particles, as shown in Figure 4.1a. To experimentally measure the probability of binding, we use optical tweezers to bring specific particles into close contact for a controlled amount of time. This allows us to probe the binding probability as function of DNA linker and inert concentration and as function of the valency of the binding partners. Specifically, we test the ability of a particle to bind to one to three particles in a sequential fashion, as shown in Figure 4.1b. A sequence of Bernoulli trials is conducted, where we first try to bind two complementary particles.

If this succeeds, we wait for at least 5 min to allow a DNA linker patch to form between the bonded particles. Then, we try to bind another particle to obtain a valency $n = 2$ and, after a second 5 min waiting period, a third particle so that we obtain a final valency $n = 3$, as depicted in Figure 4.1b.

Suppressing nonspecific interactions

The binding probability can only be accurately measured if nonspecific interactions between the particles are suppressed. To quantify the fraction of particles that bind via interactions not mediated by the DNA linkers, we first probe the binding probability of CSLBs that have no linker DNA or are functionalized with the same type of linker DNA, that is not self-complementary and therefore cannot form bonds. In our previous work[242] in Chapter 3, we have found that nonspecific interactions can be suppressed by increasing the concentration of inert DNA. There, we did not use optical tweezers to test the binding probability, but instead calculated the ensemble average by counting the fraction of bound particles after a given equilibration period of a few hours. The method that uses optical tweezers is a more direct and more controlled way of measuring the binding probability of two particles, because it allows for more control over both the duration of close contact and the applied force.

Surprisingly, as shown in Figure 4.2a, the probability to form nonspecific aggregates determined from the counting method differs strongly from the probability determined using the optical tweezers based method. By probing the fraction of particles that form nonspecific aggregates using optical tweezers, we find a lower fraction for CSLBs without DNA linkers of 0.33 ± 0.04 compared to 0.65 ± 0.08 using the counting method. Additionally, using the tweezers, we find that low concentrations of DNA already greatly suppress nonspecific interactions. While there is still a significant fraction of nonspecific aggregates at concentrations of $10^4\ \mu m^{-2}$ as determined from the counting method, when we probe the probability to form nonspecific aggregates using the tweezers, we find that they are almost completely absent for those DNA concentrations. Therefore, we conclude that after the functionalization with DNA of a sufficiently high concentration of approximately $10^4\ \mu m^{-2}$, nonspecific aggregations are completely suppressed. The discrepancy between the counting and tweezers methods implies that the aggregates that were observed using the counting method were formed before the DNA was added, most likely during the stage where the bilayer was formed on the particles using the deposition and rupture of small vesicles. Additionally, the counting method could slightly overestimate the number of clusters: as the number of clusters was determined automatically from (static) images, particles were already considered to be part of a cluster when their separation distance was smaller than 2.2 times the particle radius, as explained in detail Section 3.2.6. As shown in Figure 4.2b, increasing either the linker or inert DNA concentration leads to a decrease in nonspecific aggregation, as visualized in the confocal microscopy images.

This observation indicates that further improvements to the coating scheme may be possible. For example, using lower concentrations of salt during the bilayer coat-

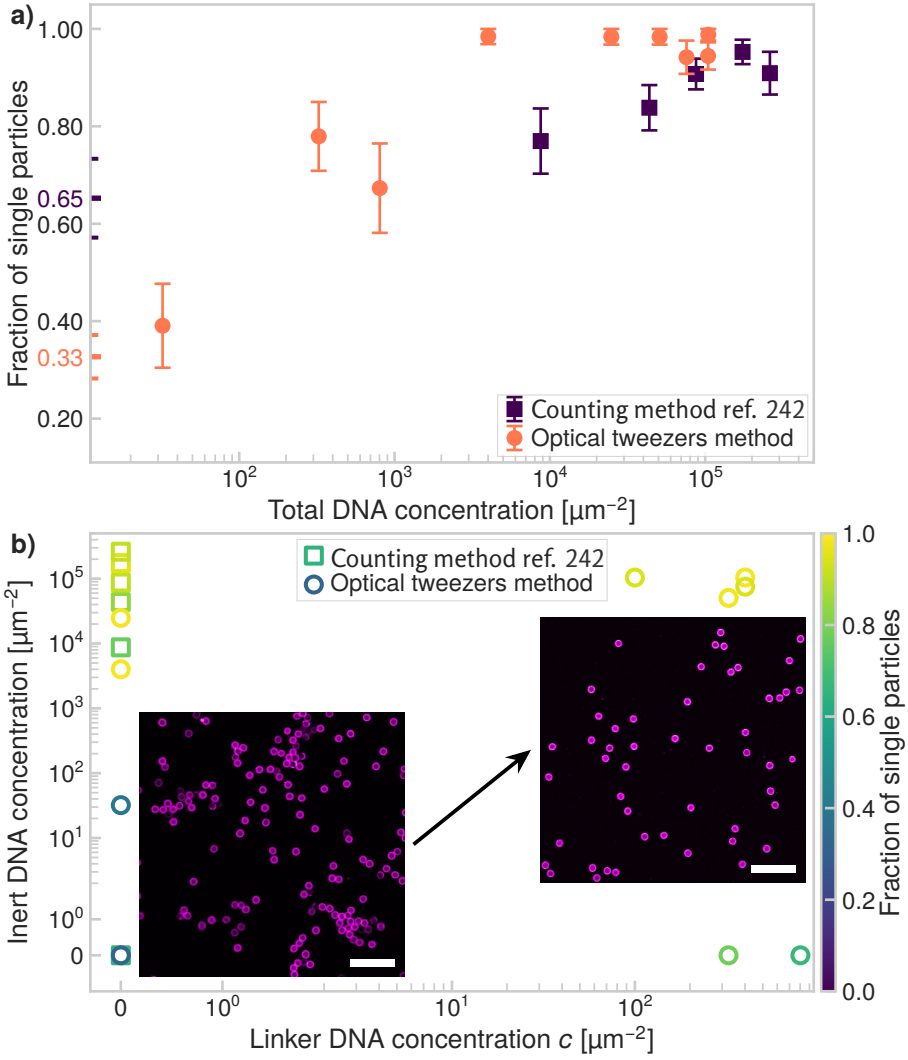

Figure 4.2: **Suppressing nonspecific interactions.** Increasing the amount of either linking or inert DNA reduces nonspecific binding, our tweezers based method reproduces earlier results obtained by counting random aggregates.[242] **a)** Fraction of single particles as function of the total amount of added DNA in terms of the surface density of both inert and linker DNA. Colored ticks indicate the fraction of single particles if no DNA is added. **b)** Plot of the fraction of single particles (color scale) as function of inert DNA and linker DNA concentration. As shown in the confocal images, randomly-bonded aggregates are frequently observed when the total DNA concentration is low (lower left), in contrast to the large percentages of single particles for sufficiently high DNA concentrations (upper right). Scale bars are 15 μm.

ing phase should slow down the formation of nonspecific aggregates by increasing the Debye screening length. In preliminary experiments, we have found that ionic strengths of approximately 15 mM are sufficient to promote the rupture and spreading of vesicles on the particle surface. Additionally, the relative concentrations between vesicles and particles should be carefully tuned. High concentrations of vesicles could induce depletion interactions that would result in nonspecific aggregation of the particles. We have found that a surface ratio between particles and SUVs close to 1:10 strikes a good balance between low vesicle concentrations and homogeneous bilayer formation.[242] In future experiments, the colloidal stability during the bilayer coating should be studied in more detail. Importantly, we conclude that these measurements show that spontaneous destabilization in an assembled structure is unlikely when the total DNA concentration exceeds 10^4 μm^{-2}.

Experimental binding probability

Having found the lowest DNA concentration of 10^4 μm^{-2} that still provides sufficient colloidal stability, we now characterize the binding probability p_1 of binding a pair of CSLBs. We have varied both the inert and linker DNA concentrations. Indeed, we observe again that when no inert DNA is added, the binding probability p_1 of forming a dimer is high even if no linker DNA is added, as shown in Figure 4.3a. More importantly, when inert DNA is added for stability, we observe an S-shaped increase in the binding probability as function of DNA linker concentration, as can be seen in Figure 4.3a. Furthermore, we note that for the lower inert DNA concentration (0.5×10^5 μm^{-2}), the transition from no binding to binding is shifted towards larger linker concentrations compared to the higher inert DNA concentration (1×10^5 μm^{-2}). For the higher valencies $n = 2$ and 3 shown in, respectively, Figure 4.3b and c, there is a qualitative difference between the two inert DNA concentrations: for the high one (1×10^5 μm^{-2}), we observe very similar binding curves for all valencies. For the lower inert DNA concentration (0.5×10^5 μm^{-2}), we note that the transition between no binding and binding is broadened as function of valency and is shifted towards larger linker concentrations as the valency increases.

Linker depletion as function of valency

This shift towards higher linker concentrations hints at a linker depletion effect. Because the amount of DNA strands on any given particle is fixed, it is reasonable to assume that for each additional 'guest' particle that binds to a given 'host' particle, the concentration of available linkers on the host particle decreases. This effect, known as linker depletion, has previously been observed in experiments where nanoparticles decorated with linkers were bound to lipid membranes[126] and in the self-assembly of DNA-functionalized emulsion droplets.[84] This mechanism of linker depletion is interesting because it could be exploited to limit the valency of colloidal clusters in self-assembly experiments.

We would like to model the observed behavior, in order to extract quantitative trends from our experimental measurements. So far, it has been proven challenging

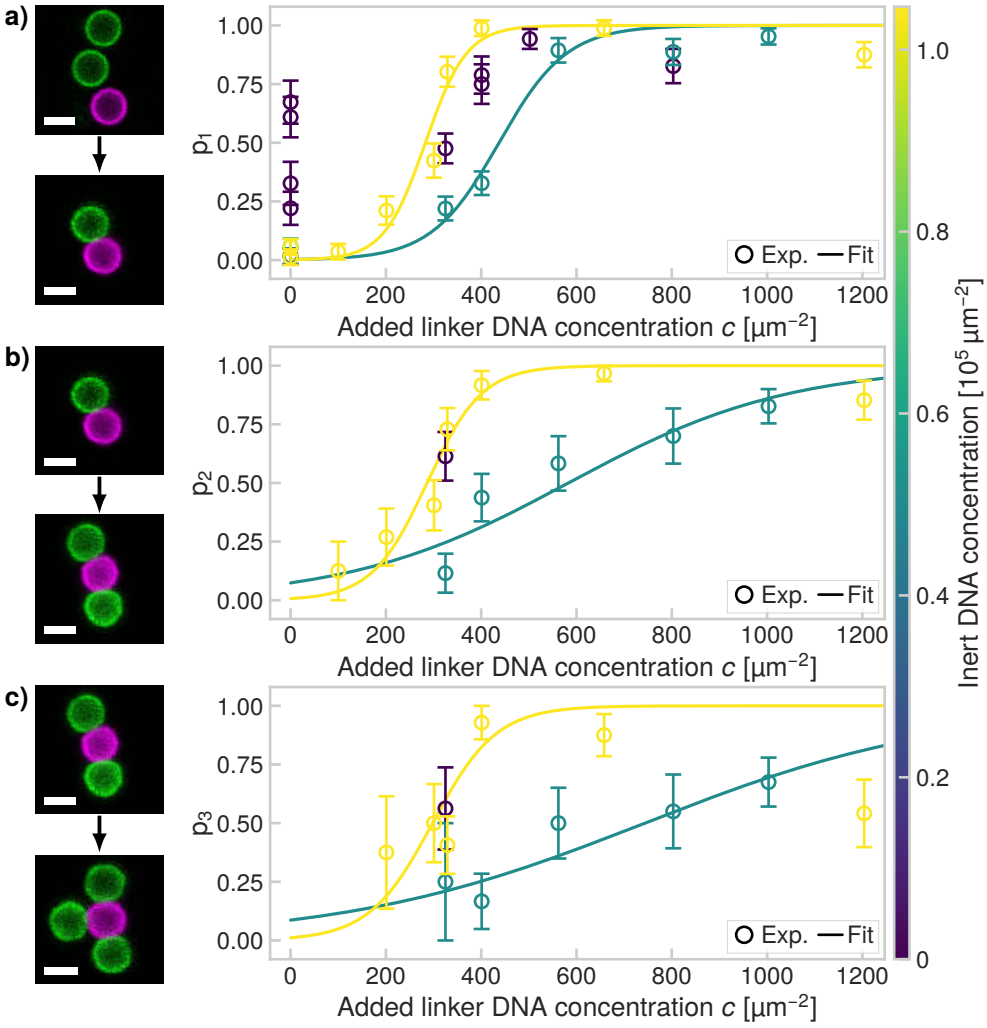

Figure 4.3: **Binding probability of DNA-functionalized CSLBs. a)** First, we have probed the probability p_1 of binding two CSLBs to each other, as depicted in the confocal images. **b)** As shown in the confocal images, for pairs of particles that were successfully bonded, we tried to bind another particle to the central particle (here, in purple) and in that way measured the probability p_2. **c)** In the same way, we determined p_3 by binding an additional particle to a cluster of valency $n = 2$, as shown in the confocal images. Scale bars are 2 μm. In all panels, we have fitted Equation 4.2 to the experimental data.

to analytically model the binding probability of DNA-coated colloids where the effects of linker mobility and linker depletion are simultaneously taken into account. These effects have been studied using numerical simulations[126,229,243] and various analytical expressions were proposed[238,239] for the case that the linkers are grafted on a surface. For DNA-functionalized emulsion droplets[84] a model was proposed that takes the mobility of the linkers into account, but there the deformability of the emulsion droplets played a large role. Unfortunately, these models are not applicable to our system, because the interactions between colloids coated with mobile linkers are not pairwise additive[229] and the CSLBs are not deformable due to the solid support given by the spherical silica particle. Additionally, existing theories assume that the binding and unbinding of the individual DNA linkers is fast, meaning that all the possible binding configurations are sampled equally. This assumption, which states that the system is in thermodynamic equilibrium, may not hold for the current system. Namely, the interactions between sticky ends are expected to be on the order of 2 k_BT (see Figure 4.5 for details) which is higher than the thermal energy and therefore the lifetime of bonds may be too long for equilibrium conditions to apply.

Therefore, to further quantify the observed trends, we have fitted the experimental binding probabilities p_n using a simple logistic model that reproduces the trends in the experimental data,

$$p_n(c) = \frac{1}{1 + \exp\left(-k_n(c - c_{n,0})\right)}, \tag{4.2}$$

where c is the DNA linker concentration in μm^{-2}, k_n is the logistic growth rate for valency n in units of μm^2 and $c_{n,0}$ is the concentration of the midpoint of the binding probability curve of valency n in units of μm^{-2}. The logistic growth rate k_n quantifies the increase in binding probability as function of linker concentration c, where the slope at $c = c_{n,0}$ is given by $p_n'(c_{n,0}) = k_n/4$. $c_{n,0}$ is the DNA linker concentration where $p_n(c_{n,0}) = 1/2$. We stress that Equation 4.2 is not a physical model but an empirical one that we use to quantify the observed trends in the experimental data in the absence of an appropriate analytical model. In future work, we hope to adapt proposed models[229,238] to our experimental system. Such models could improve the accuracy of the measured values we report here, but we find that the simple logistic function we have used here is already sufficient to describe the most important trends in our data.

Indeed, by fitting Equation 4.2 to our experimental data as shown in Figure 4.3, we note that the logistic function can be used to describe the observed dependence on the linker concentration for both concentrations of inert DNA. To quantify the possible effects of linker depletion in greater detail, in Figure 4.4, we show the values of the obtained fit parameters. In Figure 4.4a, we show the concentration c_0 where $p = 0.5$ as function of valency. There, we see an increase of c_0 for the lower inert DNA concentration (0.5×10^5 μm^{-2}), while for the higher inert DNA concentration (1×10^5 μm^{-2}) c_0 is constant. Because of the large uncertainty on c_0, we can not rule out that c_0 is constant for both inert DNA concentrations, but an increase in c_0 would

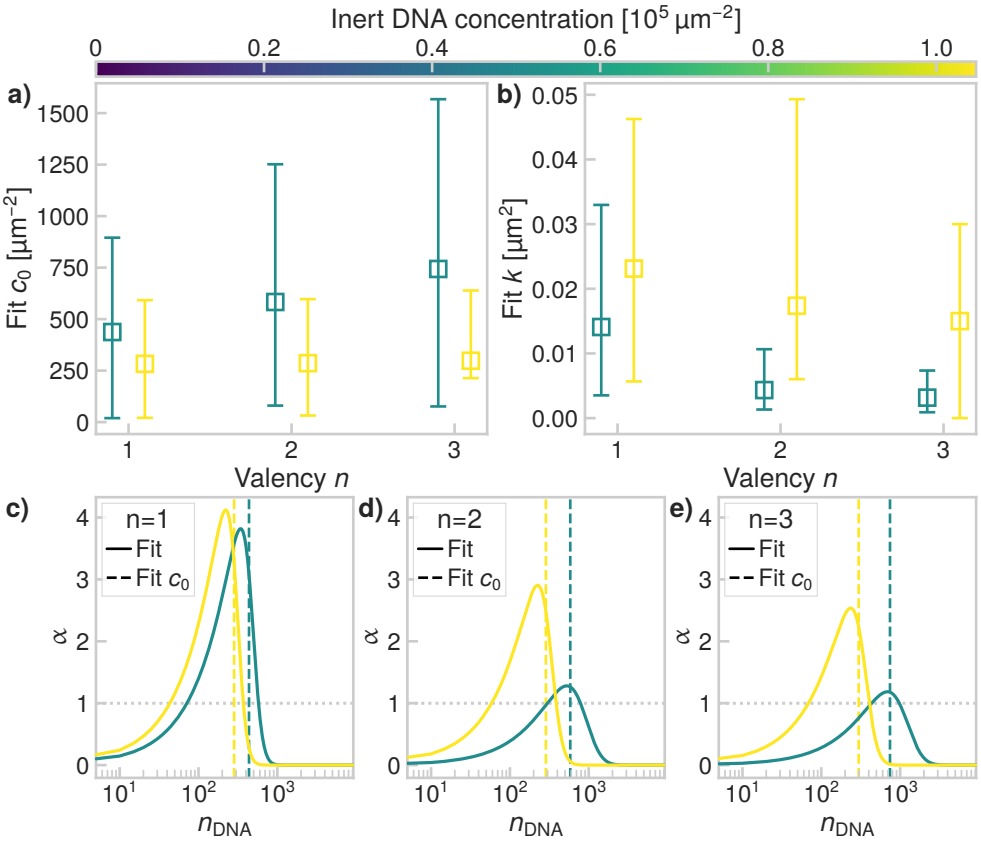

Figure 4.4: **Modeled binding probability as function of valency. a)** The midpoint concentration c_0 increases as function of valency n. **b)** The logistic growth rate k decreases as function of valency n. In panels a and b, the points are slightly displaced along the valency axis for visual separation. **c)** The selectivity α given by Equation 4.3 for valency $n = 1$. For both inert DNA concentrations, the values of α show that the binding is super selective. **d)** The inter-particle selectivity (or affinity) α given by Equation 4.3 for valency $n = 2$. We observe super-selective behavior for the high inert DNA concentration (1×10^5 μm^{-2}), for the lower inert DNA concentration (0.5×10^5 μm^{-2}) the binding is significantly less selective. **e)** The affinity α given by Equation 4.3 for valency $n = 3$. Similarly to panel d, we observe super-selective behavior for the high inert DNA concentration (1×10^5 μm^{-2}), for the lower inert DNA concentration (0.5×10^5 μm^{-2}) the binding is significantly less selective.

also be expected when linkers are depleted as function of valency. We find that the values of c_0 are consistently larger for the lower inert DNA concentration compared to the higher one.

From Figure 4.4b, it can be seen that the logistic growth rate k seems to decrease as function of valency. However, because of the large uncertainty on the fitted values of k, we can not rule out the possibility that k is constant. Nonetheless, these effects taken together suggest that the binding probability shows a complex dependence on both the DNA linker concentration and the inert DNA concentration. Where the binding probability rapidly increases around c_0 for all valencies for the high inert DNA concentration ($1 \times 10^5\ \mu m^{-2}$), as shown in Figure 4.3, the behavior is very different for the lower inert DNA concentration ($0.5 \times 10^5\ \mu m^{-2}$). For the lower inert DNA concentration, for valency $n = 1$ there is a steep increase of p around c_0, but for the higher valencies, the transition is broadened. This suggests that linker depletion also affects the inter-particle selectivity, or affinity, of the interaction.

In our multivalent system, for a certain range of interaction conditions, the dependence of the binding probability on linker concentration can result in super-selective behavior.[238] That is, below a certain threshold of the linker concentration, no binding occurs, while above this concentration threshold, the binding probability rapidly increases,[238] resulting in a step-like binding probability as function of linker concentration. The selectivity, or affinity, of a system can be characterized by the affinity parameter α:[238]

$$\alpha = \frac{d \ln p_n(c)}{d \ln n_{\mathrm{DNA}}(c)}. \tag{4.3}$$

Here, n_{DNA} is the number of DNA strands in the binding area of one of the particles, given by[85] $n_{\mathrm{DNA}} = 2\pi R_p L_{\mathrm{DNA}} c \approx 0.2c$ for our system, where the particle radius $R_p = 1.06\,\mu m$ and the length of the DNA linker $L_{\mathrm{DNA}} \approx 30\,nm$. As shown in Figure 4.4c, for valency $n = 1$, the affinity α is greater than one for certain linker concentrations, which indicates that the binding is super-selective for both inert DNA concentrations in that regime. This means that around the threshold concentration, the binding probability will increase as[238] $\propto (n_{\mathrm{DNA}})^{\alpha}$. For valencies $n = 2$ and 3 in Figure 4.4d and e, respectively, we again observe a qualitative difference between the two inert DNA concentrations. For the highest inert DNA concentration ($1 \times 10^5\ \mu m^{-2}$), the affinity of $n = 2$ and 3 is lower with respect to $n = 1$ but still greater than one for a range of linker concentrations, indicating that the behavior is super-selective there. For the lower inert DNA concentration ($0.5 \times 10^5\ \mu m^{-2}$), however, for the higher valencies, the affinity is close to or below one. This indicates a qualitative change in binding behavior for higher valencies for this concentration of inert DNA, where the binding transitions from being super-selective at valency $n = 1$ to a significantly lower affinity at valencies $n = 2, 3$.

To summarize, we have found indications that linker depletion changes the binding probability of DNA linker-functionalized CSLBs. We have tested two different concentrations of inert DNA and find a qualitatively different behavior. For the higher

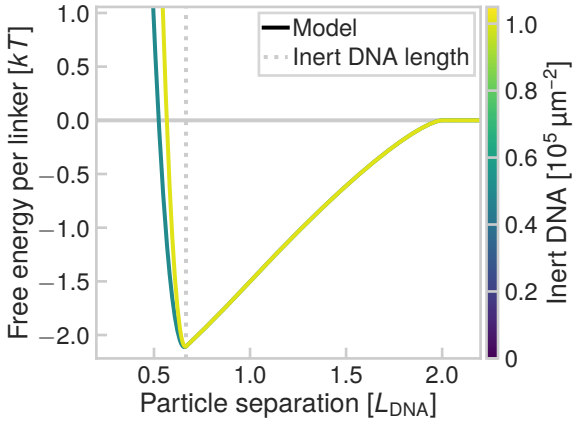

Figure 4.5: **Modeled free energy for grafted linkers based on a mean-field approach.** We used the code made available in the Python package `DNACC`.[239,247,248] We set the hybridization free energy of the linkers to $-15.5k_BT$ as calculated from the DNA sequence of the single stranded sticky end.[249] This neglects other contributions to the hybridization free energy stemming from the rest of the linker, which is a double-stranded DNA complex with a hydrophobic anchor. For a linker density of 350 µm^{-2}, close to the midpoint concentrations c_0, we observe only small differences between the two inert DNA concentrations used here.

inert DNA concentration, the effect of linker depletion is more subtle: there is only a slight broadening and shift of the binding probability as function of valency and the binding is super-selective for all three valencies that we tested. In contrast, for the lower inert DNA concentration, the transition in binding probability shifts towards higher DNA concentrations as function of valency, the transition broadens as function of valency and for valencies $n = 2, 3$ we find that the binding is no longer super-selective.

It is unclear how to explain the complex behavior that we have found in our experiments. Because the inert DNA strands ($\approx$ 20 nm) are shorter than the linker DNA strands ($\approx$ 30 nm), it is unlikely that the interaction potential is significantly altered as function of inert DNA concentration, as these strands only provide a short-range repulsive component that should in principle not affect the binding of the linkers. We have checked this hypothesis by following the mean-field approach described by Varilly et al.[239] and Angioletti-Uberti et al.[248] using the Python package `DNACC`[247] and found that indeed, as shown in Figure 4.5, the interaction potential is not significantly changed by comparing the two inert DNA concentrations at the same linker concentration of 350 µm^{-2}. Although in these models, linker mobility is not taken into account, this calculation suggests that the relative sizes and concentrations of the inert DNA and linker DNA are not sufficient to explain the observed behavior. However, we note that it is possible that other effects also influence the interaction

potential, such as excluded volume interactions between linker DNA and inert DNA.

Moreover, we hypothesize that multiple effects could simultaneously contribute to the observed trends in the experimental data. First, the actual DNA concentration on the particles is not known. We have assumed here that all the DNA strands that are added in solution are actually inserted into the bilayer on the particles, which is probably not the case. Previous measurements of the DNA linker concentration showed a large spread in the linker concentration across different particles in the same sample.[85] Such a large spread would lead to a broadening of the measured binding probability curves.

Second, the fraction of DNA linkers that are inserted into the bilayer could be affected by the relative concentrations of inert and linker DNA strands. Because of the hydrophobic anchors that are attached to the hydrophilic DNA strands, the DNA complexes could form micelles in solution depending on their concentration. This could lead to a balance between the DNA complexes that are inserted into the lipid bilayer and the DNA complexes that form micelles. This, in turn, is then affected by the total concentration of inert and linker DNA, which could result in different linker DNA coating densities at different inert DNA concentrations. However, the critical micelle concentration of these complexes is not currently known.

Similarly, the competition between linker DNA and inert DNA strands to insert into the lipid membranes could lead to lower concentrations of linker DNA inserted into the CSLBs at higher inert DNA concentrations. Interestingly, our experimental results seem to contradict this hypothesis, as the fitted c_0 for the higher inert DNA concentration is lower than that of the lower inert DNA concentration, which hints at a higher average DNA linker density for the higher inert DNA concentration.

Finally, the observed trends with increasing valency are hard to interpret because the sticky ends we have used are not permanently bonded at room temperature, as the average free energy per sticky end is at most on the order of a few k_BT, as shown in Figure 4.5. Therefore, the number of linkers in the binding patch area may not be constant in time and there could be a redistribution of linkers as function of valency.

In conclusion, the DNA linker-mediated interactions we have measured here constitute a complicated and dynamic system. To explain the observed experimental trends, more research is needed both on the experimental and theoretical aspects of multivalent interactions of mobile linkers.

4.3.2 Application to self-assembly experiments

We have characterized the experimental binding probability as function of DNA linker concentration for valencies up to three. Next, we can use these results to calculate the combined probability to form clusters of a specific valency up to $n = 3$. We do so by defining the total probability $p_{\text{tot.}}(n, c)$, which is the product of the binding probabilities of valencies up to n as given by

$$p_{\text{tot.}}(n, c) = \prod_{i=1}^{n} p_n(c). \tag{4.4}$$

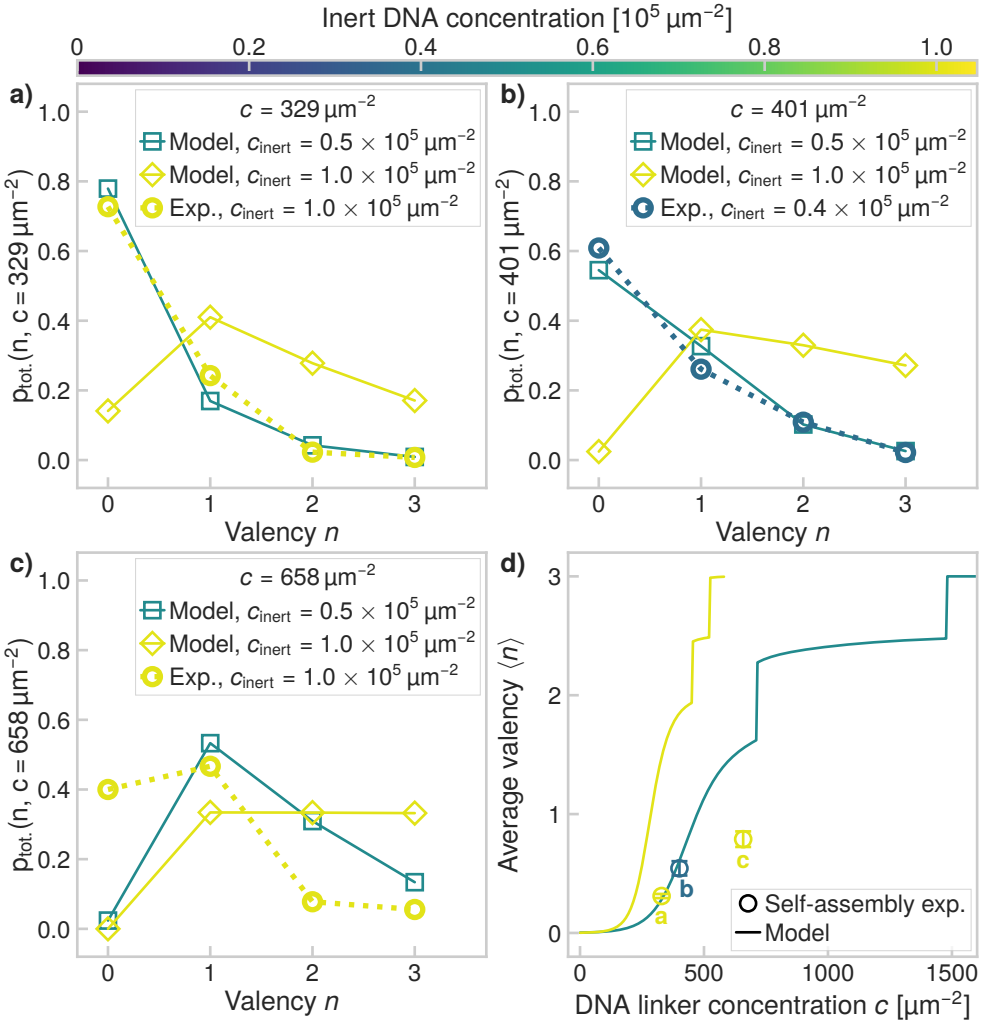

Figure 4.6: **Expected average valency as function of DNA linker and inert concentration.** In panels a-c, we show the cumulative binding probability $p_{\text{tot.}}$ based on Equation 4.4 for the DNA linker concentrations used in the self-assembly experiments shown here. In all cases, the experimental distributions are close to the obtained distributions for the lower inert DNA concentration $c_{\text{inert}} = 0.5 \times 10^5\ \mu\text{m}^{-2}$. **a)** $p_{\text{tot.}}$ for 329 μm^{-2} DNA linkers. **b)** $p_{\text{tot.}}$ for 401 μm^{-2} DNA linkers. **c)** $p_{\text{tot.}}$ for 658 μm^{-2} DNA linkers. **d)** The expected average valency as function of the initially added DNA linker concentration and inert DNA concentration (color), as calculated from Equation 4.5. Experimentally determined values from self-assembly experiments corresponding to panels a-c are indicated as well.

For a valency equal to zero, $p_{\text{tot.}}(0, c) = 1 - \sum_{i=1}^{n} p_{\text{tot.}}(i, c)$. This cumulative binding probability $p_{\text{tot.}}$ gives an upper bound on the expected valency that can be found in self-assembly experiments.

We test the predictive power of the cumulative binding probability determined from optical tweezers experiments, by performing three different self-assembly experiments, as explained in Section 4.2.3. Briefly, we have used two sets of CSLBs functionalized with complementary DNA linkers at a high number ratio of 1:30 to drive the self-assembly process towards the formation of clusters,[85] as opposed to other structures such as chains and fractal aggregates. We show the average valency for three different DNA concentrations, where the average valency was measured after at least 24 h of mixing. In Figure 4.6a-c, we show the cumulative probability for three different DNA linker concentrations used in the self-assembly experiments.

First, we consider the experiment that uses a lower inert DNA concentration, as shown in Figure 4.6b. For that combination of inert and linker DNA concentrations, as determined from Figure 4.3, the binding probability is on the order of 0.5 for $n = 1$ and significantly lower for valencies $n = 2, 3$. This implies that because of the low probability to form a duplex when two particles briefly come into close contact, the assembly process is dominated by the binding probability. Indeed, we observe good agreement between the expected and measured valency distributions in Figure 4.6b.

Second, we have performed two experiments where the inert DNA concentration was higher, as shown in Figure 4.6a and c. Starting with the experiment in Figure 4.6a, we note that for those combinations of inert and linker DNA concentrations, the expected binding probability determined from Figure 4.3 is larger than or equal to 0.5 for all three valencies. However, we find a lower average valency than would be expected from Equation 4.4. Perhaps coincidentally, the observed valency distribution coincides with the distribution predicted for the lower inert DNA concentration. For the third experiment shown in Figure 4.6c, which uses the same higher inert DNA concentration as the experiment in panel a, we observe the same: a lower than expected average valency and a distribution that seems to coincide with the distribution predicted for the lower inert DNA concentration. There could be several explanations for these observations. First, due to variations between experiments, it is possible that the actual inert DNA concentration on the particles is lower than expected. Second, other experimental factors than the binding probability alone could have led to a slower self-assembly process, such as particles that stick to the substrate or contamination of the samples by DNase enzymes, that reduce the effective concentrations of intact inert and linker DNA on the particles. While we have tried to mitigate these effects as much as possible, more experiments are needed to fully test our hypothesis.

In addition to the distribution of observed valencies, we can calculate the average valency $\langle n \rangle$, as shown in Figure 4.6d. For the experimental data, it can be seen that by tuning the DNA linker concentration, the expected average valency $\langle n \rangle$ can be tuned. We have compared the experimental average valency to our predictions by calculating the average valency based on the expected distributions of n, as shown

for a few linker concentrations in Figure 4.6a-c. We determined $\langle n \rangle$ as follows

$$\langle n \rangle = \left(\sum^{n}_{\substack{i=0 \\ p_{\text{tot.}} \leq 0.99}} p_{\text{tot.}}(i,c)\, i \right) / \sum^{n}_{\substack{i=0 \\ p_{\text{tot.}} \leq 0.99}} p_{\text{tot.}}(i,c), \tag{4.5}$$

where we used a probability of 0.99 as a cutoff value, above which we considered the binding probability to be equal to unity. In Figure 4.6d, we show the full dependency of the expected average valency on the added DNA linker concentration, up to a maximum valency of three, which is the maximum valency that we have measured both using the optical tweezers method and in these self-assembly experiments. Again, we note that the limited experimental data that is available seems to show a similar trend, in spite of differences in inert DNA concentration that would result in very different binding probabilities and therefore, average valencies, as plotted in Figure 4.6d. In an upcoming work,[250] we will study the self-assembly of these types of colloidal clusters in greater detail.

In conclusion, the experimental data shows a qualitatively similar trend as the predicted average valency for low linker concentrations. For the experimental data where the inert DNA concentration is high (1×10^5 μm^{-2}) in Figure 4.6a and c, the experimental distributions are closer to the expected distributions of the low inert DNA concentration (1×10^5 μm^{-2}). As discussed, more experiments are necessary to fully test how the total binding probability predicted by Equation 4.4 compares to the experimentally observed valencies in self-assembly experiments.

Based on our preliminary data, we conclude that the linker concentration can be used to tune the average valency of colloidal clusters in self-assembly experiments. We have exploited this dependence of the average valency on DNA linker concentration in chapters 5 and 6, where we assembled flexible colloidal chains using low linker concentrations, that ensured an average valency close to two. In future experiments, we plan to repeat these self-assembly experiments for a larger range of DNA linker concentrations in order to further test our predictions.

4.4 Conclusions

In this chapter, we have used optical tweezers to directly probe the binding probability of DNA-decorated colloid-supported lipid bilayers as function of DNA linker concentration and valency. First, we have determined the optimal parameters to provide colloidal stability. We have found that a total DNA concentration above approximately 10^4 μm^{-2} is sufficient to completely suppress nonspecific aggregation. In addition, we have shown that both linker and inert DNA complexes can be used to provide colloidal stability. Then, we have characterized the binding probability as function of DNA linker concentration and valency in terms of a simple model given by a logistic function. We have found a complex dependence on inert DNA concentration and linker DNA concentration as function of valency and conclude that more research is needed to explain these effects in terms of a physical model. Our results indicate that linker depletion effects as function of valency lead to a decrease in the

binding probability. We have shown that by varying the DNA linker concentration, the average valency of colloidal clusters can be tuned in self-assembly experiments.

Linker depletion presents a promising way to control the average valency in self-assembly experiments. The mechanism could be used to fabricate structures of the desired geometry, such as clusters of valency four, that are believed to be able to crystallize into diamond lattices that have interesting photonic properties.[59,71] The fact that CSLBs are reconfigurable due to their flexible bonds, could lead to applications in switchable materials. Beyond applications for colloidal self-assembly processes, our findings could have implications for multivalent interactions found in biological systems, such as in cell-signaling and drug-delivery systems.

Acknowledgements

We thank Ali Azadbakht for the design and setup of the Optical Tweezers and his technical support. We thank Christine Linne and Yogesh Shelke for useful discussions. We are grateful to Yogesh Shelke and Samia Ouhajji for PAA coated glass functionalization. This project received funding from the European Research Council (ERC) under the European Union's Horizon 2020 research and innovation program (grant agreement no. 758383).

5 Flexibility-induced effects in the diffusion of colloidal trimers

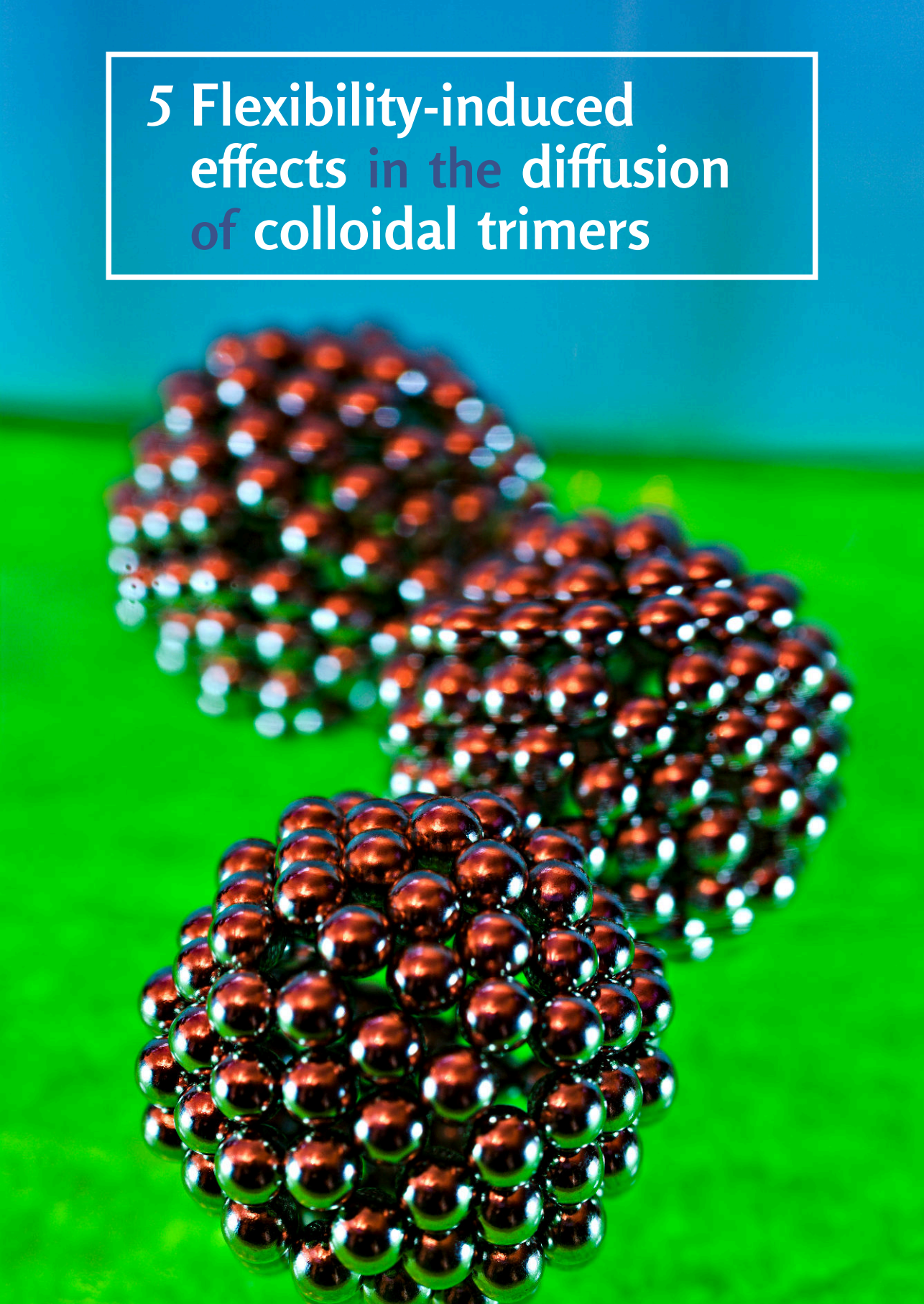

Shape changes resulting from segmental flexibility are ubiquitous in molecular and biological systems, and are expected to affect both the diffusive motion and (biological) function of dispersed objects. The recent development of colloidal structures with freely-jointed bonds have now made a direct experimental investigation of diffusive shape-changing objects possible. Here, we show the effect of segmental flexibility on the simplest possible model system, a freely-jointed cluster of three spherical particles, and validate longstanding theoretical predictions. We find that in addition to the rotational diffusion time, an analogous conformational diffusion time governs the relaxation of the diffusive motion, unique to flexible assemblies, and that their translational diffusivity differs by a small but measurable amount. We also uncovered a Brownian quasiscallop mode, where diffusive motion is coupled to Brownian shape changes. Our findings could have implications for molecular and biological systems where diffusion plays an important role, such as functional site availability in lock-and-key protein interactions.

5.1 Introduction

Many (macro)molecular systems display segmental flexibility, e.g. biopolymers such as transfer RNA,[251] intrinsically disordered proteins,[252] myosin,[251] immunoglobulins,[251] and other antibodies.[101,103,253,254] For most of these systems, the flexibility not only affects the motion of the complex but also its (biological) function.[100–104] For example, proteins often function through shape-dependent lock-and-key interactions where active sites of enzymes are reshaped during the interaction, leading to an induced fit.[255] Additionally, enzymes like adenylate kinase can accelerate biochemical reactions with remarkable specificity and efficacy thanks to a flexible “lid" that opens and closes at each reaction cycle. Because shape has a large effect on the diffusive motion of structures at the short timescales relevant to these reactions, it is expected that the diffusion of reconfigurable objects is different from rigid ones.[251,256–258] Moreover, Adeleke-Larodo et al.[155] recently proposed that changes in an enzymes flexibility upon substrate binding could be responsible for the observed enhanced diffusion of active enzymes.[259,260] Therefore, a rigorous understanding of enzyme function and diffusion requires quantitative knowledge of protein flexibility.[261]

However, direct experimental measurements of flexibility in molecular systems are challenging because they require single-molecule measurement techniques with high spatial and temporal resolution. One way to circumvent this problem is to employ colloidal particles, which have been used as model systems for (macro)molecular

structures,[17–19] because of their unique combination of microscopic size and sensitivity to thermal fluctuations. Studies on the Brownian motion of rigid colloids of various shapes such as ellipsoids,[91,95,96] boomerangs,[14,97,98] and clusters[12,13] have revealed that shape affects the diffusive motion at short timescales. Additionally, displacements are larger in directions that correspond to smaller hydrodynamic drag[12–14,16,91,97] and different diffusive modes can be coupled, e.g. helical particles rotate as they translate and vice versa.[99] At longer timescales, the influence of particle shape decreases because of rotational diffusion.[91]

While rigid assemblies have been extensively studied, little is known about the effect of flexibility. In order to numerically and experimentally investigate the effect of segmental flexibility, we study a simple model system consisting of a freely-jointed chain of three spherical colloidal particles, called flexible trimers or "trumbbells".[107,262] Numerical models were proposed to capture the diffusion of segmentally flexible objects[105–107] and the long time diffusive motion was predicted to be determined by the shape average of the instantaneous diffusivities (so called rigid-body approximation[101,263,264]). For the first time, we are able to test these models using direct experimental measurements of the diffusion of colloidal particles, thanks to the recent development of colloidal structures with freely-jointed bonds,[56,85,110,112,194,242,265] and flexible chains.[266] First, we discuss the short-time diffusion tensor of the flexible trimers, which we compared to numerical calculations and found a good agreement. Furthermore, we uncovered a Brownian quasiscallop mode, where diffusive motion is coupled to Brownian shape changes. Next, we considered the diffusive behavior at longer timescales and found that in addition to the rotational diffusion time, an analogous conformational diffusion time governs the relaxation of the diffusive motion, unique to flexible assemblies.

5.2 Methods

5.2.1 Experimental

Flexible clusters of three colloid-supported lipid bilayers (CSLBs) were prepared as described in previous work.[85,110,112,242] To test the generality of the results presented here, we used two particle sizes, namely 1.93 μm and 2.12 μm silica particles, with different methods of functionalization.

The CSLBs consisting of 2.12 μm silica particles were prepared as described in our recent work.[242] Briefly, the particles were coated with a fluid lipid bilayer by deposition of small unilamellar vesicles consisting of 98.8 mol % of the unsaturated phospholipid DOPC ((Δ9-Cis) 1,2-dioleoyl-sn-glycero-3-phosphocholine), 1 mol % of the lipopolymer DOPE-PEG(2000) (1,2-dioleoyl-sn-glycero-3-phosphoethanolamine-N-[methoxy(polyethylene glycol)-2000]) and 0.2 mol % of the dyed lipids TopFluor-Cholesterol (3-(dipyrromethene boron difluoride)-24-norcholesterol) or DOPE-Rhodamine (1,2-dioleoyl-sn-glycero-3-phosphoethanolamine-N-(lissamine rhodamine B sulfonyl)). The bilayer coating was performed in a buffer at pH 7.4 containing 50 mM sodium chloride (NaCl) and 10 mM 4-(2-Hydroxyethyl)-1-piperazineethanesulfonic

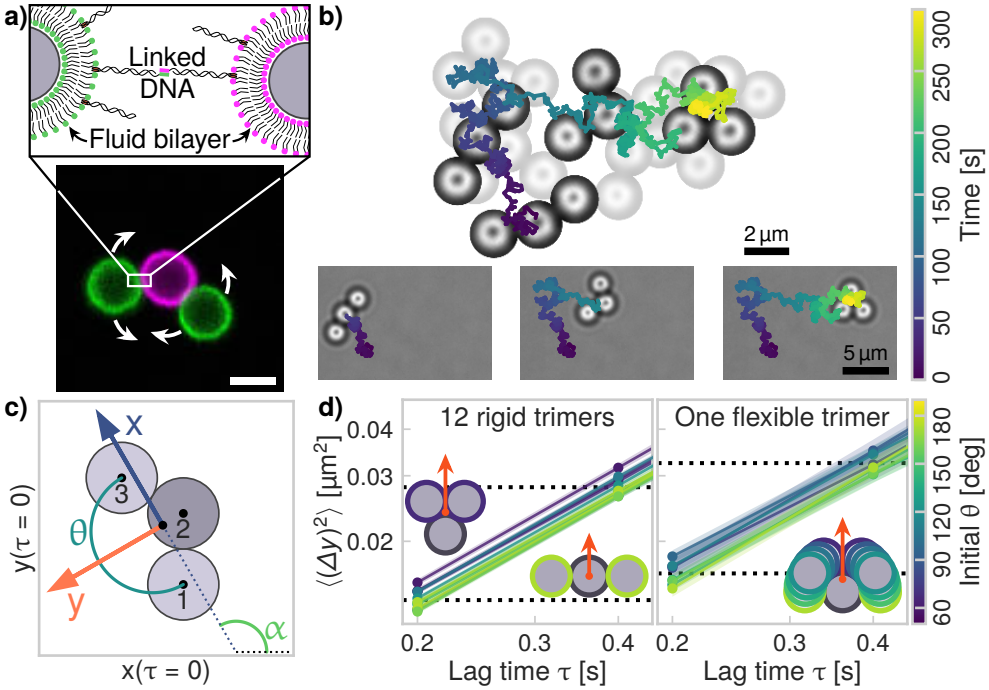

Figure 5.1: **Diffusion of flexible trimers. a)** Schematic (not to scale) of flexible trimers that are self-assembled from colloid-supported lipid bilayers. We inserted DNA linkers into the fluid lipid bilayer surrounding the particle, resulting in bonded particles that can rearrange with respect to each other. Bottom: confocal microscopy image of a flexible trimer. Scalebar is 2 µm. **b)** Overlay of brightfield microscopy images of a flexible trimer with the position of its center of mass as function of time. **c)** Illustration of the body-centered coordinate system. **d)** The mean squared displacement of rigid and flexible trimers. The translational mean squared displacement of flexible trimers in the y-direction is angle dependent for short lag times, at longer lag times this angle dependence is no longer present due to rotational and conformational relaxation, which happens on a shorter timescale than for rigid trimers (raw data).

acid (HEPES). We added double-stranded DNA (of respectively strands DS-H-A and DS-H-B of Table A.1) with an 11 base pair long sticky end and a double stearyl anchor, which inserts itself into the bilayer via hydrophobic interactions (see Figure 5.1a). When two particles with complementary DNA linkers come into contact, the sticky ends hybridize and a bond is formed. Self-assembly experiments were performed in a different buffer of pH 7.4, containing 200 mM NaCl and 10 mM HEPES. We imaged 21 trimers of 2.12 μm CSLBs, that were formed by self-assembly in a sample holder made of polyacrylamide (PAA) coated cover glass. The PAA functionalization was carried out using a protocol[202] which we modified by adding 0.008 mol % bis-acrylamide and performing the coating under a nitrogen atmosphere, both of which resulted in a more stable coating. Using an optical microscope, we imaged the clusters for 5 min at frame rates between 5 fps to 10 fps. Particle positions were tracked using a custom algorithm[242] available in TrackPy by using the `locate_brightfield_ring` function,[188] as depicted schematically in Figure 3.1.

Additionally, we analyzed 9 trimers of 1.93 μm CSLBs, with silica particles purchased from Microparticles GmbH (product code SiO_2−R-B1072). For these particles, we used a similar protocol to form supported lipid bilayers with only 2 minor modifications: first, the lipid composition we used was 98.9 mol % DOPC, 1 mol % DOPE-PEG(2000) and 0.1 mol % DOPE-Rhodamine. Second, we added Cy3-labeled DNA with a self-complementary 12 base pair sticky end and a cholesterol anchor that inserts itself into the lipid bilayer due to hydrophobic interactions. We used the DNA sequence from Leunissen et al.[72] (see Table A.1, strands PA-A and PA-B).

To image the 1.93 μm CSLBs we used a flow cell produced as detailed in the Supplementary of Montanarella et al.[267] As the base of our flow cell we used a single capillary with dimensions 3 cm × 2 mm × 200 μm. To prevent the lipid coated clusters from sticking to the class capillary, we coated the inside of the capillary with poly(2-hydroxyethyl acrylate) (pHEA) polymers. To this end, we first flushed the cell with consecutively 2 mL 2 mM NaOH solution, 2 mL water and 2 mL EtOH. We then functionalized the glass surface with the silane coupling agent 3-(methoxysilyl)propyl methacrylate (TPM) by filling the flow cell with a mixture of 1 mL EtOH, 25 μL TPM, and 5 μL 25 % v/v NH_3 in water and leaving it for 1 hour. We then washed and dried the flow cell by flushing with 2 mL ethanol and subsequently with nitrogen. We grew pHEA brushes from the surface through a radical polymerization by filling the cell with a mixture of 2.5 mL EtOH, 500 μL HEA and 20 μL Darocur 1173 photoinitiator. We initiated the reaction by placing the cell under a UV lamp with wavelength λ = 360 nm for 10 minutes. Finally, we flushed the cells with 10 mL EtOH or Millipore filtered water. We stored the coated cells filled with EtOH or Millipore filtered water and for no more than one day. Self-assembly experiments were performed in a buffer of pH 7.4, containing 50 mM NaCl and 10 mM HEPES. We imaged 9 freely-jointed trimers and 13 rigid trimers stuck in various opening angles shown in Figure 5.2 for 30 minutes with a frame rate of 5 fps. Particle positions were tracked using the 2007 Matlab implementation by Blair and Dufresne of the Crocker and Grier tracking code.[189]

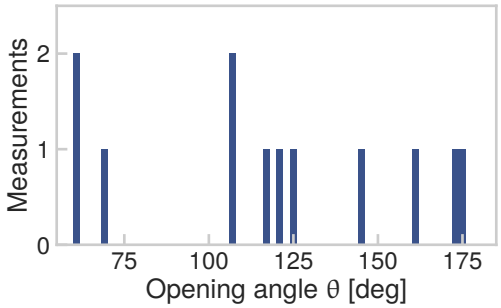

Figure 5.2: **Opening angles of rigid trimers.** The number of rigid clusters of different opening angles used in this study. Six rigid trimers have a 'compact' opening angle (below 120°) while the other six are more extended.

5.2.2 Diffusion analysis

For all analysis, we only selected trimers that showed all bond angles during the measurement time, experienced no drift and were not stuck to the substrate. After the particle positions were tracked, we determined the short-time diffusivity of the trimers as described by Equation 5.4 separately for all trimers. For each pair of frames, we determined the initial average opening angle $\overline{\theta}$ of the trimer between t and $t+\tau_{\text{short}}$, with $\tau_{\text{short}} = 0.25\,\text{s}$. Then, we stored the diffusion tensor elements separately for each initial opening angle. For short times up to $\tau_{\text{short}} = 0.25\,\text{s}$, we used a bin size of 15° while for longer times, we used two bins of 60° covering the range of $[60°, 120°)$ and $[120°, 180°]$. We scaled each element with the friction factors we obtained for that measurement, based on the diffusion coefficient for lag times up to τ_{short}. The average diffusion tensor elements were then obtained by fitting the overall slope of the mean (squared) displacements of all the individual diffusion tensor elements as a function of lag time (see Figure 5.9a, c, e and Figure 5.11a, c). We used a linear function (with zero intercept) divided into ten segments with slopes $2D_i$ (spaced evenly on a log scale), which correspond to the ith diffusion coefficient for those lag times. This resulted in the average diffusion tensor for all binned average opening angles $\overline{\theta}$ as a function of the lag time τ. For fitting, we used a standard least squares method and we estimated the error using a Bayesian method to find an estimate of the posterior probability distribution, by using a Markov chain Monte Carlo (MCMC) approach as implemented in the Python packages lmfit[246] and emcee.[207] We estimated the autocorrelation time τ_{acor} of the chain using the builtin methods and ran the analysis for at least $100\tau_{\text{acor}}$ steps, where we discarded the first $2\tau_{\text{acor}}$ steps (corresponding to a burnin phase) and subsequently used every other $\tau_{\text{acor}}/2$ steps (known as thinning). The reported values correspond to the maximum likelihood estimate of the resulting MCMC chain, the reported uncertainties correspond to the minimum and maximum of the obtained posterior probability distribution.

5.2.3 Hydrodynamic modeling

The diffusion of segmentally flexible objects can be described using hydrodynamic modeling.[107,268] To compare our experimental results to these predictions, we followed the procedure described by Harvey and coworkers.[107] Of the seven degrees

of freedom in three dimensions (three translational, three rotational, one internal degree of freedom), we considered only the four degrees of freedom of interest for our quasi-two dimensional system of sedimented clusters. Briefly, following the method outlined by Harvey and coworkers,[107] we determined the hydrodynamic resistance (or friction) tensor $\boldsymbol{R}_0$ with respect to the central particle. Using this resistance tensor, we calculated the diffusion tensor $\boldsymbol{D}_0 = kT\boldsymbol{R}_0^{-1}$, to which we apply the appropriate coordinate transformation to obtain the 7×7 diffusion tensor $\boldsymbol{D}_{\text{c.m.}}$ relative to the center of mass of the cluster. We chose the center of mass as reference point because it is a good approximation of the center of diffusion of a flexible particle: in fact, it was found to be a better choice than either the center of diffusion or resistance of a rigid cluster of the same shape.[107] In Chapter 6, we will discuss how to calculate the center of diffusion for a flexible cluster[269] and what effect it has on the diffusion tensor when used as a tracking point instead of the center of mass. Additionally, we have calculated the diffusion tensor with respect to the central particle and these results are shown in Figure 5.7.

The diffusivity of flexible colloidal clusters can be modeled using bead or bead-shell models.[270] We used three different models to describe the hydrodynamic properties of the flexible trimers: a bead model (Figure 5.3a), a bead-shell model for a rigid trimer using HydroSub[263] (Figure 5.3b) and a bead-shell model for flexible trimers (Figure 5.3c). For the bead model, we modeled the trimer using three beads (diameter of 2 μm). For the bead-shell models, we modeled the trimer using approximately 2500 to 9500 smaller beads with bead radii ranging from 54 nm to 31 nm respectively, where the beads where placed to form three 2 μm shells. We followed existing methods[271,272] for constructing the bead shell model: to summarize, the positions of the small beads were calculated by placing them on concentric circles, starting at the equator of an individual 2 μm sphere and continuing the process towards the poles of the sphere using circles of decreasing radius and finally putting one sphere at each of the poles. Three spherical bead-shell models were then put together to form a trimer and we removed overlapping beads at the contact points between the particles. The results were evaluated for multiple small bead sizes, so that the result could be linearly extrapolated[271,272] to the limit where the small bead radius approaches zero.

In Figure 5.3d, the calculated diffusivities are shown for all three models. The bead model predicts higher diffusivities compared to both bead-shell models for all different elements of the diffusion tensor. The bead-shell models agree qualitatively, but predict different magnitudes of the diffusivities due to differences in hydrodynamic interactions between the outer beads, which are higher for the flexibly-linked clusters.[251,256–258]

Because drag forces act on the surface of the particles, the bead-shell model is more accurate in describing the diffusive properties of the clusters.[263,271,272] The accurate consideration of hydrodynamic effects was found to be important for the segmentally flexible system we study: hydrodynamic interactions lead to a slower decay of the autocorrelation of the particle shape[273] and lead to an increase in the translational diffusivity.[101,251] We have used the bead-shell model of Figure 5.3c (solid

line) to model our experimental data, because it best describes our experimental data and because it can be used to model conformational changes, which are not yet implemented in the HydroSub model.

To calculate the diffusion tensor elements, we used the Rotne-Prager-Yamakawa (RPY) interaction tensor[34,275] $\boldsymbol{T}_{ij}$ to model hydrodynamic interactions between particles i and j:

$$\boldsymbol{T}_{ij} = \frac{1}{8\pi\eta_0 R_{ij}} \left[\boldsymbol{I} + \frac{\boldsymbol{R}_{ij}\boldsymbol{R}_{ij}}{R_{ij}^2} + \frac{2\sigma^2}{R_{ij}^2} \left(\frac{\boldsymbol{I}}{3} - \frac{\boldsymbol{R}_{ij}\boldsymbol{R}_{ij}}{R_{ij}^2} \right) \right], \tag{5.1}$$

where σ is the particle radius, $\boldsymbol{R}_{ij}$ is the vector between particles i and j, $\boldsymbol{I}$ is the 3×3 identity matrix, η_0 is the viscosity of the medium. Using the RPY tensor prevents singularities that may lead to the large, nonphysical numerical fluctuations[276] found when using lower order terms (Oseen tensor), higher order terms or multi-body effects.[277]

We used the RPY tensor to model the hydrodynamic interactions between the beads and followed the procedure outlined by Harvey and coworkers[107] to obtain the diffusion tensor, as explained in Section 5.3. This was done for all small bead radii and we used a linear extrapolation to zero bead size to obtain the final diffusion tensor elements.[271,272] Additionally, we used HydroSub[263] to model the diffusivity of rigid trimers of the same opening angles.

Near-wall diffusion: friction factors

Here, we have modeled the effect of the substrate using simple friction scaling factors. A comparison with more sophisticated simulations that take hydrodynamic interactions between the particles and the wall into account is given in Chapter 6. The three friction correction factors that account for substrate friction were determined in the following way:

$$\begin{aligned} \phi_{tt} &= \left\langle \boldsymbol{D}[tt]_t / (\sigma_e \boldsymbol{D}[tt]_{e,0}) \right\rangle \\ \phi_{(\alpha\alpha,\theta\theta)} &= \left\langle \boldsymbol{D}[(\alpha\alpha,\theta\theta)]_t / (\sigma_e^3 \boldsymbol{D}[(\alpha\alpha,\theta\theta)]_{e,0}) \right\rangle \\ \phi_{ij} &= \sqrt{\phi_{ii}\phi_{jj}} \quad \text{for} \quad i \neq j, \end{aligned} \tag{5.2}$$

where $\boldsymbol{D}[ij]_k$ denotes the theoretical ($k = t$) or experimental ($k = e$) diffusion tensor element and σ_e the experimental particle radius. The subscript tt denotes the translational component of the diffusivity. These factors were determined separately for each experiment, because differences in surface and particle functionalizations resulted in differences in substrate-particle and particle-particle friction, that in turn affect the diffusivity of the cluster. We separated the correction factors into these three factors because different modes of diffusion are expected to lead to different amounts of friction with the substrate.[154]

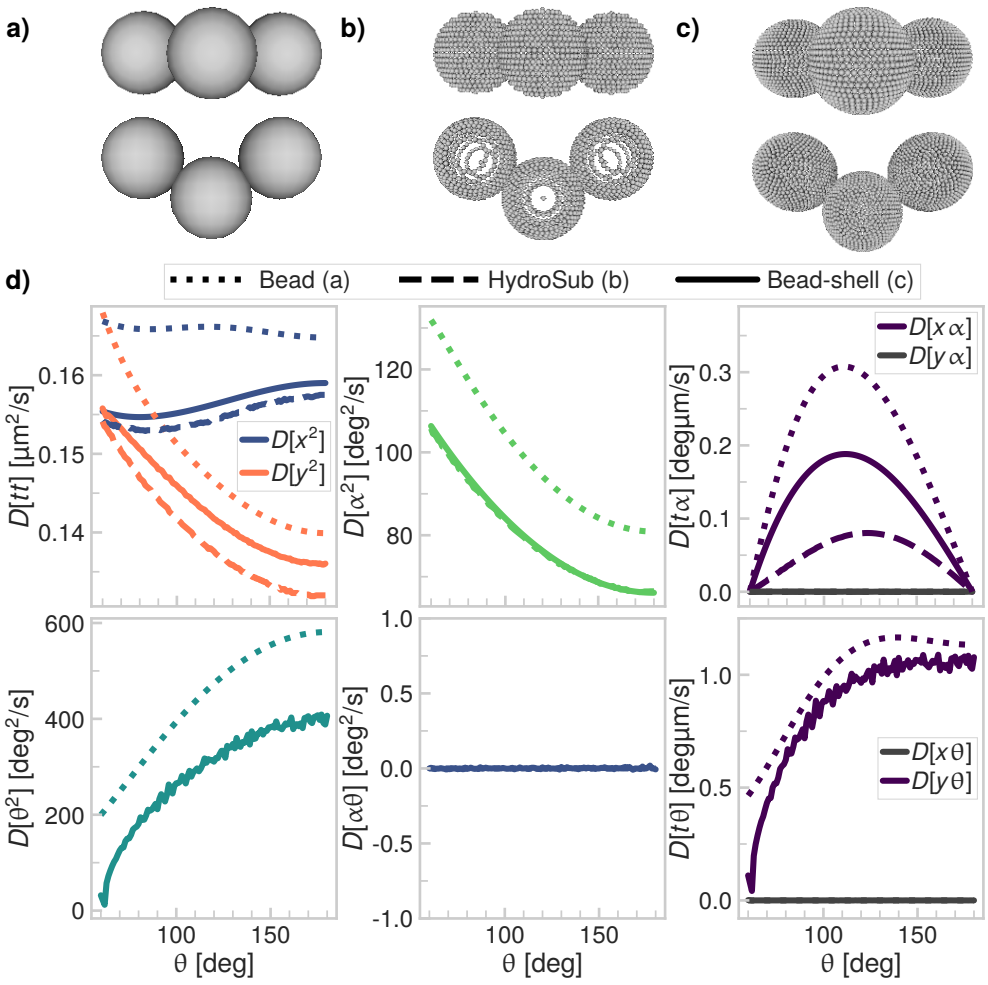

Figure 5.3: **Comparison of the diffusion tensor calculated by different hydrodynamic models.** Renderings made using FreeWRL[274] of **a)** the simple bead model, **b)** the bead-shell model (minimum radius of the small spheres $r = 55\,\text{nm}$) used by HydroSub[263] for rigid trimers, **c)** the bead-shell model (radius of the small spheres $r = 31\,\text{nm}$ to $54\,\text{nm}$, $r = 45\,\text{nm}$ is shown) we used for calculating hydrodynamic properties of flexible trimers. For all models, the radius of the large particles is $R = 1\,\mu\text{m}$. **d)** Top row, left to right: the translational diffusivity, rotational diffusivity and coupling between translational and rotational diffusivity for the bead model (a, dotted lines), the rigid bead-shell model generated with HydroSub (b, dashed lines) and the segmentally flexible bead-shell model (c, solid lines). Bottom row, left to right: the joint flexibility, coupling between shape changes and rotation and couplings between shape changes and translational diffusion.

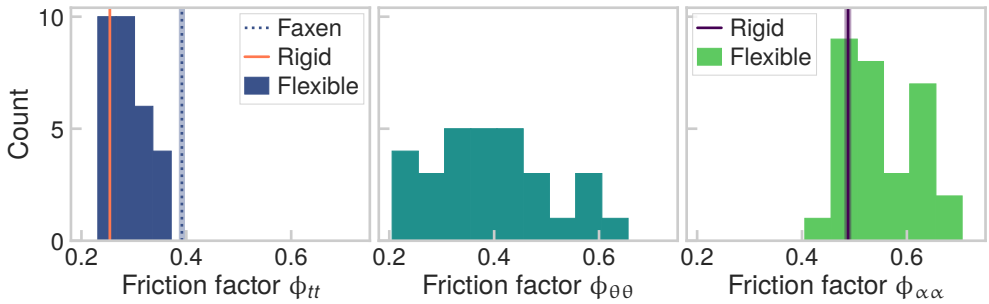

Figure 5.4: **Distribution of friction factors** as given by Equation 5.2. The mean value for $\phi_{tt} = 0.29 \pm 0.04$ is close to the lower bound of 0.39 (indicated by the dotted line, left plot) as predicted by Equation 5.3. We find an average rotational friction factor $\phi_{\alpha\alpha} = 0.55 \pm 0.07$ (center plot). The average flexibility friction factor $\phi_{\theta\theta} = 0.40 \pm 0.12$ shows a broader distribution, which we attribute to a spread in DNA linker concentration (right plot). The average friction factor of the rigid clusters is also indicated (left and right plots, $\phi_{tt,r} = 0.254 \pm 0.004$, $\phi_{\alpha\alpha,r} = 0.49 \pm 0.02$) and coincides with the friction factors we find for flexible clusters.

As a first approximation to compare the experimental diffusion of freely-jointed trimers above a substrate to models of trimers diffusing in the bulk, we use Faxen's theorem:[192]

$$\frac{D_w(h)}{D_0} = 1 - \frac{9}{16}\frac{R}{h+R} + \frac{1}{8}\left(\frac{R}{h+R}\right)^3 - \frac{45}{256}\left(\frac{R}{h+R}\right)^4 + O\left(\left(\frac{R}{h+R}\right)^5\right), \tag{5.3}$$

with D_0 the translational diffusion coefficient in the bulk, $D_w(h)$ the in-plane translational diffusion coefficient near a wall at height h and R the particle radius. We calculate an effective particle radius

$$R_{\text{eff}} = \frac{k_B T}{6\pi\eta D} = 1.8\,\mu\text{m}$$

from the short-time translational diffusion coefficient,[278] with k_B Boltzmann's constant, T the temperature, η the viscosity of the medium and $D = 0.136\,\mu\text{m}^2\,\text{s}^{-1}$ the lowest short-time translational diffusion coefficient of the trimer as predicted by the bead-shell model.

The expected Debye length[20] of our medium (at $I = 200\,\text{mM}$) is

$$\kappa^{-1} = \frac{0.304}{\sqrt{I}} \approx 0.7\,\text{nm}$$

and so we neglect electrostatic interactions between the trimer and substrate. Therefore, the height of the particle above the substrate is set by balancing the effect of

sedimentation and thermal fluctuations as expressed by the gravitational length l_g:

$$l_g = \frac{k_B T}{g \Delta \rho V},$$

with g the gravitational acceleration constant, $\Delta\rho$ the density difference between the particle and the medium and V the volume of the particle.

Using the appropriate values for the trimer, we find $l_g = 20\,\text{nm}$. By setting this as input for h in Equation 5.3, we obtain a upper bound for $D_w(h)/D_0$, equal to 0.40. A lower bound is found at $h = 0$, which gives a value of 0.39. The translational friction coefficient $D_w(h)/D_0$ that we find has an average value of 0.29 ± 0.04, as shown in Figure 5.4, which is close to the lower bound we have calculated above. The experimental value is slightly lower than the predicted lower bound, because Equation 5.3 accounts for hydrodynamic interactions only and real experiments typically show lower diffusivities because of additional sources of friction,[279] which in the present case could be explained by additional friction between the polymer coating and the particles. Moreover, a comparison with more sophisticated simulations that take hydrodynamic interactions between the particles and the wall into account is given in Chapter 6.

5.3 Results and Discussion

5.3.1 Short-time Brownian motion of flexible trimers

The flexibly-linked colloidal trimers are made by self-assembly of colloid-supported lipid bilayers (CSLBs).[85,110,112,242] Briefly, spherical colloidal silica particles are coated with a fluid lipid bilayer. DNA linkers with complementary sticky ends are inserted into the bilayer using a hydrophobic anchor. The particles are self-assembled by hybridization of the DNA sticky ends, which provide strong and specific interactions. The trimers are freely-jointed because the DNA linkers can diffuse on the fluid lipid bilayer that surrounds the particles (see Figure 5.1a). The clusters undergo translational and rotational diffusion while they are also free to change their shape (see Figure 5.1b and Supplementary Movie 1 of Verweij & Moerman *et al.*[244]). For simplicity, we used heavy silica particles so that their mobility is confined to the bottom of the container by gravity, which leads to two-dimensional Brownian motion.

For rigid objects in two dimensions, the diffusive motion can be described by a 3×3 diffusion tensor calculated from the linear increase of the mean squared displacements of the particle as function of lag time.[31] For flexible objects, this diffusion tensor has to be extended with an additional degree of freedom[107] for each internal deformation mode (here: one), and we therefore consider the 4×4 diffusion tensor $\boldsymbol{D}[ij]$. Here, $i, j \in [x, y, \alpha, \theta]$ are elements of a body-centered coordinate system (see Figure 5.1c) at the center of mass. We chose the center of mass as reference point, because for flexible objects, it is more appropriate than either the center of diffusion or resistance of a rigid cluster of the same shape.[107] In Chapter 6, we will discuss how to calculate the center of diffusion for a flexible cluster[269] and what effect it has on

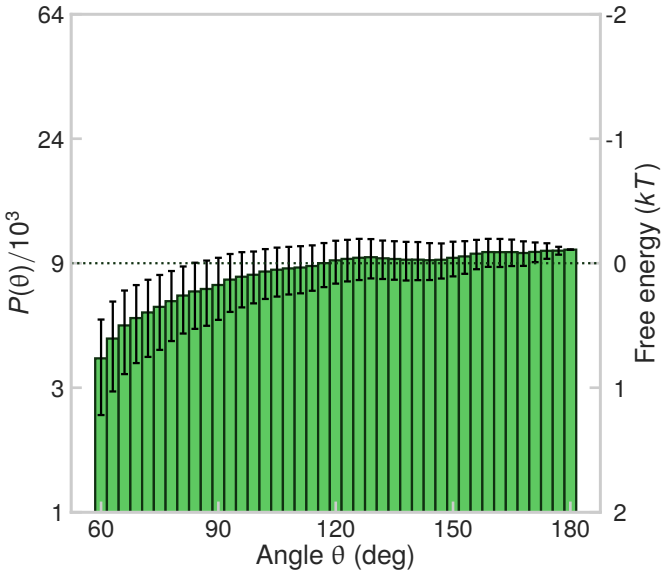

Figure 5.5: **Probability and free energy as a function of the opening angle of flexible trimers.** Probability and corresponding free energy of the opening angle of the flexible trimers used in this work (with the reference set at 180°). There is no preference for a specific opening angle within the experimental error, meaning the particles are freely-jointed, as was shown before.[242] Note that the slightly lower probability at angles smaller than $60° + \sqrt{2J\tau} \approx 69°$ (with J the joint flexibility and τ the sampling interval) is caused by boundary effects inherent to our analysis method.[242]

the diffusion tensor when used as a tracking point instead of the center of mass. In the coordinate system used here, the y-axis is perpendicular to the end-to-end vector and points away from the central particle, and the direction of the x-axis is chosen to form a right-handed coordinate system. We label the opening angle of the trimer θ and the (anticlockwise) rotation angle of the x-axis with respect to the lab frame α. We align the lab frame such that it coincides with the body-centered coordinate system at $\tau = 0$.

Shape determines the diffusion tensor for rigid objects and therefore we expect it to be important for flexible objects as well, but due to its flexibility, the cluster shape is continuously changing. Therefore, we categorize the trajectories by their (initial) average opening angle $\overline{\theta}$ of the smallest lag time interval and we use angular bins to summarize the results. The short-time diffusion tensor is calculated from experimental measurements in the following way:

$$\boldsymbol{D}[ij](\overline{\theta}) \equiv \frac{1}{2}\phi_{ij}\frac{\partial\langle\Delta i\Delta j\rangle_\tau}{\partial\tau}, \tag{5.4}$$

with τ the lag time between frames, $\langle\cdots\rangle_\tau$ denotes a time average over all pairs

of frames τ apart and $\Delta i = i(t + \tau) - i(t)$, ϕ_{ij} is a correction factor that accounts for particle-particle and particle-substrate friction (see Section 5.2.3 and Figure 5.4). The correction factors ϕ_{ij} are a first-order approximation to model the wall effect of the glass surface, that for translational diffusion agrees closely with predictions from hydrodynamic theory, as shown in Figure 5.4. A comparison with more sophisticated simulations that take hydrodynamic interactions between the particles and the wall into account is given in Chapter 6. We evaluated Equation 5.4 at $\tau = 0.25s$, set by the frame rate of our camera.

Using Equation 5.4, the resulting shape and time dependent translational diffusivity in the y-direction of twelve rigid and one flexible trimer are shown in Figure 5.1d. Initially, at short timescales, there is a clear effect of cluster shape for both flexible and rigid trimers: translational diffusion in y is highest for compact shapes. In comparison to rigid trimers, the diffusivity of the flexible trimer is slightly enhanced. Two other features unique to flexible clusters are that using a measurement of only one cluster, all possible cluster shapes are sampled and that the effect of shape vanishes on a much shorter timescale compared to the rigid clusters.

To study the diffusivity more carefully, we determined the average short time diffusion tensor of thirty flexible trimers. As shown in Figure 5.6a, the diffusion tensor elements were obtained by fitting the slope of the mean squared displacement versus lag time. We find three features that are in line with previous findings for rigid clusters[13] and that give confidence in the used analysis: first, translational diffusivity is higher along the longitudinal x-direction compared to the lateral y-direction (Figure 5.6d). Additionally, the rotational diffusivity shown in Figure 5.6b is higher for compact trimers as opposed to fully extended trimers and we observe a coupling between translational diffusion and rotational diffusion in the x-direction (Figure 5.6e).

However, flexibility gives rise to other modes that are not present in rigid assemblies. We found that the flexibility itself, as shown in Figure 5.6c, increases as function of the opening angle, leading to a four fold increase of flexibility for extended shapes compared to closed shapes. It is most likely caused by hydrodynamic interactions between the outer particles, as was predicted by earlier works.[106]

Even more strikingly, the hydrodynamic drag on the outer particles leads to an increase in opening angle θ for positive displacements along the y-axis (Figure 5.6f), which we call the Brownian quasiscallop mode. This Brownian quasiscallop mode may have implications for the accessibility of the functional site in induced fit lock-and-key interactions commonly observed in proteins.[255] We stress that this correlation does not lead to self-propulsion because it has time reversal symmetry. As the opening angle θ increases, the location of the center of mass moves in the negative y-direction of the original particle coordinate system. Therefore, this correlation is larger when the central particle is chosen as the origin of the coordinate center.

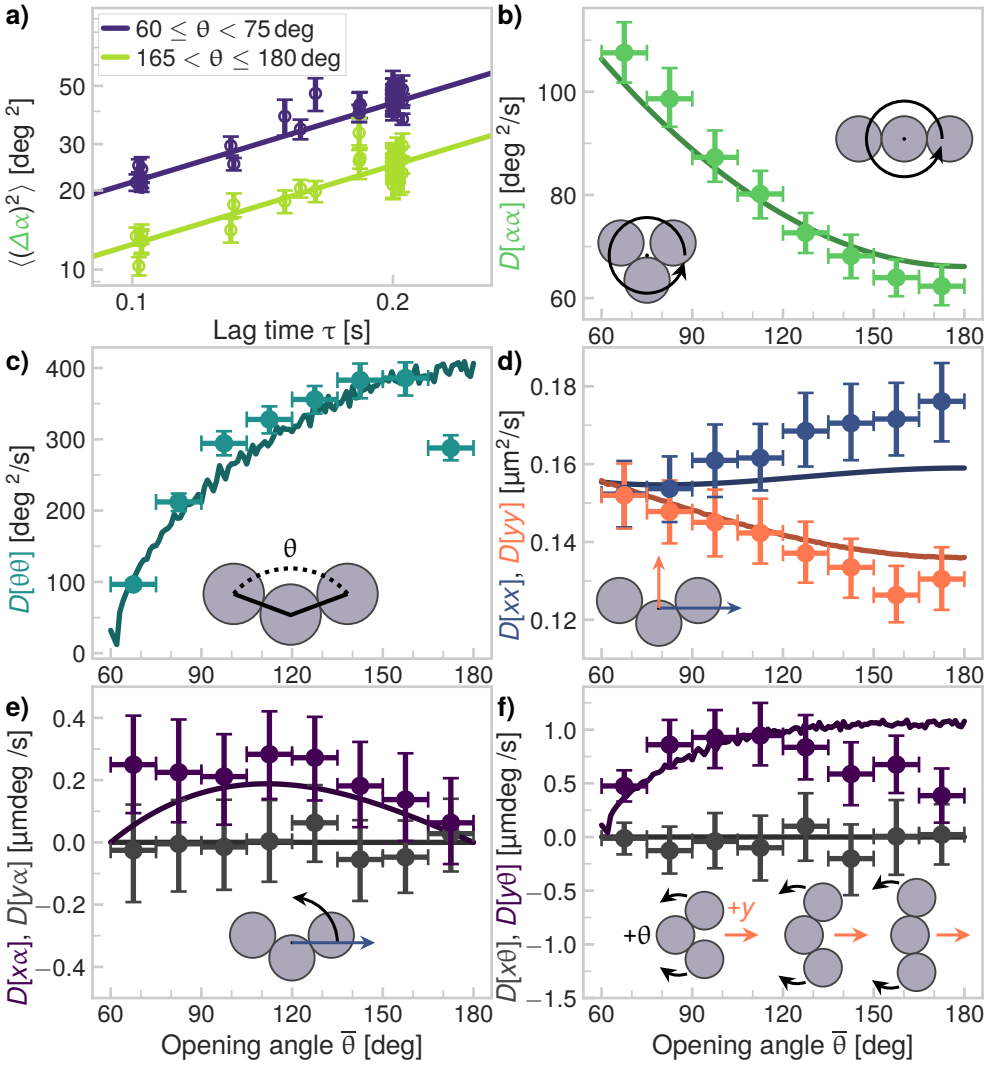

Figure 5.6: **Short-time translational, rotational, internal and coupled diffusivity** of flexible trimers (up to 0.25 s). **a)** Mean squared rotational displacements for lag times up to $\tau = 0.25$ s, for two different instantaneous opening angles $\overline{\theta}$. **b)** The rotational diffusivity is highest for the most compact shapes. **c)** The joint flexibility increases as function of opening angle θ. **d)** While equal for bent trimers, the translational diffusivity along the long axis (x) is higher than along the short axis (y). **e)** We find a correlation between counterclockwise rotation and positive x displacements. **f)** There is a coupling between translational diffusion in the y-direction and shape changes: as the cluster diffuses in the positive y-direction, the angle θ increases, leading to a Brownian scallop-like motion at short timescales. In panels b-f, the scatter points show the experimental measurements and the lines show the numerical calculations based on Harvey et al. [107]

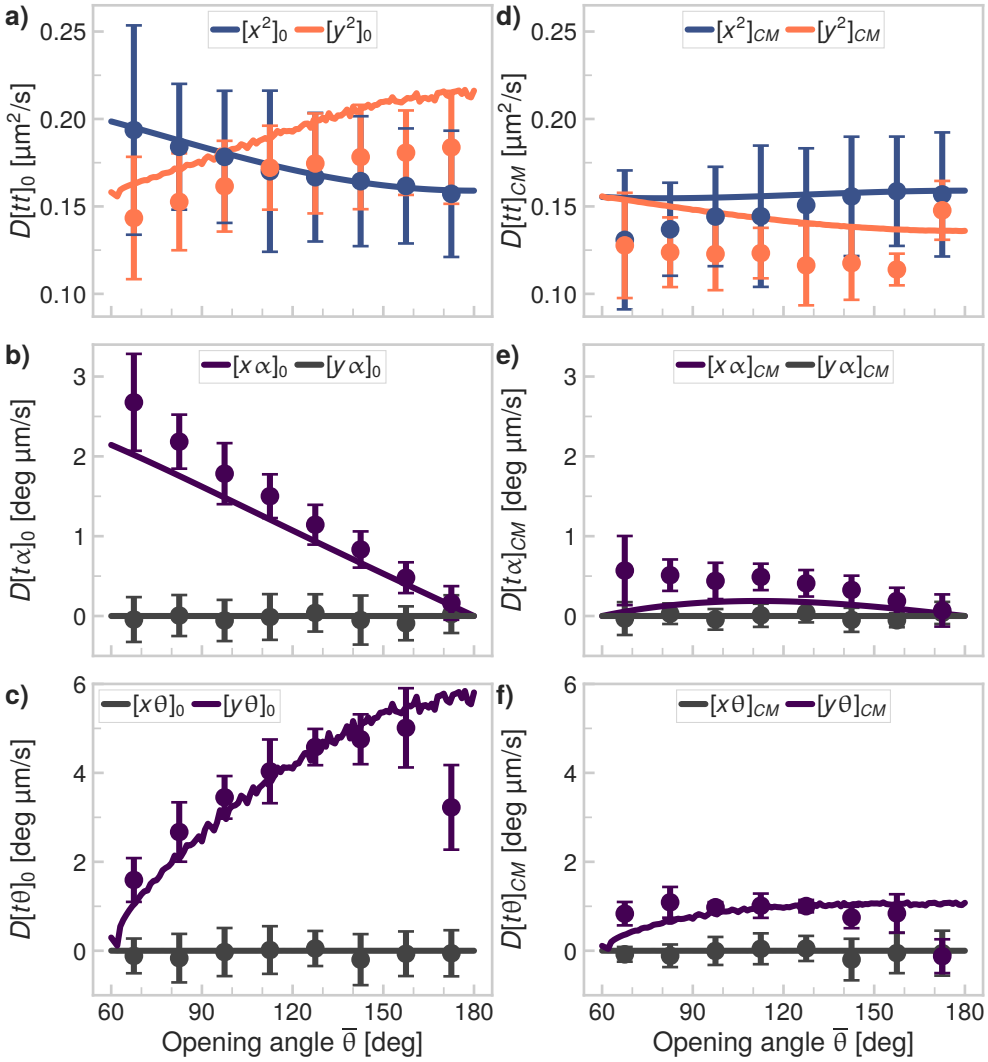

Figure 5.7: **Influence of the reference point on the diffusion tensor. a-c)** The translational (a), translational-rotational (b) and translational-conformational (c) diffusivities with the reference point chosen in the center of the central particle. **d-f)** The translational (d), translational-rotational (e) and translational-conformational (f) diffusivities with the reference point at the center of mass of the cluster. For these graphs, we transformed the data from panels a-c using the coordinate transformation described in the text from the "center particle"-based to the "center of mass"-based diffusivity. Note that the combination of experimental errors of the $D[t\alpha]$, $D[\alpha^2]$, $D[t\theta]$, $D[\theta^2]$ and $D[\alpha\theta]$ terms lead to large uncertainties and deviations, especially for the translational diffusivities. In all panels, the points show the experimental data and the lines are the predictions of the bead-shell model.

The influence of the tracking point

For purely rotational and conformational terms, the diffusivity is expected to be independent of the chosen reference point, however, for terms that include translation, the location of the reference point has a large effect on the measured diffusivity.[105,107] This can be seen in Figure 5.7: in panels a-c), we show the diffusivities calculated using the central particle as reference point. The results are remarkably different from the center of mass based results shown in Figure 5.7d-f), where we have used the diffusivities relative to the central particle to calculate the diffusivities relative to the center of mass using the coordinate transformations determined by Harvey and coworkers[107]:

$$\begin{aligned} D[tt]_{CM} = D[tt]_0 &+ D[t\alpha]_0^{\intercal} \cdot U - U \cdot D[t\alpha]_0 + U \cdot D[\alpha^2] \cdot U \\ &+ D[t\theta]_0^{\intercal} \cdot W + W^{\intercal} \cdot D[t\theta]_0 - U \cdot D[\alpha\theta]^{\intercal} \cdot W \\ &+ W^{\intercal} \cdot D[\alpha\theta] \cdot U + W^{\intercal} \cdot D[\theta^2] \cdot W \end{aligned} \tag{5.5}$$

$$D[t\alpha]_{CM} = D[t\alpha]_0 + D[\alpha^2] \cdot U + D[\alpha\theta]^{\intercal} \cdot W \tag{5.6}$$

$$D[t\theta]_{CM} = D[t\theta]_0 + D[\alpha\theta] \cdot U + D[\theta^2] \cdot W \tag{5.7}$$

We have made this comparison because the coupling terms are expected to be larger in the central particle frame. The results indeed show this larger coupling and exclude the possibility that the coupling modes we observed are artifacts of the coordinate system we used. In Chapter 6, we will discuss how to calculate the center of diffusion for a flexible cluster[269] and what effect it has on the diffusion tensor when used as a tracking point instead of the center of mass.

Because the rotational and conformational diffusivities are independent of the reference point, localization uncertainties in the determination of the position of the reference point may have a larger effect on $D[xx, yy, xy, x\alpha, y\alpha, x\theta, y\theta]$ than on $D[\alpha^2, \theta^2, \alpha\theta]$. Because of the uncertainties that are propagated when we first determine the diffusivity with respect to the central particle and then transform this to the diffusivity with respect to the center of mass (in Figure 5.7d-f), the error is larger for this method compared to the direct calculation of the diffusivities with respect to the center of mass. Therefore, the latter method should be preferred.

In summary, our experimental data allow us to test for the first time theoretical predictions made by Harvey and coworkers,[107] who modeled the diffusion of segmentally flexible objects by calculating the hydrodynamic interactions between two sub units. We applied their calculations to a bead-shell model, adapted to match the conditions of our experiments (see Section 5.2.3 and Figure 5.3) and find good agreement between the numerical calculations and the experimental data. The good agreement between the numerical results and the experimental data validates their model for the diffusivity of microscopic objects with internal degrees of freedom. For some angles and entries of the diffusion tensor, the experimental data shows small deviations from the predicted model values, especially for translational diffusion, the Brownian quasiscallop mode and the flexibility (see Figure 5.6c, d and f). We

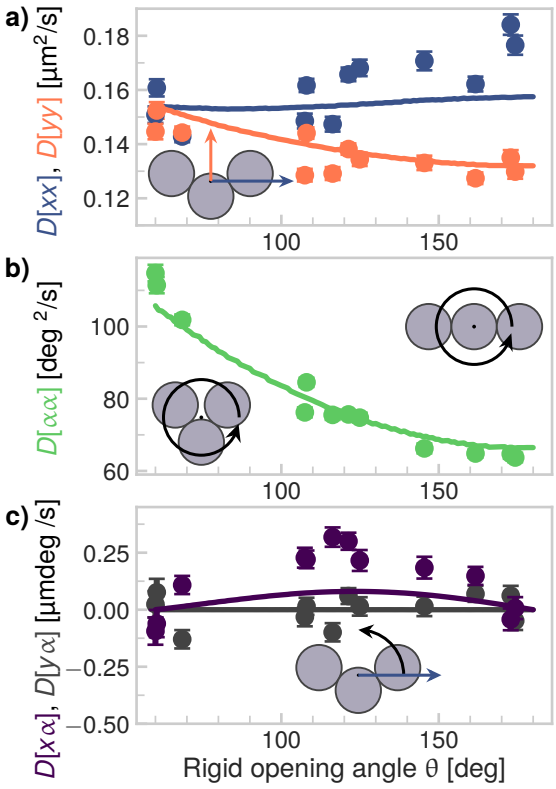

Figure 5.8: **Short-time diffusion of rigid trimers.** The **a)** translational, **b)** rotational and **c)** translational-rotational diffusivities of rigid trimers with various opening angles (see Figure 5.2 for details). In all panels, the points correspond to the experimental diffusivities (up to lag times of $\tau = 0.25\,\mathrm{s}$) and the solid lines correspond to the numerical calculations performed using HydroSub,[263] as detailed in Figure 5.3. All points are scaled by the same average friction factor as shown in Figure 5.4 in order to compare the experiments to the numerical simulations.

hypothesize that these differences may arise because the numerical calculations do not take particle-particle and particle-substrate friction into account, other than as a first-order approximate scaling using the friction factors ϕ_{ij} as defined in Equation 5.4. For example, substrate interactions were found to lead to enhanced diffusion for a model dumbbell consisting of two hydrodynamically coupled subunits.[104] More elaborate models may be used to provide higher-order corrections to the model we used here,[35] however their validity for flexible objects needs to be investigated. Moreover, our model also does not account for some out-of-plane diffusive motions against gravity, that might occur in the experiments. We will discuss these effects in greater detail in Chapter 6.

5.3.2 Flexible trimers compared to rigid trimers

In addition to flexibly-linked trimers of CSLBs, we have also studied rigid trimers of CSLBs that are frozen in a specific shape, as shown in Figure 5.2. First, we have compared their short-time diffusivity as function of their shape to bead-shell model calculations performed using HydroSub.[263] As shown in Figure 5.8, bead-shell models accurately describe their translational (Figure 5.8a), rotational (Figure 5.8b) and translational-rotational (Figure 5.8c) short-time shape-dependent diffusivities.

Then, we compared the short-term translational, rotational and coupled diffusion

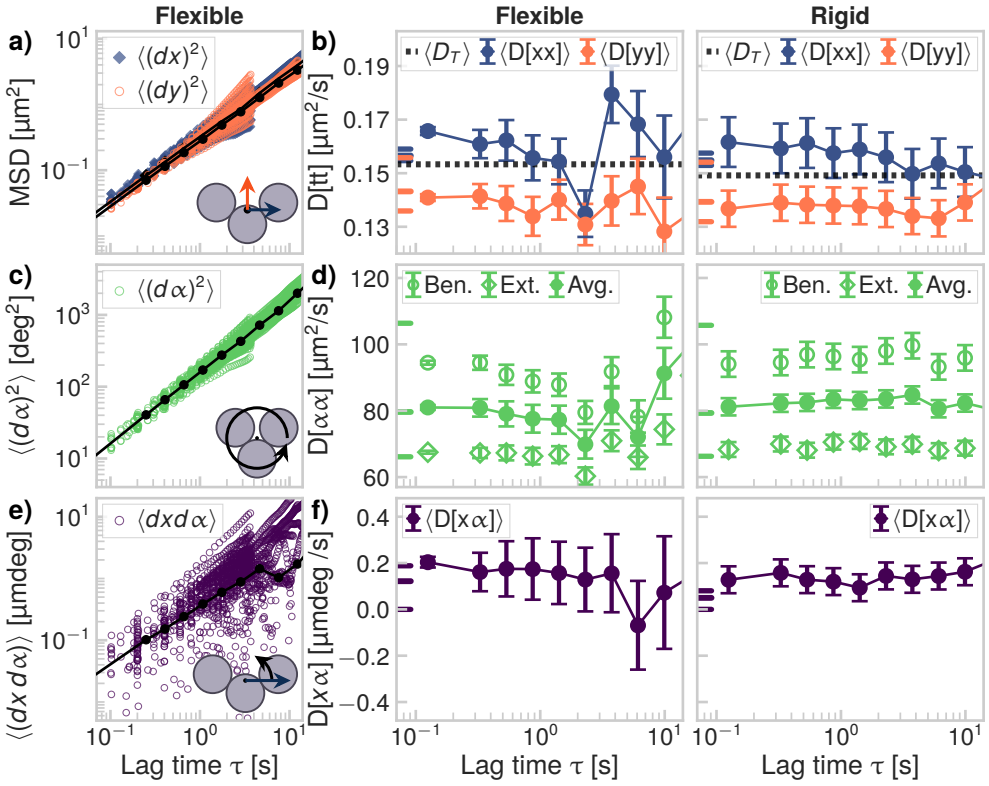

Figure 5.9: **Comparison between rigid and flexible trimers. a)** Mean squared displacements in x and y for all flexible trimers. **b)** Diffusivity in x and y as function of lag time for flexible (left) and rigid (right) trimers. The average translational diffusivity $\langle D_T(\tau_0 = 0.25\,\mathrm{s})\rangle$ (dotted lines) is $(2.7 \pm 0.3)\,\%$ higher for flexible clusters compared to rigid clusters. **c)** Mean squared angular displacements for all flexible trimers. **d)** Rotational diffusivity as function of lag time for flexible (left) and rigid (right) trimers. Bent configurations (Ben.) correspond to $\overline{\theta} < 120°$ and extended configurations (Ext.) to $\overline{\theta} \geq 120°$. **e)** Mean squared coupled displacements in x and α for all flexible trimers. **f)** Rotation-translation coupling in x and α as function of lag time for flexible (left) and rigid (right) trimers. In panels a, c and e, colored points are experimental data, black points and lines represent the fitted slopes. In panels b, d and f, numerical short-time diffusivities calculated based on Harvey et al.[107] are indicated by colored ticks on the y-axis, showing minimum, mean, and maximum shape-dependent values from bottom to top.

coefficients of flexible trimers to rigid trimers that are frozen in a particular shape and find that while they are qualitatively similar, there are experimentally measurable differences. Specifically, we measure that the average short time diffusion constant $\langle D_T(\tau_0 = 0.25\,\mathrm{s})\rangle$ of rigid trimers is $(2.7 \pm 0.3)\,\%$ lower ($(15 \pm 2)\,\%$ lower without friction scaling) than that of flexible trimers (Figure 5.9b, dotted lines), a small but measurable effect corroborated by the numerical models (see Section 5.2.3 and Figure 5.3). The rotational diffusion constants for flexible and rigid trimers are equal within the experimental uncertainty (Figure 5.9d), while the rotation-translation coupling mode between x and α is slightly higher for flexible trimers at the shortest lag time (Figure 5.9f). These findings agree qualitatively with numerical predictions[256–258] for hinged chains of spheres of higher aspect ratio (20:1 instead of 3:1 for the trimers). For these hinged rods, a 10 % increase in the translational diffusivity and a higher rotational diffusivity were found compared to rigid rods, which was attributed to hydrodynamic interactions between the subunits.[108,251]

The collective diffusion constant depends on size polydispersity

We have shown that freely-jointed trimers diffuse slightly faster than rigid trimers; their diffusion constant differs by approximately 3 %. When reporting such a small difference, it is important to exclude other effects that could lead to similar variations in the diffusion constant. Therefore, we here address the effect of size polydispersity on the average diffusion constant of a collection of particles. We consider an ensemble of particles, whose sizes are normally distributed around an average radius, $\bar{a}$, and with a standard deviation, σ. We assume that the particles exhibit Stokes diffusion so that each particle i has a size dependent diffusion constant

$$D_i = \frac{k_B T}{6\pi\eta a_i}.$$

Therefore, the smaller particles in the ensemble diffuse faster than the larger particles.

The experimental average diffusion constant of this ensemble of particles, $\bar{D}$, can be found by tracking the motion of many individual particles, calculating their individual diffusion constants and averaging those. One might assume that this average diffusion constant equals the diffusion constant of a monodisperse sample of particles with the same average size, but this turns out to be generally not true:

$$\bar{D} \neq \frac{k_B T}{6\pi\eta\bar{a}} \equiv D_{\bar{a}}.$$

The reason for this inequality is that the diffusion constant scales nonlinearly with size. Therefore, the diffusion constants of small particles are weighted more heavily than those of large particles, which skews the distribution of diffusion constant and shifts the average away from $D_{\bar{a}}$.

We asked how much the collective diffusion constant of a polydisperse sample would deviate from that of a monodisperse sample and how this deviation depends on size polydispersity. To this end, we first define the relative polydispersity as

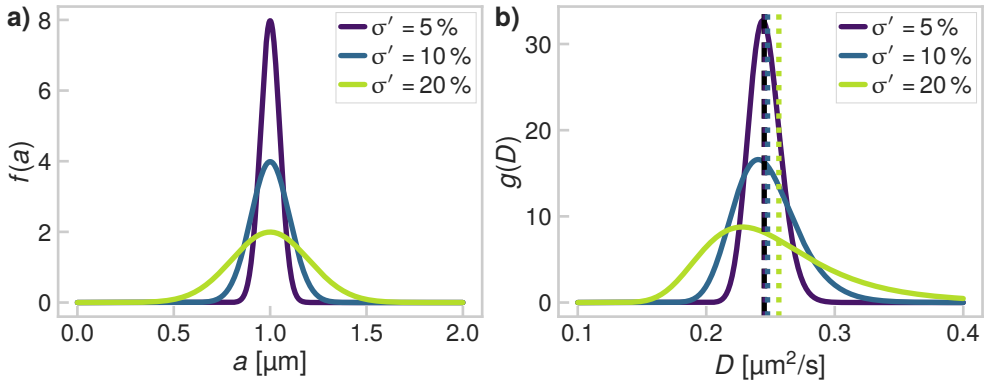

Figure 5.10: **The collective diffusion constant depends on size polydispersity. a)** Three hypothetical particle size distribution with an average particle radius of 1 µm and relative polydispersities of 5 %, 10 % and 20 %. **b)** The distributions in diffusion constant corresponding to the three particle size distribution in panel a. The average diffusion constants are indicated by dashed lines. The average diffusion constant of a monodisperse sample is indicated by a black dashed line.

$\sigma' = \sigma/\bar{a}$, which is a value between 0 and 1. The normalized distribution of particle sizes is then

$$f(a) = \frac{1}{\sigma'\bar{a}\sqrt{2\pi}} \exp\left[-\frac{1}{2}\left(\frac{a-\bar{a}}{\sigma'\bar{a}}\right)^2\right]. \tag{5.8}$$

Because the size is normally distributed and the diffusion constant scales with size as $1/a$, the diffusion constant exhibits a reciprocal normal distribution:

$$g(D) = \frac{D_{\bar{a}}}{D^2\sigma'\sqrt{2\pi}} \exp\left[-\frac{1}{2}\left(\frac{D_{\bar{a}}}{\sigma'}(1/D - 1/D_{\bar{a}})\right)^2\right]. \tag{5.9}$$

Figure 5.10a shows the hypothetical size distributions of three sets of particles with an average radius of 1 µm and relative polydispersities of 5 %, 10 % and 20 %. Figure 5.10b shows the diffusion constant distributions that correspond to these particle ensembles. Note that the diffusion constant is, unlike the size, not normally distributed. Instead, it has a tail of faster diffusion coefficients, corresponding to small particle sizes. Note also that the most probable diffusion constant shifts with polydispersity. This is also due to the $1/a$ scaling of the diffusion constant and can intuitively be explained by the fact that a range of large particles give a similarly small diffusion constant. This increases the probability of measuring this small diffusion constant and shifts the peak in the distribution. These properties of the distribution cause the average diffusion constant of a polydisperse sample (indicated by dashed lines in Figure 5.10b) to shift compared to the monodisperse case (indicated by a black dashed line). How much the diffusion constant is underestimated depends

on the size polydispersity. We intentionally chose large polydispersities to show the effect clearly. Note that at for a size polydispersity of 5 % the distribution of diffusion constants still looks rather symmetric.

The average diffusion constant of the particle ensemble is

$$\bar{D} = \int_{D=-\infty}^{D=\infty} D\, g(D)\, dD. \tag{5.10}$$

The integral in Equation 5.10 cannot be solved analytically, but we solved it numerically and compared it to the diffusion constant corresponding to particles with an average size $D_{\bar{a}}$. As integration limits we used 0 and $100 \times D_{\bar{a}}$ in order to probe all nonzero elements of the distribution function. We found that a 5 % polydispersity results in an underestimation of the diffusion constant by only 0.25 %. To underestimate the diffusion constant by 3 %, the relative polydispersity needs to be at least 17 %. We found that these results are independent of the particle size. This finding indicates that the measured 3 % increase of flexible trimers compared to rigid trimers cannot be due to size polydispersity alone, because the employed particles have a size polydispersity of only 2.6 %.

While polydispersity does not drastically alter the collective diffusion of microparticle suspensions, where σ' is typically around 5 %, it could play a large role in the diffusion of nanoparticles, where a σ' on the order of 100 % is not uncommon.[280] For example, gold nanoparticles with relative polydispersities on order of 10 % are considered very monodisperse and can only be made in a small parameter range.[281] Using Equation 5.10 we predict that the collective diffusion constant of a sample with 100 % polydispersity is 63 % larger than a monodisperse sample with the same average size, highlighting the importance of considering this effect in nanoparticle suspensions.

Flexibility-induced relaxation effects

The last way in which flexibility affects the diffusivity of a cluster is through the timescales on which effects of the initial cluster shape and orientation on the diffusive motions vanish. For rigid elongated particles it was shown that the timescale on which translational diffusivity in the x- and y-directions become equal with respect to the lab frame is set by the rotational diffusion time $\gamma_r = (D[\alpha\alpha])^{-1}$, with $D[\alpha\alpha]$ in rad^2/s.[91] To study this effect for our rigid and freely-jointed trimers, we analyze the motion of the clusters by defining the lab frame in such a way that the center of mass of the trimer at lag time $\tau = 0$ is at the origin and the body-centered x- and y-axes coincide with the original lab frame (see Figure 5.1c), an approach inspired by earlier works on rigid anisotropic particles.[97] Using the values for the short time rotational diffusion coefficients for compact and extended trimers, we find that for both rigid and flexible trimers $30\,\text{s} \leq \gamma_r \leq 60\,\text{s}$. Indeed, by looking at the translational (Figure 5.9b) diffusivity of rigid trimers, we see that the effect of shape on the diffusivity is preserved up to the maximum lag time we consider (10 s). The rotational

diffusivity (Figure 5.9d) of the rigid trimers stays constant within error (up to at least 10 s).

However, for flexible trimers, the story is different. There exists a second timescale that can average out orientation-dependent effects in diffusion: the timescale of shape changes, which we define as $\gamma_s = (D[\theta\theta])^{-1}$, analogous to the definition of the rotational diffusion time. Using the values for the short time flexibility coefficients for compact and extended trimers, we find that for our flexible trimers $8\,\mathrm{s} \leq \gamma_s \leq 35\,\mathrm{s}$. Therefore, we hypothesize that for flexible trimers, internal deformations lead to faster relaxation of the shape-dependency we observe at short lag times and therefore also the relaxation of differences between translational diffusion in the x- and y-directions.

Consistent with our hypothesis, the effect of the initial opening angle appears to be lost on a shorter timescale than what one would expect from the rotational diffusion time. In Figure 5.9d, the rotational diffusivity of flexible trimers is not constant in time, as is the case for rigid trimers, which shows that shape changes affect the diffusivity at longer lag times. The same effect can be seen in Figure 5.11b, where the cluster flexibility of compact and extended clusters become equal after about a second. Therefore, for lag times longer than 0.5 s, we only consider the shape-averaged diffusivities. As can be seen from the translational diffusivity (Figure 5.9b), the shape-averaged diffusivity in x and y become equal after 1 s to 3 s and this is also the timescale on which the rotational diffusivity is no longer constant (Figure 5.9d) and the translation-rotation coupling vanishes (Figure 5.9f). Moreover, we observe for both translational, rotational and translation-rotation coupled diffusion that after lag times larger than 2 s, larger fluctuations occur which we attribute to the effect of continuous shape changes (see Figure 5.9b, d and f).

Short timescale relaxation of differences between clusters in extended and compact conformations exist also for the conformational diffusion tensor elements. The flexibility (shown in Figure 5.11a, b) is smaller for trimers in bent conformations than in extended conformations and the difference vanishes after approximately 2 s due to shape changes. Figure 5.11b shows an overall decrease of flexibility with lag time, because the range wherein the joint angle can vary is bounded by the two outermost particles. Furthermore, the magnitude of $D[y\theta]$ (shown in Figure 5.11c, d), which represents the Brownian quasiscallop mode, vanishes on the same timescale of approximately 2 s, set by the conformational relaxation time $8\,\mathrm{s} \leq \gamma_s \leq 35\,\mathrm{s}$.

5.4 Conclusions

In conclusion, we studied the Brownian motion of flexible trimers and found features that are unique to flexible objects. We found a hydrodynamic coupling between conformational changes and translations perpendicular to the particle's long axis (y-direction), which we call the Brownian quasiscallop mode because of its resemblance to scallop propulsion at high Reynolds numbers. We found that this coupling persists over several seconds, a timescale relevant for biomolecular interactions, implying that it might affect the association of flexible proteins and other biomolecules. Secondly, we

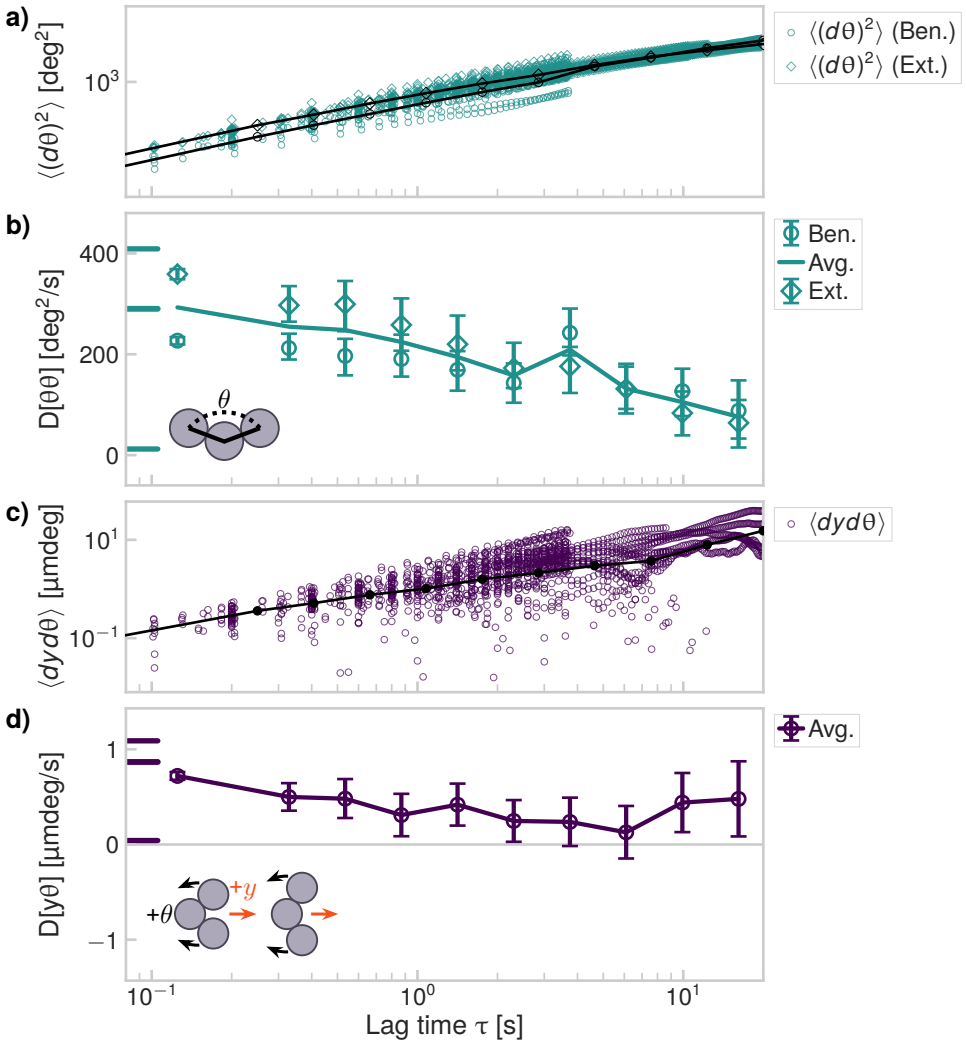

Figure 5.11: **Cluster flexibility and Brownian quasiscallop mode as function of time. a)** Mean squared angular displacements of θ for all flexible trimers. **b)** The flexibility decreases as function of lag time because of hard-sphere repulsion between the two outer particles. **c)** Mean squared coupled displacements of y and θ for all flexible trimers. **d)** The Brownian quasiscallop mode relaxes on a timescale of a few seconds because of conformational and rotational diffusion. In panels a and b, bent configurations (Ben.) correspond to $\overline{\theta} < 120°$ and extended configurations (Ext.) to $\overline{\theta} \geq 120°$. In panels a and c, colored points are experimental data, black points and lines represent the fitted slopes. In panels b and d, numerical short time diffusivities calculated based on Harvey et al.[107] are indicated by colored ticks on the y-axis, showing minimum, mean, and maximum shape-dependent values from bottom to top.

found that the long-time translational diffusion of the freely-jointed trimers was three to fifteen per cent higher than that of their rigid counterparts. This enhancement was predicted for hinged rods,[256–258] but contrasts with theoretical results on dumbbells of two hydrodynamically-coupled subunits, in which extensile shape fluctuations were shown to decrease the translational diffusion coefficient.[104,155] Further theoretical and experimental studies are needed to predict the effect of flexibility on diffusivity, since different internal degrees of freedom can have opposing effects. Finally, we showed that the transition from short- to long-time diffusion depends not (only) on the rotational diffusion time but mainly on a timescale related to conformational changes of the particle. We were able to describe our experimental findings using a hydrodynamic modeling procedure that combines bead-shell modeling with the approach of Harvey and coworkers.[107] We hope this work inspires other researchers to more confidently apply this method in the context of the diffusion of segmentally flexible systems such as biopolymers and proteins.

Acknowledgments

This chapter is based on the following publication:

Flexibility-induced effects in the Brownian motion of colloidal trimers.
R.W. Verweij*, P.G. Moerman*, N.E.G. Ligthart, L.P.P. Huijnen, J. Groenewold, W.K. Kegel, A. van Blaaderen and D.J. Kraft
Phys. Rev. Research, 2, 033136 (2020). doi:10.1103/PhysRevResearch.2.033136

This project has received funding from the European Research Council (ERC) under the European Union's Horizon 2020 research and innovation program (grant agreement no. 758383) and from the NWO graduate programme.

*These authors contributed equally.

6 Conformations and diffusion of flexibly-linked colloidal chains

For biologically relevant macromolecules such as intrinsically disordered proteins, internal degrees of freedom that allow for shape changes have a large influence on both the motion and function of the compound. A detailed understanding of the effect of flexibility is needed in order to explain their behavior. Here, we study a model system of freely-jointed chains of three to six colloidal spheres, using both simulations and experiments. We find that in spite of their short lengths, their conformational statistics are well described by two-dimensional Flory theory, while their average translational and rotational diffusivity follow the Kirkwood-Riseman scaling. Their maximum flexibility does not depend on the length of the chain, but is determined by the near-wall in-plane translational diffusion coefficient of an individual sphere. Furthermore, we uncover shape-dependent effects in the short-time diffusivity of colloidal tetramer chains, as well as nonzero couplings between the different diffusive modes. Our findings may have implications for understanding both the diffusive behavior and the most likely conformations of macromolecular systems in biology and industry, such as proteins, polymers, single-stranded DNA and other chain-like molecules.

6.1 Introduction

For biologically relevant (macro)molecules, internal degrees of freedom that allow for shape changes have a large influence on both the motion and function of the compound.[100–104] Examples of flexible systems found in nature include bio-polymers such as DNA and transfer RNA,[251] antibodies[101,103,253,254] and intrinsically disordered proteins (IDPs).[252,282] IDPs in particular display large shape changes, due to unstructured (and therefore flexible) regions of small hydrophilic units that typically function as linkers between more structured domains. These are involved in important cellular processes such as signaling and transcription. Additionally, they are often involved in disease-related gene truncations or translocations. The coupled binding and folding of these flexible regions lead to a large number of possible interactions within the same set of proteins.[282] Even for more rigid proteins, shape changes can be an important factor, for example in protein breathing, that involves slow collective movements of larger secondary structures.[283] Therefore, quantitative knowledge of structural flexibility is necessary to understand the transport properties and function of flexible biopolymers and proteins.[261]

Measuring molecular shape changes calls for single-molecule techniques with a simultaneously high spatial and temporal resolution. As a simpler alternative, colloidal particles have been widely used as model systems for (macro)molecular structures since the early 20th century,[18,19,284] because of their unique combination of microscopic size and sensitivity to thermal fluctuations. Although colloidal particles are frequently used as model systems, the study of colloidal particles is interesting in its own right, as colloids can in principle form the building blocks of materials with novel properties, such as photonic bandgap materials.[2] Colloidal structures of reconfigurable shape are expected to aid in the assembly of these structures, because they allow the formed materials to quickly relax towards their thermodynamic equilibrium configuration, thereby mitigating "hit-and-stick" equilibration issues.[77,196] In addition, they could provide ways to build switchable materials.[285]

While the Brownian motion of rigid colloids of various shapes has been extensively studied, for example for ellipsoids,[91,95,96] boomerangs,[14,97,98] and clusters,[12,13] most compounds found in nature show some degree of flexibility, which may affect their transport properties. It was proposed to calculate their diffusive properties in an approximate way, by treating the structure as an (instantaneously) rigid body and take the ensemble average of all possible 'snapshots' of conformations, the so called rigid body approximation.[101,264,286,287] However, the accuracy of this approximation is as of yet unclear: importantly, deviations between this approximation and the real transport properties can become larger as function of the flexibility of the molecule.[288]

Recently, we have studied both numerically and experimentally the effect of segmental flexibility[244] in a simple model system consisting of a freely-jointed chain of three spherical colloidal particles, also called trimers or trumbbells.[107,262] This was made possible for the first time thanks to the development of colloidal structures with freely-jointed bonds.[110] Similar to rigid particles, we found that shape affects the diffusive motion of the colloid at short timescales and that displacements are larger in directions that correspond to smaller hydrodynamic drag. By comparing our flexible trimers to rigid ones, we found that the flexibility of the trimers led to a higher translational diffusion coefficient. Furthermore, we uncovered a Brownian quasiscallop mode, where diffusive motion is coupled to Brownian shape changes. At longer timescales, in addition to the rotational diffusion time, an analogous conformational diffusion time governs the relaxation of the diffusive motion, unique to flexible assemblies.[244] These effects taken together show that the rigid body approximation is not sufficient to model the rich behavior of flexible objects. However, in the case of long polymer chains, Kirkwood-Riseman theory,[286] which is based on the rigid body approximation, is able to at least describe equilibrium properties such as the average translational diffusion coefficient.[289] This is attractive because, if accurate, it would provide a simple and quick way to calculate the equilibrium long time diffusion coefficients typically measured in light scattering experiments.

Here, we study flexible chains of three to six particles using both experiments and simulations. Conceptually, the longer chains most resemble a flexible polymer, modeled by beads on a chain, while the shorter chains are expected to show devi-

ations from predictions based on polymer theory. We set out to test to what extent the conformations of our bead chains can be described by polymer theory and to what extent their equilibrium diffusivity can be described by simple scalings such as the Kirkwood-Riseman model. First, we analyze their conformational free energy in several different ways and compare our findings to two-dimensional Flory theory. Then, we study the shape-dependent short-time diffusivity of the trimer and tetramer chains and calculate the full diffusion tensor as function of instantaneous shape. By also determining the shape-averaged translational diffusivity, rotational diffusivity and flexibility for chains of three to six spheres, we show how these scale as function of chain length. Overall, we find a good agreement between the experimental measurement and the simulations, except for translational diffusivity. In that case, we hypothesize that the difference in surface slip in the experiments, where the substrate has a finite slip length due to the hydrogel surface, and simulations, where we use a no-slip boundary condition, lead to the higher translational diffusivity in the experiments. We hope our work aids the study of diffusivity of flexible objects found in complex mixtures relevant in, for example, the cosmetic, pharmaceutical and food industries, as well as in biological systems. Our findings may have implications for understanding both the diffusive behavior and the most likely conformations of macromolecular systems in biology and industry, such as polymers, single-stranded DNA and other chain-like molecules.

6.2 Materials and Methods

6.2.1 Experimental

Flexible chains of colloid-supported lipid bilayers (CSLBs) were prepared as described in previous work,[85,110,112,242] specifically, we followed the exact same procedure as in Chapter 5[244] and used silica particles of two different radii to test the generality of our findings. We now briefly summarize the experimental procedure from Chapter 5.[244]

The CSLBs consisting of $(2.12 \pm 0.06)\,\mu m$ silica particles were prepared as described in our recent works.[242,244] Briefly, the particles were coated with a fluid lipid bilayer by deposition and rupture of small unilamellar vesicles consisting of 98.8 mol % of the phospholipid DOPC ((Δ9-Cis)-1,2-dioleoyl-sn-glycero-3-phosphocholine), 1 mol % of the lipopolymer DOPE-PEG(2000) (1,2-dioleoyl-sn-glycero-3-phosphoethanolamine-N-[methoxy(polyethylene glycol)-2000]) and 0.2 mol % of the fluorescently-labeled lipids TopFluor-Cholesterol (3-(dipyrromethene boron difluoride)-24-norcholesterol) or DOPE-Rhodamine (1,2-dioleoyl-sn-glycero-3-phosphoethanolamine-N-(lissaminerhodamine B sulfonyl)). The bilayer coating was performed in a buffer at pH 7.4 containing 50 mM sodium chloride (NaCl) and 10 mM 4-(2-Hydroxyethyl)-1-piperazineethanesulfonic acid (HEPES). We added double-stranded DNA (of respectively strands DS-H-A and DS-H-B, see Table A.1) with an 11 base pair long sticky end and a double stearyl anchor, which inserts itself into the bilayer via hydrophobic interactions (see Figure 6.1a, left panel). The sticky

end of strand DS-H-A is complementary to the sticky end of strand DS-H-B, which allows them to act as linkers. Self-assembly experiments were performed in a different buffer of pH 7.4, containing 200 mM NaCl and 10 mM HEPES. Chains of 2.12 μm CSLBs were formed by self-assembly in a sample holder made of polyacrylamide (PAA) coated cover glass.[244] Confocal microscopy images of the coated particles are shown in Figure 6.2a, for chain lengths of $n = 3$ to 6 particles.

Additionally, we analyzed chains of (1.93 ± 0.05) μm CSLBs, with silica particles purchased from Microparticles GmbH (product code SiO_2−R-B1072). We followed the same protocol with two minor modifications: first, the lipid composition was 91.2 mol % DOPC, 8.7 mol % DOPE-PEG(2000) and 0.1 mol % DOPE-Fluorescein. Second, we added double-stranded DNA with a self-complementary 12 base pair sticky end (i.e. a palindromic sequence) and a cholesterol anchor that inserts itself into the lipid bilayer due to hydrophobic interactions (see Table A.1, strands PA-A and PA-B). To image the 1.93 μm CSLBs we used a flow cell coated with poly(2-hydroxyethyl acrylate) (pHEA) polymers.[244] Self-assembly experiments were performed in a buffer of pH 7.4, containing 50 mM NaCl and 10 mM HEPES.

6.2.2 Microscopy

Chains were imaged for at least 5 min (frame rates between 5 and 19 fps) at room temperature using an inverted confocal microscope (Nikon Eclipse Ti-E) equipped with a Nikon A1R confocal scanhead with galvano and resonant scanning mirrors. A 60× water immersion objective (NA=1.2) was used. 488 and 561 nm lasers were used to excite, respectively, the Fluorescein or TopFluor and Rhodamine dyes. Laser emission passed through a quarter wave plate to avoid polarization of the dyes and the emitted light was separated by using $500 - 550$ nm and $565 - 625$ nm filters.

To complement the data obtained from self-assembled chains, we used optical tweezers to assemble specific chain lengths. Briefly, we employed a homemade optical setup consisting of a highly focused trapping laser manufactured by Laser QUANTUM (1064 nm wavelength). The laser beam entered the confocal microscope through the fluorescent port, after first passing through a beam expander and a near-infrared shortpass filter. The same objective was used for imaging and to focus the trapping laser beam. During the trapping, the quarter wave plate was removed from the light path.

Particle positions were tracked using a custom algorithm[242] available in TrackPy by using the `locate_brightfield_ring` function[188] or using a least-square fit of a Mie scattering based model implemented in HoloPy.[186] Both methods agree to an accuracy of at least 1 px, however we have found that the Mie scattering based model is more robust for tracking multiple particles in close proximity to each other. For all analysis, we only selected clusters that showed all bond angles during the measurement time, experienced no drift and were not stuck to the substrate. An overview of the total number of measurements, the total duration and the total number of frames per chain length is shown in Table 6.1.

Table 6.1: Overview of the amount of measurements, the total duration and the total number of frames per chain length, for the experimental and simulated data.

n	**Measurements**		**Total length [min]**		**Total frames**	
	Exp.	Sim.	Exp.	Sim.	Exp.	Sim.
3	30	30	275	900	9.3×10^4	3.8×10^7
4	69	50	305	1500	2.5×10^5	6.4×10^7
5	13	20	75	600	4.7×10^4	2.5×10^7
6	5	20	41	600	4.1×10^4	2.5×10^7

Table 6.2: **Permutation data.** For all chain lengths n, we generated the $P(N_\theta, n-2)$ configurations obtained by permuting all possible combinations of opening angles. Interpenetrating configurations, which are forbidden due to short-range repulsive forces between particles, were removed from this permutation data and the percentages of these configurations relative to the total number of configurations between 60 and 300 deg, as well as between 0 and 360 deg (fully freely-jointed case) are shown.

n	$\delta\theta$ [deg]	$P(N_\theta, n-2)$	**Interpen. [%]** (60-300 deg)	**Interpen. [%]** (0-360 deg)
3	0.01	2.4×10^4	0	33.3
4	0.04	3.6×10^7	6.3	58.3
5	0.50	1.1×10^8	14.0	74.5
6	2.00	2.0×10^8	21.9	84.7

6.2.3 Simulations

We have performed Brownian dynamics simulations with hydrodynamic interactions following the method outlined in Sprinkle et al. [290] using the open-source RigidMultiblobsWall package.[291] Hydrodynamic interactions are calculated using the Stokes equations with no-slip boundary conditions. The hydrodynamic mobility matrix is approximated using the Rotne-Prager-Blake (RPB) tensor,[35] which is a modified form of the Rotne-Prager-Yamakawa (RPY) tensor[34,275,292] and accounts for a bottom wall, which is unbounded in the transverse directions. These corrections to the RPY tensor are combined with the overlap corrections described in Wajnryb et al. [292] to prevent particle-particle and particle-wall overlap. The RPB mobility inaccurately describes near-field hydrodynamic interactions and therefore breaks down for small separation distances. This can be overcome by adding a local pairwise lubrication correction to the RPB resistance matrix as described in detail in Sprinkle et al. [290] Based on the full lubrication-corrected hydrodynamic mobility matrix, the Ito overdamped Langevin equation is solved to describe the effect of thermal fluctuations.

We include a gravitational force on the particles to confine them to diffuse close to the bottom wall, as in the experiments. Inter-particle bonds are modeled by harmonic springs of stiffness $1000 k_B T/R^2$ and equilibrium length $2R$, where $R = 1.06\,\mu\text{m}$ is the particle radius. The bond angle is not restricted. We set the temperature $T = 298\,\text{K}$, the viscosity of the fluid $\eta = 8.9 \times 10^{-4}\,\text{Pa s}$, the gravitational acceleration $g = 9.81\,\text{m s}^{-2}$, the particle mass $m_p = 9.5 \times 10^{-15}\,\text{kg}$ (by assuming a particle density of $1900\,\text{kg m}^{-3}$) and the simulation timestep $\Delta t = 1.42\,\text{ms}$. For the firm potential that prevents overlap, we use a strength of $4 k_B T$ and a cutoff distance $\delta_{\text{cut}} = 10^{-2}$.[290,293] We initialized the particle chains in a linear configuration (all opening angles 180°). Then, these initial configurations were randomized by running the integration for a simulated time of 60 s prior to saving the configurations, to ensure a proper equilibration of the particle positions, bond lengths, velocities and opening angles. The particle positions were saved every 8 simulation steps to obtain a final framerate of approximately 90 fps. An overview of the total number of simulations, the total duration and the total number of saved frames per chain length is shown in Table 6.1.

For comparison to the simulated and experimental data, we generated data in which the chains are completely non-interacting and freely-jointed up to steric exclusions in the following manner: we generated all $(n-2)$-permutations of the N_θ opening angles θ_i, which gives a total number of $P(N_\theta, n-2) = N_\theta!/(N_\theta - (n-2))!$ combinations of θ_i. Here, the number of opening angles is $N_\theta = (360 - 2 \times 60)/(\delta\theta)$, where $\delta\theta$ denotes the bin width. Then, we removed those combinations that are forbidden because of steric exclusions between particles, resulting in the final allowed combinations, which we call "permutation data". In Table 6.2, we show the bin widths $\delta\theta$ for each n, as well as the total number of generated permutations $P(N_\theta, n-2)$. The percentage of permutations that was removed due to steric exclusions is shown, as well as the total number of configurations that would result in interpenetrating particles for the completely freely-jointed case, where θ can vary between 0 and 360 deg.

6.2.4 Data analysis

For all fits reported in this work, used a Bayesian method to find an estimate of the posterior probability distribution, by using an Affine Invariant Markov chain Monte Carlo (MCMC) Ensemble sampler method as implemented in the Python packages `lmfit`[246] and `emcee`.[207] This allowed us to obtain accurate estimates of the error and the maximum likelihood estimate (MLE) of the parameters. Parameter values were initialized using a standard least-square fit, appropriate bounds on the parameter values were implemented as priors. We estimated the autocorrelation time τ_{acor} of the MCMC chain using the built-in methods and ran the analysis for at least $100\tau_{\text{acor}}$ steps, where we discarded the first $2\tau_{\text{acor}}$ steps (corresponding to a burnin phase) and subsequently used every other $\tau_{\text{acor}}/2$ steps (known as thinning). We used 500 independent chains (or walkers). The reported values correspond to the maximum likelihood estimate of the resulting MCMC chains, the reported uncertainties correspond to the 16$^{\text{th}}$ and 84$^{\text{th}}$ percentiles of the obtained posterior probability distribution.

6.2.5 Diffusion tensor analysis

Definition of the diffusion tensor

We determined the short-time diffusivity of the clusters, both as function of their instantaneous shape, as well as averaged over all possible configurations. Because the chains are sedimented to the bottom substrate, we consider only the quasi-2D, in-plane diffusivity. For the flexible trimers, we followed the methods outlined in Chapter 5.[244] For the flexible tetramer chains, we calculated a 5×5 diffusion tensor, where the four degrees of freedom correspond to translational diffusivity in x and y, rotational diffusivity and the flexibilities of the tetramer, which are described by the diffusivities of the opening angles θ_1, θ_2. Specifically, the x- and y-directions are schematically shown for one configuration in Figure 6.1b and defined by Equation 6.4. The rotation angle used for determining the rotational diffusivity is indicated in Figure 6.1b and is the angle of the $x(\tau)$ relative to $x(\tau = 0)$, i.e. the angle of the body-centered x-axis of the current frame relative to the body-centered x-axis of the reference frame at $\tau = 0$. The flexibilities are calculated from the mean-squared displacements of the opening angles θ_1, θ_2, which are depicted in Figure 6.1b. θ_1 is defined in such a way that it is always less than or equal to 180 deg and this defines how we assign the magnitude of θ_2, specifically, whether it is acute or obtuse.

The diffusion tensor elements of the tetramer chains were determined analogously to the trimers.[244] Briefly, for each pair of frames, we determined the initial shape of the chain, which is determined by θ_1, θ_2. The short time diffusion tensor is then calculated from the trajectories in the following way:

$$\boldsymbol{D}[ij](\theta_1, \theta_2) \equiv \frac{1}{2} \frac{\partial \langle \Delta i(\theta_1, \theta_2) \Delta j(\theta_1, \theta_2) \rangle_\tau}{\partial \tau}, \tag{6.1}$$

with τ the lag time between frames, $\langle \cdots \rangle_\tau$ denotes a time average over all pairs of frames τ apart and $\Delta i(\theta_1, \theta_2) = i(\theta_1, \theta_2, t + \tau) - i(\theta_1, \theta_2, t)$ is the displacement of the i-th diffusion tensor element, which depends on the instantaneous shape given by θ_1, θ_2. The average diffusion tensor elements $\boldsymbol{D}[ij]$ were obtained by fitting the overall slope of the mean (squared) displacements as a function of lag time τ. We considered lag times up to 0.17 s, given by the frame rate of the experimental data. We only considered trajectories where the variation in θ_1, θ_2 did not exceed the edges of the bin describing the initial shape. Then, we calculated the diffusion tensor elements separately for each initial shape. For fitting the slopes, we used a MCMC sampling method described in Section 6.2.4, where we used a linear model without an offset. For longer chains, we only considered the shape-averaged, quasi-2D translational diffusion coefficient D_T, which corresponds to in-plane diffusivity above the wall. Additionally, we determined the rotational diffusion coefficient $D[\alpha\alpha]$ from the mean squared angular displacement of the x-axis (defined in Equation 6.4, see Figure 6.1b for a schematic depiction), which describes the rotational diffusivity around an axis perpendicular to the substrate. Finally, we determine the overall cluster flexibility $D[\boldsymbol{\theta\theta}]$ by calculating the mean squared displacements of the $(n-2)$ opening angles

θ_i as follows:

$$\langle |\Delta\boldsymbol{\theta}|^2 \rangle = \langle |(\Delta\theta_1, \ldots, \Delta\theta_{n-2})|^2 \rangle, \tag{6.2}$$

so that the flexibility $D[\boldsymbol{\theta}\boldsymbol{\theta}]$ is given by

$$\langle |\Delta\boldsymbol{\theta}|^2 \rangle = 2(n-2)D[\boldsymbol{\theta}\boldsymbol{\theta}]t, \tag{6.3}$$

analogously to the other diffusion tensor elements.

The influence of the tracking point

As tracking point, we considered the center of mass (c.m.) and the center of diffusion (c.d.), because the choice of origin is expected to affect the magnitude of the diffusion tensor.[105,269] The c.d. was calculated from $\boldsymbol{A}_{ij}$ defined by Equation 2.16 of Cichocki et al.[269] using the RPB tensor[35] with lubrication corrections as the inter-particle mobility matrix $\boldsymbol{\mu}_{ij}$. This tensor includes wall corrections, as discussed previously in Section 6.2.3. The c.d. was determined from the simulated particle positions, because the height above the bottom wall was not measured experimentally, but is needed to calculate the wall corrections. The direction of the body-centered x- and y-axes was determined as function of the tracking point $\boldsymbol{r}_{t.p.}$, which defines the origin of the body-centered coordinate frame. We define $\boldsymbol{r}_{t.p.} = \rho_1\boldsymbol{r}_1 + \rho_2\boldsymbol{r}_2 + \cdots + \rho_n\boldsymbol{r}_n$, which defines the location of the tracking point as a linear combination of the particle positions (Equation 2.2 and 2.3 of Cichocki et al.[269]). $\boldsymbol{\rho} = (\rho_1, \rho_2, \ldots, \rho_n)$ is a weight vector which determines how much weight is accorded to each particle in the calculation of the tracking point $\boldsymbol{r}_{t.p.}$. As an example, for a trimer, $\boldsymbol{\rho} = (1/n = 1/3, 1/3, 1/3)$ when the tracking point is chosen to be the center of mass.

The direction of the x-axis was chosen as

$$\hat{\boldsymbol{x}} = \pm \left[\frac{\boldsymbol{r}_{t.p.,1} + \cdots + \boldsymbol{r}_{t.p.,s_1}}{\rho_1 + \cdots + \rho_{s_1}} - \frac{\boldsymbol{r}_{t.p.,s_2} + \cdots + \boldsymbol{r}_{t.p.,n}}{\rho_{s_2} + \cdots + \rho_n} \right], \tag{6.4}$$

where $\boldsymbol{r}_{t.p.,i}$ is the i-th coordinate of the tracking point and the bead chain is split into two parts with equal numbers of particles according to

$$\begin{cases} s_1 = s_2 = \lceil \frac{n}{2} \rceil & \text{for odd } n \\ s_1 = \lceil \frac{n}{2} \rceil, s_2 = s_1 + 1 & \text{for even } n \end{cases} \tag{6.5}$$

Note that for a trimer, with the tracking point at the c.m. (i.e. $\boldsymbol{\rho} = (1/3, 1/3, 1/3)$), $\hat{\boldsymbol{x}}$ is parallel to the end-to-end vector, which is the same definition as in our previous work.[244] $\hat{\boldsymbol{y}}$ is then chosen such that $\hat{\boldsymbol{x}}$ and $\hat{\boldsymbol{y}}$ form a right-handed coordinate system, where the direction of $\hat{\boldsymbol{y}}$ is chosen to point away from the central part of the cluster towards the tracking point, i.e. along $\boldsymbol{r}_{t.p.} - \left(\boldsymbol{r}_{s_1} + \boldsymbol{r}_{s_2}\right)/2$. This orientation was determined for every frame, which fixed the orientation of the body-centered coordinate system $\boldsymbol{x}(\tau = 0), \boldsymbol{y}(\tau = 0)$. For subsequent lag times, the direction of $\boldsymbol{y}(\tau)$ was chosen such that $\boldsymbol{y}(\tau = 0) \cdot \boldsymbol{y}(\tau) > 0$, i.e. the direction of $\boldsymbol{y}$ does not change sign. The resulting coordinate system relative to the c.d. is visualized for the tetramer chains in Figure 6.1b and c.

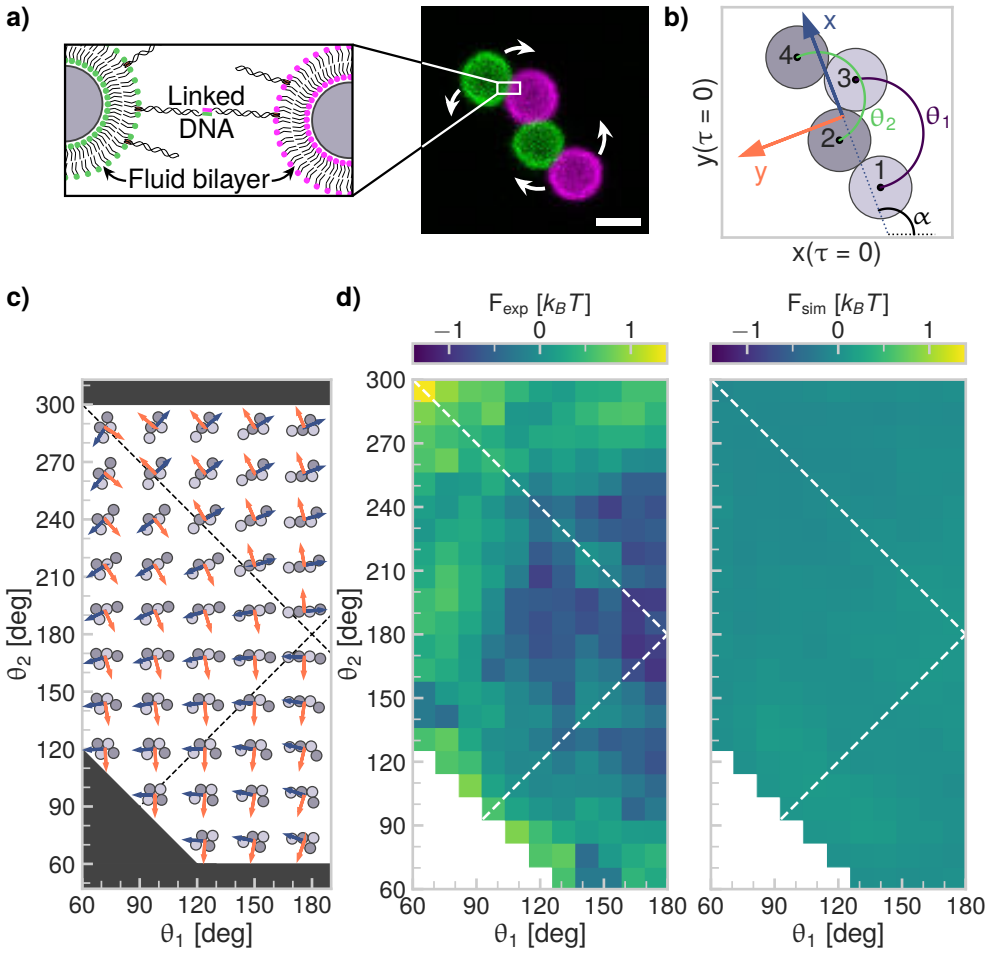

Figure 6.1: **Flexibly linked colloidal tetramers. a)** Flexibly linked colloidal chains are created from DNA functionalized colloid-supported lipid bilayers (CSLBs). The particles are bound by the DNA linkers, which can diffuse in the fluid lipid bilayer, yielding reconfigurable assemblies. Right: Confocal image of a tetramer chain, where the different colors, stemming from fluorescently labeled lipids, indicate the two different particle types that are functionalized with complementary DNA linkers. Scalebar is 2 µm. **b)** The coordinate system used for quantifying the diffusion of tetramer chains, relative to the center of diffusion (see Section 6.2.5). **c)** Schematics of possible configurations for the tetramer, as function of the two opening angles θ_1, θ_2. Some configurations are sterically prohibited because the particles cannot interpenetrate (as indicated by the dark grey area). The dashed lines indicate the two symmetry axes of the opening angles, $\theta_2 = \theta_1$ and $\theta_2 = 360\,\text{deg} - \theta_1$. **d)** The free energy of both experimental (left) and simulated (right) chains of four particles in terms of θ_1, θ_2.

6.3 Results and Discussion

6.3.1 Conformations of flexible chains

Shape as function of the trimer segments

Does a diffusing flexible chain of micron-sized spherical particles have preferred configurations? This is a natural question to ask, because increasing the number of spheres per chain increases the percentage of overlapping configurations (see Table 6.2) and could potentially change the hydrodynamic interactions. We answer this question by considering the free energy of such chains, which were made by the assembly of colloid-supported lipid bilayers (CSLBs).[85,110,112,242,244] These particles are bonded by DNA linkers, which provide specific bonds between the particles. Because the linkers can diffuse in the fluid lipid bilayer, the bonded particles can move with respect to each other (see Figure 6.1a for a schematic). We compared our experimental data to Brownian dynamics simulation data, where hydrodynamic interactions between particles and the substrate are taken into account via the Rotne-Prager-Blake (RPB) tensor,[35] overlap corrections[292] and a local pairwise lubrication correction[290] (see Section 6.2.3 for details).

We analyzed the free energy of clusters of $n = 3$ to 6 particles as function of their conformation using different methods. For a chain of three particles, a trimer, a single parameter, the opening angle θ, can describe the conformations.[244] We have shown before that flexible trimers do not show a preference for any given opening angle and therefore conformation.[242,244] For a chain of four of such particles (see Figure 6.1a for a microscopy image), there are two angles that characterize the shape of the cluster, θ_1 and θ_2, which are the opening angles of the two "trimer segments" (groups of three adjacent, bonded spheres) that make up the chain. The definition of the opening angles is shown in Figure 6.1b. For the tetramer chains, we obtained a 2D-histogram of opening angles for θ_1, θ_2 between 60° to 300°, using the simulated and experimental data. These two internal degrees of freedom lead to a large number of possible chain configurations, as shown in Figure 6.1c. Some configurations are forbidden because of steric exclusions, as indicated by the grey areas. The symmetry lines of the opening angles $\theta_2 = \theta_1$ and $\theta_2 = 360\,\mathrm{deg} - \theta_1$ are indicated as well. The configurations are symmetric around these lines except for the fact that we break this symmetry by choosing which angle to label as θ_1 and which as θ_2, because this has consequences for the orientation of the body centered coordinate system, as shown in Figure 6.1b and defined in Equation 6.4.

From the probability density function calculated from the histogram, we determined the free energy using Boltzmann weighing,

$$\frac{F}{k_B T} = -\ln p + \frac{F_0}{k_B T}, \tag{6.6}$$

where F is the free energy, k_B is the Boltzmann constant, T is the temperature, p is the probability density and F_0 is an arbitrary constant offset to the free energy that

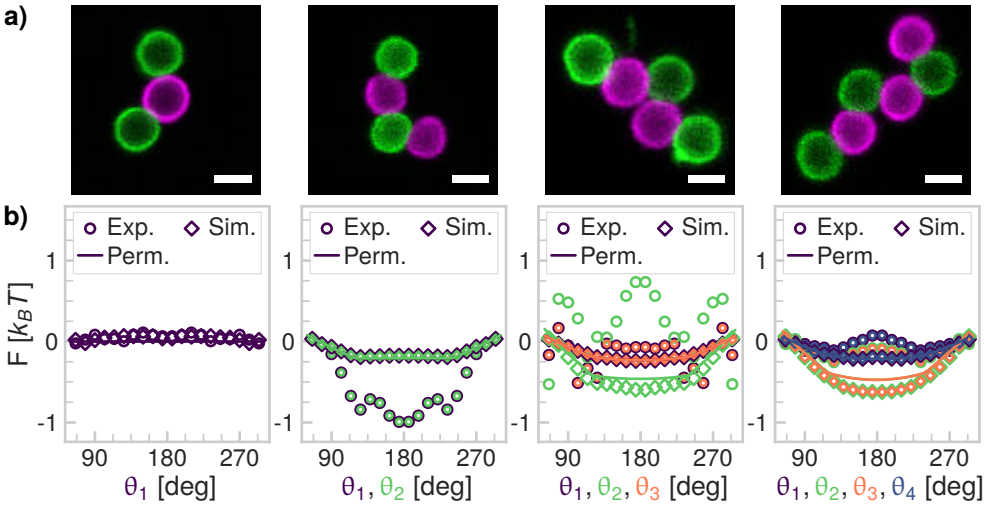

Figure 6.2: **Flexibly-linked colloidal chains. a)** Confocal microscopy images of, left to right, a trimer ($n = 3$), tetramer ($n = 4$), pentamer ($n = 5$) and hexamer ($n = 6$) chain. Scalebars are 2 µm. **b)** The free energy in terms of the opening angles of groups of three particles ("trimer segments"), of, left to right, trimers, tetramers, pentamers and hexamers. The main contribution to the free energy is the configurational entropy of the chains. ∘ Experimental, ⋄ simulated and permutation data (Perm.) are shown, different colors indicate different opening angles.

we have chosen such that the average free energy is equal to zero. Except for steric restrictions and hydrodynamic interactions, we expect inter-particle interactions to be weak. Therefore, we hypothesize that there are mainly entropic contributions to the free energy and that enthalpic contributions are small. The resulting free energy is shown in Figure 6.1d. Like flexible trimers,[242,244] chains of four particles are freely-jointed, as evidenced by the fact that differences in their free energy as function of opening angles θ_1, θ_2 are on the order of $1\,k_BT$ in Figure 6.1d in the experiments and below $0.1\,k_BT$ in the simulations. Differences smaller than or comparable to the thermal energy are difficult to measure experimentally and are of limited physical relevance. Therefore, we conclude that there is no appreciable preference for any given conformation and the tetramer chains are thus freely-jointed. We use the term "freely-jointed" in the sense that the chains are free to move without any preferred state, up to steric exclusions stemming from short-range repulsions between the particles that prevent them from interpenetrating.

Increasing the number of beads in the chain increases the percentage of sterically inaccessible configurations (see Table 6.2) and could potentially alter the hydrodynamic interactions. To answer whether these effects lead to preferred configurations, we study chains consisting of n=3 to 6 particles, as shown in confocal microscopy images in Figure 6.2a. Because visualization as a joined histogram becomes increas-

ingly complex as the chain length increases, we first consider the free energy of their separate $(n-2)$ opening angles, as shown in Figure 6.2b. First, we obtained probability density functions of their $n-2$ opening angles θ_i, where θ_i is the i-th opening angle, as defined in Figure 6.3a, analogously to the choice of opening angles θ_1, θ_2 in Figure 6.1b. In other words, we consider the free energy as function of the opening angles of the trimer segments of the chains. We label the first particle with $i = 1$ and number the rest of the chain consecutively. Because there are two choices for the first particle on either end of the chain, which opening angle is labeled by the first index is not unique. Therefore, we include both choices in our analysis. Additionally, we include both choices of defining θ_1 as either obtuse or acute and then use the same convention for the other opening angles.

Whilst a trimer (n=3) shows no preference for any specific configuration,[242,244] the tetramer chains do show a small preference for straight opening angles, as evidenced by the differences in free energy between compact opening angles and straight opening angles in Figure 6.2b. These deviations are largest in the experimental data, but also present to a lesser degree in the simulation data and the permutation data. The deviations in the simulated and permutation data can only stem from steric exclusions, which cause some configurations to be inaccessible: for a tetramer chain, angles below 60 deg or above 300 deg and combinations where $\theta_1 + \theta_2 < 180$ deg or $\theta_1 + \theta_2 > 540$ deg are not possible due to steric restrictions. Seeing that we have strong indications that the bond angles are freely-jointed up to steric exclusions in the simulated and permutation data, we believe that the larger deviations in the experimental data in Figure 6.1d and Figure 6.2b, compared to the simulation and permutation data, are mostly caused by experimental noise. This can be mitigated by collecting more data, however, the amount of data needed to characterize the free energy in sufficient angular detail is very large (see Table 6.1 for a comparison between the amount of simulated and experimental data). Because the experimental deviations are below the thermal energy, we conclude that also in the experiments, there is no preference for any of the sterically allowed configurations.

For the free energy of the pentamer chains in Figure 6.2b, we observe some larger deviations of the experimental data compared to the permutation and simulated data. Specifically, the central angle seems to show a preference for closed angles, as evidenced by the lower free energy for $\theta_2 = 60$ deg and 300 deg. However, the difference between the compact angles and the stretched angles is small, i.e. less than $1.5\,k_BT$. Considering the free energy of the hexamer chains, we observe that the distribution of the outer opening angles θ_1, θ_4 is flatter than the distribution of the inner opening angles θ_2, θ_3, especially in the simulated and permutation data. Interestingly, there is a clear trend in the free energy of flexible chains, going from a flat free energy for $n = 3$ to a free energy that shows a minimum at 180 deg and becomes increasingly smooth as the chain length increases. The location of the minimum and the good agreement with the permutation data show that the deviations from a flat free energy most likely stem from the steric exclusions at compact opening angles.

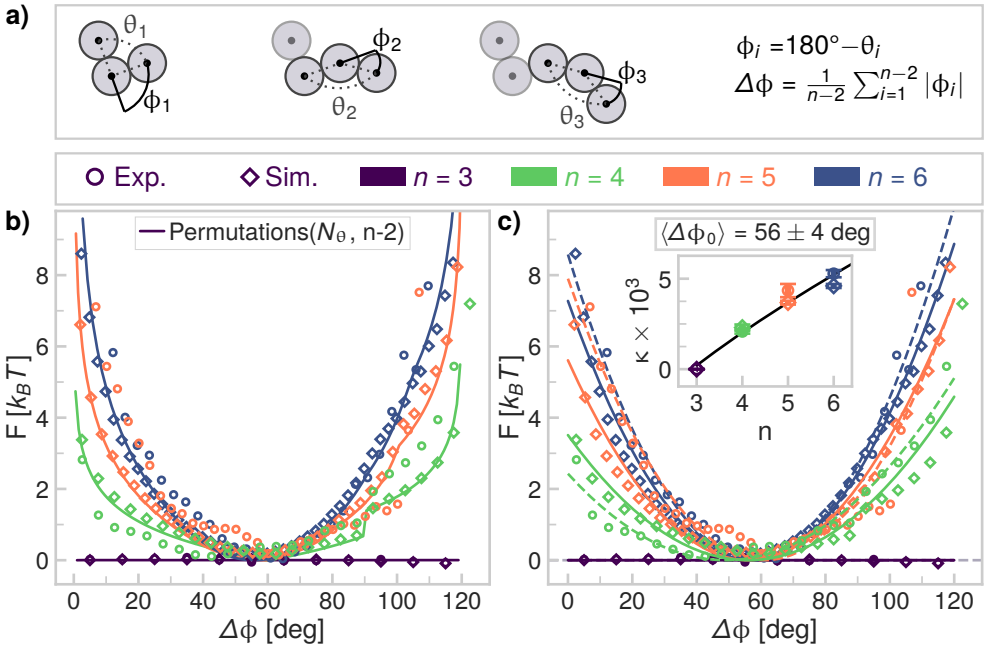

Figure 6.3: **Average bending angle of flexible colloidal chains. a)** Top: we define a quantity $\Delta\phi$ which measures how much the chain shape deviates from a straight line. Bottom: Markers for the ∘ experimental and ⋄ simulated data, together with the color coding legend for the different chain lengths n, as used in panels b and c are shown above those panels. **b)** Comparison between the free energy calculated for experimental, simulated and the $P(N_\theta, n-2)$ permutation data, as function of $\Delta\phi$. **c)** Free energy in terms of $\Delta\phi$ and fit of Equation 6.8 (fit values shown in the insets). Additionally, we fit Equation 6.9 to determine the scaling of κ as function of n, as shown in the inset.

Shape as function of the average bending angle $\Delta\phi$

So far, we have considered the free energy in terms of the individual opening angles or trimer segments. To analyze the overall shapes these colloidal chains can adopt in more detail, we define the average bending angle $\Delta\phi$, as shown schematically in Figure 6.3a. This allows us to study the overall shape of the chains by collapsing the $(n-2)$-dimensional description of the shape in terms of opening angle, onto a single measure of chain shape. We converted all pairs of opening angles to the single average bending angle,

$$\Delta\phi = \frac{1}{n-2}\sum_{i=1}^{n-2}\left|\phi_i\right|, \tag{6.7}$$

as defined in Figure 6.3a. We then obtained the probability density function in terms of $\Delta\phi$ and converted this to a free energy using Equation 6.6, as shown in Figure 6.3b. By taking this approach, we find that as the number of particles n is increased, a preferred average bending angle arises at $\Delta\phi_0 = (56 \pm 4)\,\mathrm{deg}$, close to the average of 60 deg between no bending (0 deg) and maximal bending (120 deg), for the experimental, simulated and permutation data. Additionally, the free energy profiles of all chain lengths show the same shape, where the difference in free energy between the most likely and least likely configurations increases as the chain length increases.

The free energy in terms of $\Delta\phi$ effectively quantifies the average bending angle, or put simply, bending free energy, which is expected to be harmonic based on the worm like chain model.[294] We fitted a harmonic potential V to the resulting free energy of the form

$$V = \frac{\kappa}{2b}\left(\Delta\phi - \Delta\phi_0\right)^2, \tag{6.8}$$

with fit parameters κ the stiffness of the potential well in units of $\mathrm{k_BT/deg^2}$ and $\Delta\phi_0$ the center of the potential well in deg, as shown in Figure 6.3c. We find that the potential well stiffness κ increases as the number of particles increases (see second inset of Figure 6.3c) as predicted by polymer theory.[294] Namely, we fit

$$\kappa = \alpha\frac{b}{4}(n-1)^{\nu} - \kappa_0, \tag{6.9}$$

where $\kappa_0 = (5.1 \pm 0.7) \times 10^{-3}\,\mathrm{k_BT/deg^2}$ fixes the value of κ for $n = 3$ and $\alpha = (13 \pm 1) \times 10^{-3}\,\mathrm{k_BT/deg^2}$ is a positive constant. We added κ_0 to the model described by Wiggins and Nelson[294] to ensure that $\kappa = 0$ for $n = 3$ as we observe from our data. Additionally, we added the scaling parameter α to ensure the proper magnitude of κ. Clearly, for $n = 3$, the chain is freely-jointed and therefore $\kappa = 0$. For larger chains, the probability to observe deviations from a straight configuration decreases as the number of configurations with steric exclusions increases (see Table 6.2), as is evidenced by the agreement between the permutation, the experimental and the simulated data in Figure 6.3b. Therefore, the bending stiffness that we measure is an effective parameter, purely arising from these steric exclusions.

Distribution of the end-to-end distance and radius of gyration: a comparison with polymer theory

We now compare the behavior of our flexibly linked particle chains to predictions from two-dimensional Flory theory for self-avoiding polymers. We are interested in first testing whether our colloidal chains show the same behavior as long polymers in terms of RMS end-to-end distance and radius of gyration, as was shown for chains of flexibly linked oil droplets.[194] Then, we compare the distributions of the end-to-end distance and radius of gyration of the colloidal chains to predictions from polymer theory, to elucidate where finite-size effects start to play a dominant role in the configurational free energy of chain-like molecules. In Figures 6.4–6.5, we have compared

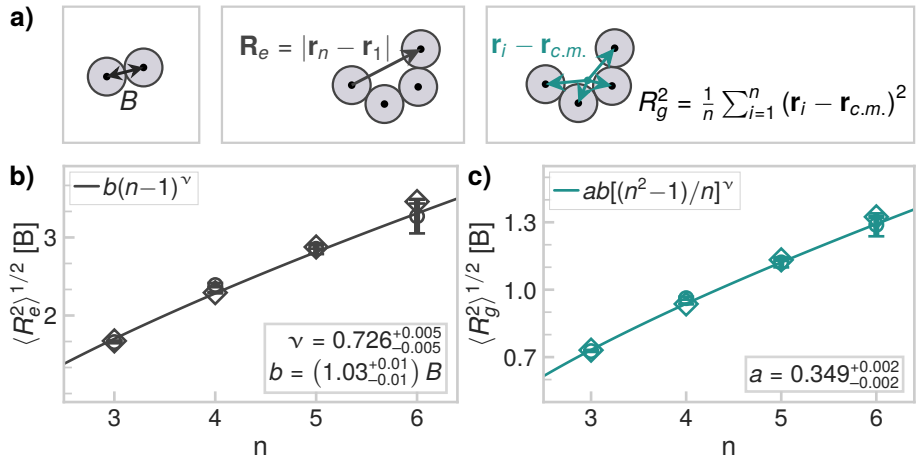

Figure 6.4: **RMS end-to-end distance and radius of gyration of flexible colloidal chains. a)** Left: the bond length B. Center: the end-to-end distance R_e. Right: definition of the radius of gyration R_g. **b)** Average R_e and fit of Equation 6.12 (fit values shown). **c)** Average R_g and fit of Equation 6.13 (fit values shown).

different measures for the conformations found in our experimental and simulated data, which we will discuss shortly. We compare these to predictions from polymer theory by simultaneously fitting Equations 6.12–6.15 to the corresponding values. We used a, b, ν, K, γ and C_g as fit parameters and report the maximum likelihood estimates (MLE), the error is given by the 16$^{\text{th}}$ and 84$^{\text{th}}$ percentiles of the posterior probability distributions (see Section 6.2.4 for details).

To compare our data to predictions based on polymer theory, we calculated the end-to-end distance R_e, where

$$R_e = |\boldsymbol{r}_n - \boldsymbol{r}_1|\,, \tag{6.10}$$

here $\boldsymbol{r}_i$ is the position of the i-th sphere. Additionally, we determined the radius of gyration R_g as follows,

$$R_g = \left[\frac{1}{n^2}\sum_{i=1}^{n}|\boldsymbol{r}_i - \boldsymbol{r}_{c.m.}|^2\right]^{1/2}, \tag{6.11}$$

with $\boldsymbol{r}_{c.m.}$ the center of mass (c.m.) of the cluster. Both R_e and R_g were normalized by the average interparticle distance B of each measurement and are schematically shown in Figure 6.4a. For long polymers, the root mean square (RMS) value of R_e can be described by a power law,[295]

$$\langle R_e^2 \rangle^{1/2} = b(n-1)^\nu, \tag{6.12}$$

where b is the Kuhn length (we expect $b \approx B$) and the Flory exponent $\nu = 3/(d+2) = 3/4$ for a self-avoiding walk in $d = 2$ dimensions.[296] Analogously, the RMS of R_g scales as[295]

$$\langle R_g^2 \rangle^{1/2} = ab[(n^2-1)/n]^{\nu}, \tag{6.13}$$

where the scaling constant $a \approx 1/\sqrt{6} \approx 0.41$.[297] We first test whether the behavior of our colloidal chains is comparable to long polymers in terms of RMS end-to-end distance and radius of gyration, as was shown for chains of flexibly linked oil droplets.[194]

Indeed, we find that the scaling of the RMS end-to-end distance and the RMS radius of gyration of these colloidal chains agree well with the predictions from polymer theory, as shown in Figure 6.4b (RMS end-to-end distance) and Figure 6.4c (RMS radius of gyration). For the Flory exponent we find $\nu = 0.726 \pm 0.005$, which is close to the exact value of $3/4$ for self-avoiding polymers in 2D and in agreement with the value found for flexibly linked chains of droplets ($\nu = 0.72 \pm 0.03$).[194] The Flory exponent is slightly lower than the expected value of $3/4$, this might be explained by the fact that we study a quasi-2D system, in which the particles have some freedom to move in the out-of-plane direction (for three dimensions $\nu \approx 0.6$[297]). In the simulations, we find an average center height of $(1.03^{+0.05}_{-0.02})R$ above the substrate (over a random subset of 1 % of the data, 7×10^5 positions). Although these excursions are small, they may lead to the slightly lower value of ν. On top of that, the slightly lower ν may be caused by the small number of beads per chain.

Next, we find that the Kuhn length $b = (1.03 \pm 0.01)B$ is in agreement with the hypothesis that it should be equal to the average bond length. In the experiments, the bond length is approximately twice the particle radius, plus the thickness of the bilayer ($\approx 4\,\mathrm{nm}$) and the length of the DNA linkers ($\approx 30\,\mathrm{nm}$). This leads to an estimated experimental bond length of $B \approx 1.03(2R)$. In the simulations, because of the harmonic potential that keeps the particles bonded, we find an average bond length of $B \approx (1.01 \pm 0.01)2R$ (over a random subset of 1 % of the data, 6×10^7 bonds). The fact that the Kuhn length is slightly greater than the bond length B may be explained by the greater-than-zero effective bending stiffness we have found in Figure 6.3c. As shown in Figure 6.4b, we find a shape factor $a = 0.349 \pm 0.002$, which is close to the expected value of $a \approx 0.41$[297] and the value found for flexibly linked chains of droplets ($a = 0.30 \pm 0.02$).[194]

So far we have found that the RMS end-to-end distance and radius of gyration of our colloidal chains show the same behavior as long polymers. When we look in greater detail into the free energy as function of end-to-end distances in Figure 6.5a, we see that our simulated data agrees very well with the permutation data, as well as the experimental data. Slightly larger deviations can be seen in the experimental data for n=5 and 6, this is due to the fact that because the number of configurations is very large for longer chains, increasingly larger amounts of data are needed to probe the equilibrium distribution (see Table 6.1 for a comparison between the amount of simulated and experimental data).

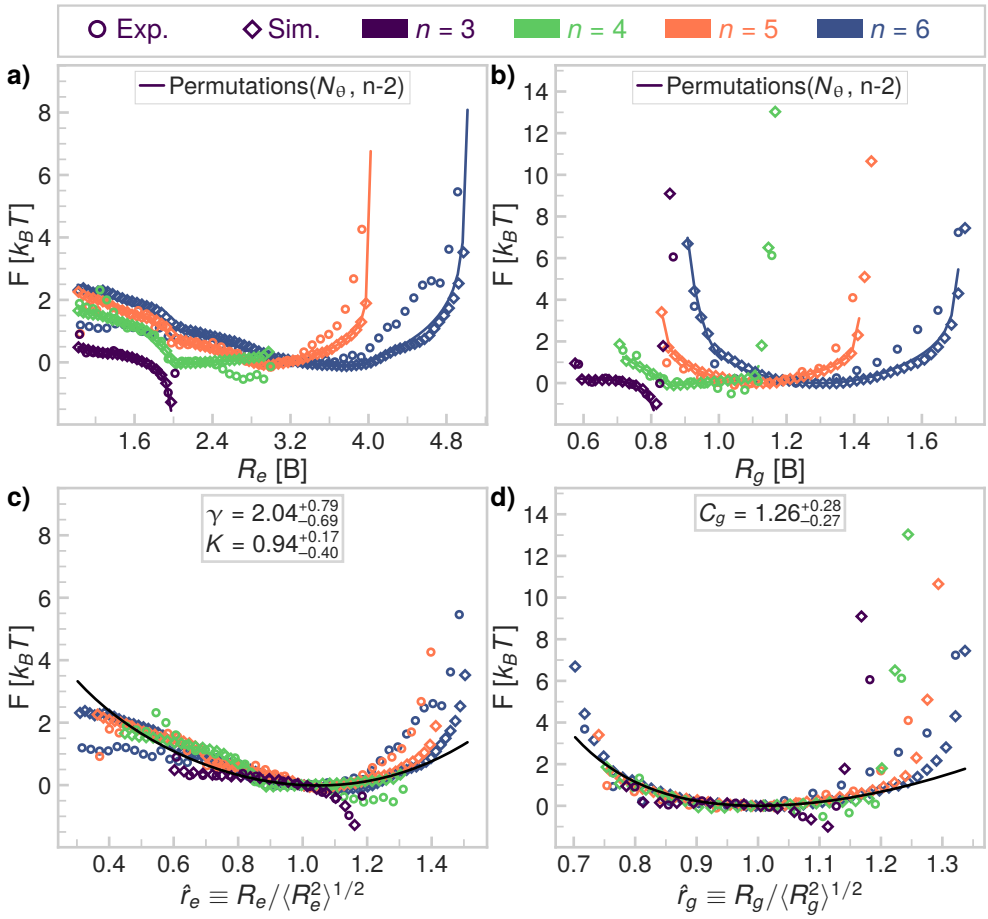

Figure 6.5: **Distributions of end-to-end distances and radii of gyration of flexible colloidal chains.** Markers for the ∘ experimental and ⋄ simulated data, together with the color coding legend for the different chain lengths n, as used in all are shown on top. **a-b)** Comparison between the free energy calculated for experimental, simulated and the $P(N_\theta, n-2)$ permutation data, as function of R_e (panel a) and R_g (panel b). **c)** Free energy in terms of $\hat{r}_e$ and fit of Equation 6.14 (fit values shown). **d)** Free energy in terms of $\hat{r}_g$ and fit of Equation 6.15 (fit values shown).

Based on polymer theory, the free energy of the reduced end-to-end distance $\hat{r}_e \equiv R_e/\langle R_e^2\rangle^{1/2}$ should collapse onto a master curve. For long, self-avoiding polymers, the free energy $F_e(\hat{r}_e)$ is expected to be equal to[298,299]

$$\frac{F_e(\hat{r}_e)}{k_BT} = (K\hat{r}_e)^\delta - (t+2)\ln\hat{r}_e - K^\delta \tag{6.14}$$

with $\delta = 1/(1-\nu)$, $t = (\gamma-1)/\nu$, K a positive constant and γ a positive exponent. This is indeed what we observe in Figure 6.5c. Furthermore, we see the agreement between model and simulated data is better for longer chains of n=5,6 compared to the shorter chains of n=3,4, where finite size effects play a larger role.

Finally, the free energy as function of the radius of gyration in Figure 6.5b is also very well described by the permutation data. It can be collapsed onto a master curve as function of the reduced radius of gyration $\hat{r}_g \equiv R_g/\langle R_g^2\rangle^{1/2}$ as given by[300]

$$\frac{F_g(\hat{r}_g)}{k_BT} = 2C_g\left[\frac{1}{\alpha}(\hat{r}_g)^{-d\alpha} + \frac{d}{\delta}(\hat{r}_g)^\delta + 1 - d\right], \tag{6.15}$$

with $\alpha = 1/(d\nu-1)$ and C_g a positive normalization constant. The resulting free energy is shown in Figure 6.5d. In terms of the reduced radius of gyration, deviations from the model are small even for n=4, while only the shortest chains of n=3 spheres show some deviations because of their finite size.

In summary, in this section we have characterized the conformations of flexibly linked colloidal chains of n=3 to 6 spheres. We find that while the chains are completely freely-jointed, some configurations are forbidden because they would result in interpenetrating particles. This affects the measured end-to-end distance and radius of gyration, especially for the shorter chains of n=3 and 4. Despite these finite size effects, we conclude that the conformations of all chains can be well described by polymer theory based on self-avoiding random walks. Based on the generality of the model and the agreement between model and data, we expect this to be true in general for other micron-sized objects in which self-avoidance plays a significant role.

6.3.2 Shape effects in the diffusion of flexible trimer and tetramer chains

Having characterized the equilibrium conformations of flexibly linked colloidal chains, we now analyze their shape-dependent short-time diffusive properties. Recently, we have studied the effect of flexibility on the diffusivity of the shortest chain, a freely-jointed trimer.[244] Similar to rigid particles, we found that shape affects the diffusive motion of the colloid at short timescales and that displacements are larger in directions that correspond to smaller hydrodynamic drag. Furthermore, we uncovered a Brownian quasiscallop mode, where diffusive motion is coupled to Brownian shape changes. At longer timescales, in addition to the rotational diffusion time, an analogous conformational diffusion time governs the relaxation of the diffusive motion, unique to flexible assemblies.[244]

The choice of coordinate system affects the magnitude of the diffusion tensor. For all rigid objects, there exist a tracking point relative to which the diffusion elements are independent of the lag time considered, called the center of hydrodynamic stress. Although such a point does not exist in general for flexible objects,[301] an analogous tracking point can be found where the magnitude of the diffusion tensor elements is minimal and therefore, close to the time-independent values at long lag times, called the center of diffusivity (c.d.).[269] We compare the results of two choices of tracking points, namely, the center of mass (c.m.) of the cluster which is another common choice, and the center of diffusivity (c.d.).[105,269]

The calculation of the c.d. is described in Section 6.2.5. We find that the c.d. is very close to the c.m. for all chain lengths, but a slightly larger weight is given to the outer particles compared to the particles in the center of the chain, as shown in Figure 6.7. The directions of the x- and y-axis of the body-centered coordinate system depends on the choice of reference point as given by Equation 6.4. For the trimer and tetramer chains, using the c.d. as tracking point, the body centered coordinate systems are shown in Figure 6.6a and Figure 6.1b/c, respectively. The rotational diffusivity is calculated from the angular displacements of the x-axis, or equivalently, rotations around an out-of-plane z axis perpendicular to x and y, as indicated in Figure 6.1b and Figure 6.6a. All diffusion tensor elements are calculated from Equation 6.1, the method is explained in detail in Section 6.2.5. The magnitude of the diffusion tensor elements relative to the c.m. compared to their magnitude relative to the c.d. is given in Figure 6.8 for a trimer. We find that for a trimer, differences in diffusivities relative to the c.m. and c.d. are only measurable for the rotational-translational coupling term and the Brownian quasiscallop mode, because the c.m. is very close to the c.d, as is shown in Figure 6.6a and in Figure 6.7.

The diffusivity of flexible trimers: simulations compared to experiments

We have analyzed the diffusivity of flexibly-linked trimers with respect to the c.d. and we now compare the experimental measurements to our simulations. As shown in Figure 6.6c, for the shape-dependent short-time rotational diffusivity, there is a quantitative agreement between the experiments and simulations for most opening angles. Next, we consider the flexibility, which is defined as half the slope of the mean squared angular displacements of the opening angle θ and defines how fast the chain changes its shape, defined analogously to Equation 6.1 for the tetramer chains and given for the trimers in our previous work.[244] As shown in Figure 6.6d, we measure a lower flexibility in the experiments compared to the simulations. This is caused by inter-particle friction stemming from the DNA linker patch embedded in the lipid membrane. Namely, it was found that increasing the DNA linker concentration leads to a decrease in the flexibility.[85]

Finally, we note that the experimental translational diffusivity is higher than the translational diffusivity obtained from the simulated data, as can be seen in Figure 6.6b. As a consequence, the experimentally determined translation-rotation coupling in Figure 6.6e, as well as the Brownian quasiscallop mode in Figure 6.6f are

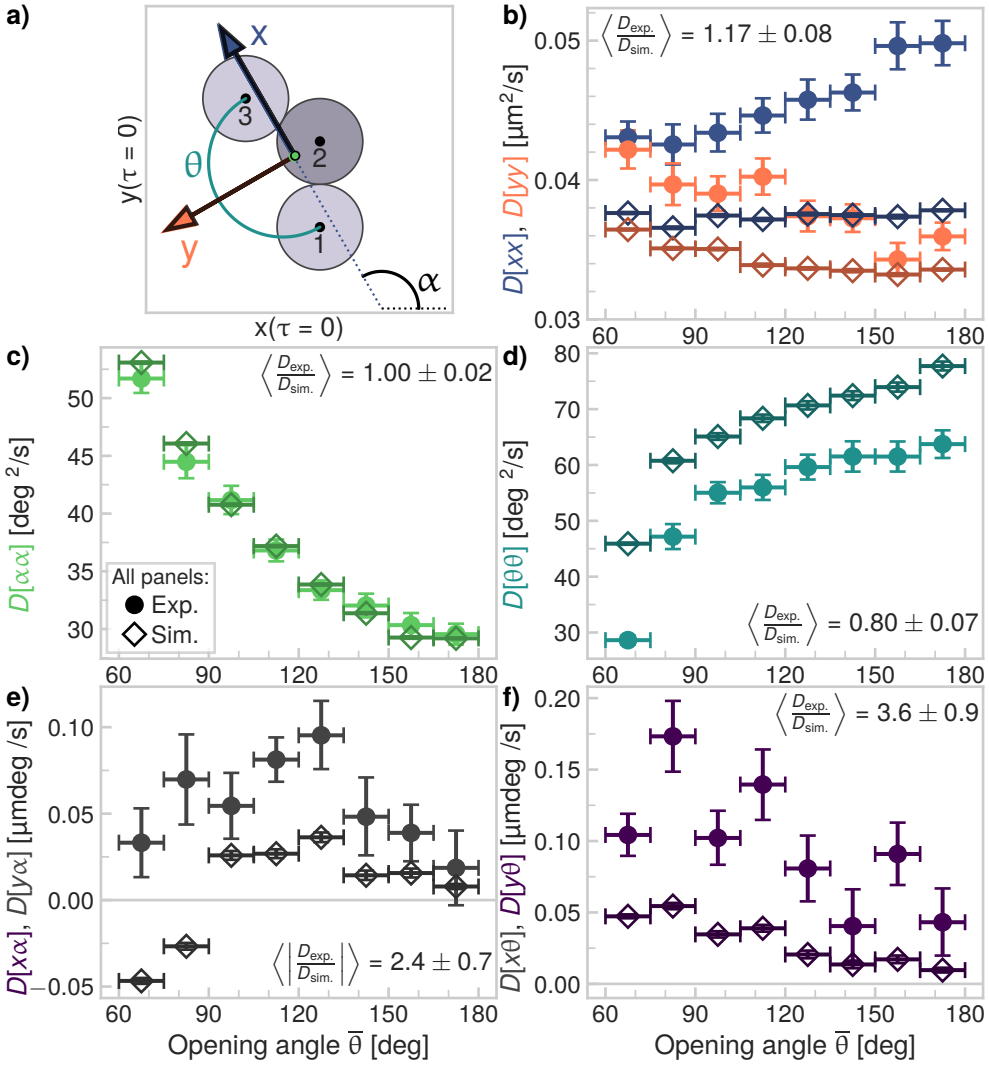

Figure 6.6: **Diffusivity of flexible trimers: experimental and simulated values.** Comparison between • experimental data and ⋄ simulated data (both $0.1 \leq \tau \leq 0.25$ s). **a)** Schematic depiction of the coordinate system of a trimer, as given by Equation 6.4. The colored arrows are calculated with respect to the c.d., while the black arrows are relative to the c.m. The difference between the two tracking points is very small, as shown in Figure 6.7. **b)** The experimental translational diffusivities are larger than the simulated ones, most likely caused by the difference in slip conditions in the experiments and simulations. **c)** The experimental rotational diffusivity is very close to the simulated values. **d)** The experimental flexibility is lower than the simulated values, because of friction stemming from the DNA linker patch. **e)** Translation-rotation coupling term $D[x\alpha]$. **f)** Translation-flexibility coupling term: the Brownian quasiscallop mode $D[y\theta]$.[244]

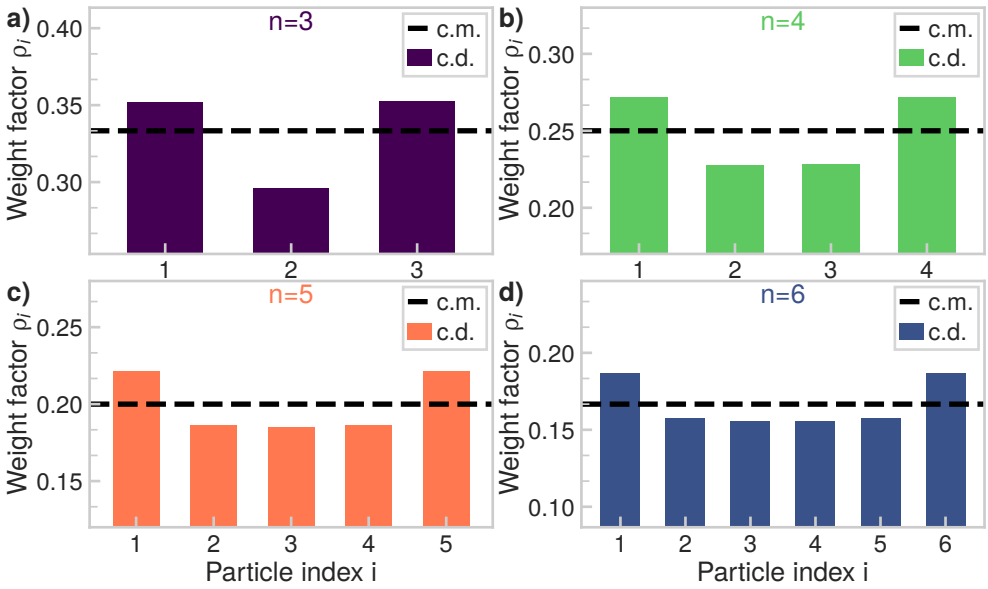

Figure 6.7: **Center of diffusion (c.d.) versus center of mass (c.m.): weight factors.** Weight factors ρ for the c.m. and the c.d., for **a)** trimer (n=3) **b)** tetramer (n=4) **c)** pentamer (n=5) **d)** hexamer (n=6) chains. For the c.d., more weight is accorded to the outer particles compared to the inner particles of the chain. However, differences between the c.m. and the c.d. are small for all chain lengths.

also higher than the values determined from the simulations. This is likely caused by the fact that we model the substrate as a no-slip surface in the simulations, whereas in the experiment the substrate is coated with a hydrogel to prevent particles from sticking, which has a nonzero slip length. We think that this nonzero slip length in the experiments leads to higher translational diffusivities in the experiments, because the particles move further away from the glass and so there is less friction caused by the effectively more viscous water layer close to the no-slip glass substrate.

Effect of tracking point, bin width and lag time on the diffusivity of flexible trimers

The choice of coordinate system affects the magnitude of the diffusion tensor. For all rigid objects, there exist a tracking point relative to which the diffusion elements are independent of the lag time considered, called the center of hydrodynamic stress. Although such a point does not exist in general for flexible objects,[301] an analogous tracking point can be found where the magnitude of the diffusion tensor elements is minimal and therefore, close to the time-independent values at long lag times, called the center of diffusivity (c.d.).[269] We compare the results of two choices of tracking points, namely, the center of mass (c.m.) of the cluster which is another common choice, and the center of diffusivity (c.d.).[105,269]

First, as shown in Figure 6.7, the c.d. is very close to the c.m. for all chain lengths. A slightly larger weight is given to the outer particles for the c.d. compared to the c.m., but this has only a very small effect on the location of the c.d. Second, we compare the magnitude of the diffusion tensor of a flexible trimer relative to the c.m. as in our previous work[244] and relative to the c.d. (this work). As shown in Figure 6.8, the translational (Figure 6.8b), rotational (Figure 6.8c) and flexibility (Figure 6.8d) terms of the diffusion tensor are only slightly affected by changing the tracking point from the c.m. to the c.d. This is easily explained by the fact that the position of the c.d. only changes by approximately 6 % for the smallest opening angle compared to the c.m., as shown in Figure 6.8a. However, the coupling terms are lower with respect to the c.d. as shown in Figure 6.8e for the translation-rotation coupling term and in Figure 6.8f for the Brownian quasiscallop mode. The fact that these coupling terms are lower is expected, because the magnitude of the diffusion tensor is expected to be the lowest relative to the c.d., as it is closest to the long-time diffusion tensor, for which short-time correlations or memory effects are expected to vanish.

The simulations allow us to probe the diffusivity at arbitrarily high frame rates and thus arbitrarily short lag times τ, which is the time delay between the pairs of frames considered in the calculation of the mean squared displacements. There is a marked effect of lag time on the flexibility, as shown in Figure 6.9d. For the simulated data, we show the results for a lag time of 0.05 s (diamonds) and 0.1 to 0.25 s (squares, same lag time as experimental data). The lag times of the experimental data range from 0.1 to 0.25 s, as set by the frame rate of the camera. The simulated data with longer lag times are close to the experimental data. However, when we analyze the simulated data using a shorter lag time, we find a large increase in the flexibility. This difference can easily be explained by considering the mean squared angular displacement of the opening angle in Figure 6.9a. Especially for the larger opening angles, we see that the mean squared displacements show a plateau at longer lag times, leading to a smaller apparent flexibility when the data is fitted using a linear model. The effect of lag time is also present in the Brownian quasiscallop mode in Figure 6.9f. For terms not directly related to flexibility, such as translational diffusivity in Figure 6.9b, rotational diffusivity in Figure 6.9c and translation-rotation coupling in Figure 6.9e, we see there is no appreciable effect of different lag times.

This plateauing for flexibility-related diffusion terms is caused by the calculation method of the shape-dependent diffusivity. That is, we consider only those pairs of frames where the shape of the particle stays within the limits of the particular opening angle bin of the first frame. Therefore, if the flexibility is high, a large percentage of frames will exceed the initial bin and these will not be considered in the analysis. The frames where the bin is not exceeded, as a result, are those in which the flexibility is lower, which leads to the apparent decrease in flexibility at longer lag times.

To solve this, larger bin widths can be used at the expense of a lower resolution in opening angle. We tested this in Figure 6.9d and found that indeed, the values for the flexibility were higher, while the other diffusion tensor elements were not affected (see Figure 6.9, crosses). In fact, by using a larger bin width, we measure

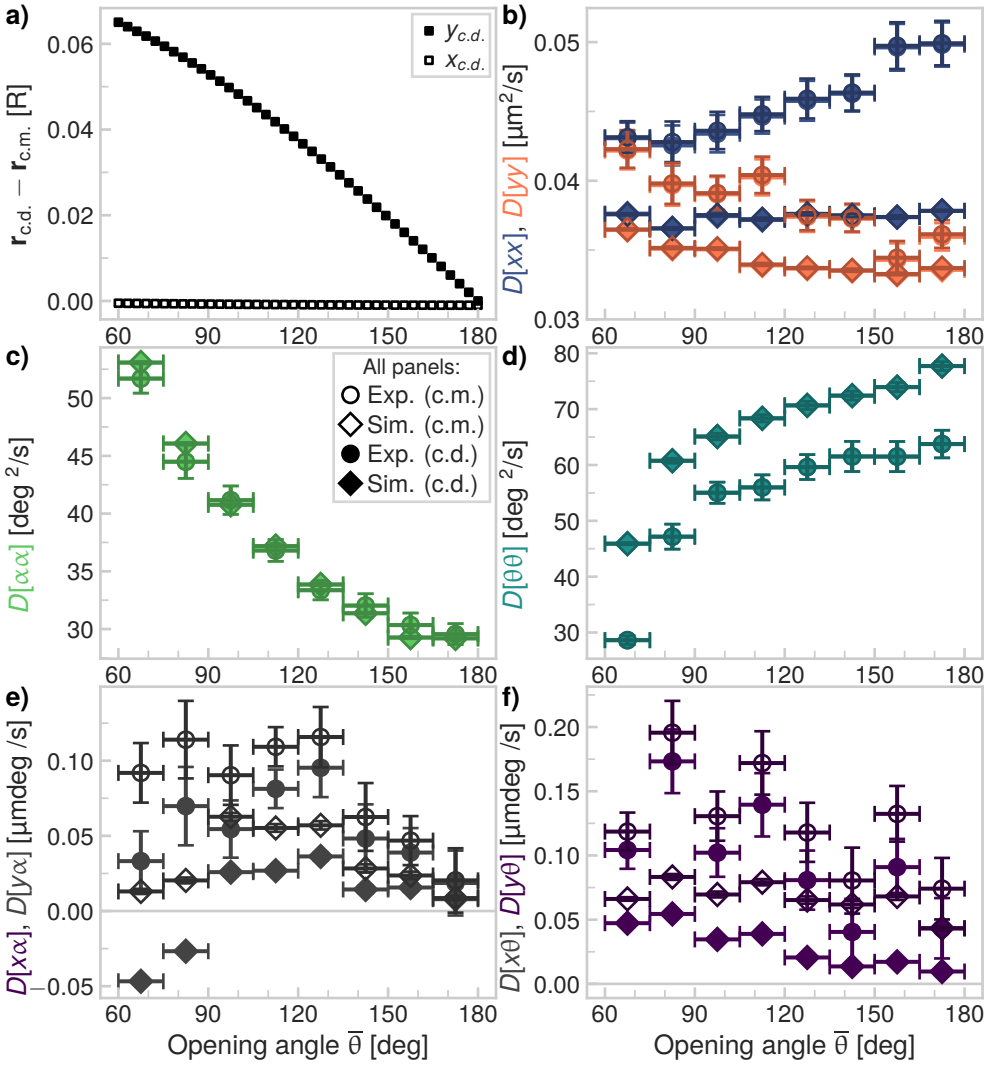

Figure 6.8: **Center of diffusion (c.d.) versus center of mass (c.m.) as tracking point.** For all panels, open points correspond to the c.m. as tracking point while filled points refer to the c.d. as tracking point. ∘ experimental data, ⋄ simulated data (both $0.1 \leq \tau \leq 0.25$ s). **a)** The c.d. of flexible trimers is very close to the c.m.: there is only a small deviation of approximately 6 % for the smallest opening angles. The difference $\boldsymbol{r}_{c.d.} - \boldsymbol{r}_{c.m.}$ on the y-axis is given in terms of R. **b)** The translational diffusivity changes only slightly with respect to a different tracking point. **c)** The rotational diffusivity does not change as function of tracking point. **d)** Also for the flexibility term, there is no influence of tracking point. **e)** The effect of tracking point for rotation-translation coupling is more pronounced: values are lower when the c.d. is used as tracking point. **f)** Also for the Brownian quasiscallop mode, the values are lower when using the c.d. as tracking point instead of the c.m.

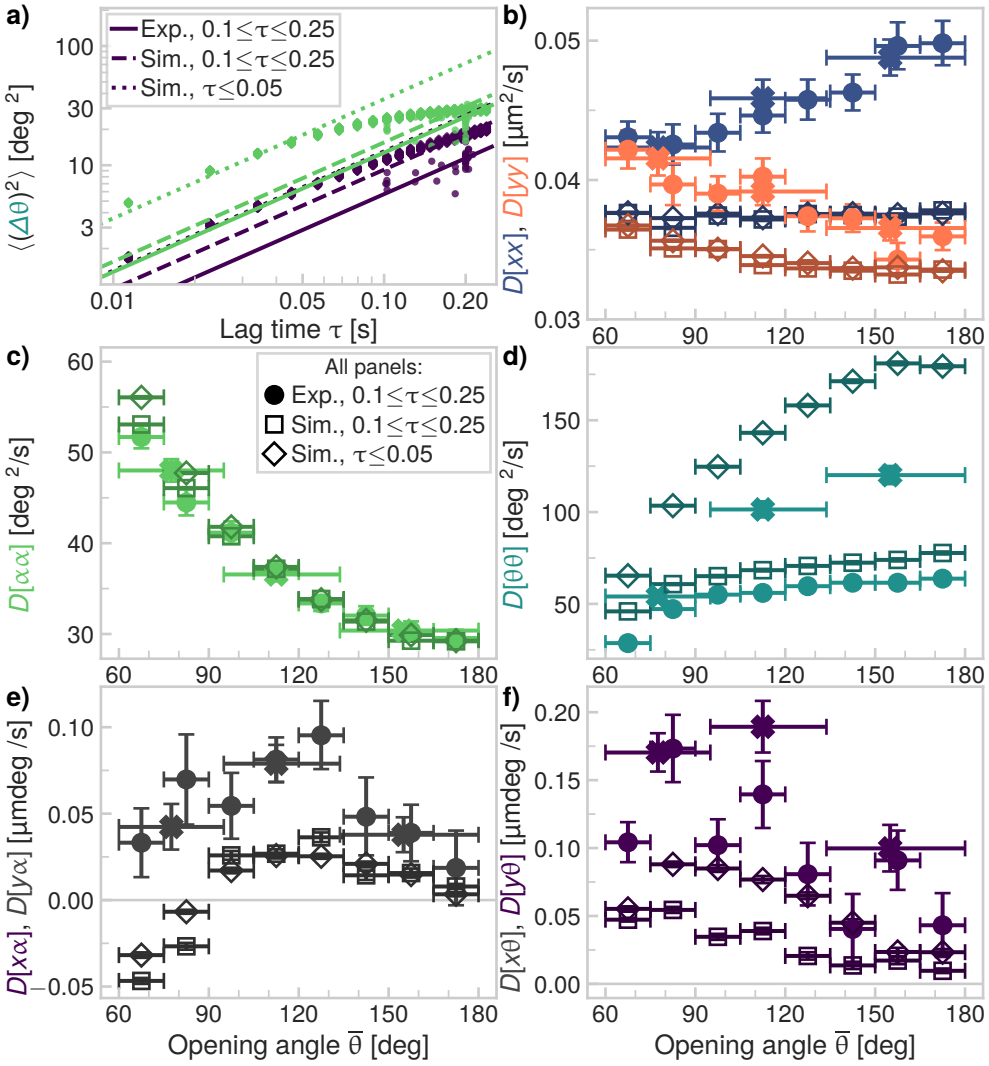

Figure 6.9: **Trimer: effect of varying the bin size / lag time** Comparison between • experimental data, × experimental data with a larger bin width (both $0.1 \leq \tau \leq 0.25\,\mathrm{s}$) and simulated data: ⋄ $\tau \leq 0.05\,\mathrm{s}$, □ $0.1 \leq \tau \leq 0.25\,\mathrm{s}$. **a)** Mean-squared angular displacement of the opening angle reveals caging effects at longer lagtimes, which are more pronounced for higher flexibilities, an effect inherent to the analysis method. **b)** The translational diffusivities are less sensitive to the choice of lagtimes. The experimental translational diffusivities are larger than the simulated ones. **c)** The rotational diffusivities are largely unaffected by the different choices for lagtimes (except for small opening angles), the experimental data agrees with the simulated data. **d)** The flexibility is highly sensitive for the choice of lagtimes. **e)** Translation-rotation coupling terms. **f)** Translation-flexibility coupling terms, including the Brownian quasiscallop mode $D[y\theta]$,[244] which is sensitive to the choice of lagtimes.

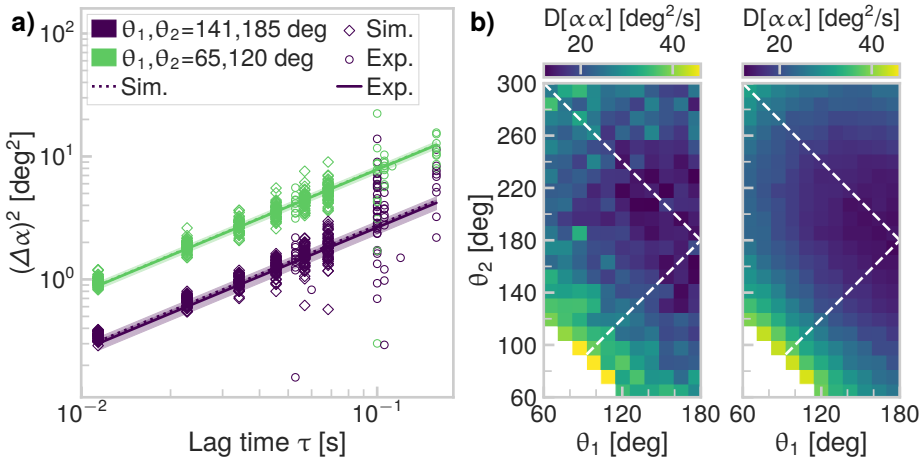

Figure 6.10: **Rotational diffusion of flexible tetramer chains. a)** The mean squared angular displacement for a compact configuration (green) is larger than that of an extended configuration (purple). The elements of the diffusion tensor are obtained by fitting the slope of mean squared displacements. **b)** The rotational diffusivity is highest for compact shapes. The left plot shows experimental data and the right plot shows simulated data. For fitting, we use a maximum lag time $\tau = 0.17\,\mathrm{s}$. The dashed lines indicate the two symmetry axes of the opening angles, $\theta_2 = \theta_1$ and $\theta_2 = 360\,\mathrm{deg} - \theta_1$.

the "true" short-time flexibility: the ratio between the experimental flexibility for the smaller bins (circles in Figure 6.9d) and the simulated flexibility for the experimental lag times (squares in Figure 6.9d) is equal to 0.78 ± 0.07. By using the larger bins, the ratio between the experimental flexibility and the simulated flexibility at short lag times (diamonds in Figure 6.9d) is also equal to 0.77 ± 0.07.

In conclusion, the diffusivity of the c.d. is very close to that relative to the c.m. Interestingly, the interplay of lag time and bin width has a critical effect on the measured short-time diffusion tensor elements related to shape changes and should be carefully considered in the analysis of experimental data.

The diffusivity of flexible colloidal tetramer chains

Having established that the simulations can faithfully describe the short-time shape dependent diffusivity of flexible trimers, in addition to the equilibrium conformations of flexible chains, we now analyze the diffusivity of flexible tetramer chains. In Figure 6.10a, we show that the rotational diffusivity for compacter shapes is higher than that of more extended shapes for two examples, $\theta_1, \theta_2 = 65, 120\,\mathrm{deg}$ (compact) and $\theta_1, \theta_2 = 141, 185\,\mathrm{deg}$ (extended). Furthermore, we conclude that the simulated data agrees with the experimental data, within experimental error. This can also be seen for the rotational diffusivity as function of opening angles θ_1, θ_2 in Figure 6.10b.

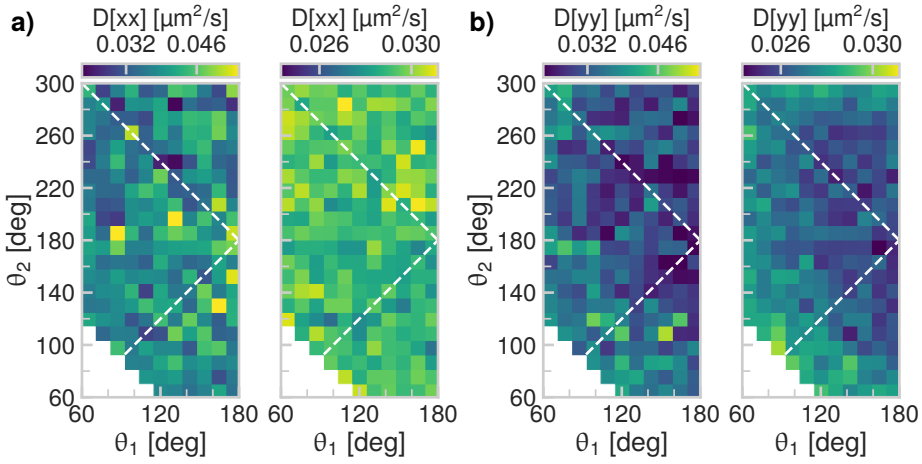

Figure 6.11: **Translational diffusion of flexible tetramer chains.** In both panels, the left plot shows experimental data and the right plot shows simulated data. For fitting, we use a maximum lag time $\tau = 0.17\,\mathrm{s}$. The dashed lines indicate the two symmetry axes of the opening angles, $\theta_2 = \theta_1$ and $\theta_2 = 360\,\mathrm{deg} - \theta_1$. **a)** The translational diffusivity in the x-direction as function of the opening angles θ_1, θ_2, as depicted in Figure 6.1b and c. **b)** Translational diffusivity in the y-direction, which is lower for chains with a stretched angle (θ_1, θ_2 close to 180 deg). For both translational terms, we use different color scales for the experimental and simulated data, because the experimental diffusivities are higher than the simulated ones.

The symmetry lines of the opening angles $\theta_2 = \theta_1$ and $\theta_2 = 360\,\mathrm{deg} - \theta_1$ are indicated as well. The configurations are symmetric around these lines except for the fact that we break this symmetry by choosing which angle to label as θ_1 and which as θ_2, because this has consequences for the orientation of the body centered coordinate system, as shown in Figure 6.1c and defined in Equation 6.4. However, for the rotational diffusivity we only consider angular rotations of the x-axis and therefore the rotational diffusivity is indeed symmetric with respect to the symmetry lines of the opening angles.

For the translational diffusivity in the x-direction (Figure 6.11a) and y-direction (Figure 6.11b) we note that the experimental diffusivity is again slightly larger than the simulated one, similar to the trimers in Figure 6.6b. Again, this is because of the no-slip condition in the simulations versus the hydrogel surface used in experiments to prevent particles from sticking, which has a nonzero slip length. Because the translational diffusivity does not depend on whether the x-axis points to one end of the chain or the other, or equivalently, whether the y-axis points towards one side or the other, we expect that translational diffusivity is symmetric with respect to the symmetry lines of the opening angles. This is indeed true: we observe little shape dependence for translational diffusivity in the x-direction in Figure 6.11a, variations

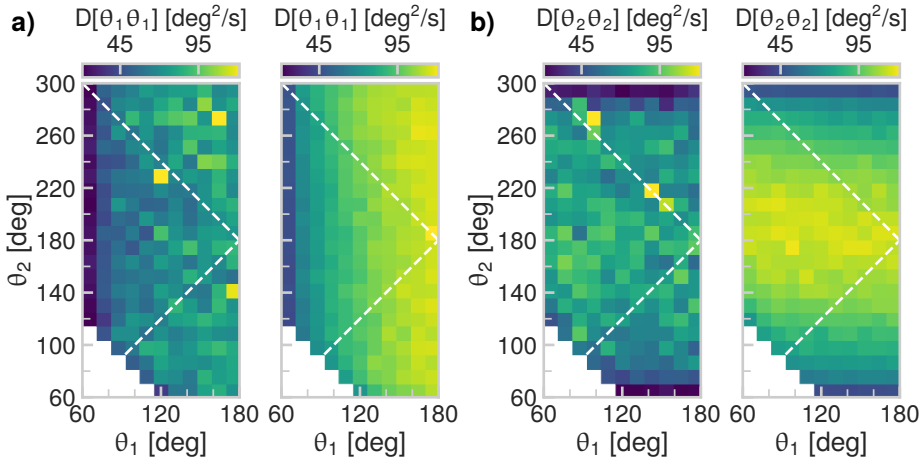

Figure 6.12: **Flexibility of tetramer chains.** In both panels, the left plot shows experimental data and the right plot shows simulated data. For fitting, we use a maximum lag time $\tau = 0.17\,\mathrm{s}$. The dashed lines indicate the two symmetry axes of the opening angles, $\theta_2 = \theta_1$ and $\theta_2 = 360\,\mathrm{deg} - \theta_1$. **a)** The flexibility in the opening angle θ_1 shows a maximum for $\theta_1 = 180\,\mathrm{deg}$. **b)** The flexibility in the opening angle θ_2 also has its maximum value for $\theta_2 = 180\,\mathrm{deg}$.

are likely due to experimental noise. On the contrary, the diffusivity in the y-direction in Figure 6.11b is lower for more extended shapes, which correspond to larger surface areas and therefore, a larger hydrodynamic drag. We note that it is also symmetric with respect to the opening angle symmetry lines.

Interestingly, for the diffusivity of the opening angles in Figure 6.12a (θ_1) and Figure 6.12b (θ_2), we note that the flexibility is highest for opening angles θ_1, θ_2 close to 180 deg (i.e. more extended chains). This is in agreement with the trends we have observed for the flexible trimers in Figure 6.6d and our previous work[244] and suggests that hydrodynamic interactions between the particles slow down shape changes for small inter-particle separation distances. Furthermore, we note that the flexibility is not symmetric around the opening angle symmetry lines, because we have broken the symmetry in this case, by labeling one angle as θ_1 and the other one as θ_2.

The experimental flexibility data in Figure 6.6d shows the same trends as the simulated data but is lower in magnitude. Because the flexibility depends on the concentration of DNA linkers,[85] which cause additional friction in the bond area, this could also explain the lower flexibility found in the experimental data, absent in the simulations. Similarly to what we have found for the trimers in Figure 6.6d, we find that the experimental flexibility in θ_1 is $(71 \pm 12)\,\%$ of the simulated one, for θ_2 this is $(75 \pm 14)\,\%$. Therefore, we conclude that the lower magnitude is indeed caused by friction stemming from the DNA linker patch.

The off-diagonal elements of the diffusion tensor describe possible coupling terms.

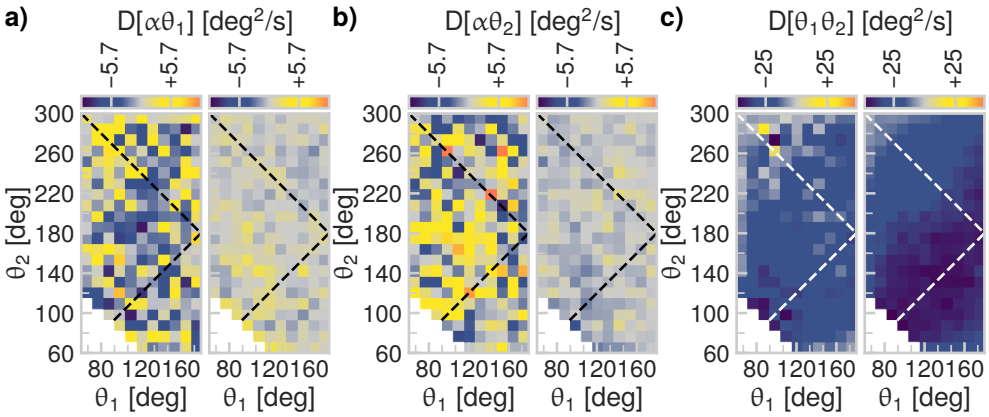

Figure 6.13: **Diffusion of flexible tetramer chains: coupling terms.** In all panels, the left plot shows experimental data and the right plot shows simulated data. For fitting, we use a maximum lag time $\tau = 0.17\,\mathrm{s}$. The dashed lines indicate the two symmetry axes of the opening angles, $\theta_2 = \theta_1$ and $\theta_2 = 360\,\mathrm{deg} - \theta_1$. **a)** The rotation-flexibility coupling $\mathrm{D}[\alpha\theta_1]$ is close to zero. **b)** The rotation-flexibility coupling $\mathrm{D}[\alpha\theta_2]$ is also close to zero. **c)** There is a strong negative coupling in flexibilities of the two opening angles θ_1, θ_2.

We have calculated those terms and find that there is no significant coupling between rotational diffusivity and flexibility, as shown in Figure 6.13a for the coupling between α and θ_1 and in Figure 6.13b for $\mathrm{D}[\alpha\theta_2]$. This is the same result we have found for flexible trimers[244] and we hypothesize this can be generalized to larger chain lengths as well.

However, there is a strong negative coupling between diffusivities in the two opening angles θ_1, θ_2, as shown in Figure 6.13c, which is symmetric with respect to the symmetry lines of the opening angles. In fact, the negative coupling is strongest around the symmetry line $\theta_1 = \theta_2$ and lowest for zig-zag like structures near $\theta_1 = 60\,\mathrm{deg}$ and $\theta_2 = 300\,\mathrm{deg}$. By comparing Figure 6.13c to the schematics of possible conformations in Figure 6.1c, the configurations where the negative couplings are highest, are those where the outer particles are both on the same side of the coordinate system, namely the positive y plane. There, the hydrodynamic interactions between the particles are largest and therefore also the negative coupling is largest.

Interestingly, we also find small, but nonzero coupling terms for translation-rotation coupling. By comparing the two translation-rotation coupling terms, we note that $y\alpha$ in Figure 6.14d is small compared to $x\alpha$ in Figure 6.14a, for both the experimental and simulated data. This means that displacements in the positive x-direction (see Figure 6.1c) will lead to counter-clockwise rotations of the chain, similarly to the $x\alpha$ coupling we found for the trimers,[244] as also shown here in Figure 6.6e.

Lastly, by comparing the translation-flexibility coupling terms for both opening

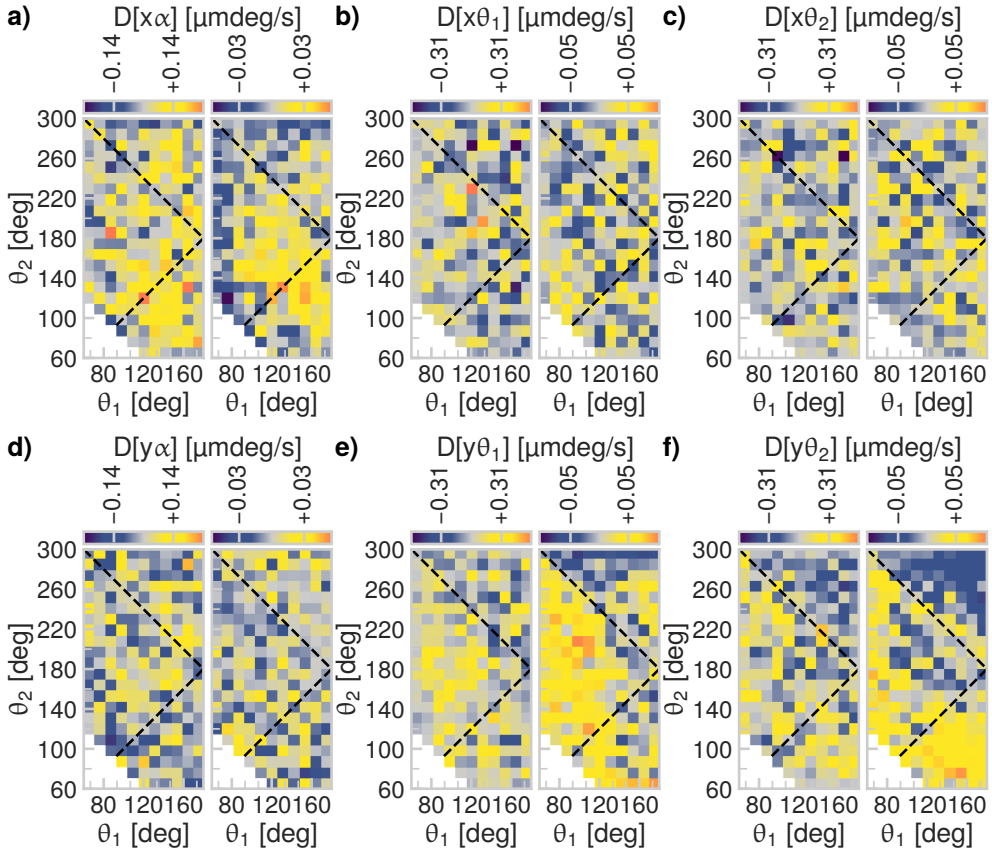

Figure 6.14: **Diffusion of flexible tetramer chains: translational coupling terms.** In all panels, the left plot shows experimental data and the right plot shows simulated data. The color scales of the experimental and simulated data are different, because the experimental translational diffusivity is higher than the simulated one. For fitting, we use a maximum lag time $\tau = 0.17\,\mathrm{s}$. The dashed lines indicate the two symmetry axes of the opening angles, $\theta_2 = \theta_1$ and $\theta_2 = 360\,\mathrm{deg} - \theta_1$. **a)** There is a small translation-rotation coupling D[xα]. **b)** The translation-flexibility coupling D[xθ_1] is close to zero. **c)** The translation-flexibility coupling D[xθ_2] is also close to zero. **d)** The translation-rotation coupling D[yα] is zero as well. **e)** There exists a nonzero translation-flexibility coupling D[yθ_1]. **f)** The translation-flexibility coupling D[yθ_2] is also nonzero.

angles in the x-direction, shown in Figure 6.14b for $x\theta_1$ and Figure 6.14c for $x\theta_2$, and in the y-direction, see Figure 6.14e for $y\theta_1$ and Figure 6.14f for $y\theta_2$, we observe that the coupling terms related to the y-direction are larger in magnitude than those in the x-direction. For the x-direction, there are no clear trends for either opening angle, in both the simulated and the experimental data, as shown in Figure 6.14b and c. On the contrary, for translation-flexibility coupling terms in the y-direction, we find couplings, analogously to the Brownian quasiscallop mode we have found for trimers,[244] also shown in Figure 6.6f.

By looking closely at the coupling between y and θ_1 diffusivity in Figure 6.14e, we observe that the coupling is positive for angles above the symmetry line $\theta_1 = \theta_2$ and below the symmetry line $\theta_1 = 360\,\text{deg} - \theta_2$. If we look at the configurations for these angles in Figure 6.1c, we observe that positive y-displacements lead to an opening of one end of the chain, namely the trimer segment with opening angle θ_1, similar to the Brownian quasiscallop mode for trimers. We see the same effect for configurations below the symmetry line $\theta_1 = \theta_2$ and in fact, the coupling is symmetric around this symmetry line. For configurations above the other symmetry line, $\theta_1 = 360\,\text{deg} - \theta_2$, there are strongly negative correlation terms, especially near $\theta_2 = 300\,\text{deg}$. By again studying the configurations for these angles in Figure 6.1c, we note that this is indeed what would be expected to happen for the trimer segment with opening angle θ_1, based on our earlier findings of the Brownian quasiscallop mode in trimers. Apart from the expected negative correlations we expect from the Brownian quasiscallop mode of a trimer, there are also positive values in this region. However, we cannot compare them directly, because the coordinate system, and therefore the direction of the y-axis, is different in the case of a tetramer chain. Specifically, it is not centered on the trimer segment. Therefore, the coupling we have observed is similar to, but more complex than the Brownian quasiscallop mode in trimers.

Analogously, we observe the same effects for the coupling between diffusivity in the y-direction and the other opening angle θ_2, as shown in Figure 6.14f. Starting below the symmetry line $\theta_1 = \theta_2$, the coupling is positive, as expected. Above the other symmetry line $\theta_1 = 360\,\text{deg} - \theta_2$, we observe the opposite, negative coupling, which is in line with our previous results for the opening angle θ_1. Between the two symmetry lines, something more complicated happens, analogously to the area above the symmetry line $\theta_1 = 360\,\text{deg} - \theta_2$ for the D[yθ_1] coupling discussed previously. There, we observe a positive coupling for configurations close to $\theta_1 = 60\,\text{deg}$, as expected from the Brownian quasiscallop mode and the other coupling term D[yθ_1]. For the other configurations in the area between the symmetry lines, we observe both positive and negative coupling terms. Therefore, we conclude that there the behavior is also more complex than one would expect based on the assumption that the individual trimer segments show Brownian quasiscallop modes. This is likely due to the displacement of the coordinate system from the center of the trimer segment, as well as possible hydrodynamic couplings between shape changes, as we have observed in Figure 6.13c.

In summary, in this section we have shown that for both trimers and tetramers,

the flexibility determined from the experimental data is reduced to approximately 75 to 80 % of the flexibility determined from simulations, because of friction of the DNA linker patch, which is not modeled in the simulations. We have found marked flexibility-induced effects on the diffusivity of flexible tetramer chains, namely an increase in flexibility for the more elongated configurations and nonzero couplings between translational diffusivity and both rotational diffusivity and flexibility, as well as a strongly negative coupling between diffusivity of the two opening angles. We have established that the simulations can adequately model our experimental findings, especially for terms that do not relate to translational diffusivity. For the translational terms, the slip conditions on the surface play a crucial role and require further careful consideration in future works.

6.3.3 Shape-averaged diffusion of flexible chains

We have studied the short-time, shape dependent diffusivity of flexible trimer and tetramer chains. For the longer pentamer (n=5) and hexamer (n=6) chains, studying the diffusion tensor as function of shape is more challenging because of the greater number of opening angles and consequently, greater number of degrees of freedom. Therefore, we take an approach known as the rigid-body approximation [101,264,286,287] and study the shape-averaged short-time diffusivity.

In Figure 6.15a we show the translational diffusivity as function of chain length for experimental and simulated data, relative to the c.d. and the c.m. As we have argued before in Section 6.3.2, different choices of tracking points can lead to different magnitudes of the diffusion tensor elements. For flexible objects, the c.d. is the most appropriate tracking point to use, because it gives the smallest values of the diffusion tensor elements and therefore the obtained values are closer to the long time diffusivities. [269] For the flexible colloidal chains, the c.d. turns out to be very close to the c.m. for all chain lengths, but a slightly larger weight is given to the outer particles compared to the particles in the center of the chain. Because the c.m. is very close to the c.d. (see Figure 6.7 for a comparison), we conclude that for our flexibly linked chains, there is no appreciable difference between the two different choices of tracking point, both for the experimental and simulated data.

In Figure 6.15a, we see a clear scaling of diffusion coefficient D_T with chain length and hypothesize that this scaling can be described by polymer theory. In Kirkwood-Riseman theory, [286] the translational diffusion coefficient is expected to be proportional to $\propto \langle R_g^2 \rangle^{-\nu/2}$. Indeed, we find that for the experimental data, the fitted $\nu = 0.7 \pm 0.5$ is close to the expected value of 3/4. More clearly, for the simulated data, we find $\nu = 0.77 \pm 0.02$. Again, the average experimental translational diffusivity is higher than the simulated one, because of differences in the surface slip conditions, as explained in Section 6.3.2. Therefore, Kirkwood-Riseman theory can be used to describe the scaling of the translational diffusivity of the chains as function of their length.

Additionally, we have calculated the lower bound on the short-time diffusion coefficient $D_{c.d.}$, because its value should be close to the long-time diffusion coefficient

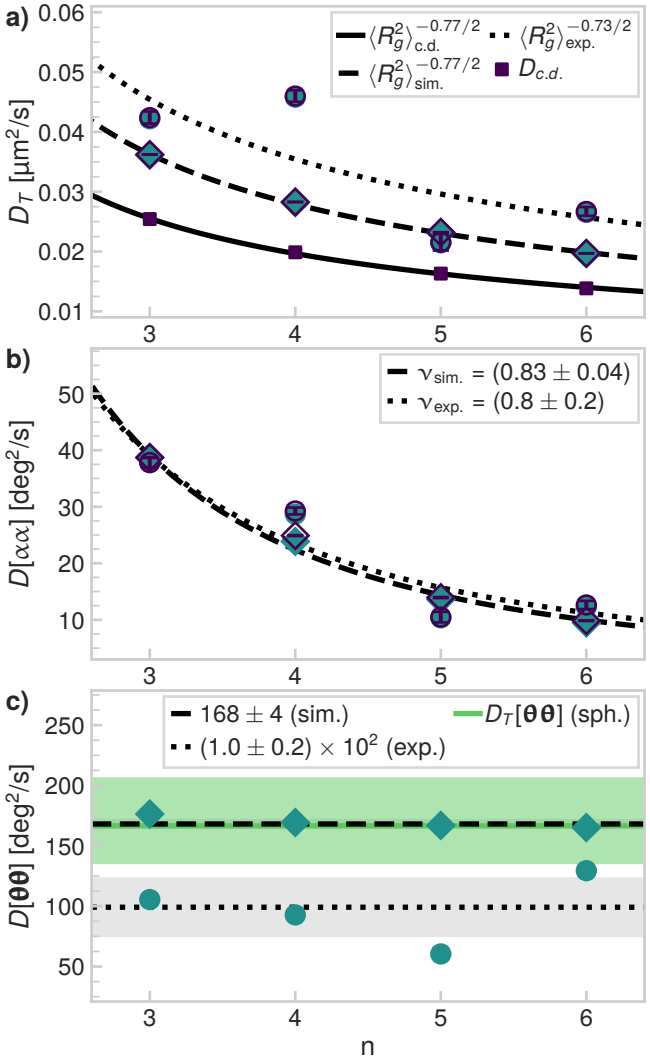

Figure 6.15: **Average diffusivity of flexible colloidal chains.** All panels: ∘ experimental data ($\tau \leq 0.25\,s$), ⋄ simulated data ($\tau \leq 0.05\,s$). **a)** In plane translational diffusion coefficient D_T as function of chain length. **b)** Rotational diffusion coefficient $D[\alpha\alpha]$ (around the axis normal to the substrate) as function of chain length. **c)** Flexibility coefficient $D[\boldsymbol{\theta\theta}]$ as function of chain length. The flexibility does not depend on chain length, the median values plus standard deviations are indicated for both the experimental and simulated data.

typically measured in scattering experiments.[269] We determined $D_{c.d.}$ from the matrix $\boldsymbol{A}_{ij}$ defined by Equation 2.16 of Cichocki et al.[269] using the RPB tensor[35] with lubrication corrections as the inter-particle mobility matrix $\boldsymbol{\mu}_{ij}$ (see also Section 6.2.5 for details). Indeed, we find that its value is always lower than the simulated or experimental values, which indicates that memory effects, or in other words, time correlations, play a large role in the translational diffusivity of our clusters. We find the same scaling as function of chain length as for the experimental and simulated data, namely, $\nu = 0.77 \pm 0.02$, as predicted by Kirkwood-Riseman theory.

Next, having characterized the translational diffusivity of the flexible chains, we now consider their rotational diffusivity $D[\alpha\alpha]$. While there is no unique choice for which axis to use to quantify the rotational diffusivity of a shape-changing object, we use the definition in Equation 6.4 for consistency. As shown in Figure 6.15b, the simulated data agree with the experimental data and the differences between using the c.m. or the c.d. as tracking point are minimal. We use an approximate expression to describe the rotational diffusivity of our flexible chains in the rigid rod limit:[286]

$$D[\alpha\alpha] \propto \frac{\ln\left(2L/d\right)}{L^3}, \tag{6.16}$$

with L the length of the rod and d its diameter. Setting $d = b$ (the Kuhn length) and $L = b\left(1 + (n-1)^{\nu}\right)$, which is the average end-to-end distance plus the Kuhn length, we obtain a reasonable fit with ν close to the expected 3/4, as shown in Figure 6.15b. Specifically, we find $\nu = 0.8 \pm 0.2$ for the experimental data and $\nu = 0.83 \pm 0.04$ for the simulated data. Therefore, we conclude that while the shape dependent short time diffusivity of flexible colloidal chains shows clear flexibility effects as discussed in Section 6.3.2, the scaling of the shape-averaged translational and rotational diffusion coefficients can be described very well by the rigid body approximation.

In Section 6.3.2, we have found couplings between translational diffusivity and both rotational diffusivity and the flexibility of trimers and tetramers, for the shape-dependent diffusion tensor. We have calculated the shape-averaged translation-flexibility and translational-rotational coupling terms with respect to both the c.m. and the c.d., as shown in Figure 6.16. The shape-averaged translation-flexibility coupling modes in the y-direction are positive for a trimer, which corresponds to the Brownian quasiscallop mode[244] of the shape-dependent diffusion tensor, as shown in Figure 6.16a. For longer chain lengths, this coupling term is averaged out, most likely because of the negative correlation we have found between the flexibility of the two opening angles of the tetramer chain, which indicates that such coupling terms may be present for longer chain lengths as well. Because the coordinate system is not centered on the trimer segment, overall shape changes are taken into account. We find that overall, there is no average coupling between translational diffusivity in the y-direction and the overall flexibility $D[\boldsymbol{\theta}\boldsymbol{\theta}]$.

On the contrary, in Figure 6.16b, we see that there is a positive coupling between rotational diffusivity and translational diffusivity in the x-direction, which decreases

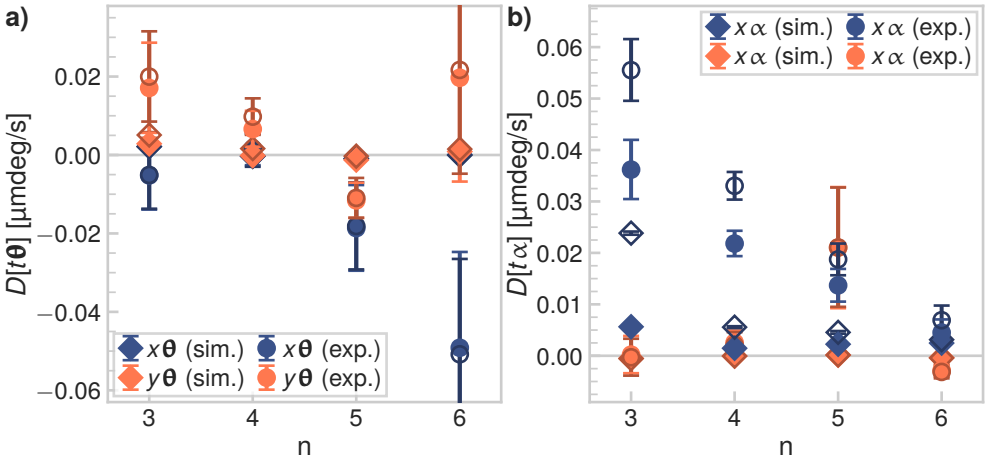

Figure 6.16: **Shape-averaged coupling terms as function of chain length.** In all panels, filled symbols are with respect to the c.d. and unfilled symbols are with respect to the c.m. **a)** The shape-averaged translation-flexibility coupling modes in the y-direction are positive for a trimer (Brownian quasiscallop mode) but average out for larger chain lengths. **b)** The shape-averaged translation-rotation coupling mode in the x-direction is positive for trimers and decreases as function of chain length.

as function of chain length. This is the same coupling we have found for the shape-dependent diffusion tensor of both trimers[244] and tetramers.

Finally, we consider the shape-averaged flexibility $D[\boldsymbol{\theta}\boldsymbol{\theta}]$ by calculating the slope of the mean squared angular displacements of the $n-2$ opening angles $\langle|\Delta\boldsymbol{\theta}|^2\rangle$ as function of lag time, as defined by Equations 6.2–6.3. First, we observe that the mean squared displacements of $\Delta\boldsymbol{\theta}$ increase linearly with lag time, similarly to the other diffusion tensor terms. Moreover, we find that the flexibility is independent of the length of the chain, as shown in Figure 6.15c.

As we have seen for the shape-dependent short-time flexibilities of the trimer and tetramer in Figure 6.6d and Figure 6.12 respectively, the average experimental flexibility is approximately 75 to 80 % of the average flexibility in the simulations. We hypothesize that the lower flexibility in the experiments is caused by inter-particle friction stemming from the DNA linkers. This is also supported by the observation that while the experimental flexibility shows large fluctuations, that are due to experimental differences in DNA concentration between particles and samples, the flexibility in the simulations shows a very narrow distribution. For the shape-averaged flexibility, we find that the experimental flexibility averaged over all chain lengths is (60 ± 15) % of the simulated one, where the spread is most likely caused by the spread in the DNA linker concentration.

For trimers of flexibly-linked emulsion droplets, it was proposed that for small displacements of the opening angle, the maximum value of the flexibility is expected

to be dominated by the translational friction coefficient of the particles.[194] However, in the droplet-based system, the flexibility was found to be unaffected by the DNA linker concentration.[194] Because of this difference, we test whether the same behavior applies to our flexibly linked chains of colloidal particles, in spite of the presumably different dynamics, caused by the friction of the DNA linker patch in the lipid bilayer and with the particle surface. By considering small displacements of the particles, one can define an equivalent "translational" flexibility coefficient $D_T[\boldsymbol{\theta\theta}]$, which is linked to D_T as $D_T[\boldsymbol{\theta\theta}] = (\pi R/180\,\mathrm{deg})^{-2} D_T$. If the flexibility is dominated by translational diffusivity of the individual spheres, we can calculate its maximum magnitude from D_T. This would in turn mean that the flexibility scales with the particle radius as $1/R$, in the same way as translational diffusivity and not as $1/R^3$, as we[244] and others assumed in previous works.[107]

Indeed, using the methods explained in Section 6.2.3, for an individual sphere at a height of $(1.03^{+0.05}_{-0.02})R$ above the substrate, which corresponds to the heights of the spheres in the chains as found in the simulations, we find a translational diffusion coefficient between 0.046 and 0.071 $\mu m^2\,s^{-1}$. For comparison, the bulk diffusion coefficient of the spheres, far from the substrate, is 0.229 $\mu m^2\,s^{-1}$. Note that even a small change in the height above the substrate has a large effect on the calculated diffusion coefficient, therefore, the spread in the translational diffusion coefficient in Figure 6.15 is most likely larger than the reported spread, which is estimated from the fit of a linear model to the MSD using the method described in Section 6.2.4. In the same way, the uncertainty in the expected flexibility calculated from the translational diffusivity of an individual sphere is also large. The equivalent range of flexibilities $D_T[\boldsymbol{\theta\theta}]$ based on these values is shown in green in Figure 6.15c. Because the value of the equivalent $D_T[\boldsymbol{\theta\theta}]$ of an individual sphere is very close to the flexibilities we find in our simulations, we conclude that the maximum flexibility is indeed set by the translational diffusion coefficient of the individual spheres.

6.4 Conclusions

In conclusion, we have studied flexibly linked colloidal chains of three to six spheres using both simulations and experiments. We have analyzed their conformational free energy in several different ways. First, we found that the chains are freely-jointed, except for configurations that are forbidden because of steric restrictions due to interpenetrating particles. Furthermore, apart from some deviations because of their finite length, two-dimensional Flory theory for infinitely long polymers can describe their conformational free energy in terms of reduced end-to-end distance and radius of gyration very well. We found that the effective bending stiffness, which measures deviations from opening angles close to straight angles, scales according to the worm-like chain model.

Then, we have studied the shape-dependent short-time diffusivity of the trimer and tetramer chains. We found that the simulations can adequately model the experimental diffusion tensor of flexible trimers. For the flexibly-linked tetramers, we have

found that shape affects the short-time diffusion tensor in ways similar to what we have found for the shorter trimers. Namely, translational and rotational diffusivity are highest in directions that correspond to the lowest projected surface area, in other words, the more compact shapes, and the flexibility is highest for the more elongated shapes. Furthermore, there are nonzero couplings between translational diffusivity and both rotational diffusivity and flexibility, similar to what we found for the flexible trimers. Additionally, there is a strong negative coupling between the diffusivities of the two opening angles.

By determining the shape-averaged translational and rotational diffusivity for chains of three to six spheres, we found that these scale as function of chain length according to Kirkwood-Riseman theory. Their maximum flexibility does not depend on the length of the chain, but is determined by the near-wall in-plane translational diffusion coefficient of an individual sphere. The experimental flexibility is approximately 75 to 80 % of the flexibility calculated from the simulated data, because of friction of the DNA linker patch.

Overall, we found a good agreement between the experimental measurements and the simulations, except for translational diffusivity. In that case, we hypothesize that the difference in surface slip in the experiments, where there is a finite slip length due to the hydrogel surface, and in the simulations, where we use a no-slip boundary condition, lead to a higher translational diffusivity in the experiments. We hope our work aids the study of diffusivity of flexible objects found in complex mixtures relevant in, for example, the cosmetic, pharmaceutical and food industries, as well as in biological systems. Our findings may have implications for understanding both the diffusive behavior and the most likely conformations of macromolecular systems in biology and industry, such as polymers, single-stranded DNA and other chain-like molecules.

Acknowledgments

This chapter is based on the following publication:

Conformations and diffusion of flexibly linked colloidal chains.
R.W. Verweij, P.G. Moerman, L.P.P. Huijnen, N.E.G. Ligthart, I. Chakraborty, J. Groenewold, W.K. Kegel, A. van Blaaderen and D.J. Kraft
Journal of Physics: Materials, in press (2021). doi:10.1088/2515-7639/abf571

We thank Ali Azadbakht for the design and setup of the Optical Tweezers and his technical support. We are grateful to Aleksandar Donev and Brennan Sprinkle for fruitful discussions and for providing us with example code for the simulations. We thank Piotr Szymczak for useful discussions about the center of diffusion. The simulations were partly performed using the ALICE compute resources provided by Leiden University. J. Groenewold wishes to thank the program for Chang Jiang Scholars and Innovative Research Teams in Universities (no. IRT 17R40) and the 111 Project of the PRC. This project has received funding from the European Research Council (ERC) under the European Union's Horizon 2020 research and innovation program (grant agreement no. 758383) and from the NWO graduate program.

7 Conformations and diffusion of colloidal rings and dominoes

Ring polymers are special in a topological sense: they do not have a beginning or an end. This results in interesting diffusive and rheological properties. Here, we study model systems of micron-sized flexible rings and dominoes, created from colloid-supported lipid bilayers. We characterize their conformational and diffusive properties. We find that rings and dominoes have a larger translational and rotational diffusion coefficient when compared to chains, while they are less flexible. We show that the flexibility of the rings and dominoes scales as the number of excess floppy modes per bond. Our findings could have implications for the behavior of both synthetic and biological ring polymers, as well as for the dynamic modes of floppy colloidal materials.

7.1 Introduction

Ring polymers have unique properties compared to linear polymers, due to their topologically closed structure that has no beginning or end.[302] Blends of looped and linear polymers can display rich viscoelastic properties[303] that are not only interesting from a physicists' perspective, but can also be used for the design of materials[304] with multifunctional and switchable properties. For example, it was found that tiny fractions of linear polymer chains added to a melt of ring polymers already drastically change their dynamic and rheological properties.[305]

In biological systems, studying the impact of the topological constraints of ring polymers can potentially shed light on how genomes fold themselves into volumes whose linear dimensions are many orders of magnitude smaller than their contour lengths.[306] Interestingly, their diffusivity was found to differ from that of linear polymers: at short timescales, ring polymers exhibit sub-diffusive behavior, long after the stress has completely relaxed, contrary to linear polymers. An explanation of this observation, beyond the fact that shape fluctuations do not necessarily contribute to the overall ring diffusion, requires a detailed understanding of their dynamics.[306,307] However, to measure the dynamics of ring polymers, single-molecule techniques with a simultaneously high spatial and temporal resolution are needed.

Here, we study experimentally and numerically a model system of micron-sized colloidal rings and dominoes, built from spherical colloid-supported lipid bilayers (CSLBs).[85,110,112,242] Colloidal particles may be used as model systems for macromolecules, because of their unique combination of microscopic size and their sensitivity to thermal fluctuations.[18,19,284] Additionally, colloidal particles are useful in their own right, as they could, as an example, provide ways to build switchable materials[285] with novel properties not found in nature. In this work, we consider rings of four to six spherical particles, as well as dominoes of six particles and study both

their conformational and diffusive behavior. Dominoes are clusters of six particles where an additional bond is present compared to rings of the same size, so that the graph of particles and bonds forms a domino, or equivalently, (2, 3)-grid or 3-ladder graph.[308] We find that while the smaller rings and the dominoes show no preferred shapes, preferences arise for the larger rings. Both the translational and rotational diffusivity of the rings and dominoes is greater than that of chains of the same size, while their flexibility is lower. We show that their flexibility scales as the number of excess floppy modes per bond. Our findings could have implications for the behavior of both synthetic and biological ring polymers, as well as for the dynamic modes of floppy colloidal materials.

7.2 Materials and Methods

7.2.1 Experimental

Flexible rings and dominoes of colloid-supported lipid bilayers (CSLBs) were prepared as described in previous work.[85,110,112,242] Specifically, we followed the exact same procedure as in Chapter 5, which we now briefly summarize.

The CSLBs consisting of $(2.12 \pm 0.06)\,\mu$m silica particles were prepared as described in our recent works.[242,244] Briefly, the particles were coated with a fluid lipid bilayer by deposition and rupture of small unilamellar vesicles consisting of 98.8 mol % of the phospholipid DOPC ((Δ9-Cis) 1,2-dioleoyl-sn-glycero-3-phosphocholine), with 1 mol % of the lipopolymer DOPE-PEG(2000) (1,2-dioleoyl-sn-glycero-3-phosphoethanolamine-N-[methoxy(polyethylene glycol)-2000]) and 0.2 mol % of the fluorescently-labeled TopFluor-Cholesterol (3-(dipyrromethene boron difluoride)-24-norcholesterol) or, alternatively, the same amount of the fluorescently-labeled DOPE-Rhodamine (1,2-dioleoyl-sn-glycero-3-phosphoethanolamine-N-(lissaminerhodamine B sulfonyl)). The bilayer coating was performed in a buffer at pH 7.4 containing 50 mM sodium chloride (NaCl) and 10 mM 4-(2-Hydroxyethyl)-1-piperazineethanesulfonic acid (HEPES). We added double-stranded DNA (of respectively strands DS-H-A and DS-H-B, see Table A.1) with an 11 base pair long sticky end and a double stearyl anchor, which inserts itself into the bilayer via hydrophobic interactions, as shown Figure 7.1c. The sticky end of strand DS-H-A is complementary to the sticky end of strand DS-H-B, which allows them to act as linkers. Self-assembly experiments were performed in a different buffer of pH 7.4, containing 200 mM NaCl and 10 mM HEPES. Chains of 2.12 μm CSLBs were formed by self-assembly in a sample holder made of polyacrylamide (PAA) coated cover glass.[244] A confocal microscopy image of the coated particles is shown in Figure 7.1a for a tetramer loop.

7.2.2 Microscopy

Loops and dominoes were imaged for at least 5 min (frame rates between 5 and 19 fps) at room temperature using an inverted confocal microscope (Nikon Eclipse Ti-E) equipped with a Nikon A1R confocal scanhead with galvano and resonant scanning mirrors. A 60× water immersion objective (NA=1.2) was used. 488 and 561 nm lasers

Table 7.1: Overview of the number of measurements, the total duration and the total number of frames per ring size, for the experimental and simulated data, for loops and dominoes.

n	Type	Measurements		Duration [min]		Total frames	
		Exp.	Sim.	Exp.	Sim.	Exp.	Sim.
4	Ring	12	20	92	600	8.5×10^4	2.5×10^7
5	Ring		20		600		2.5×10^7
6	Ring	2	20	11	600	1.2×10^4	2.5×10^7
6	Domino	4	20	75	600	8.5×10^4	2.5×10^7
7	Ring		10		300		1.3×10^7

were used to excite, respectively, the Fluorescein or TopFluor and Rhodamine dyes. Laser emission passed through a quarter wave plate to avoid polarization of the dyes and the emitted light was separated by using 500 – 550 nm and 565 – 625 nm filters.

To complement the data obtained from self-assembled loops and dominoes, we used optical tweezers to assemble specific cluster sizes. For the hexamer loops, the probability of forming such a loop using the self-assembly method we used here is low, therefore these were formed exclusively using optical tweezers. Briefly, we employed a homemade optical setup consisting of a highly focused trapping laser manufactured by Laser QUANTUM (1064 nm wavelength). The laser beam entered the confocal microscope through the fluorescent port, after first passing through a beam expander and a near-infrared shortpass filter. The same objective was used for imaging and to focus the trapping laser beam. During the trapping, the quarter wave plate was removed from the light path.

Particle positions were tracked using a custom algorithm[242] available in TrackPy by using the `locate_brightfield_ring` function[188] or using a least-square fit of a Mie scattering based model implemented in HoloPy.[186] Both methods agree to an accuracy of at least 1 px, however we have found that the Mie scattering based model is more robust for tracking multiple particles in close proximity to each other. For all analysis, we only selected rings and dominoes that showed all bond angles during the measurement time, experienced no drift and were not stuck to the substrate. An overview of the total number of measurements, the total duration and the total number of frames per ring size is shown in Table 7.1.

7.2.3 Simulations

We have performed Brownian dynamics simulations with hydrodynamic interactions following the method outlined in Sprinkle et al.[290] using the open-source RigidMultiblobsWall package.[291] The procedure is identical to the method described in Chapter 6, which we now briefly summarize. Hydrodynamic interactions are calculated using the Stokes equations with no-slip boundary conditions. The hydrodynamic

Table 7.2: **Permutation data.** For the rings and dominoes, we generated the $P(N_\theta, n-2)$ configurations obtained by permuting all possible combinations of opening angles. Interpenetrating configurations, which are forbidden due to excluded volume interactions between particles, were removed from this permutation data. The percentages of clusters of the correct topology are calculated relative to the total number of configurations for permutations of the opening angles between 60 and 300 deg.

n	**Type**	$\delta\theta$ [deg]	$P(N_\theta, n-2)$	**Correct topology [%]**
4	Ring	0.04	3.6×10^7	8.3×10^{-3}
5	Ring	0.5	1.1×10^8	2.4×10^{-2}
6	Ring	2.0	2.0×10^8	5.2×10^{-2}
6	Domino	2.0	2.0×10^8	8.8×10^{-4}

mobility matrix is approximated using the Rotne-Prager-Blake (RPB) tensor,[35] which is a modified form of the Rotne-Prager-Yamakawa (RPY) tensor[34,275,292] and accounts for a bottom wall, which is unbounded in the transverse directions. These corrections to the RPY tensor are combined with the overlap corrections described in Wajnryb et al.[292] to prevent particle-particle and particle-wall overlap. The RPB mobility inaccurately describes near-field hydrodynamic interactions and therefore breaks down for small separation distances. This can be overcome by adding a local pairwise lubrication correction to the RPB resistance matrix as described in detail in Sprinkle et al.[290] Based on the full lubrication-corrected hydrodynamic mobility matrix, the Ito overdamped Langevin equation is solved to describe the effect of thermal fluctuations.

We include a gravitational force on the particles to confine them to diffuse close to the bottom wall, as in the experiments. Inter-particle bonds are modeled by harmonic springs of stiffness $1000 k_B T/R^2$ and equilibrium length $2R$, where $R = 1.06\,\mu$m is the particle radius. The bond angle is not restricted. We set the temperature $T = 298$ K, the viscosity of the fluid $\eta = 8.9 \times 10^{-4}$ Pa s, the gravitational acceleration $g = 9.81\,\mathrm{m\,s^{-2}}$, the particle mass $m_p = 9.5 \times 10^{-15}$ kg (by assuming a particle density of $1900\,\mathrm{kg\,m^{-3}}$) and the simulation timestep $\Delta t = 1.42$ ms. For the firm potential that prevents overlap, we use a strength of $4k_BT$ and a cutoff distance[290,293] $\delta_{\mathrm{cut}} = 10^{-2}$. We initialized the particle loops in the configuration given by the regular polygon of the same size and we used a rectangular configuration, i.e. all opening angles equal to 90 or 180 deg, for the hexamer dominoes. Then, these initial configurations were randomized by running the integration for a simulated time of 60 s prior to saving the configurations, to ensure a proper equilibration of the particle positions, bond lengths, velocities and opening angles. The particle positions were saved every 8 simulation steps to obtain a final framerate of approximately 90 fps. An overview of the total number of simulations, the total duration and the total number of saved frames per cluster type is shown in Table 7.1.

For comparison to the simulated and experimental data, we generated data in which the rings or dominoes are completely non-interacting and freely-jointed up to steric exclusions in the following manner: we generated all $(n-2)$-permutations of the N_θ opening angles θ_i, which gives a total number of $P(N_\theta, n-2) = N_\theta!/(N_\theta - (n-2))!$ combinations of θ_i. Here, the number of opening angles is $N_\theta = (360 - 2 \times 60)/(\delta\theta)$, where $\delta\theta$ denotes the bin width. Then, we removed those combinations that are forbidden because of steric exclusions between particles. After removing these configurations, we checked if the topology of the structure was correct and removed configurations of the wrong topology, resulting in the final allowed combinations, which we call "permutation data". In Table 7.2, we show the bin widths $\delta\theta$ for each n, as well as the total number of generated permutations $P(N_\theta, n-2)$ and the percentage of configurations of the correct topology, i.e. either a ring or a domino.

7.2.4 Diffusion tensor analysis

Definition of the diffusion tensor

We determined the short-time diffusivity of the rings and dominoes, both as function of their instantaneous shape for the tetramer rings, as well as averaged over all possible configurations for all loops and dominoes. Because the rings are sedimented to the bottom substrate, we consider only the quasi-2D, in-plane diffusivity. For the flexible tetramer loops, we calculated a 4×4 diffusion tensor, where the four degrees of freedom correspond to translational diffusivity in x and y, rotational diffusivity and the flexibility of the tetramer loop, which is described by the diffusivity of the opening angle θ. Specifically, the x- and y-directions are schematically shown for one configuration in Figure 7.2a and defined by Equation 7.4. The rotation angle used for determining the rotational diffusivity is indicated in Figure 7.2a and is the angle of the $x(\tau)$ relative to $x(\tau = 0)$, i.e. the angle of the body-centered x-axis of the current frame relative to the body-centered x-axis of the reference frame at $\tau = 0$. The flexibility is calculated from the mean-squared displacement of the opening angle θ, which is depicted in Figure 7.1e. θ is defined in such a way that it is always less than or equal to 120 deg.

The diffusion tensor elements of the tetramer loops were determined analogously to the trimers.[244] Briefly, for each pair of frames, we determined the initial shape of the ring, which is characterized by the opening angle θ. The short time diffusion tensor is then calculated from the trajectories in the following way:

$$\boldsymbol{D}[ij](\theta) \equiv \frac{1}{2} \frac{\partial \langle \Delta i(\theta) \Delta j(\theta) \rangle_\tau}{\partial \tau}, \tag{7.1}$$

with τ the lag time between frames, $\langle \cdots \rangle_\tau$ denotes a time average over all pairs of frames τ apart and $\Delta i(\theta) = i(\theta, t+\tau) - i(\theta, t)$ is the displacement of the i-th diffusion tensor element, which depends on the instantaneous shape given by θ. The average diffusion tensor elements $\boldsymbol{D}[ij]$ were obtained by fitting the overall slope of the mean (squared) displacements as a function of lag time τ. We considered lag times up to

0.25 s, set by the frame rate of the experimental data. We only considered trajectories where the variation in θ did not exceed the edges of the bin describing the initial shape. That is, we divided the possible values of θ in bins and calculated the short-time diffusivity for all combinations of lag times where $\theta(\tau)$ remained in the same bin as $\theta(0)$, which were then stored according to their respective θ-bins. In that way, we calculated the diffusion tensor elements separately for each initial shape.

For fitting the slopes, we used a Bayesian method to find an estimate of the posterior probability distribution, by using an Affine Invariant Markov chain Monte Carlo (MCMC) Ensemble sampler method as implemented in the Python packages `lmfit`[246] and `emcee`.[207] This allowed us to obtain accurate estimates of the error and the maximum likelihood estimate (MLE) of the parameters. Parameter values were initialized using a standard least-square fit, appropriate bounds on the parameter values were implemented as priors. We estimated the autocorrelation time τ_{acor} of the MCMC chain using the built-in methods and ran the analysis for at least $100\tau_{\text{acor}}$ steps, where we discarded the first $2\tau_{\text{acor}}$ steps (corresponding to a burnin phase) and subsequently used every other $\tau_{\text{acor}}/2$ steps (known as thinning). We used 500 independent chains (or walkers). The reported values correspond to the maximum likelihood estimate of the resulting MCMC chains, the reported uncertainties correspond to the 16$^{\text{th}}$ and 84$^{\text{th}}$ percentiles of the obtained posterior probability distribution. For fitting the MSDs, we used a linear model with zero intercept.

For all rings and dominoes, we considered the shape-averaged, quasi-2D translational diffusion coefficient D_T, which corresponds to in-plane diffusivity above the wall. Additionally, we determined the rotational diffusion coefficient $D[\alpha\alpha]$ from the mean squared angular displacement of the x-axis (defined in Equation 7.4, see Figure 7.7a for a schematic depiction for the hexamer loop), which describes the rotational diffusivity around an axis perpendicular to the substrate. Finally, we determine the overall cluster flexibility $D[\boldsymbol{\theta\theta}]$ by calculating the mean squared displacements of the $(n-2)$ opening angles θ_i as follows:

$$\langle|\boldsymbol{\Delta\theta}|^2\rangle = \langle|(\Delta\theta_1, \ldots, \Delta\theta_{n-2})|^2\rangle, \tag{7.2}$$

so that the flexibility $D[\boldsymbol{\theta\theta}]$ is given by

$$\langle|\boldsymbol{\Delta\theta}|^2\rangle = 2(n-2)D[\boldsymbol{\theta\theta}]t, \tag{7.3}$$

analogously to the other diffusion tensor elements.

The definition of the coordinate system

As tracking point, we considered the center of diffusion (c.d.) which coincides with the center of mass of colloidal rings and dominoes, because the choice of origin is expected to affect the magnitude of the diffusion tensor.[105,269] The coordinate system used here is identical to the coordinate system described in Chapter 6 and we briefly summarize its definition here. The c.d. was calculated from $\boldsymbol{A}_{ij}$ defined by Equation 2.16 of Cichocki et al.[269] using the RPB tensor[35] with lubrication corrections as the

inter-particle mobility matrix $\boldsymbol{\mu}_{ij}$. This tensor includes wall corrections, as discussed previously in Section 7.2.3. The c.d. was determined from the simulated particle positions, because the height above the bottom wall was not measured experimentally, but is needed to calculate the wall corrections. The direction of the body-centered x- and y-axes was determined as function of the tracking point $\boldsymbol{r}_{t.p.}$, which defines the origin of the body-centered coordinate frame. We define $\boldsymbol{r}_{t.p.} = \rho_1\boldsymbol{r}_1 + \rho_2\boldsymbol{r}_2 + \cdots + \rho_n\boldsymbol{r}_n$, which defines the location of the tracking point as a linear combination of the particle positions (Equation 2.2 and 2.3 of Cichocki et al.[269]). $\boldsymbol{\rho} = (\rho_1, \rho_2, \ldots, \rho_n)$ is a weight vector which determines how much weight is accorded to each particle in the calculation of the tracking point $\boldsymbol{r}_{t.p.}$. As an example, for a tetramer ring, $\boldsymbol{\rho} = (1/n = 1/4, 1/4, 1/4, 1/4)$ when the tracking point is chosen to be the c.d., or equivalently, the center of mass.

The direction of the x-axis was chosen as

$$\hat{\boldsymbol{x}} = \pm\left[\frac{\boldsymbol{r}_{t.p.,1} + \cdots + \boldsymbol{r}_{t.p.,s_1}}{\rho_1 + \cdots + \rho_{s_1}} - \frac{\boldsymbol{r}_{t.p.,s_2} + \cdots + \boldsymbol{r}_{t.p.,n}}{\rho_{s_2} + \cdots + \rho_n}\right], \tag{7.4}$$

where $\boldsymbol{r}_{t.p.,i}$ is the i-th coordinate of the tracking point and the bead chain is split into two parts with equal numbers of particles according to

$$\begin{cases} s_1 = s_2 = \lceil \frac{n}{2} \rceil & \text{for odd } n \\ s_1 = \lceil \frac{n}{2} \rceil, s_2 = s_1 + 1 & \text{for even } n \end{cases} \tag{7.5}$$

$\hat{\boldsymbol{y}}$ is then chosen such that $\hat{\boldsymbol{x}}$ and $\hat{\boldsymbol{y}}$ form a right-handed coordinate system, where the direction of $\hat{\boldsymbol{y}}$ is chosen to point away from the central part of the cluster towards the tracking point, i.e. along $\boldsymbol{r}_{t.p.} - \left(\boldsymbol{r}_{s_1} + \boldsymbol{r}_{s_2}\right)/2$. This orientation was determined for every frame, which fixed the orientation of the body-centered coordinate system $\boldsymbol{x}(\tau = 0), \boldsymbol{y}(\tau = 0)$. For subsequent lag times, the direction of $\boldsymbol{y}(\tau)$ was chosen such that $\boldsymbol{y}(\tau = 0) \cdot \boldsymbol{y}(\tau) > 0$, i.e. the direction of $\boldsymbol{y}$ does not change sign. The resulting coordinate system relative to the c.d. is visualized for the tetramer loops in Figure 7.2a.

7.3 Results and Discussion

7.3.1 Free energy of flexible tetramer loops

To identify the most likely conformations of micron-sized, flexible ring-like structures in solution, we have studied an experimental model system of colloidal loops and dominoes. Additionally, we have compared our experimental data to Brownian dynamics simulation data, where hydrodynamic interactions between particles and the substrate are taken into account via the Rotne-Prager-Blake (RPB) tensor,[35] overlap corrections[292] and a local pairwise lubrication correction[290] (see Section 7.2.3 for details). The experimental colloidal loops were formed from four or six spherical colloid-supported lipid bilayers (CSLBs).[85,110,112,242] As shown in Figure 7.1c, CSLBs are colloidal silica particles surrounded by a fluid lipid bilayer, which is formed by the rupture and subsequent spreading of small unilamellar vesicles. DNA linkers

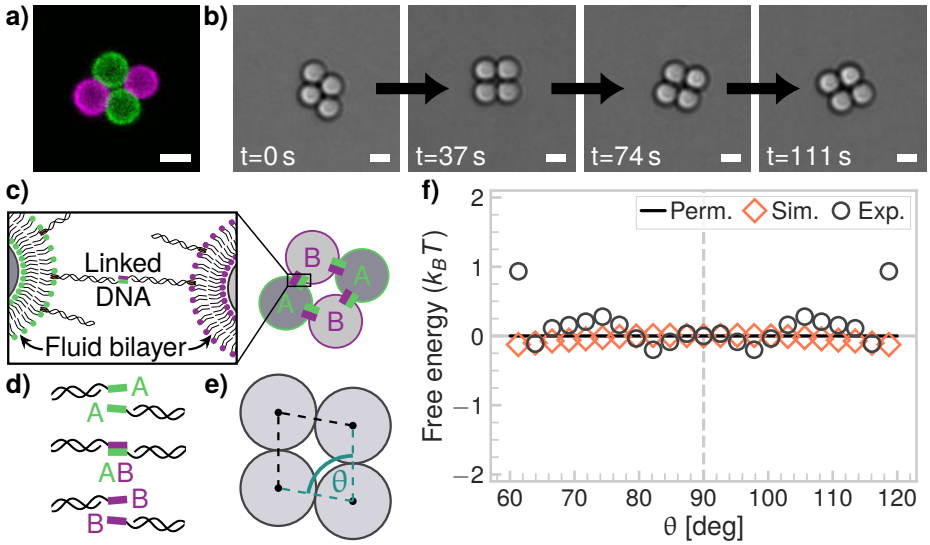

Figure 7.1: **Free energy of flexible tetramer loops. a)** Confocal image and **b)** bright field snapshots of a flexible tetramer ring, which shows shape changes. Scalebars are 2 μm. **c)** The flexible rings are built from colloid-supported lipid bilayers (CSLBs). CSLBs consist of spherical silica colloids coated with a fluid lipid bilayer. DNA linkers are inserted into the bilayer using a hydrophobic anchor. Because the bilayer is fluid, the linkers can diffuse on the surface and therefore, the particles can move with respect to each other whilst staying bonded. **d)** The DNA linkers are functionalized with two complementary sticky ends A and B, so that particles functionalized with A-type linkers can only form bonds with particles coated with B-type linkers. **e)** The definition of the opening angle θ. **f)** The free energy of tetramer rings shows small fluctuations in the ∘ experimental and ⋄ simulated data, but these are insignificant compared to the thermal energy k_BT and absent in the permutation data (Perm.).

with hydrophobic anchors can be inserted into this lipid bilayer. We have used two types of DNA linkers with different single-stranded overhangs, or sticky ends, which we label A and B. As depicted in Figure 7.1d, the A-type sticky end is complementary to the B-type sticky end and therefore, bonds can be formed between the A and B strands only. After such bonds have formed, particles can still rearrange with respect to each other, because the DNA linkers can diffuse in the fluid lipid bilayer. The use of two different sticky ends A and B that are complementary to each other has a distinctive advantage over using a single, self-complementary or palindromic sticky end. Namely, by using two distinct sticky ends, we can prevent adhesion between two opposing A-type or B-type particles in the ring, which would, for a tetramer loop, cause it to lose its reconfigurability. Namely, the tetramer loop would become mechanically rigid because of the extra bond. Moreover, the structure would no longer have a ring topology. In Figure 7.1a, we show a confocal microscopy image

of a tetramer ring. Additionally, in Figure 7.1b we show a time series imaged using brightfield microscopy, in which shape transitions between a diamond and a square configuration of the loop can be observed.

To answer whether there is a preference of either the diamond or square configuration, or even some intermediate configuration, we analyze the free energy of the flexible tetramer loops as function of their opening angle θ, which is schematically depicted in Figure 7.1e. We analyzed the free energy of colloidal rings as function of their shape by calculating the probability density function of the opening angle. From the probability density function calculated from the histogram, we determined the free energy using Boltzmann weighing,

$$\frac{F}{k_B T} = -\ln p + \frac{F_0}{k_B T}, \tag{7.6}$$

where F is the free energy, k_B is the Boltzmann constant, T the temperature, p is the probability density and F_0 is a constant offset to the free energy. As shown in Figure 7.1f, in the simulation data there is a very small preference of $\approx 0.1 k_B T$ for the diamond configuration ($\theta \approx 60$ or 120 deg). On the contrary, in the experimental data, there seems to be a small preference of $\approx 0.3 k_B T$ for $\theta \approx 82$ or 98 deg. Because these preferences are negligible compared to the thermal energy, we conclude that all configurations are essentially equally probable.

7.3.2 Diffusion of flexible tetramer loops

Because all configurations are equally probable, the tetramer loops continuously change their shape. This could have implications for their short-time diffusive behavior, as we have observed previously for colloidal chains[244] (see also Chapter 5 and 6). In Figure 7.2b, we show the shape-dependent, short-time translational diffusivity of the flexible tetramer rings with respect to the coordinate system shown in Figure 7.2a, which is defined in Section 7.2.4. The agreement between the simulated and experimental data is good. In the simulation data, there is virtually no difference between the diffusivity in the x- (Figure 7.2c) and y-direction (Figure 7.2d). Variations in the experimental data are larger, but likely caused by the experimental uncertainty.

The fact that the translational diffusivity does not depend on shape implies that the translational diffusivity of the tetramer rings can be described by the diffusion coefficient of a sphere of some effective radius. Using the lubrication-corrected RPB tensor described in Section 7.2.3, we have calculated the diffusion coefficients of spheres of radii $R_{\text{eq.vol.}}$ and R_g, located just above the substrate. Here $R_{\text{eq.vol.}} = \sqrt[3]{4}R$, i.e. the radius of a sphere with the same volume as the tetramer loop, with $R = 1.06$ μm the radius of an individual sphere of the ring. The radius of gyration R_g is given by

$$R_g = \left[\frac{1}{n^2} \sum_{i=1}^{n} |\boldsymbol{r}_i - \boldsymbol{r}_{c.m.}|^2 \right]^{1/2}, \tag{7.7}$$

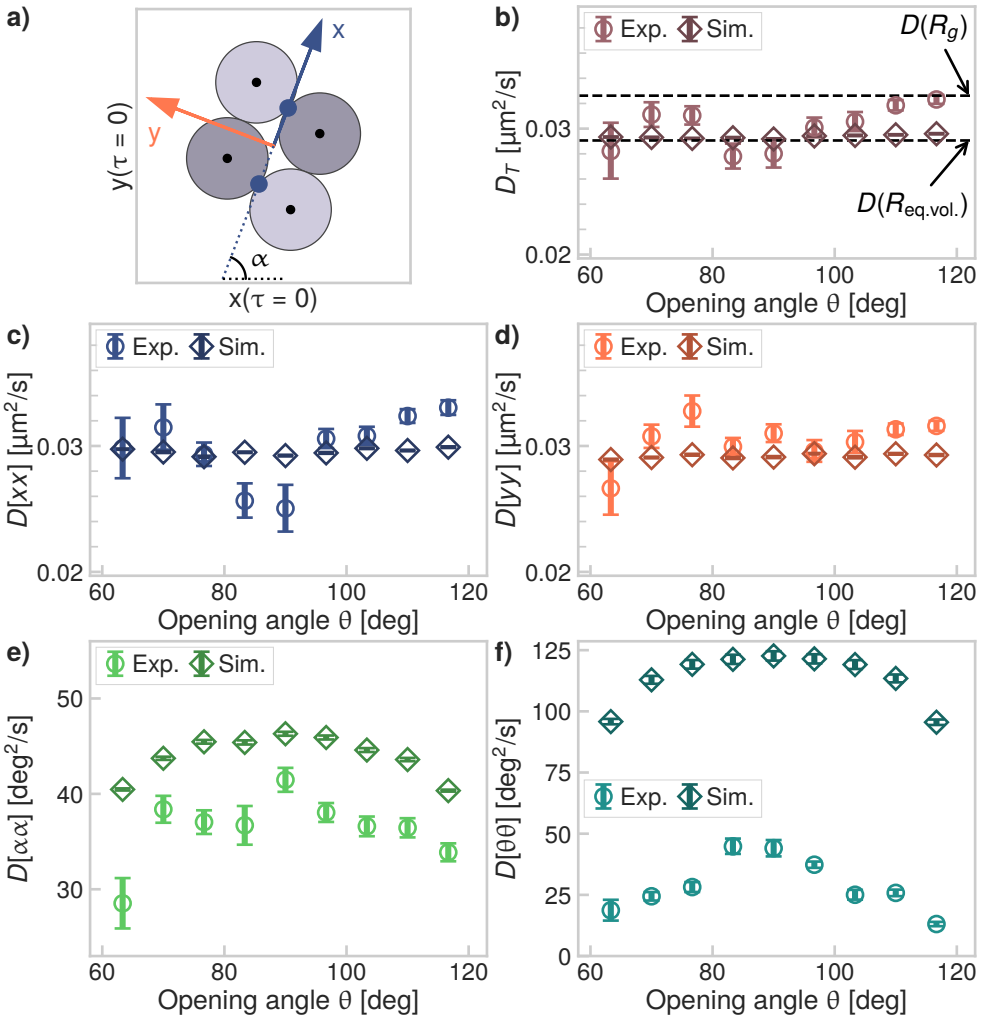

Figure 7.2: **Diffusion of flexible tetramer loops. a)** An illustration of the coordinate system used to analyze the diffusivity of the tetramer rings, as defined in Section 7.2.4. In panels b-f, we have compared the diffusion tensor elements calculated from ⋄ simulated and ∘ experimental data. **b)** The in-plane translational diffusion coefficient D_T. We find that $\langle D_{\text{exp.}}/D_{\text{sim.}} \rangle = 1.03 \pm 0.05$. The translational diffusion along the **c)** x- and **d)** y-directions. **e)** The rotational diffusivity, for which $\langle D_{\text{exp.}}/D_{\text{sim.}} \rangle = 0.83 \pm 0.05$. **f)** Compared to the simulated flexibility, the experimental flexibility is much lower, namely $\langle D_{\text{exp.}}/D_{\text{sim.}} \rangle = 0.25 \pm 0.07$. Both the rotational diffusivity and flexibility terms show a clear maximum for the square configurations, where θ is close to 90 deg. All off-diagonal diffusion tensor elements are close to zero.

where $\boldsymbol{r}_i$ is the position of the i-th sphere and $\boldsymbol{r}_{c.m.}$ is the position of the center of mass of the loop. The resulting near-wall diffusion coefficients are indicated in Figure 7.2b, where we plot the in-plane diffusion coefficient D_T. Comparison of the obtained diffusion coefficients to the experimental and simulated data brings us to the conclusion that the diffusivity of the tetramer rings is captured best by the diffusion coefficient of an effective sphere of the same volume, e.g. a sphere of radius $R_{\text{eq.vol.}}$.

Next, we consider the rotational diffusivity of the loops, which is defined as the in-plane rotation of the x-axis or, equivalently, rotation of the cluster around the out of plane axis, for a plane parallel to the substrate. From Figure 7.2e, we see that the experimentally measured rotational diffusivity is slightly lower than the simulated rotational diffusivity, but both show the same shape dependence. Specifically, the more compact square configuration has a higher rotational diffusivity than the more extended diamond structure, as expected.

Finally, from Figure 7.2f, we conclude that also the flexibility of the tetramer loop depends on its shape: the flexibility is larger for square configurations than for diamond configurations. This indicates that more open structures have a higher flexibility, as we have also observed for chains in Chapter 6. For chains of CSLBs, we have found that the experimental flexibility is 75 to 80 % of the flexibility of the simulated chains, which is probably caused by friction of the DNA linker patch (see Chapter 6). For the tetramer loops, however, we observe a drastically lower flexibility, namely, the experimental flexibility is just 25 % of the simulated one, as shown in Figure 7.2f. This indicates that the tetramer loops experience more interparticle friction compared to the tetramer chains. We will discuss this difference in more detail in Section 7.3.5.

7.3.3 Conformations of pentamer rings

Now that we have characterized the conformations and diffusivity of flexible colloidal tetramer rings, we ask how the possible ring conformations change by increasing the ring size, as this also increases the degrees of freedom of the loop. In order to build a larger ring in our experiments, we need an even number of spheres, because only the A-type DNA linker-coated colloids can bind to the B-type ones, as depicted in Figure 7.1d. This limitation could be overcome in future experiments by using a larger variety of sticky ends, or by using palindromic sequences, where steps should be taken to prevent the formation of more than two bonds per particle. Instead, here we briefly discuss the possible conformations of pentamer loops using only simulated data, before discussing hexamer rings in greater detail.

As shown in Figure 7.3a, the free energy in terms of the opening angles of the pentamer ring shows a preference for angles smaller than 120 deg, for both the simulated and permutation data. This is in contrast with the flat free energy landscape that we have observed for the tetramer rings. The angles are defined in Figure 7.3 and because the angles are indistinguishable, we have used all five opening angles to calculate the free energy.

Next, we have looked at correlations between opening angles θ_i and $\theta_{j>i}$. For the tetramer loop, the two opening angles are perfectly correlated according to θ_2 =

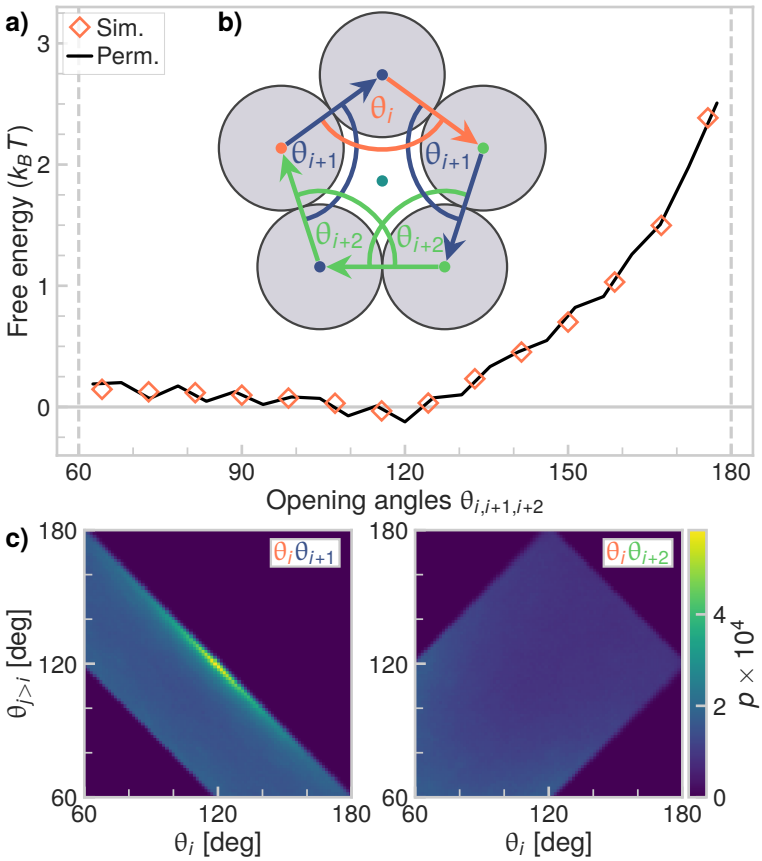

Figure 7.3: **Conformations of pentamer loops. a)** The free energy of pentamer loops as function of one of the opening angles θ_j, with $j \in [i, i+1, i+2]$. The free energy increases as function of θ_j because of constraints imposed by the ring structure. The simulated and permutation data are shown. **b)** Schematic showing the definition of the opening angles θ_j. Three angles are needed to fully describe the conformation of a pentamer ring. **c)** Correlations between the opening angles θ_i and $\theta_{j>i}$ for the simulated data.

180 deg $- \theta_1$. Adding an additional particle to the ring structure also adds a degree of freedom. This can be shown from the Maxwell counting rule, which counts the number of bonds $n_{B,R}$ needed for structural rigidity as[309]

$$n_{B,R} = dn - \frac{d(d+1)}{2} = 2n - 3 \tag{7.8}$$

with $d = 2$ the number of dimensions and n the number of particles. For a loop, there are $n_B = n$ bonds between particles and therefore there are $n_{B,R} - n = n - 3$ degrees of freedom or floppy modes. Going from one floppy mode for the tetramer loop to two for the pentamer loop decreases the correlations between the opening angles, as shown in Figure 7.3c. While the possible combinations of angles $\theta_i\theta_j$ for $j > i$ are still partially constrained by the ring structure, more combinations are geometrically allowed compared to the smaller tetramer rings. We observe that the correlations between any two neighboring opening angles, i.e. θ_i and θ_{i+1}, are stronger than correlations between the more distant opening angles θ_i and θ_{i+2}.

7.3.4 Conformations of hexamer rings and dominoes

We have shown how the free energy of the opening angles of a tetramer loop differs from a pentamer loop, that has an additional floppy mode. The pentamer loop could not be assembled using our experimental scheme. In the experiments, only loops with an even number of particles can be formed, because of the two complementary sticky ends that we use for binding. Therefore, we now study the experimentally accessible extension of the tetramer loop by adding two particles to the ring, so that we obtain hexamer rings. The hexamer rings were formed manually using optical tweezers, because the probability to form them via self-assembly is low. This limitation could be overcome in other ways as well, for example by using template-assisted self-assembly techniques[3] or by using multiple DNA strands to achieve a more fine-grained control over the self-assembly process.[56] In Figure 7.4a, we show a confocal microscopy image of a hexamer ring. From brightfield snapshots in Figure 7.4b, we see that these hexamer rings show a greater variety of shapes compared to the tetramer rings. While the tetramer loop only has one internal degree of freedom, the hexamer loop has three internal degrees of freedom. Its shape can be characterized by four opening angles, depicted in the schematic of Figure 7.4d.

Next, we analyze the free energy of hexamer loops as function of the opening angles in order to determine whether some conformations are preferred over others. Because the loop has no beginning or end, all angles are equivalent and we make a single histogram of the values of all six opening angles. Using Equation 7.6, we obtain the free energy in terms of opening angle, which is shown in Figure 7.4c. For opening angles below $\theta_j \approx 150$ deg, the resulting free energy shows only small variations compared to the thermal energy, for the simulation, permutation and experimental data. For angles larger than $\theta_j \approx 150$ deg, the free energy increases as function of the opening angle and the difference between $\theta_j = 150$ deg and 240 deg is on the order of $4k_BT$. Angles greater than 180 deg correspond to compact and curved structures,

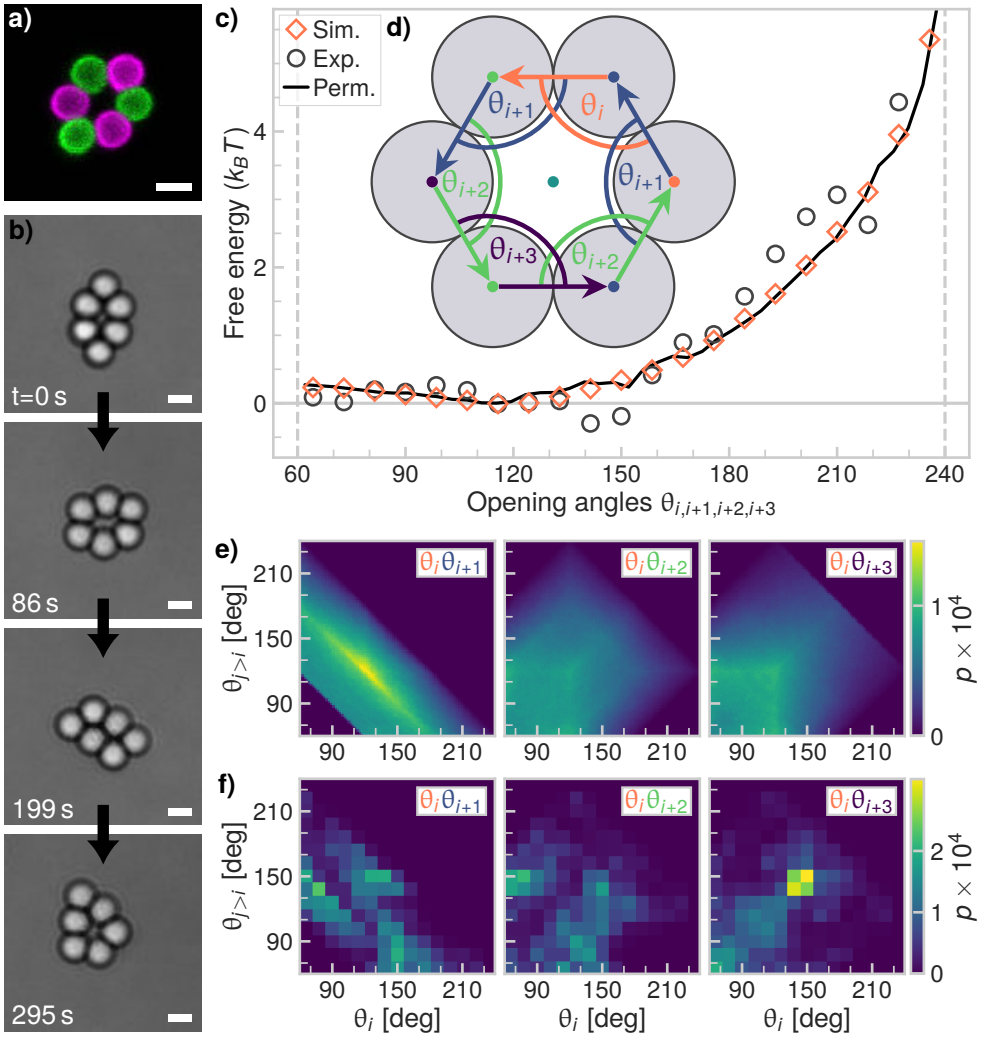

Figure 7.4: **Flexible colloidal hexamer rings. a)** Confocal image. Scalebar is 2 µm. **b)** Snapshots of hexamer rings. A variety of shapes can be observed. Scalebars are 2 µm. **c)** The free energy of hexamer loops as function of the opening angles θ_j, with $j \in [i, i+1, i+2, i+3]$. The free energy increases as function of θ_j because of constraints imposed by the ring structure. The simulated, the permutation and the experimental data are shown. **d)** Schematic showing the definition of the opening angles θ_j. Four angles are needed to fully describe the conformation of a hexamer ring. **e-f)** Correlations between the opening angles θ_i and $\theta_{j>i}$ for **e)** the simulated data and **f)** the experimental data.

which explains why these opening angles are not observed as often as others. For example, there is only one structure in which one of the opening angles is equal to 240 deg.

To study the interplay of the opening angles of the hexamer loops in greater detail, we have calculated the correlations between angles $\theta_i\theta_j$ with $j > i$ for the angles defined in Figure 7.4d, as shown in Figure 7.4e and f for the simulated and experimental data, respectively. For the experimental data, trends are hard to distinguish and more data is needed to disentangle the effect of the four degrees of freedom. Correlations in the simulated data are easier to discern, as shown in Figure 7.4e. The first thing that stands out is that any two neighboring angles are more strongly correlated than more distant opening angles, as can be seen by comparing the correlations between $\theta_i\theta_{i+1}$ to those between $\theta_i\theta_{i+2}$ and $\theta_i\theta_{i+2}$. This is qualitatively the same as what we have observed for pentamer loops. For opening angles θ_i, θ_{i+1} specifically, there is a strong negative correlation given by $\theta_{i+1} \approx 240\,\text{deg} - \theta_i$. Moreover, as expected from the geometry of the ring, it can be seen that the sum of the angles needs to stay within the range $180\,\text{deg} \leq \theta_i + \theta_{i+1} \leq 300\,\text{deg}$. For the correlations between more distant opening angles, the range of accessible angles in Figure 7.4e and f is larger for $\theta_i\theta_{i+2}$ and $\theta_i\theta_{i+3}$ compared to $\theta_i\theta_{i+1}$. Specifically, $\theta_i + \theta_{i+2,i+3} \leq 360\,\text{deg}$ and $\left|\theta_i - \theta_{i+2,i+3}\right| \leq 120\,\text{deg}$. These constraints arise from the topological constraint that the particles form a ring and from the fact that particles cannot interpenetrate each other.

In addition to hexamer rings, hexamer dominoes can also be formed via self-assembly. In fact, their formation is more likely than that of hexamer rings, because they can be obtained from a greater number of initial cluster topologies, such as tetramer loops and related structures. The structure we call a hexamer domino is a (2, 3)-grid, 3-ladder or domino graph[308] where the particles are situated on the vertices, as shown in the confocal image of Figure 7.5a and in the brightfield snapshots of Figure 7.5d. As depicted by the schematic in Figure 7.5b, the hexamer domino has the same structure as the hexamer ring of Figure 7.4, but one extra bond, as indicated by the yellow circle.

Because of the extra bond, the hexamer dominoes behave very differently compared to the hexamer rings. While the rings have three floppy modes, the dominoes have only two, as given by Equation 7.8. Their possible variety in shapes is therefore smaller, as shown in Figure 7.5d. In turn, their conformations can be uniquely described by two opening angles instead of four angles for the hexamer loop, as shown in the schematic in Figure 7.5c, where we also define the indices of all six opening angles. Taking the same approach as for the hexamer rings, we have calculated the free energy as function of the opening angles. However, because for the dominoes not all opening angles are indistinguishable from each other, we consider the opening angles $\theta_{\alpha,i}$ and $\theta_{\beta,j}$ separately, as shown in Figure 7.5e for the experimental, simulated and permutation data. The resulting free energy landscape is markedly different from the one for hexamer rings in Figure 7.4c because of the additional bond that is formed. For $\theta_{\alpha,i}$, the free energy landscape is very similar to that of the tetramer loops in

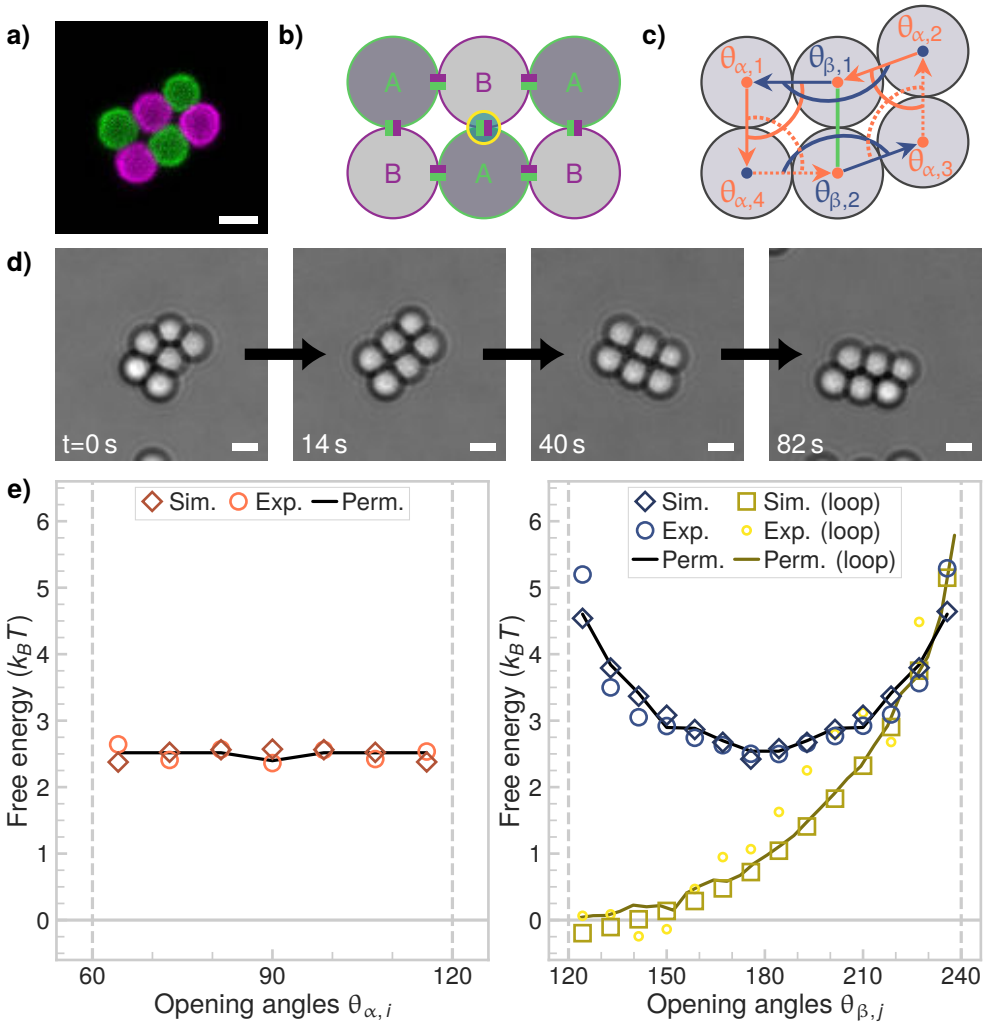

Figure 7.5: **Flexible hexamer dominoes. a)** Confocal image of a hexamer domino cluster. Scalebar is 2 µm. **b)** An additional bond is formed for the hexamer dominoes compared to the loops shown in Figure 7.4, as indicated by the yellow circle. **c)** Schematic of the definition of the opening angles. Only two angles are needed to fully describe the conformations of the dominoes. **d)** Brightfield microscopy images of hexamer dominoes. Due to the additional bond compared to the rings in Figure 7.4, a smaller variety of shapes is possible. Scalebars are 2 µm. **e)** The free energy of hexamer dominoes as function of the opening angles $\theta_{\alpha,i}$ (left) and $\theta_{\beta,j}$ (right), as defined in panel c. The simulated, the permutation and the experimental data are shown.

Figure 7.1f. This makes sense because the hexamer domino essentially consists of two flexible tetramer loops that share one side. The angles $\theta_{\beta,j}$ are the opening angles between the two tetramer loop segments, as indicated in the schematic in Figure 7.5c. For those angles, the most likely value lies around 180 deg. We show the free energy of the hexamer rings in the same panel of Figure 7.5e. It is clear that the free energy of the dominoes for $\theta_{\beta,j}$ partially overlaps with the free energy of the hexamer rings for $\theta_{\beta,j} > 210$ deg, because both correspond to compactly curved shapes. For the dominoes, the free energy is symmetric around 180 deg as curving the structure as shown in Figure 7.5c "upwards" (e.g. $\theta_{\beta,1} > 180$ deg) or conversely, "downwards" (e.g. $\theta_{\beta,1} < 180$ deg) results in the same shape.

In conclusion, in this section we have characterized the possible conformations of flexibly-linked colloidal hexamer rings and dominoes. Contrary to the tetramer loops, we have found that there are preferred values of the opening angles for the hexamer loops and dominoes. These have, compared to tetramer loops, one and two additional degrees of freedom for dominoes and rings, respectively. Our results show that the exact topology of a flexible structure and especially the number of floppy modes, have a large effect on whether or not certain conformations are preferred over others.

7.3.5 Gyration radii of rings, dominoes and chains

So far, we have characterized the behavior of flexibly linked tetramer, pentamer and hexamer loops, in addition to flexible hexamer dominoes. Now, we compare their conformational and diffusive behavior to each other and to flexibly linked chains of the same number of spheres. A natural measure to compare the tetramer and hexamer rings is the radius of gyration R_g as defined in Equation 7.7, which is a measure for the size of the loops. Furthermore, it is often used to quantify the extent of polymer chains, or, as we have discussed in Chapter 6, for flexibly-linked colloidal bead-chains.

The theoretical radius of gyration of tetramer loops is constant and its value is equal to $b/\sqrt{2} \approx 0.708b$, with b the bond length. From the experimental and simulated data, we obtain R_g values of $(0.71 \pm 0.01)b$ and $(0.708 \pm 0.004)b$, respectively. This slight spread around the expected value of R_g can be attributed to variations in the bond length b. These variations are most likely caused by tracking uncertainties and the limited wiggle room stemming from the DNA linkers in the experimental data. In the simulated data, these variations stem from the variations in particle separation distance allowed by the harmonic potential that keeps the particles bonded. Altogether, deviations from the expected radius of gyration are small. Tetramer chains on the other hand, show a variation in R_g from $0.71b$ to $1.12b$ with a median value of $0.93b$ (see Chapter 6). That is, their minimal size measured by R_g is equal to the size of a loop, which is the most compact structure of four particles, but on average the chains are more extended. This has implications for the diffusivity as well, which we will discuss in Section 7.3.6.

Contrary to tetramer loops, the radius of gyration of pentamer rings is not constant.

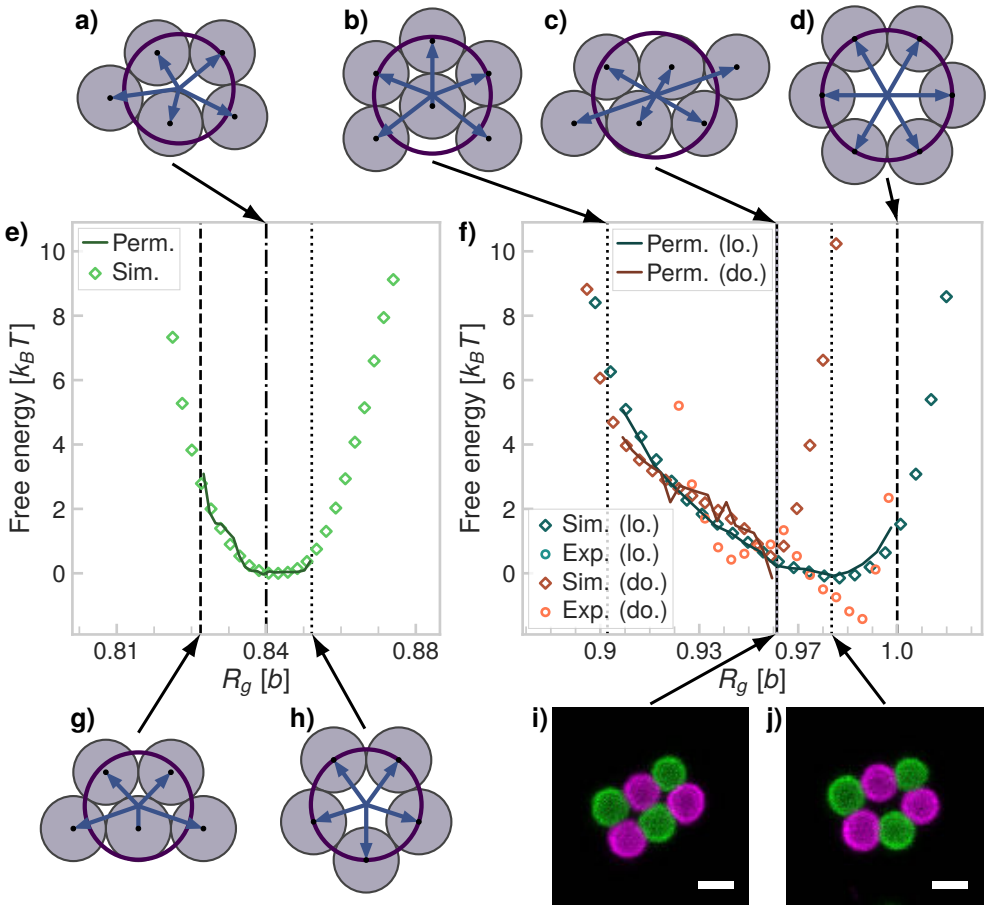

Figure 7.6: **Radius of gyration of pentamer and hexamer rings and dominoes.** Schematics of **a)** a pentamer ring, **b)** the most compact hexamer ring, **c)** a hexamer ring or domino, **d)** the regular hexagon, which is the most extended hexamer ring. **e-f)** The free energy as function of the radius of gyration normalized by the average bond length b for **e)** pentamer and **f)** hexamer loops (lo.) and dominoes (do.). Experimental, simulated and permutation (Perm.) data are shown. The R_g values corresponding to the schematics are indicated on the plot, as well as the R_g values corresponding to the structures shown in the confocal images of panels i and j. **g-h)** Schematics of **g)** the most compact and **h)** the most extended pentamer loop. **i-j)** Confocal images of **i)** a hexamer domino and **j)** a hexamer ring. Scale bar are 2 µm. In panels a-d and g-h, a circle centered at the c.m. with a radius equal to the radius of gyration is shown for all structures.

In Figure 7.6e, the free energy of pentamer rings is shown in terms of R_g. There is a preference for structures of R_g value between the conformation shown in the schematic of Figure 7.6a and the most extended structure with the largest R_g, which is the regular pentagon schematically shown in Figure 7.6h. The free energy of the most compact conformation, which is depicted in Figure 7.6g, is approximately $3k_BT$ higher than that of the more extended structures. We note that the range of R_g in the simulated data exceeds that of the permutation data, which again is caused by variations in the bond length b. However, these variations are smaller than 5 % of the average R_g. Again, the radius of gyration of the rings is much smaller than that of the pentamer chains in Chapter 6, which varies between the smallest value observed for the ring structure in Figure 7.6g and approximately $4b$. This will affect their diffusivity as well, as we will discuss in Section 7.3.6.

Following the same trend, the hexamer rings show larger variations in R_g compared to the pentamer rings. The distribution between the most compact shape depicted in Figure 7.6b and the most extended shape in Figure 7.6d is not symmetric: we find a minimum in the free energy in terms of R_g for structures that correspond to the confocal microscopy image shown in Figure 7.6j, as can be seen from the free energy plotted in Figure 7.6f. In the same graph, we show the free energy of hexamer dominoes in terms of R_g. We find that the possible variation in R_g is smaller for the dominoes compared to the rings, as is expected because they have one degree of freedom less than the rings and as a result, can adopt a smaller variety of conformations. Additionally, the dominoes are on average more compact than the rings, but show the same trend in free energy as function of R_g. This difference indicates that the average diffusivity of hexamer dominoes will also differ from hexamer rings, as we will discuss in Section 7.3.6, where we will also compare their diffusivity to hexamer chains. Finally, we stress that R_g does not uniquely define the shape of the rings and dominoes, as can be seen by comparing the schematic of Figure 7.6c to the confocal image of Figure 7.6i, which have a different conformation but the same value of R_g. Nonetheless, we have shown that the radius of gyration is a useful measure to compare the free energy of a variety of different structures of different topologies in terms of their extent, which in turn affects their diffusive properties.

7.3.6 Shape-averaged diffusivity of rings, dominoes and chains

Having shown that the radius of gyration of the rings and dominoes is smaller on average than that of chains, we now compare the average diffusivities of rings, dominoes and chains. To do so, we analyze the diffusivity of the relative to the same definition of the coordinate system for all structures as defined by Equation 7.4 and depicted schematically in Figure 7.2a for the tetramer loops, in Figure 7.7a for the hexamer rings and in Chapter 6 for the chains.

First, we compare the average translational diffusivity of all structures in Figure 7.7b. The translational diffusivity of rings decreases as function of their size, as expected and as we have previously shown for flexible chains. In the experiments, however, both diffusivities are the same, and we conclude that more data is needed to reliably

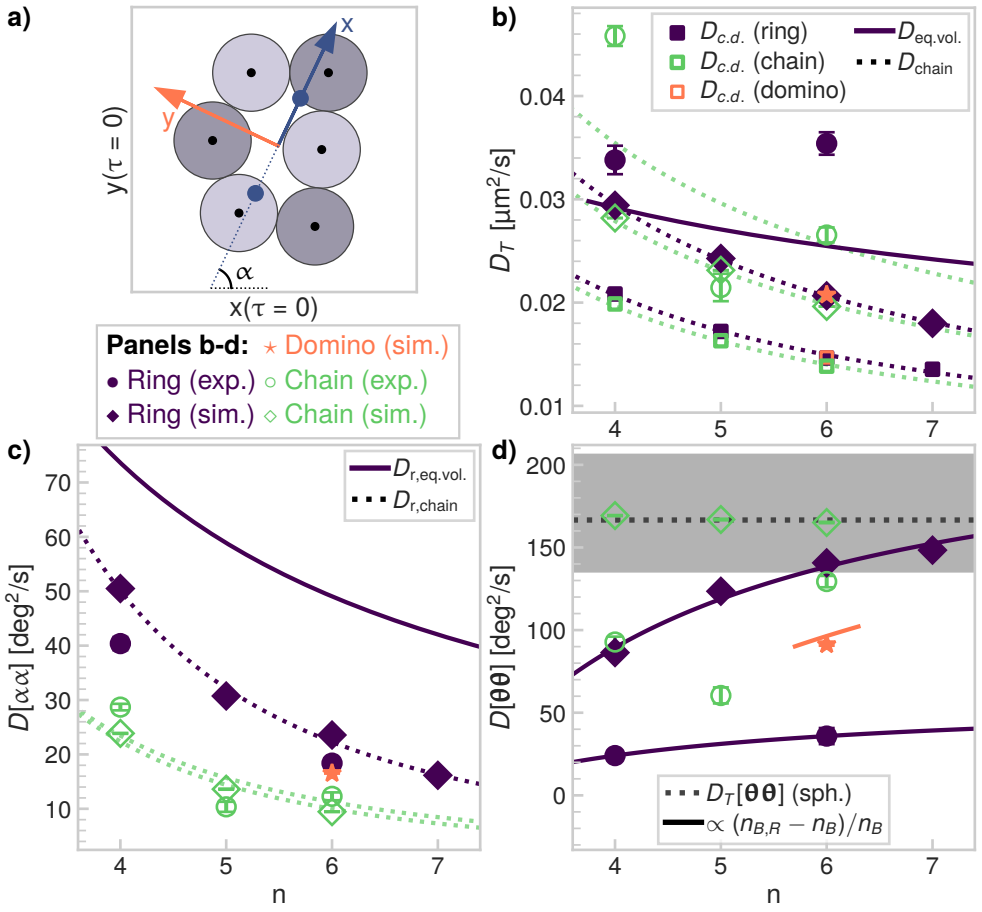

Figure 7.7: **Shape-averaged diffusivity of rings, dominoes and chains. a)** A schematic depiction of the coordinate system used to analyze the diffusivity of hexamer rings, as defined in Section 7.2.4. For all structures, the same equations are used to determine their coordinate system. The symbols and colors that correspond to the different structures are indicated in the legend. **b)** Translational diffusivity of rings, dominoes and chains. **c)** Rotational diffusivity of rings, dominoes and chains. **d)** The flexibility of rings, dominoes and chains, compared to the expected flexibility $D_T[\boldsymbol{\theta\theta}]$, as calculated from the translational diffusivity of a single sphere. We find that the flexibility of rings and dominoes shows the same scaling as function of n, as given by Equation 7.11.

determine the diffusivity of the hexamer rings. Nevertheless, for the tetramer rings, the experimental diffusivity is slightly larger than in the simulations, as we had observed previously for the flexible chains in Chapter 6. We hypothesize this is due to the no-slip boundary condition on the substrate that is used in the simulations, while in the experiments the substrate is a hydrogel that has a finite slip length, as we have argued in Chapter 6. We find that the hexamer dominoes have the same translational diffusion coefficient as the hexamer rings. This is unexpected, because by comparing their average radii of gyration, we have found that $\langle R_g \rangle$ of the dominoes is smaller than that of the rings, as shown in Figure 7.6. However, the differences between the two are very small, which may explain why their diffusion coefficients are very similar.

Compared to chains of the same size, the translational diffusivity of the rings in the simulation data is slightly larger, as is expected based on our analysis in Figure 7.6, where we have found that the average radius of gyration of the rings is smaller than that of the chains (characterized in Chapter 6). This can also be seen from the lower bound on the diffusivity $D_{c.d.}$ as calculated from the matrix $\boldsymbol{A}_{ij}$ defined by Equation 2.16 of Cichocki et al.[269] using the RPB tensor[35] with lubrication corrections as the inter-particle mobility matrix $\boldsymbol{\mu}_{ij}$, as explained in Section 7.2.4. For the experimental data, the trends are less clear and more data is needed to fully elucidate their behavior.

The rotational diffusivity of the rings, dominoes and the chains are shown in Figure 7.7c. There, we see that both the experimental and simulated rotational diffusivity of the rings is larger than that of the chains, because of their smaller average radius of gyration. For the same reason, the rotational diffusivity of the rings decreases as function of their size and the rotational diffusivity of the dominoes is smaller than that of the rings. We hypothesize that the reason why we measure a lower rotational diffusivity for the dominoes compared to the rings and not a lower translational diffusivity can be explained as follows. Based on the Stokes relations, the rotational diffusivity scales as $1/R^3$, while the translational diffusivity scales as $1/R$. Therefore, small differences in the average radius have a larger effect on the rotational diffusion coefficient than on the translational one, which may explain why the differences between the dominoes and rings are only appreciable for the rotational terms.

Having discussed the relative magnitudes of the translational and rotational diffusivity of all structures, we now consider the scaling of these terms for the rings as function of their size. There are different scalings that could reasonably be expected. First, for tetramer rings in Figure 7.2b, we have found that the shape-dependent short-time diffusivity can be accurately described by the diffusion coefficient of a sphere of the same volume as the ring, which we label as $D_{\text{eq.vol.}}$ in Figure 7.7b. Here, we used the lubrication-corrected RPB tensor described in Section 7.2.3 to calculate the diffusion coefficients of spheres of radii $R_{\text{eq.vol.}} = \sqrt[3]{n}R$, located just above the substrate. While it is clear from Figure 7.7b that $D_{\text{eq.vol.}}$ is close to the diffusion coefficient of the flexible tetramer rings, for larger ring sizes $D_{\text{eq.vol.}}$ deviates greatly from the diffusion coefficients obtained from the simulated data. Moreover, the rotational diffusion coefficients $D_{\text{r,eq.vol.}}$ predicted from spheres of the same volume as

the rings overestimates the rotational diffusivity as found from the simulated data, as shown in Figure 7.7c. Additionally, we have compared our data to the translational and rotational diffusion coefficients of a spheroid, calculated using the Perrin friction factors.[31,310] For this comparison, we have used the lengths of the long and small axes of the spheroid, as well as a prefactor that models additional substrate friction as fitting parameters. Similarly to the diffusion coefficients calculated from a sphere of the same volume, we observed large deviations between the spheroid model and the simulated diffusion coefficients (not shown).

Instead, we find that both the translational and rotational diffusivity of the rings can be accurately modeled by the scalings we had previously found for flexible chains in Chapter 6, namely

$$D_{chain} \propto \left(a b_K \left[(n^2 - 1)/n \right]^{\nu} \right)^{-\nu/2} \tag{7.9}$$

$$D_{r,chain} \propto \frac{\ln\left(2L/b_K\right)}{L^3}, \tag{7.10}$$

where we use the values we have determined in Chapter 6. Namely, the constant $a = 0.349 \pm 0.002$, $b_K = (1.03 \pm 0.01)b$ is the Kuhn length (approximately equal to the average bond length), ν is the Flory factor (expected to be 3/4 for chains in 2D) and we set $L = b_K(1 + (n-1)^{\nu})$. Briefly, D_{chain} and $D_{r,chain}$ are derived from Kirkwood-Riseman theory for the diffusivity of polymers using the rigid body approximation,[286] as explained in detail in Chapter 6. We have only fitted the simulated data using these expressions, in order to obtain the scaling from the experimental data, more measurements are necessary. From the fit of the translational diffusivity of the rings we obtain $\nu = 0.81 \pm 0.01$ and from the fit of the rotational diffusivity we find $\nu = 0.83 \pm 0.04$. These are close to each other and moreover, close to the values obtained in Chapter 6 for chains, where we have found $\nu = 0.77 \pm 0.02$ for the translational and $\nu = 0.83 \pm 0.04$ for the rotational diffusivity of flexible chains. This good agreement between the proposed scaling and the simulated and experimental data shows that the rings behave on average more as rod-like objects than as sphere-like objects, in terms of their diffusivity.

Finally, we consider the shape-averaged flexibility in Figure 7.7d as defined by Equation 7.3. The experimentally measured flexibility of the rings is much lower than the simulated flexibility, namely, the experimental value is (27 ± 1) % of the simulated value on average. For the flexible chains, we have found that the experimental flexibility is 75 to 80 % of the simulated flexibility, which we attribute to friction of the DNA linker patch not modeled in the simulations, as discussed in Chapter 6. This is also true for the rings, but because the difference in experimental and simulated flexibility is much larger for the rings, there could be an additional source of friction present for the rings that is not modeled in the simulation data. Alternatively, while for the chains, the number of average bonds per particle is always less than one ($n_B/n = (n-1)/n$), for the rings, the average number of bonds per particle is

always equal to one ($n_B/n = n/n$). Therefore, the average friction per particle, stemming from the DNA linker patch, might be larger for the individual spheres in a ring compared to those in a chain of the same length. Additionally, because the friction depends on the DNA linker concentration in the patch area,[85] it could be that by performing more experiments using different DNA linker concentrations, we recover the same behavior as we previously observed for chains in Chapter 6.

Counter-intuitively, we find that for both the simulated and experimental data, the flexibility of the rings increases as function of ring size. This is unexpected because, for the chains, we have found that the flexibility is set by the translational diffusivity of the individual spheres, as indicated in Figure 7.7d by $D_T[\boldsymbol{\theta\theta}]$ and discussed in Chapter 6. For the rings however, the flexibility is lower than this value, both in the simulated and experimental data. Therefore, we hypothesize that both the smaller separation distances between particles in the rings, as well as the additional topological constraint of the ring structure, leads to a lower flexibility compared to the more extended chains. Indeed, as shown in Figure 7.7d, we find that the simulated data of the rings can be described by the following scaling based on Equation 7.8

$$D[\boldsymbol{\theta\theta}] = D_{\boldsymbol{\theta\theta},0} + \Delta D_{\boldsymbol{\theta\theta}} \frac{n_{B,R} - n_B}{n_B} = D_{\boldsymbol{\theta\theta},0} + \Delta D_{\boldsymbol{\theta\theta}} \frac{n-3}{n}, \tag{7.11}$$

where $D_{\boldsymbol{\theta\theta},0}$ and $\Delta D_{\boldsymbol{\theta\theta}}$ are fit parameters, n_B is the number of bonds and $n_{B,R}$ is the number of bonds required for structural rigidity as given by Equation 7.8. The good agreement between the simulated data and Equation 7.11 implies that the flexibility of the rings scales as the number of excess floppy modes given by $n_{B,R} - n_B$, as obtained from the Maxwell counting rule given in Equation 7.8, divided by the total number of bonds n_B. By fitting the simulated data of the flexible rings, we find $D_{\boldsymbol{\theta\theta},0} = (40 \pm 9)\,\mathrm{deg}^2/\mathrm{s}$ and $\Delta D_{\boldsymbol{\theta\theta}} = (196 \pm 21)\,\mathrm{deg}^2/\mathrm{s}$. Now that we know this scaling is valid for the simulated data, we can fit the same relation to the experimental data, for which we find that $D_{\boldsymbol{\theta\theta},0} \approx 12\,\mathrm{deg}^2/\mathrm{s}$ and $\Delta D_{\boldsymbol{\theta\theta}} \approx 47\,\mathrm{deg}^2/\mathrm{s}$. We find that values of the fit parameters determined from the experimental data are respectively 29 and 24 % of the fit parameters determined from the simulated data, which is also close to the average ratio between the experimental data and simulated data, which is (27 ± 1) %. Therefore, we conclude that the experimental data follows the same scaling.

Interestingly, we can further test whether the proposed scaling is valid by comparing the flexibility of the hexamer dominoes to the flexibility predicted by Equation 7.11. According to the proposed scaling, the relation between $D[\boldsymbol{\theta\theta}]$ and n should be different for rings and dominoes, because of the different number of bonds. For the rings, we have found that $D[\boldsymbol{\theta\theta}] \propto (n-3)/n$, while for the dominoes $D[\boldsymbol{\theta\theta}] \propto (n-4)/(n+1)$ if Equation 7.11 holds. In Figure 7.7d, we plot the expected scaling for the hexamer dominoes using the fit values obtained from the simulated data of the rings. We find that indeed, the simulated flexibility of the hexamer dominoes is close to the predicted value based on Equation 7.11. While more work is required to conclusively show that the scaling we have found is indeed valid

for both rings and dominoes, we have presented strong indications that this is the case. This finding could also have implications for the expected flexibility of floppy colloidal crystal structures, for which we expect the flexibility will be lower than $D_T[\boldsymbol{\theta\theta}]$ as well, according to the scaling we have found here.

7.4 Conclusions

In this chapter, we have studied the possible conformations and the diffusive behavior of flexibly-linked colloidal rings. We have found that the tetramer loops show no preference for any configuration and freely change their shape from square- to diamond-like conformations. Their short-time diffusivity only weakly depends on shape and their translational diffusion can be described by the diffusion coefficient of a sphere of the same volume.

In addition to tetramer rings, we have studied the possible conformations of larger rings. The added degrees of freedom lead to preferred configurations for rings larger than the tetramer ring. Furthermore, we have compared hexamer rings to hexamer dominoes, that have an additional bond compared to the rings. For the dominoes, the preferred conformations lie between those of the hexamer loops and the tetramer loops because of the unique topology of the dominoes, which can be thought of as consisting of two coupled tetramer loops.

Finally, we have compared the shape-averaged diffusivity of rings, dominoes and chains. The shape-averaged short time diffusivity of rings decreases as function of their size and the rings diffuse slightly faster than chains of the same number of spheres, because the rings have a smaller average radius of gyration. The same trends can be observed for the rotational diffusivity. Both scale according to the scaling we have found for flexible chains in Chapter 6, where we have modeled the clusters as instantaneously rigid by following the Kirkwood-Riseman theory.[286]

The flexibility of rings, however, is smaller compared to the flexibility of the chains. We have found strong indications that the flexibility of the rings and dominoes scale as the number of excess floppy modes of the structure divided by the total number of bonds. This finding could have implications for the assembly of floppy colloidal crystal structures, for which we expect the flexibility will be severely hindered as well. As an example, the scaling we have found predicts that for a square $n \times n$ floppy colloidal crystal, the flexibility will scale as $(2n-3)/(2n^2-2n)$ which is a decreasing function for $n \geq 2$ and approaches zero in the limit of infinitely large n. For future work, it would be interesting to test whether the proposed scaling is valid for these square floppy lattices as well and if so, up to what lattice size. More broadly, our findings could have implications for the diffusive behavior of both synthetic and biological ring polymers.

Acknowledgments

We thank Loes Huijnen and Indrani Chakraborty for additional experimental data. We thank Ali Azadbakht for the design and setup of the Optical Tweezers and his technical support. We are grateful to Aleksandar Donev and Brennan Sprinkle for

fruitful discussions and for providing us with example code for the simulations. The simulations were partly performed using the ALICE compute resources provided by Leiden University. This project has received funding from the European Research Council (ERC) under the European Union's Horizon 2020 research and innovation program (grant agreement no. 758383).

8 Outlook: Flexibly-linked patchy particles

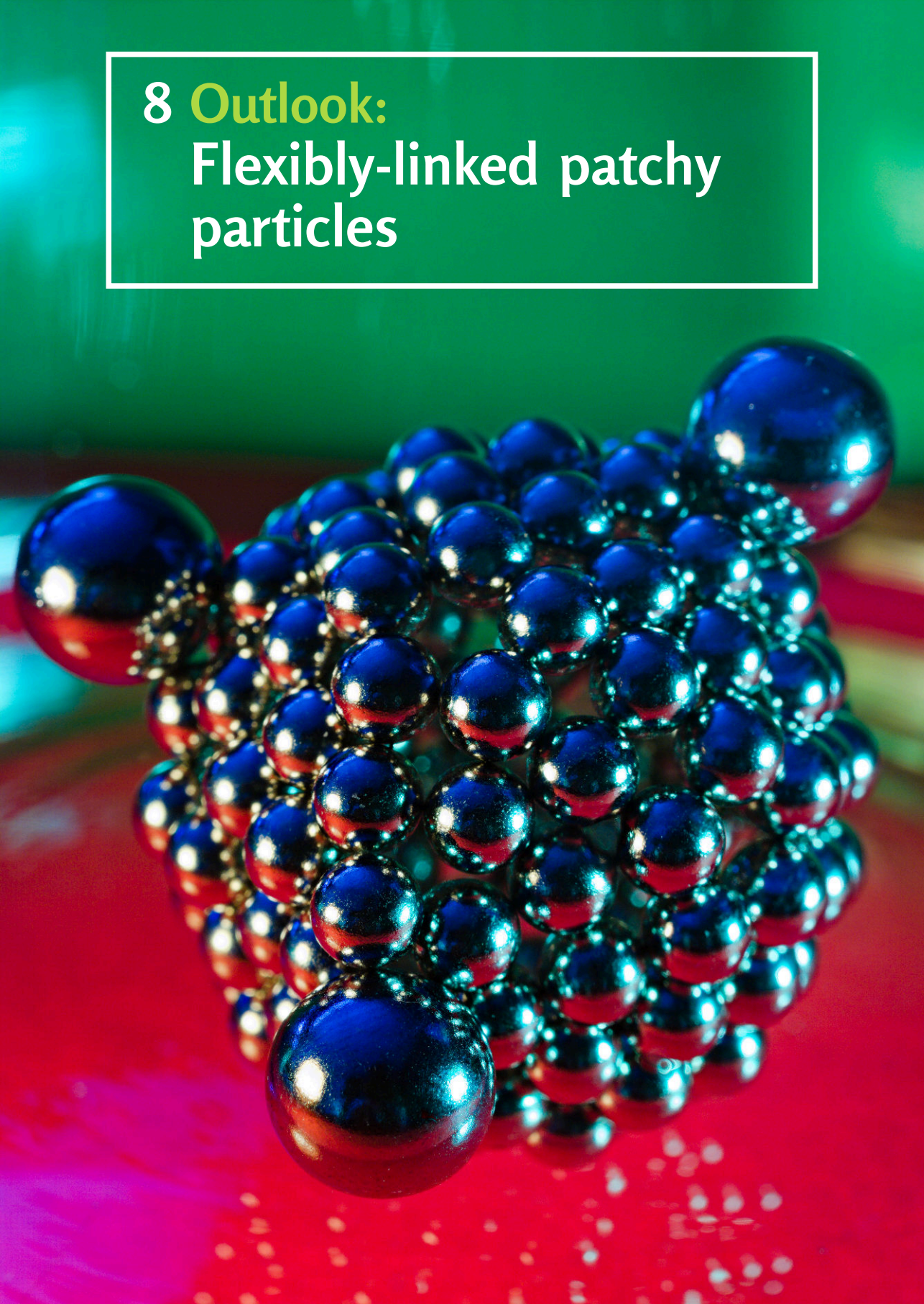

In this thesis, we have studied flexibly-linked structures of spherical colloid-supported lipid bilayers (CSLBs) that are held together by DNA linkers, which can freely move over the surface of the colloids. Because the interaction between such particles is isotropic, the number of crystal structures that could be formed using high volume fractions of these particles is limited. A great challenge in materials science is the controlled bottom-up self-assembly of materials with highly sought after properties,[311] such as materials of specific crystal lattices,[28,312] materials that have photonic bandgaps[59,71] or more general colloidal meta-materials,[313] with properties not found in naturally occurring materials. The successful fabrication of such materials using colloidal self-assembly processes requires a great amount of control over the interactions between the colloidal building blocks. In addition, it is often desirable to constrain the relative motions of two functional elements,[85] for example to enable the fabrication of nano- to micron-sized robotic devices.[121–125]

Anisotropic or directional interactions may provide a solution to overcome these issues. One way to encode anisotropic interactions into colloidal building blocks is by making use of patchy particles.[28,53] Patchy particles are colloids that have distinct patches on their surface, which are modified to serve as specific interaction sites. In other words, the patches provide a different inter-particle interaction than the bulk portion of the particle, which leads to directional interactions. A wide variety of colloidal patchy particles is available.[28,51] For example, patchy particles can be made from particle-laden emulsion droplets.[80,314] Other techniques include patchy particle synthesis by colloidal fusion[81] or by photoprinting techniques.[82] The method we focus on here is based on the induced phase separation between crosslinked polymer particles and a polymerizable monomer swelling solution, resulting in particles with protrusions.[52,83] These patchy particles can be used for further hierarchical assembly.[315]

Broad applicability of patchy particles in self-assembly processes requires linking agents that can provide bonding with a high specificity. Such specificity can be obtained by functionalizing the patches with DNA linkers that have sticky ends which can provide a high binding specificity.[80,82,316] These sticky ends are pieces of single-stranded DNA that specifically hybridize to their complementary sequence and therefore can act as an "intelligent glue" between the micron-sized patchy particles.

In this short outlook, we propose a method to functionalize liquid protrusions of colloidal particles with DNA linkers that can diffuse over the surface of the liquid patches,

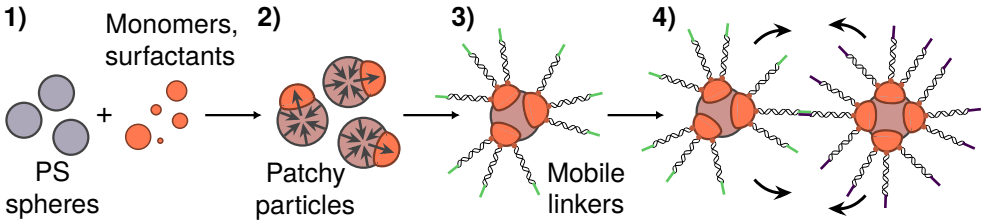

Figure 8.1: **Flexibly-linked patchy particles.** Schematic of DNA-decorated patchy particles, not to scale. **1)** Surfactant-stabilized polystyrene particles (grey) are swollen with a surfactant-stabilized styrene emulsion (orange). **2)** Elastic stress of the polymer network induced by swelling leads to patch formation. **3)** DNA linkers are inserted into the liquid patches via their hydrophobic anchors. Because the patches are fluid, the DNA linkers are expected to be mobile. **4)** Self-assembly via DNA-mediated interactions results in flexibly-linked patchy particles.

thereby paving the way towards patchy particles with both directional and mobile bonds. This combination of properties is highly desirable, because colloidal structures of reconfigurable shape are expected to be able to relax more quickly towards their thermodynamic equilibrium configuration than rigid structures, thereby mitigating equilibration issues.[77] In addition, they could provide ways to build switchable materials.[285] Here, we propose a method to realize such structures experimentally and we discuss our finding from preliminary experiments.

Proposed method for patchy particles with mobile linkers

We propose the following method, as schematically depicted in Figure 8.1. First, particles with liquid protrusions are obtained by swelling crosslinked polymer particles with an emulsion of monomers and surfactants (Figure 8.1 steps 1 and 2). DNA linkers with hydrophobic anchors are inserted into the protrusions, which can be used for further hierarchical self-assembly of the particles (Figure 8.1 steps 3 and 4). Specifically, in Figure 8.1 step 1, crosslinked polystyrene (PS) microparticles are swollen with a surfactant-stabilized styrene monomer emulsion.[52,83] In our experiments, we have used 1.5 %v/v divinylbenzene (DVB) crosslinked polystyrene spheres* (diameter (1.42 ± 0.04) µm) containing 10 % 3-(trimethoxysilyl) propyl methacrylate (TPM), as prepared by a dispersion polymerization procedure.[317] We have tested particles that were dispersed in a 1 %w/w aqueous solution of sodium dodecyl sulfate (SDS) or in a polyvinyl alcohol (PVA) solution of the same weight percentage. The styrene swelling emulsion was prepared by mixing 8.5 %v/v styrene in water and the mixture was subsequently emulsified for 2 min at 8000 rpm and then for 10 s at 10 000 rpm, using a IKA T18 Ultra Turrax homogenizer. As a surfactant, we have used both PVA, SDS and a combination of 99 mol % unsaturated DOPC ((Δ9-Cis)-

*Particle synthesis was performed by Vera Meester, see subsection "Cross-Linked Particle Synthesis" of the Experimental Section of Meester and Kraft[317] for details.

1,2-dioleoyl-sn-glycero-3-phosphocholine) phospholipids with 1 mol % of the lipopolymer DOPE-PEG(2000) (1,2-dioleoyl-sn-glycero-3-phosphoethanolamine-N-[methoxy(polyethylene glycol)-2000]). Additionally, for some of the experiments where we used lipids as surfactants, we have used 0.2 mol % of the fluorescently-labeled phospholipid DOPE-Rhodamine (1,2-dioleoyl-sn-glycero-3-phosphoethanolamine-N-(lissamine rhodamine B sulfonyl)).

Then, as depicted in Figure 8.1 step 2, the swelling of the particles with monomer solution induces an elastic stress in the crosslinked polymer network of the particles. This elastic stress leads to the formation of a liquid patch of monomer solution, which protrudes from the particle.[318] The size of the protrusions can be tuned by varying the concentration of the surfactant or by changing the swelling ratio S of particle to swelling emulsion volume.[52,83] Here, we have typically used $S = 8$. After the protrusions have formed, in Figure 8.1 step 3, DNA linkers with hydrophobic anchors are inserted into the hydrophobic liquid protrusions. We have used double-stranded DNA with a double stearyl anchor, where a single-stranded overhang can function as a sticky end. We used two sets of DNA strands with complementary sticky ends that can act as linkers, of respectively strands DS-H-A and DS-H-B of Table A.1. We expect that since the protrusions are fluid, the linkers can diffuse on the protrusion surface, similarly to systems of emulsion droplets functionalized with DNA linkers.[56,84,194,216,265] Finally, in Figure 8.1 step 4, we schematically show how two such patchy particles decorated with DNA linkers with complementary sticky ends might self-assemble into a flexible structure.

Balancing colloidal stability and patch functionalization

We have tested the proposed procedure by swelling PS particles with a styrene emulsion stabilized by various SDS concentrations. As shown in Figure 8.2a, anisotropic particles with multiple protrusions were formed. We reproduced earlier studies, in which it was shown that by increasing the surfactant concentration, more numerous and smaller protrusions can be obtained,[83] as can be seen from Figure 8.2a. Additionally, we found that, as expected, increasing the surfactant concentration improves the colloidal stability of the particles. Specifically, as shown in Figure 8.2a, we found that the particles aggregated for SDS concentrations below the critical micelle concentration (CMC) of SDS but showed good colloidal stability above the CMC.

Having established the conditions required to form anisotropic particles with protrusions, we proceeded with the functionalization of the liquid protrusions. This was tested by adding DNA linkers with hydrophobic anchors to the particles. The DNA linkers are expected to spontaneously insert into the hydrophobic protrusions because of their hydrophobic double stearyl anchors, as has been demonstrated for comparable systems of emulsion droplets.[56,84,194,216,265]

As a first step, we functionalized SDS-stabilized styrene emulsions with DNA linkers, before swelling the polymer particles. As shown in Figure 8.2b, for SDS concentrations well below the CMC, we observed a fluorescent signal stemming from the fluorescently-labeled DNA linkers on the outer surface of the emulsion

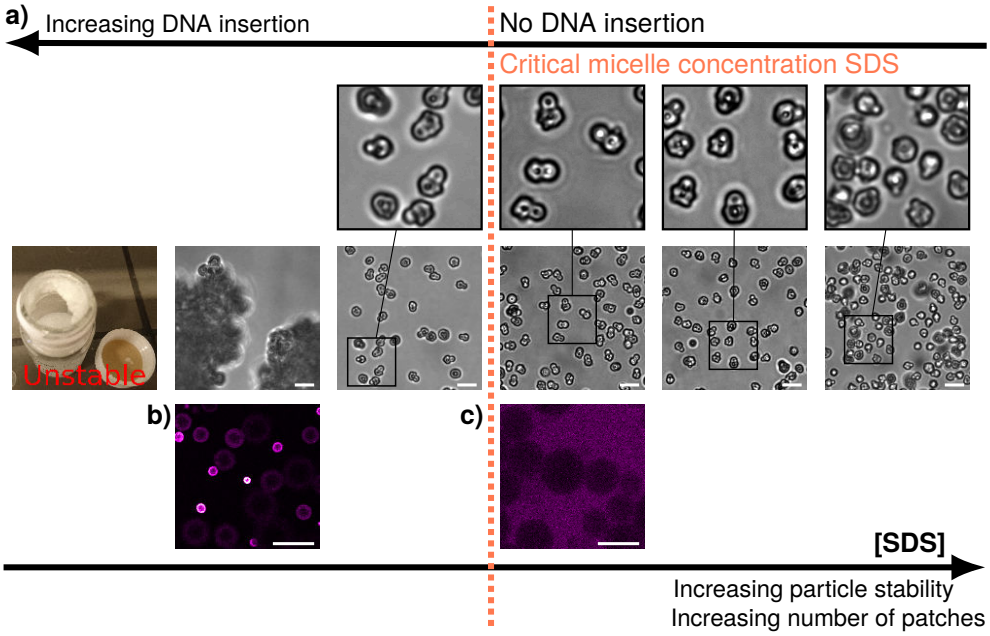

Figure 8.2: **DNA linker insertion into SDS-stabilized liquid protrusions. a)** Anisotropic particles with protrusions were obtained by swelling crosslinked polystyrene particles with an emulsion of styrene monomers, which was stabilized by SDS. Increasing the SDS concentration leads to smaller protrusions and a higher colloidal stability. On the other hand, DNA linkers can only be inserted into the styrene phase when the concentration of SDS is below the critical micelle concentration (CMC, 0.26 %w/w), but this leads to nonspecific aggregation of the particles. **b)** Fluorescence stemming from dyed DNA linker strands indicates that below the CMC of SDS, DNA can be inserted into an emulsion of styrene. **c)** Above the CMC of SDS, no DNA linkers are inserted into the styrene phase, as evidenced by the lack of fluorescent signal. Scale bars are 10 µm.

droplets, as expected. However, for higher concentrations of SDS, we found that the DNA linkers could no longer be inserted into the emulsion droplets, as evidenced by the lack of fluorescent signal on the outside of the droplets in Figure 8.2c. We therefore conclude that it is likely that SDS forms micelles with the hydrophobic anchors of the DNA linkers, as we had observed for CSLBs in Chapter 3. This would slow down or inhibit the insertion of the DNA linkers into the emulsion droplets. Alternatively, at these high surfactant concentrations, the emulsion droplet surface could already be fully covered by SDS molecules, which would also prevent the insertion of DNA linkers.

Unfortunately, the surfactant concentrations for which DNA linkers could be inserted into the emulsion droplets have no overlap with the surfactant concentrations for which the protrusion-decorated particles were found to be stable. Therefore, to overcome this problem, we have tried to first functionalize emulsions with DNA linkers at lower surfactant concentrations. Using 0.1 %w/w SDS, we found that the DNA linkers could be successfully inserted into the emulsion droplets (Figure 8.2b). Then, we added these DNA-decorated emulsions to the polystyrene seed particles in order to swell the particles and thereby induce the formation of protrusions. This approach was not successful, most likely because the emulsion droplets were sterically stabilized by the DNA linkers and therefore were not able to swell the colloids. Namely, after adding the DNA-functionalized emulsion to the particles, we did not observe swelling of the seed particles or the formation of protrusions. However, in future experiments, this method could be tried again using either lower DNA linker concentrations or longer incubation times.

As an alternative to using SDS as a surfactant, other surface active compounds may be employed, such as phospholipids. Phospholipids have been used to form fluid monolayers on emulsion droplets, into which DNA linkers have been successfully inserted.[56,84,194,216,265] Indeed, by using phospholipids as surfactants during the preparation of the styrene swelling emulsion, we found that particles with protrusions could be formed. This is shown by the fluorescent signal stemming from dyed phospholipids in Figure 8.3a and b, where two examples of particles with a protrusion are shown. It can be seen that in both examples, one lobe of the particle has a brighter signal than the other, indicating the presence of a protrusion of styrene monomer stabilized by the lipid molecules, of which a small fraction was fluorescently-labeled. To prevent the formation of nonspecific aggregates in this SDS-free system, before swelling, the particles were additionally stabilized by a low amount (0.1 %w/w) of polyvinyl alcohol (PVA) and we added 1 mol % of DOPE-PEG(2000) to the emulsions for additional steric stability.

First mobile structures

Subsequently, these protrusion-decorated particles were functionalized with DNA linkers. As a requisite for successful self-assembly of these particles via DNA-mediated binding, a buffer of sufficient ionic strength is needed.[223] This allows for the proper hybridization of the complementary sticky ends that are responsible for binding, as

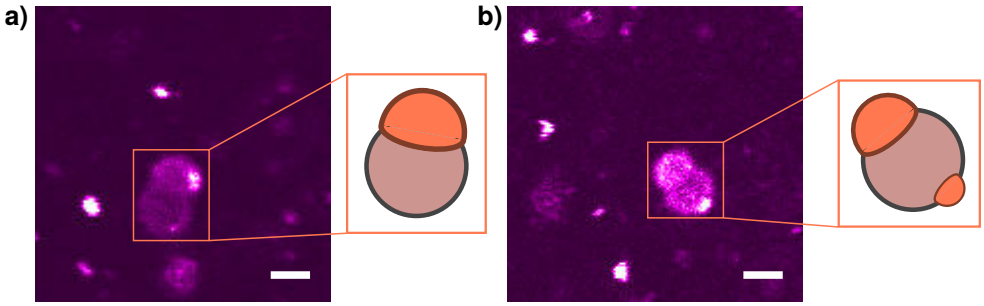

Figure 8.3: **Colloids with lipid-stabilized protrusions functionalized with DNA linkers.** Confocal images of particles with protrusions, the fluorescent signal stems from dyed lipids. Schematics indicate the possible arrangement of the protrusions (orange) on the swollen seed particle (grey/orange). Scale bars are 2 μm.

the negative charges of the DNA backbone need to be electrostatically screened by counter-ions. We observed that the protrusions on the particles that were formed while using a buffer were smaller than the protrusions we had observed by using only ultra-pure water. However, the protrusion size could be increased by using a higher swelling ratio.

After mixing two batches of these anisotropic particles with protrusions functionalized with complementary DNA linkers, we observed various mobile structures. First, as shown in Figure 8.4a, we could observe a large number of particles that were moving on emulsion droplets left in the mixture after the swelling of the particles. From these observations, we concluded that the emulsion droplets were still fully fluid and that adhered particles could move on the surface of these droplets. However, it is unclear whether the particles were attached via DNA-mediated bonds or through adsorption.

In addition to these Pickering-like emulsions, several clusters and chain-like aggregates could be observed, as shown in Figure 8.4b, that displayed some flexibility. For those structures, we observed overall shape changes and changes in the relative orientations of the individual particles. These results demonstrate that in principle, assemblies of anisotropic particles with mobile bonds can be formed by using particles with liquid protrusions as building blocks. However, for these structures as well, it is unclear how they are bonded, i.e. by the DNA linkers or via other nonspecific interactions, which has to be further tested in future experiments.

Conclusions and next steps

In conclusion, we have shown that it is possible to synthesize anisotropic particles with liquid protrusions and to functionalize these protrusions with DNA linkers with hydrophobic anchors. Future experiments are necessary, in order to characterize the self-assembly behavior of this type of particles, as well as the flexibility of the resulting structures.

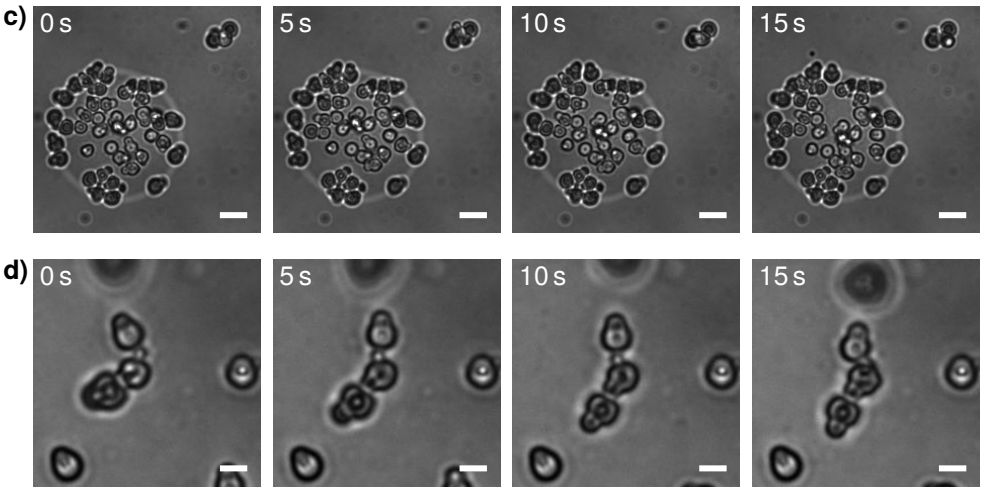

Figure 8.4: **Flexible aggregates of protrusion-decorated particles. a)** Time series of protrusion-decorated particles diffusing on an emulsion droplet, together with a flexible structure in the top right corner. **b)** Example of a flexibly-linked chain-like aggregate of anisotropic particles with protrusions. Scale bars are 5 μm.

Alternative methods to synthesize patchy particles of reconfigurable shape should be explored as well. We will discuss some examples, which we characterize by the combination of body and patch phases, where we consider liquid or solid phases. In that sense, the particles we have discussed so far consist of a solid body, which is formed by the polystyrene sphere, and of multiple liquid patches, which are formed by the styrene protrusions, as indicated in Figure 8.5b.

Other kinds of patchy particles that consist of a solid body with liquid patches may be used to obtain reconfigurable clusters. For example, it may be possible to encode patchy interactions into colloid-supported lipid bilayers (CSLBs), by inducing phase-separation of the lipid membrane surrounding the particles.[319] Here, the body is formed by the solid colloid that supports the fluid lipid bilayer. This is an integral part of the patchy particle because it fixes its overall shape. Then, the particles can feature multiple patches, formed by the different lipid domains. As shown in Figure 8.5a, phase separation results in the formation of specific lipid ordered (green) and lipid disordered domains, into which DNA linkers (purple) with suitable lipid anchors are expected to preferentially partition.[319] If the linkers are mobile in the phase-separated bilayer, flexible structures could be formed using these particles.

The partitioning of linkers into different lipid phases was also demonstrated for linker-functionalized Janus vesicles,[320,321] as shown in Figure 8.5c. These Janus vesicles can be thought of as patchy particles, where both the body and the patch are liquid: namely, they are both formed by different lipid domains. Various types of linkers can be employed, such as DNA linkers[320] or biotin-Avidin based linkers.[321] In

contrast to the phase-separated CSLBs in Figure 8.5a, the shape of the vesicles is not fixed and the Janus vesicles therefore deform upon binding, as shown in Figure 8.5c. This deformation could potentially affect their reconfigurability because of geometric constraints and an increase in inter-particle friction because the size of the contact area becomes larger upon deformation of the vesicles. While the successful formation and assembly of these type of Janus vesicles has been firmly established,[320,321] the degree of reconfigurability of the formed structures remains to be further investigated.

Instead of using liquid patches, solid patches may alternatively be used. For example, as shown in Figure 8.5d, solid polystyrene particles that can act as patches can be bound to liquid oil emulsion droplets,[216] which then form the liquid body of the patchy particle. In this specific system, the solid patches were found to be immobile on the emulsion droplet surface because of gelation of the emulsion droplet.[216] We expect that this problem can be overcome by using a different oil as the emulsion droplets, as was already demonstrated for isotropically-functionalized emulsion droplets that can form reconfigurable structures via DNA linker-mediated binding.[56,84,194,265] For emulsion droplets decorated by mobile solid particles, hierarchical assembly of the patchy particles via bonding of the solid patches on different patchy particles may lead to reconfigurable structures.

Lastly, for all systems discussed so far, either the body or the patch was required to be liquid in order for the structures to show flexibility. In contrast, reconfigurable assemblies can also be formed by using patchy particles that are completely solid. We discuss two examples: first, as shown in Figure 8.5e, patchy particles that are bonded by attractive critical Casimir forces between the patches can be used to obtain reconfigurable structures.[322] The reconfigurability stems from the fluidity of the solvent and the fluctuating nature of the critical Casimir interaction based bond. Second, by using attractive depletion interactions, reconfigurable clusters can be obtained from particles that have specific indentations (the "locks") into which spherical particles of the correct shape (the "keys") can fit via a lock and key interaction,[323] as shown in Figure 8.5f. In this system, the lock particles can be thought of as being patchy in the sense that they have a specific patch where the curvature differs from the body of the particle. Furthermore, this patch can be employed for directional bonding, as shown in Figure 8.5f. Both of these systems rely on specific properties of the solvent to ensure stable bonding and reconfigurability, which may limit their applicability in biological systems.

To conclude, we hope that the type of particles discussed here, because of their unique combination of directional interactions with flexible bonds, will lead to a higher degree of control over the self-assembly of reconfigurable colloidal structures in future studies. Ultimately, this may facilitate the formation of synthetic structures with currently unavailable designer material properties, resulting in smart and switchable colloidal structures.

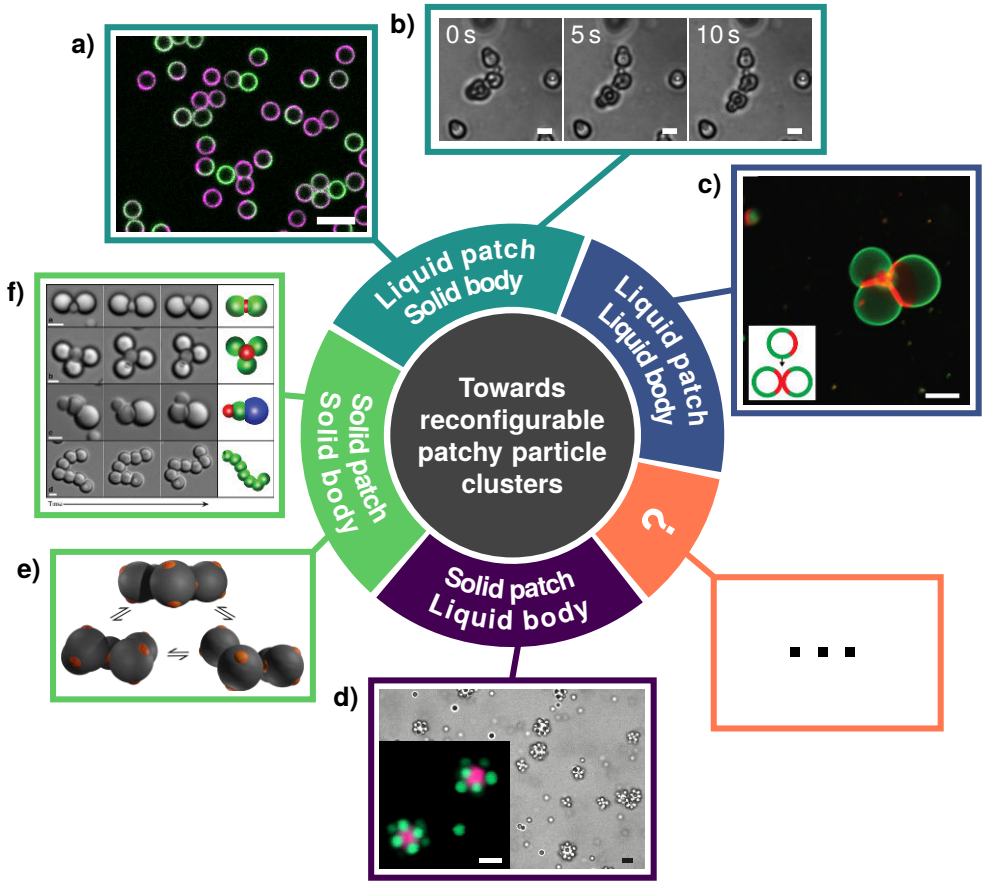

Figure 8.5: **Towards reconfigurable colloidal clusters of patchy particles: existing and envisioned methods. a)** Patchy particles from phase-separated CSLBs. DNA linkers (purple) could preferentially partition into one of the two phases: a liquid ordered phase (green) or a liquid disordered phase, thereby allowing for directional bonding. Scale bar is 5 µm. **b)** Particles presented here, as discussed in Figure 8.4. Scale bars are 5 µm. **c)** Aggregation of biotin-decorated Janus (phase-separated) liposomes upon incubation with avidin. Scale bar is 20 µm. **d)** Bright field and confocal (inset) microscopy images of colloidal clusters consisting of oil droplets (inset: magenta) surrounded by multiple attached polystyrene particles (inset: green) and freely dispersed polystyrene particles. Scale bars are 2 µm. **e)** 3D reconstruction of colloidal cyclopentane. The patchy particles remain bonded via critical Casimir interactions. **f)** Flexible structures of colloidal spheres and patchy particles with a spherical cavity, that bind spontaneously and reversibly via depletion interactions. Scale bars are 2 µm. *Attribution: a) Adapted with permission from Rinaldin.*[319] *c) Reprinted (adapted) with permission from Wang et al.*[321] *Copyright 2018 American Chemical Society. d) Republished with permission of IOP Publishing, from Van Der Wel et al.*[216] *e) Adapted with permission from Swinkels et al.*[322] *f) Reprinted (adapted) by permission from Springer Nature: Sacanna et al.*[323] *Copyright Springer Nature 2010.*

Acknowledgements

We thank Vera Meester for the synthesis of the crosslinked polystyrene particles and for useful discussions.

Appendix: list of DNA sequences

Table A.1: **Summary of all DNA strand sequences and their names.** Sticky ends are marked in cursive.

Name	Sequence
CH-10-A	Cholesterol-TEG-5′-TTT-GAA-CGC-TCT-GTA-ATC-GGG-CTA-AC-3′
CH-10-B	Cholesterol-TEG-3′-GTT-AGC-CCG-ATT-ACA-GAG-CGT-TCT-TT-3′
CH-10-H	Obtained by hybridization of CH-10-A and CH-10-B
CH-20-B	Cholesterol-TEG-3′-TTT-TAG-CGA-TGG-GAA-GCG-TGT-CAG-TTA-GAT-CTC--TCG-GGA-CGG-AAT-GC-5′
CH-20-S-I	Cholesterol-TEG-5′-TTT-ATC-GCT-ACC-CTT-CGC-ACA-GTC-AAT-CTA-GAG--AGC-CCT-GCC-TTA-CGA- 3′
CH-20-I	Obtained by hybridization of CH-20-B and CH-20-S-I
CH-20-S-A	Cholesterol-TEG-5′-TTT-ATC-GCT-ACC-CTT-CGC-ACA-GTC-AAT-CTA-GAG--AGC-CCT-GCC-TTA-CGA-*GTA-GAA-GTA-GG*-3′-6FAM
CH-20-S-B	Cholesterol-TEG-5′-TTT-ATC-GCT-ACC-CTT-CGC-ACA-GTC-AAT-CTA-GAG--AGC-CCT-GCC-TTA-CGA-*CCT-ACT-TCT-AC*-3′-Cy3
CH-20-H-A	Obtained by hybridization of CH-20-B and CH-20-S-A
CH-20-H-B	Obtained by hybridization of CH-20-B and CH-20-S-B
DS-B	5′-TCG-TAA-GGC-AGG-GCT-CTC-TAG-ACA-GGG-CTC-TCT-GAA-TGT-GAC-TGT--GCG-AAG-GTG-ACT-GTG-CGA-AGG-GTA-GCG-ATT-TT-3′
DS-S-I	Double Stearyl-HEG-5′-TTT-ATC-GCT-ACC-CTT-CGC-ACA-GTC-AAT-CTA--GAG-AGC-CCT-GCC-TTA-CGA-3′
DS-S-A	Double Stearyl-HEG-5′-TT-TAT-CGC-TAC-CCT-TCG-CAC-AGT-CAC-CTT--CGC-ACA-GTC-ACA-TTC-AGA-GAG-CCC-TGT-CTA-GAG-AGC-CCT-GCC-TTA--CGA-*GTA-GAA-GTA-GG*-3′-6FAM
DS-S-B	Double Stearyl-HEG-5′-TT-TAT-CGC-TAC-CCT-TCG-CAC-AGT-CAC-CTT--CGC-ACA-GTC-ACA-TTC-AGA-GAG-CCC-TGT-CTA-GAG-AGC-CCT-GCC-TTA--CGA-*CCT-ACT-TCT-AC*-3′-Cy3
DS-H-I	Obtained by hybridization of DS-B and DS-S-I
DS-H-A	Obtained by hybridization of DS-B and DS-S-A
DS-H-B	Obtained by hybridization of DS-B and DS-S-B
PA-A	Cholesterol-5′-TTT-ATC-GCT-CCC-TTC-GCA-CAG-TCA-ATC-TAG-AGA-GCC--CTG-CCT-TAC-GAT-ATT-GTA-CAA-TA-3′-Cy3
PA-B	Cholesterol-5′-CGT-AAG-GCA-GGG-CTC-TCT-AGA-TTG-ACT-GTG-CGA-AGG--GTA-GCG-ATT-TT-3′
PA-C	Obtained by hybridization of PA-A and PA-B

Summary

In this thesis, we have studied the impact of particle shape anisotropy, multivalent interactions and flexibility on systems of colloidal particles. The study of these effects was motivated first by a desire to understand the rich underlying physics that governs these systems and second, because of their possible relevance to understanding processes found in biology. For example, to shed light on how shape changes affect the biological function[100–104] of biopolymers[251] and proteins.[252,282] Additionally, colloidal particles can be employed for medical applications, such as for targeted drug-delivery.[7–9,114–117] In addition to biological and medical examples, there exists a great variety of applications where colloidal particles can serve as model systems.[17–19,127–129,195]

A general introduction to several aspects of soft matter and specifically, colloid science that are relevant to this thesis are given in **Chapter 1**.

In **Chapter 2**, we report on our discovery that colloidal dimer particles have preferred orientations with respect to the substrate above which they diffuse, due to electrostatic repulsion between substrate and particle, which is greatly affected by the anisotropic shape of the dimer particles. Our results highlight the rich dynamics that nonspherical particles exhibit in the proximity of walls and can aid in developing quantitative frameworks for the dynamics of arbitrarily-shaped particles in confinement.

On top of the effects of a fixed and anisotropic particle shape, we have studied colloidal systems that have internal degrees of freedom that allow for shape changes. We have extensively characterized the properties of colloid-supported lipid bilayers[85,110–112] (CSLBs), that consist of solid micron-sized colloidal particles surrounded by a fluid lipid bilayer. In **Chapter 3**, we have first characterized how the formation of CSLBs can be optimized, leading to CSLBs that have a high colloidal stability and a homogeneous bilayer that is fully fluid. Then, in **Chapter 4**, we have studied the multivalent interactions between DNA linker-functionalized CSLBs that can form flexible bonds. We have found that linker depletion effects[84,126] can be used to limit the valency of self-assembled clusters made of CSLBs.

By taking advantage of the ability to limit the valency of clusters of CSLBs using low DNA linker concentrations, we have formed flexibly-linked colloidal chains of three to six CSLBs, as discussed in **Chapters 5–6**. These can serve as model system for e.g. biopolymers[251] and intrinsically disordered proteins,[252,282] in which shape changes affect the biological function of the compound.[100–104] We have compared

experimental and simulated data to predictions based on polymer theory. Moreover, we have quantitatively measured the full diffusion tensor of these flexible chains and have found marked flexibility-induced effects, such as a Brownian quasiscallop mode, where translational displacements are coupled to shape changes and a second timescale set by the flexibility of the chain, which leads to a faster relaxation of the influence of particle shape on diffusion.

In **Chapter 7** we have assembled flexible rings of four and six CSLBs, that mimic ring polymers,[302] which are of great interest due to their unique topology[302,306] and their diffusive[306,307] and rheological behavior.[303,305] We have quantified the differences between flexible chains, loops and domino lattices, where we found a lower flexibly and a higher diffusivity of the loops and lattices compared to the chains. We argued that the flexibility of the loops and lattices scales as the number of excess floppy modes per bond. This scaling could have implications for the flexibility of floppy colloidal materials.

Finally, we have provided a short outlook in **Chapter 8** on how to synthesize flexibly-linked particles with directional interactions. Because of their unique combination of directional interactions with flexible bonds, we hope that these type of particles will lead to a higher degree of control over the self-assembly of reconfigurable colloidal structures in future studies.

In conclusion, our work demonstrates the rich dynamics and possibilities for applications of reconfigurable colloidal systems. Using experiments and simulations, we have found marked flexibility-induced effects in the behavior of reconfigurable colloidal structures. We hope our findings further the study of the diffusivity of flexible objects found in complex mixtures relevant in, for example, the cosmetic, pharmaceutical and food industries, as well as in biological systems. Our results may have implications for understanding both the diffusive behavior and the most likely conformations of macromolecular systems in biology and industry, such as polymers, single-stranded DNA and other chain-like molecules.

Samenvatting

De titel van mijn proefschrift, *"Anisotropy, multivalency and flexibility-induced effects in colloidal systems,"* laat zich — voor zover dat mogelijk is — in het Nederlands vertalen als *"De invloed van anisotropie, multivalentie en beweeglijkheid op colloïdale systemen."* In deze samenvatting zal ik proberen de betekenis van de titel verder te verduidelijken en zal ik de inhoud van mijn proefschrift kort beschrijven.

Colloïdale systemen komen overal in het dagelijks leven voor: een aantal voorbeelden zijn melk, wolken, slagroom, fotografische film, kaas, rook en spekjes. Maar ze worden ook op grote schaal toegepast in de industrie, bijvoorbeeld bij de productie van voedsel, verf, cosmetica of geneesmiddelen. Een colloïdaal systeem bestaat uit een medium waarin zich deeltjes bevinden met een grootte van ongeveer een nanometer tot en met enkele tientallen micrometers. Dit is bijvoorbeeld te zien in Figuur 10.1a voor de vetdruppeltjes waar melk voor een groot deel uit bestaat, die een paar micrometer groot zijn. Ter vergelijking: een draad uit een spinnenweb is ongeveer één tot tien micrometer dik. Een voorbeeld van colloïdale mengsels zijn verven en inkten, deze bestaan uit vaste deeltjes die zich bevinden in een vloeibaar medium, vaak water of terpentijn. Zowel het medium als de deeltjes kunnen voorkomen in vaste, vloeibare of gasvormige toestand. Wat colloïden zo bijzonder maakt is hun grootte en dan met name de consequenties van het feit dat colloïden rond een micrometer groot zijn. Ze zijn namelijk nog net groot genoeg om met een normale lichtmicroscoop te zien, maar zijn wel gevoelig voor thermische fluctuaties in het medium, net zoals moleculen en atomen. Hierdoor kunnen ze dienen als model systeem voor de veel kleinere en daardoor lastiger waar te nemen moleculen en atomen.

Onder invloed van specifieke aantrekkingskrachten en thermische fluctuaties in de vloeistof kunnen de deeltjes spontaan samenklonteren tot grotere structuren, een proces dat bekend staat als **zelfassemblage**. Op grotere schaal zou dat te vergelijken zijn met een bak vol Lego blokjes die flink geschud wordt, waarbij tijdens het schudden spontaan bouwwerken ontstaan, zonder dat je de juiste blokjes daarvoor zelf bij elkaar hoeft te brengen. Bij zelfassemblage wordt het feit dat alleen bepaalde deeltjes (of blokjes) op elkaar passen gebruikt om specifieke structuren te bouwen. Zoals weergegeven in Figuur 10.1b kan dit niet alleen werken voor colloïdale systemen, maar ook voor objecten die je met het blote oog kunt zien, zolang de interacties tussen de bouwstenen zo afgesteld zijn dat de juiste structuur wordt gevormd.

Om het zelfassemblage-proces beter te kunnen controleren, is het belangrijk om heel specifiek de sterkte van de bindingskrachten te kunnen kiezen. Een mogelijkheid om dit te doen is via meerwaardige, of **multivalente interacties**. Dat zijn interacties

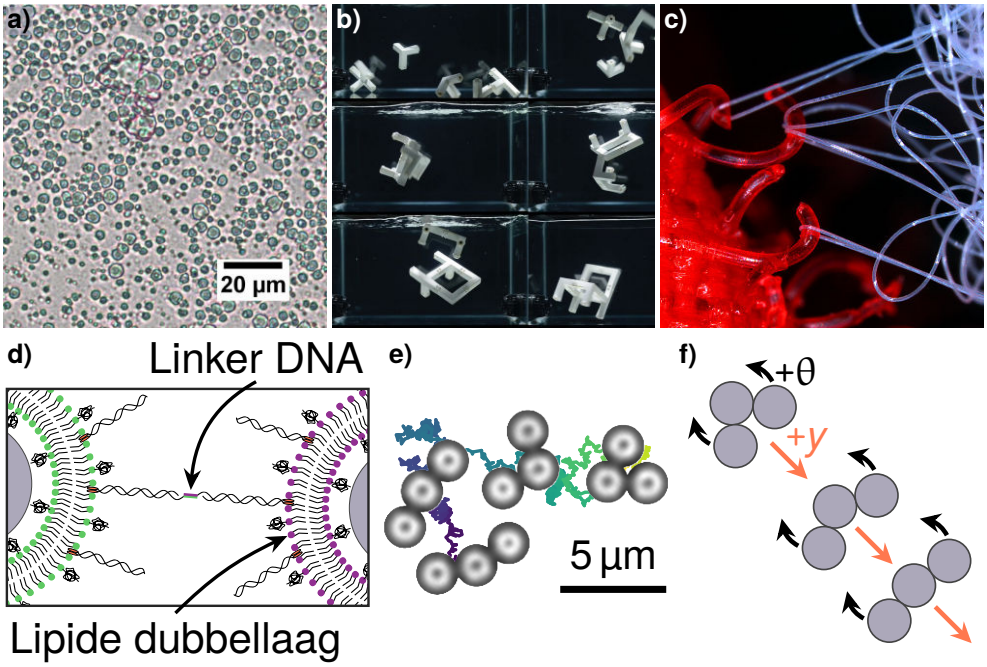

Figuur 10.1: **a)** Microscopie afbeelding van biologische weidemelk, waarin de colloïdale vetdruppeltjes waar melk voor een groot deel uit bestaat duidelijk zichtbaar zijn. **b)** Zelfassemblage gedurende zeven uur van een stoeltje van ongeveer 10 cm groot. Stromend water en specifieke, directionele geometrische en magnetische interacties zorgden voor de succesvolle zelfassemblage. **c)** Multivalente interacties in klittenband. De binding tussen één paar – bestaande uit een haakje en een lusje – is zeer zwak, maar door de grote hoeveelheid bindingen kan het klittenband veel grotere krachten weerstaan. **d)** Deeltjes-gedragen lipide dubbellagen bestaan uit colloïdale deeltjes die zijn omringd door een vloeibare lipide dubbellaag, waarin mobiele DNA linkers kunnen worden toegevoegd. Doordat de linkers kunnen bewegen in de vloeibare lipide dubbellaag, kunnen deeltjes die via de linkers met elkaar binden zich ten opzichte van elkaar herschikken. **e)** De Brownse beweging van een flexibel colloïdaal microscharnier. Willekeurige verplaatsingen, vormveranderingen en rotaties zijn zichtbaar. **f)** De Brownse quasi-schelpbeweging: bij verplaatsing opent het microscharnier zich als een schelp en vice-versa. *Bronvermelding: a) Uit Braun et al.* [324] *(CC BY 4.0). b) Uit Papadopoulou et al.* [325] *(herdrukt met toestemming). c) "Velcro photomicrograph" door Trazyanderson* [326] *(CC BY-SA 4.0), via Wikimedia Commons.*

waarbij heel veel zwakke verbindingen tussen twee deeltjes leiden tot een grote effectieve bindingskracht. Een voorbeeld uit het dagelijks leven is klittenband: zoals te zien is in Figuur 10.1c blijven hierbij kleine haakjes, die vast zitten op het ene oppervlak, steken in de harige laag die vastzit op het andere oppervlak. Als je aan één haakje zou trekken, zou die gemakkelijk los komen, maar de grote hoeveelheid haakjes samen zorgt ervoor dat de twee oppervlakken stevig aan elkaar vastzitten.

Een tweede mogelijkheid om het zelfassemblage-proces te sturen is door gebruik te maken van zogenaamde **anisotrope interacties**. Hierbij werken de krachten alleen in een bepaalde richting ten opzichte van het deeltje, in tegenstelling tot bij isotrope interacties, waarbij de interacties in alle richtingen gelijk zijn. Lego blokjes zijn bijvoorbeeld ook anisotroop: je kunt ze alleen met de juiste kanten naar elkaar gericht in elkaar klikken. Hiervan is ook gebruik gemaakt om de poten van het stoeltje uit Figuur 10.1b op de juiste manier in elkaar te zetten.

De effectiviteit van zelfassemblage wordt ook bepaald door kinetische factoren. Denk hierbij bijvoorbeeld aan onder welke hoek de deeltjes aan elkaar plakken. Dit kan bepalend zijn voor de vorm van de uiteindelijke structuur die gevormd wordt. De snelheid van het proces wordt beïnvloed door hoe vaak en hoe lang de colloïden met elkaar in contact komen. Dit hangt af van de concentratie van de deeltjes, maar ook van hoe gemakkelijk deze door het medium kunnen bewegen: de mate van hydrodynamische frictie van de deeltjes bepaalt voor een groot deel hun diffusie-eigenschappen.

De **diffusie**, of Brownse beweging, van colloïdale deeltjes is een belangrijk onderdeel van dit proefschrift. De Brownse beweging is voor het eerst beschreven door de botanicus Robert Brown in 1827. Het wordt mooi omschreven in de vertaalde woorden van Jean-Baptiste Perrin:[19] *"... alle deeltjes die zich in de vloeistof bevinden bewegen zich, in plaats van met een ordelijke opgaande of neergaande beweging afhankelijk van hun dichtheid, juist totaal willekeurig. Ze komen en gaan, stoppen, komen weer in beweging, stijgen, dalen en gaan weer omhoog, zonder ook maar de neiging te hebben om tot stilstand te komen."* Met zijn experimenten kon Perrin de constante van Avogadro bepalen. Deze constante komt voor in een formule die door Einstein was opgesteld om de gemiddelde kwadratische verplaatsing van moleculen in een vloeistof te voorspellen. Samen bewezen zij zo de realiteit van moleculen en legden de basis voor het onderzoek naar diffusie.

De colloïdale deeltjes zijn dus voortdurend in beweging. De hoeveelheid wrijving die ze daarbij ondervinden is afhankelijk van hun vorm. Door te begrijpen hoe deze wrijving afhangt van vorm kunnen we moleculaire processen in de biologie en industrie uiteindelijk beter begrijpen. Wat dit lastig maakt, is dat veel biologische structuren zoals cellen, eiwitten en DNA-strengen voortdurend van vorm veranderen. Deze vormveranderingen hebben natuurlijk invloed op de hoeveelheid wrijving die zij ervaren. Het begrijpen van de wisselwerking tussen **vormveranderingen en wrijving** in colloïdale systemen is een belangrijk onderwerp van dit proefschrift.

Bovenstaande onderwerpen komen samen in **dit proefschrift**, waar we met behulp van colloïdale modelsystemen hebben geprobeerd om een gedeeltelijk antwoord te

geven op fundamentele vraagstukken aangaande het gedrag van microscopische objecten.

Hoofdstuk 1 is een korte inleiding in de wereld van de colloïden, die hier kort in het Nederlands is samengevat. Het omvat een uitgebreidere bespreking van de belangrijkste concepten die van belang zijn voor dit proefschrift, met onder andere afbeeldingen van DNA strengen en colloïdale deeltjes.

In **Hoofdstuk 2** bespreken we de beweging van colloïdale deeltjes die bestaan uit twee bollen: zogenaamde halterdeeltjes. Specifiek gebruiken we een speciale holografische microscopie techniek om de beweging in de buurt van een oppervlak in 3D te kunnen volgen. We ontdekten daarbij dat de deeltjes niet vlak liggen ten opzichte van het oppervlak, maar zich onder een hoek boven het oppervlak bewegen. Dit wordt waarschijnlijk veroorzaakt door elektrostatische interacties, maar moet verder onderzocht worden. Onze resultaten laten zien dat deeltjes die niet bolvormig zijn, interessant gedrag vertonen in de buurt van oppervlakken, wat van belang kan zijn vanuit een fundamenteel oogpunt en met het oog op biologische en industriële toepassingen.

De halterdeeltjes uit Hoofdstuk 2 zijn een voorbeeld van rigide deeltjes: nadat ze gebonden zijn, kunnen ze niet meer van vorm veranderen. Om het effect van vormveranderingen te kunnen bestuderen, maken we gebruik van **deeltjes-gedragen lipide dubbellagen**. Dit is een lipide dubbellaag, een materiaal waaruit de buitenkant van een biologische cel bestaat, die ondersteund wordt door een colloïdaal deeltje. Een schematische weergave van een deeltjes-gedragen lipide dubbellaag is te zien in Figuur 10.1d. De lipide dubbellaag vormt een vloeibare schil rondom het deeltje. In deze vloeibare schil kunnen stukjes DNA worden toegevoegd, die een speciale functionele groep hebben. Via deze functionele groepen kunnen we ervoor zorgen, dat twee DNA strengen met de juiste functionele groepen aan elkaar kunnen binden. Het DNA kan zo dienen als een soort lijm tussen de deeltjes, die alleen plakt tussen de juiste paren deeltjes. Dit zorgt ervoor dat we het zelfassemblage proces beter kunnen sturen. Doordat de lipide dubbellaag waarin de stukjes DNA zich bevinden vloeibaar is, kunnen de DNA linkers zich over het oppervlak van het deeltje bewegen. Daardoor kunnen gebonden deeltjes zich ook nog ten opzichte van elkaar bewegen, wat te zien is in Figuur 10.1e.

In **Hoofdstuk 3** beschrijven we hoe deeltjes-gedragen lipide dubbellagen het beste gemaakt kunnen worden voor gebruik in zelfassemblage. Daarbij is de vloeibaarheid en homogeniteit van de lipide dubbellaag van groot belang. Vervolgens zoeken we in **Hoofdstuk 4** verder uit hoe we dit zelfassemblage proces kunnen sturen door middel van multivalente interacties. Daaruit blijkt dat de hoeveelheid deeltjes die kunnen binden aan een gegeven colloïdaal deeltje afhankelijk is van de concentratie van DNA linkers, een effect dat bekend staat als linker verzadiging.

Door gebruik te maken van linker verzadiging, hebben we in **Hoofdstukken 5–6** flexibele kettingen van deeltjes-gedragen lipide dubbellagen gemaakt, zoals afgebeeld in Figuur 10.1e. Deze flexibele ketens kunnen dienen als modelsystemen voor (bio)polymeren en eiwitten, waarbij de vorm mogelijkerwijs de biologische functie

kan beïnvloeden. We hebben het gedrag van de flexibele colloïdale kettingen vergeleken met voorspellingen uit de polymeertheorie en met hydrodynamische simulaties. Bij de analyse van de diffusie-eigenschappen van de deeltjes vonden we dat er duidelijke effecten zijn van vormveranderingen op de beweging. Een voorbeeld hiervan is de Brownse quasi-schelpbeweging bij colloïdale microscharnieren. Daarbij zijn vormveranderingen gekoppeld aan verplaatsingen: als het deeltje in een bepaalde richting beweegt, "opent" het scharniertje zich en vice-versa, zoals geïllustreerd in Figuur 10.1f.

Naast flexibele kettingen en microscharnieren hebben we in **Hoofdstuk 7** flexibele colloïdale ringen gemaakt, die kunnen dienen als modelsysteem voor ringpolymeren. Voor de ringen hebben we gevonden dat de hoeveelheid interne vrijheidsgraden per deeltje invloed heeft op de flexibiliteit van de ringen.

Als laatste beschrijven we in **Hoofdstuk 8** recente experimenten waarin we anisotrope deeltjes gebruiken die maar in bepaalde richtingen kunnen binden, maar wel nog van vorm kunnen veranderen. We verwachten dat dit soort deeltjes van groot belang kunnen zijn voor het maken van intelligente materialen.

Samenvattend beschrijft dit proefschrift hoe colloïdale bouwstenen die van vorm kunnen veranderen zich gedragen en een geschikt modelsysteem vormen, waarmee het gedrag van flexibele structuren in biologische en industriële toepassingen beter doorgrond kan worden.

List of publications

In this thesis:

1. **Conformations and diffusion of flexibly linked colloidal chains.**
   R.W. Verweij, P.G. Moerman, L.P.P. Huijnen, N.E.G. Ligthart, I. Chakraborty, J. Groenewold, W.K. Kegel, A. van Blaaderen and D.J. Kraft
   Journal of Physics: Materials, in press (2021). doi:10.1088/2515-7639/abf571 In: Chapter 6.

2. **Height distribution and orientation of colloidal dumbbells near a wall.**
   R.W. Verweij*, S. Ketzetzi*, J. Graaf and D.J. Kraft
   Phys. Rev. E, 102, 062608 (2020). doi:10.1103/PhysRevE.102.062608 In: Chapter 2.

3. **Flexibility-induced effects in the Brownian motion of colloidal trimers.**
   R.W. Verweij*, P.G. Moerman*, N.E.G. Ligthart, L.P.P. Huijnen, J. Groenewold, W.K. Kegel, A. van Blaaderen and D.J. Kraft
   Phys. Rev. Research, 2, 033136 (2020). doi:10.1103/PhysRevResearch.2.033136 In: Chapter 5.

4. **Colloid supported lipid bilayers for self-assembly.**
   M. Rinaldin*, R.W. Verweij*, I. Chakraborty and D.J. Kraft
   Soft Matter, 15, 1345-1360 (2019). doi:10.1039/C8SM01661E In: Chapter 3.

Other:

5. **Dumbbell impurities in 2D crystals of repulsive colloidal spheres induce particle-bound dislocations.**
   V. Meester, C. van der Wel, R.W. Verweij, G. Biondaro, D.J. Kraft
   Under review (submitted Oct. 2020).

6. **Micrometer-sized TPM emulsion droplets with surface-mobile binding groups.**
   C. van der Wel, G.L. van de Stolpe, R.W. Verweij, D.J. Kraft
   J. Phys. Condens. Matter, 30, 094005 (2018). doi:10.1088/1361-648x/aaab22

7. **Preparation of colloidal organosilica spheres through spontaneous emulsification.**
   C. van der Wel, R.K. Bhan, R.W. Verweij, H.C. Frijters, Z. Gong, A.D. Hollingsworth, S. Sacanna and D.J. Kraft
   Langmuir, 33, 8174-8180 (2017). doi:10.1021/acs.langmuir.7b01398

8. **Colloidal recycling: reconfiguration of random aggregates into patchy particles.**
   V. Meester, R.W. Verweij, C. van der Wel and D.J. Kraft
   ACS Nano, 10, 4322-4329 (2016). doi:10.1021/acsnano.5b07901

*These authors contributed equally.

About the author

I was born on June 13th, 1992 in the Dutch village Heemskerk and grew up in the neighboring city of Beverwijk. I received my secondary education at the Gymnasium Felisenum in Velsen-Zuid, where I graduated cum laude in 2010. Next, I started my Bachelor studies in Physics at Leiden University. During my Bachelor studies, I additionally obtained a Propaedeutics degree in Computer Science and a Propaedeutics degree in Astronomy. Next to my studies, I worked as a tutor for high school students and as a web developer. I was a member of the student rowing association Asopos de Vliet. In 2014, I finished my Bachelor degree in Physics with the research project titled "Close-packed colloidal clusters" supervised by Vera Meester and Daniela Kraft.

Then, I started my Master studies in Physics at Leiden University, where I specialized in Biological and Soft Matter Physics. During this time, I was a member of the student canoe association Levitas. As part of my studies, I completed two research projects. The first project was titled "Simulation of diffusion-weighted MRI" and was supervised by Joor Arkesteijn, Frans Vos and Lucas van Vliet (Delft University). In this project, we collaborated with Farida Grinberg and Ezequiel Farrher from Forschungszentrum Jülich (Germany). For my second project titled "Synthesis of polymerizable emulsions and bulk synthesis of mobile clusters", I was supervised by Casper van der Wel and Daniela Kraft. I obtained my Master degree in Physics in 2016.

Shortly afterwards, I started my PhD under the supervision of Daniela Kraft, which resulted in the present thesis on the effects of anisotropy, multivalency and flexibility on colloidal systems. In addition to the research presented here, I have supervised four students during their research projects. I was a Teaching Assistent for the "Diffusion" and "Experimental Physics" courses. I have attended the Han-sur-Lesse Winterschool for Physical Chemistry (Belgium) twice and I followed a Master course on "Deep learning and Neural networks". Additionally, I attended several conferences to which I collaborated several poster presentations. I won the prize for the best poster at the Dutch Chemistry conference CHAINS (2017). I have given a talk during the International Soft Matter Conference (Edinburgh, UK, 2019). During my PhD studies, I collaborated with Melissa Rinaldin for Chapter 3, with Pepijn Moerman, Jan Groenewold, Willem Kegel and Alfons van Blaaderen (Utrecht University) for Chapters 5–6 and with Joost de Graaf (Utrecht University) and Stefania Ketzetzi for Chapter 2.

After my PhD studies, I will start as Modeler Air Quality at the *Rijksinstituut voor Volksgezondheid en Milieu* (RIVM, National Institute for Public Health and the Environment).

Acknowledgments

I am deeply grateful to a number of people that helped me during the course of my PhD studies. First, I would like to thank my supervisor Daniela Kraft for her excellent scientific advice, her overall support, enthusiasm and positive attitude: I could not have asked for a better PhD advisor. I thank Martin van Hecke for being my extra promotor and for useful discussions. I am grateful to the members of the Doctoral Committee for their critical assessment of my work.

Next, I would like to thank the people that have collaborated with me on parts of this thesis. I would like to thank Joost de Graaf (Utrecht University) and Stefania Ketzetzi for their contributions to Chapter 2. Joost, thank you for your insightful and speedy contributions, that often arrived late at night. Stefania, you have been a great office mate and I have enjoyed working together with you on this project. Thank you for all of your support and for being my paranymph. I would like to thank my other office mate, Melissa Rinaldin, not only for being a great colleague but also for her extensive contributions to Chapter 3. I am grateful to Indrani Chakraborty, who not only taught me how to make colloid supported lipid bilayers but also contributed additional data to Chapters 3, 6 and 7. I am heavily indebted to our collaborators from Utrecht University: Pepijn Moerman, Nathalie Ligthart, Willem Kegel, Jan Groenewold and Alfons van Blaaderen, who have made significant contributions to Chapters 5 and 6. Pepijn, thanks a lot for the pleasant collaboration and all of your input. I am grateful to Aleksandar Donev (NYU) and Brennan Sprinkle (NYU) for their advise on the simulations in Chapters 6 and 7. I thank Piotr Szymczak (University of Warsaw) for useful discussions about the center of diffusion of flexible objects.

During my PhD studies, I had the pleasure of supervising a number of students during their research projects: Max Ruckriegel, Loes Huijnen, Sarah Smolders and Nick Oikonomeas. Max, thank you for being my first student, I have enjoyed working together. Loes, thank you for your great contributions to Chapters 5–7 and the nice collaboration. Sarah, thank you for paving the way for the measurements in Chapter 2. Nick, thank you for your exploratory experiments that led to Chapter 2, the interesting discussions on holographic microscopy and machine learning and the great collaboration. On that note, I would like to thank Vera Meester and Casper van der Wel, who have been fantastic supervisors during my own respective Bachelor and Master research projects and have inspired me to pursue a PhD in colloid science. I would like to express my gratitude to my high school teacher Winfried Appelman for showing me how exciting Physics can be. I am grateful to my university teacher Robert-Jan Kooman for enthusing me about Mathematics. I thank Kick Moors for his invaluable advise.

I thank the LION and Graduate School secretaries for their administrative support and want to express my deepest gratitude in particular to Daniëlle Duijn-ter Veer, for all her help and patience. I would like to thank the IT department for their support and am grateful for access to the Maris and ALICE computing clusters. I thank the

fine mechanical and electronic departments for their technical support.

I would like to thank all former and present members of the Leiden Soft Matter groups for their useful feedback during meetings but moreover, for the nice coffee breaks, long lunches, borrels and group outings. You have made it a pleasure to work each day, even on days when experimental results were scarce. I especially thank Rachel Doherty for keeping the lab running and for her experimental support. Finally, I am deeply grateful to Ali Azadbakht for building the Optical Tweezers setup and for teaching me how to use it.

Als laatste wil ik mijn vrienden bedanken voor hun geduld bij het aanhoren van mijn uitleg over mijn onderzoek en voor hun vriendschap. Ik wil mijn familie bedanken voor al hun steun. Wim en Fieneke Tesselaar, bedankt voor alle goede zorgen toen ik een tijdje bij jullie mocht inwonen, daarvoor en ook daarna. Ik bedank mijn tante Loes voor de logeerplek in Leiden en voor inspirerende gesprekken over studiekeuzes en onderzoek. Ook ben ik mijn opa Peter en oma Luck erg dankbaar, zij zijn heel nauw betrokken geweest bij mijn opvoeding en hebben mij altijd gesteund. Ik bedank mijn ouders Alexander & Désirée en mijn broertje Maurits voor al hun steun. In het bijzonder ben ik mijn moeder heel erg dankbaar, bij wie ik altijd terecht kon voor hulp en advies. Als laatste wil ik mijn partner Mark bedanken voor alles: dit proefschrift heeft ook van jou veel gevergd, maar je bent mij altijd blijven steunen.

Bibliography

1. H. Míguez, S. M. Yang, and G. A. Ozin. Optical properties of colloidal photonic crystals confined in rectangular microchannels. *Langmuir*, 19(8):34793485, 2003.
2. M. He, J. P. Gales, É. Ducrot, Z. Gong, G.-R. Yi, S. Sacanna, and D. J. Pine. Colloidal diamond. *Nature*, 585(7826):524–529, 2020.
3. Y. Xia, Y. Yin, Y. Lu, and J. McLellan. Template-assisted self-assembly of spherical colloids into complex and controllable structures. *Adv. Funct. Mater.*, 13(12):907–918, 2003.
4. W. B. Rogers, W. M. Shih, and V. N. Manoharan. Using DNA to program the self-assembly of colloidal nanoparticles and microparticles. *Nat. Rev. Mater.*, 1(3):1–14, 2016.
5. E. Dickinson. Colloids in food: ingredients, structure, and stability. *Annu. Rev. Food Sci. Technol.*, 6:211–233, 2015.
6. D. P. Otto, A. Otto, and M. M. De Villiers. Differences in physicochemical properties to consider in the design, evaluation and choice between microparticles and nanoparticles for drug delivery. *Expert Opin. Drug Deliv.*, 12(5):763–777, 2015.
7. S. Scalia, P. M. Young, and D. Traini. Solid lipid microparticles as an approach to drug delivery. *Expert Opin. Drug Deliv.*, 12(4):583–599, 2015.
8. D. S. Kohane. Microparticles and nanoparticles for drug delivery. *Biotechnology and bioengineering*, 96(2):203–209, 2007.
9. A. M. Carmona-Ribeiro. Preparation and characterization of biomimetic nanoparticles for drug delivery. In *Nanoparticles in Biology and Medicine: Methods and Protocols*, pages 283–294. Humana Press, Totowa, NJ, 2012.
10. H. Löwen. Colloidal soft matter under external control. *J. Phys.: Condens. Matter*, 13(24): R415R432, 2001.
11. B. Carrasco and J. G. De La Torre. Hydrodynamic properties of rigid particles: Comparison of different modeling and computational procedures. *Biophys. J.*, 76(6):3044–3057, 1999. doi:10.1016/S0006-3495(99)77457-6.
12. J. Fung and V. N. Manoharan. Holographic measurements of anisotropic three-dimensional diffusion of colloidal clusters. *Phys. Rev. E*, 88(2):020302, 2013. doi:10.1103/PhysRevE.88.020302.
13. D. J. Kraft, R. Wittkowski, B. Ten Hagen, K. V. Edmond, D. J. Pine, and H. Löwen. Brownian motion and the hydrodynamic friction tensor for colloidal particles of complex shape. *Phys. Rev. E*, 88(5):050301, 2013. doi:10.1103/PhysRevE.88.050301.
14. A. Chakrabarty, F. Wang, K. Sun, and Q. H. Wei. Effects of translation-rotation coupling on the displacement probability distribution functions of boomerang colloidal particles. *Soft Matter*, 12(19):4318–4323, 2016. doi:10.1039/c6sm00568c.
15. S. Chemburu, K. Fenton, G. P. Lopez, and R. Zeineldin. Biomimetic Silica Microspheres in Biosensing. *Molecules*, 15(12):1932–1957, 2010.
16. M. Hoffmann, C. S. Wagner, L. Harnau, and A. Wittemann. 3D Brownian diffusion of submicron-sized particle clusters. *ACS Nano*, 3(10):3326–3334, 2009. doi:10.1021/nn900902b.
17. A. Einstein. Über die von der molekularkinetischen Theorie der Wärme geforderte Bewegung von in ruhenden Flüssigkeiten suspendierten Teilchen. *Annalen der Physik*, 322(8): 549–560, 1905. doi:10.1002/andp.19053220806.
18. W. Sutherland. LXXV. A dynamical theory of diffusion for non-electrolytes and the molecular mass of albumin. *London Edinburgh Philos. Mag. J. Sci.*, 9(54):781–785, 1905. doi:10.1080/14786440509463331.

19. J. Perrin. Mouvement brownien et réalité moléculaire. *Ann. Chim. Phys.*, 18:104, 1909.
20. J. N. Israelachvili. *Intermolecular and surface forces*. Academic press, 2011.
21. L. Teulon, Y. Hallez, S. Raffy, F. Guerin, E. Palleau, and L. Ressier. Electrostatic directed assembly of colloidal microparticles assisted by convective flow. *J. Phys. Chem. C*, 123(1): 783–790, 2018.
22. V. A. Parsegian. *Van der Waals forces: a handbook for biologists, chemists, engineers, and physicists*. Cambridge University Press, 2005.
23. H. N. Lekkerkerker and R. Tuinier. Depletion interaction. In *Colloids and the depletion interaction*, pages 57–108. Springer, 2011.
24. L. Rossi, S. Sacanna, W. T. M. Irvine, P. M. Chaikin, D. J. Pine, and A. P. Philipse. Cubic crystals from cubic colloids. *Soft Matter*, 7(9):4139–4142, 2011.
25. S. Sacanna, L. Rossi, and D. J. Pine. Magnetic click colloidal assembly. *J. Am. Chem. Soc.*, 134(14):6112–6115, 2012.
26. G. I. Vega-Bellido, R. A. DeLaCruz-Araujo, I. Kretzschmar, and U. M. Córdova-Figueroa. Self-assembly of magnetic colloids with shifted dipoles. *Soft Matter*, 15(20):4078–4086, 2019.
27. A. Sánchez-Iglesias, M. Grzelczak, T. Altantzis, B. Goris, J. Perez-Juste, S. Bals, G. Van Tendeloo, S. H. Donaldson Jr, B. F. Chmelka, J. N. Israelachvili, et al. Hydrophobic interactions modulate self-assembly of nanoparticles. *ACS Nano*, 6(12):11059–11065, 2012.
28. Q. Chen, S. C. Bae, and S. Granick. Directed self-assembly of a colloidal kagome lattice. *Nature*, 469(7330):381–384, 2011.
29. S. Faber, Z. Hu, G. H. Wegdam, P. Schall, et al. Controlling colloidal phase transitions with critical casimir forces. *Nat. Commun.*, 4(1):1–6, 2013.
30. T. A. Nguyen, A. Newton, D. J. Kraft, P. G. Bolhuis, and P. Schall. Tuning patchy bonds induced by critical casimir forces. *Materials*, 10(11):1265, 2017.
31. J. Happel and H. Brenner. *Low Reynolds number hydrodynamics with special applications to particulate media*. Springer, 1983. doi:10.1007/978-94-009-8352-6.
32. H. Faxen. The resistance against the movement of a rigour sphere in viscous fluids, which is embedded between two parallel layered barriers. *Ann. Phys.*, 4:79–89, 1922.
33. K. Zahn, J. M. Méndez-Alcaraz, and G. Maret. Hydrodynamic interactions may enhance the self-diffusion of colloidal particles. *Phys. Rev. Lett.*, 79(1):175, 1997.
34. J. Rotne and S. Prager. Variational Treatment of Hydrodynamic Interaction in Polymers. *J. Chem. Phys.*, 50(11):4831–4837, 1969. doi:10.1063/1.1670977.
35. J. W. Swan and J. F. Brady. Simulation of hydrodynamically interacting particles near a no-slip boundary. *Physics of Fluids*, 19(11):113306, 2007. doi:10.1063/1.2803837.
36. A. Furukawa and H. Tanaka. Key role of hydrodynamic interactions in colloidal gelation. *Phys. Rev. Lett.*, 104(24):245702, 2010.
37. P. P. Lele, J. W. Swan, J. F. Brady, N. J. Wagner, and E. M. Furst. Colloidal diffusion and hydrodynamic screening near boundaries. *Soft Matter*, 7:6844–6852, 2011. doi:10.1039/C0SM01466D.
38. J. Ortega-Vinuesa, A. Martın-Rodrıguez, and R. Hidalgo-Alvarez. Colloidal stability of polymer colloids with different interfacial properties: mechanisms. *J. Colloid Interface Sci.*, 184(1):259–267, 1996.
39. S. Flicker and S. Bike. Measuring double layer repulsion using total internal reflection microscopy. *Langmuir*, 9(1):257–262, 1993.
40. A. Dolan and S. F. Edwards. Theory of the stabilization of colloids by adsorbed polymer. *Proc. R. Soc. A*, 337(1611):509–516, 1974.

41. K. Ueno, A. Inaba, M. Kondoh, and M. Watanabe. Colloidal stability of bare and polymer-grafted silica nanoparticles in ionic liquids. *Langmuir*, 24(10):5253–5259, 2008.
42. E. B. Zhulina, O. V. Borisov, and V. A. Priamitsyn. Theory of steric stabilization of colloid dispersions by grafted polymers. *J. Colloid Interface Sci.*, 137(2):495–511, 1990.
43. J. Rädler, H. Strey, and E. Sackmann. Phenomenology and Kinetics of Lipid Bilayer Spreading on Hydrophilic Surfaces. *Langmuir*, 11(11):4539–4548, 1995. doi:10.1021/la00011a058.
44. P. S. Cremer and S. G. Boxer. Formation and Spreading of Lipid Bilayers on Planar Glass Supports. *The J. Phys. Chem. B*, 103(13):2554–2559, 1999.
45. R. P. Richter, R. Bérat, and A. R. Brisson. Formation of solid-supported lipid bilayers: an integrated view. *Langmuir*, 22(8):3497–3505, 2006.
46. Y. Jing, H. Trefna, M. Persson, B. Kasemo, and S. Svedhem. Formation of supported lipid bilayers on silica: relation to lipid phase transition temperature and liposome size. *Soft Matter*, 10(1):187–95, 2014.
47. J. Grdadolnik, F. Merzel, and F. Avbelj. Origin of hydrophobicity and enhanced water hydrogen bond strength near purely hydrophobic solutes. *Proc. Natl. Acad. Sci. U.S.A.*, 114(2):322–327, 2017.
48. G. M. Whitesides and B. Grzybowski. Self-Assembly at All Scales. *Science*, 295:1644–1225, 2002.
49. M.-P. Valignat, O. Theodoly, J. C. Crocker, W. B. Russel, and P. M. Chaikin. Reversible self-assembly and directed assembly of DNA-linked micrometer-sized colloids. *Proc. Natl. Acad. Sci. U.S.A.*, 102(12):4225–4229, 2005.
50. P. L. Biancaniello, A. J. Kim, and J. C. Crocker. Colloidal interactions and self-assembly using DNA hybridization. *Phys. Rev. Lett.*, 94(5):058302, 2005.
51. W. Li, H. Palis, R. Mérindol, J. Majimel, S. Ravaine, and E. Duguet. Colloidal molecules and patchy particles: complementary concepts, synthesis and self-assembly. *Chem. Soc. Rev.*, 49(6):1955–1976, 2020.
52. D. J. Kraft, W. S. Vlug, C. M. van Kats, A. van Blaaderen, A. Imhof, and W. K. Kegel. Self-assembly of colloids with liquid protrusions. *J. Am. Chem. Soc.*, 131(3):1182–1186, 2009.
53. É. Duguet, C. Hubert, C. Chomette, A. Perro, and S. Ravaine. Patchy colloidal particles for programmed self-assembly. *Comptes Rendus Chimie*, 19(1-2):173–182, 2016.
54. S. Sacanna, M. Korpics, K. Rodriguez, L. Colón-Meléndez, S.-H. Kim, D. J. Pine, and G.-R. Yi. Shaping colloids for self-assembly. *Nat. Commun.*, 4(1):1–6, 2013.
55. M. Hadorn and P. Eggenberger Hotz. DNA-Mediated Self-Assembly of Artificial Vesicles. *PLoS ONE*, 5(3):e9886, 2010.
56. Y. Zhang, A. McMullen, L. L. Pontani, X. He, R. Sha, N. C. Seeman, J. Brujic, and P. M. Chaikin. Sequential self-assembly of DNA functionalized droplets. *Nat. Commun.*, 8(1): 21, 2017.
57. D. Ortiz, K. L. Kohlstedt, T. D. Nguyen, and S. C. Glotzer. Self-assembly of reconfigurable colloidal molecules. *Soft Matter*, 10(20):3541–3552, 2014.
58. K. L. Kohlstedt and S. C. Glotzer. Self-assembly and tunable mechanics of reconfigurable colloidal crystals. *Phys. Rev. E*, 87(3), 2013.
59. J. D. Joannopoulos, P. R. Villeneuve, and S. Fan. Photonic crystals: putting a new twist on light. *Nature*, 386(6621):143–149, 1997.
60. Y. Lin, P. R. Herman, C. E. Valdivia, J. Li, V. Kitaev, and G. A. Ozin. Photonic band structure of colloidal crystal self-assembled in hollow core optical fiber. *Appl. Phys. Lett.*, 86(12):121106, 2005.

61. E. Sackmann. Supported membranes: Scientific and practical applications. *Science*, 271 (5245):43–48, 2007.
62. C. Madwar, G. Gopalakrishnan, and R. B. Lennox. Interfacing living cells and spherically supported bilayer lipid membranes. *Langmuir*, 31(16):4704–4712, 2015.
63. S. Mashaghi, T. Jadidi, G. Koenderink, and A. Mashaghi. Lipid Nanotechnology. *Int. J. Mol. Sci.*, 14:4242–4282, 2013.
64. M. Rinaldin, P. Fonda, L. Giomi, and D. J. Kraft. Geometric pinning and antimixing in scaffolded lipid vesicles. *Nat. Commun.*, 11(1):1–10, 2020.
65. P. Fonda, M. Rinaldin, D. J. Kraft, and L. Giomi. Interface geometry of binary mixtures on curved substrates. *Phys. Rev. E*, 98(3):032801, 2018.
66. F. Gentile, M. Moretti, T. Limongi, A. Falqui, G. Bertoni, A. Scarpellini, S. Santoriello, L. Maragliano, R. Proietti Zaccaria, and E. Di Fabrizio. Direct imaging of DNA fibers: the visage of double helix. *Nano Lett.*, 12(12):6453–6458, 2012.
67. Sponk. Difference DNA-RNA, 2010. URL `commons.wikimedia.org/wiki/File:Difference_DNA_RNA-DE.svg`.
68. M. P. Ball. Ligation, 2007. URL `commons.wikimedia.org/wiki/File:Ligation.svg`.
69. Y. Wang, Y. Wang, X. Zheng, É. Ducrot, J. S. Yodh, M. Weck, D. J. Pine, E. Ducrot, J. S. Yodh, M. Weck, and D. J. Pine. Crystallization of DNA-coated colloids. *Nat. Commun.*, 6: 7253, 2015.
70. C. A. Mirkin, R. L. Letsinger, R. C. Mucic, and J. J. Storhoff. A DNA-based method for rationally assembling nanoparticles into macroscopic materials. *Nature*, 382(6592): 607–609, 1996.
71. D. Nykypanchuk, M. M. Maye, D. Van Der Lelie, and O. Gang. DNA-guided crystallization of colloidal nanoparticles. *Nature*, 451(7178):549–552, 2008.
72. M. E. Leunissen, R. Dreyfus, R. Sha, T. Wang, N. C. Seeman, D. J. Pine, and P. M. Chaikin. Towards self-replicating materials of DNA-functionalized colloids. *Soft Matter*, 5(12): 2422–2430, 2009. doi:10.1039/b817679e.
73. M. E. Leunissen and D. Frenkel. Numerical study of DNA-functionalized microparticles and nanoparticles: Explicit pair potentials and their implications for phase behavior. *The J. Chem. Phys.*, 134(8):084702, 2011.
74. N. Geerts and E. Eiser. DNA-functionalized colloids: Physical properties and applications. *Soft Matter*, 6(19):4647–4660, 2010.
75. L. Di Michele and E. Eiser. Developments in understanding and controlling self assembly of DNA-functionalized colloids. *Phys. Chem. Chem. Phys.*, 15(9):3115–3129, 2013. doi:10.1039/c3cp43841d.
76. L. Di Michele, F. Varrato, J. Kotar, S. H. Nathan, G. Foffi, and E. Eiser. Multistep kinetic self-assembly of DNA-coated colloids. *Nat. Commun.*, 4:2007, 2013.
77. M. L. Mansfield, L. Rakesh, and D. A. Tomalia. The random parking of spheres on spheres. *J. Chem. Phys.*, 105(8):3245–3249, 1996.
78. Y. Wang, Y. Wang, X. Zheng, É. Ducrot, M.-G. Lee, G.-R. Yi, M. Weck, and D. J. Pine. Synthetic strategies toward DNA-coated colloids that crystallize. *J. Am. Chem. Soc.*, 137 (33):10760–10766, 2015.
79. H. R. Vutukuri, J. Stiefelhagen, T. Vissers, A. Imhof, and A. van Blaaderen. Bonding assembled colloids without loss of colloidal stability. *Adv. Mater.*, 24(3):412–416, 2012.
80. Y. Wang, Y. Wang, D. R. Breed, V. N. Manoharan, L. Feng, A. D. Hollingsworth, M. Weck, and D. J. Pine. Colloids with valence and specific directional bonding. *Nature*, 491(7422): 51–55, 2012.

81. Z. Gong, T. Hueckel, G.-R. Yi, and S. Sacanna. Patchy particles made by colloidal fusion. *Nature*, 550(7675):234–238, 2017.
82. J. S. Oh, G.-R. Yi, D. J. Pine, et al. Photo-printing of faceted DNA patchy particles. *Proc. Natl. Acad. Sci. U.S.A.*, 117(20):10645–10653, 2020.
83. D. J. Kraft, J. Hilhorst, M. A. P. Heinen, M. J. Hoogenraad, B. Luigjes, and W. K. Kegel. Patchy polymer colloids with tunable anisotropy dimensions. *JPCB*, 2011.
84. L. Feng, L.-L. Pontani, R. Dreyfus, P. Chaikin, and J. Brujic. Specificity, flexibility and valence of DNA bonds guide emulsion architecture. *Soft Matter*, 9(41):9816–9823, 2013.
85. I. Chakraborty, V. Meester, C. Van Der Wel, and D. J. Kraft. Colloidal joints with designed motion range and tunable joint flexibility. *Nanoscale*, 9(23):7814–7821, 2017. doi:10.1039/c6nr08069c.
86. T. Witten Jr and L. M. Sander. Diffusion-limited aggregation, a kinetic critical phenomenon. *Phys. Rev. Lett.*, 47(19):1400, 1981.
87. M. Kolb and J. Rémi. Chemically limited versus diffusion limited aggregation. *Journal de Physique Lettres*, 45(20):977–981, 1984.
88. Ved1123. Time reversible flow demonstration in a taylor-couette system, 2018. URL `commons.wikimedia.org/wiki/File:Time_reversible_flow_demonstration_in_a_Taylor-Couette_system.png`.
89. H. I. Andersson and F. Jiang. Forces and torques on a prolate spheroid: Low-reynolds-number and attack angle effects. *Acta Mechanica*, 230(2):431–447, 2019.
90. G. Bagheri and C. Bonadonna. On the drag of freely falling non-spherical particles. *Powder Technology*, 301:526–544, 2016.
91. Y. Han, A. M. Alsayed, M. Nobili, J. Zhang, T. C. Lubensky, and A. G. Yodh. Brownian motion of an ellipsoid. *Science*, 314(5799):626–630, 2006. doi:10.1126/science.1130146.
92. M. Von Smoluchowski. Zur kinetischen theorie der brownschen molekularbewegung und der suspensionen. *Annalen der Physik*, 326(14):756–780, 1906.
93. G. Stokes. On the effect of internal friction of fluids on the motion of pendulums. In *Transactions of the Cambridge Philosophical Society*, volume 9, chapter X, section IV, equation 126, page 51. Cambridge Philosophical Society, 1856.
94. V. Totlani and M. Chinnan. Effect of stabilizer levels and storage conditions on texture and viscosity of peanut butter. *Peanut Science*, 34(1):1–9, 2007.
95. A. Meunier. Friction coefficient of rod-like chains of spheres at very low Reynolds numbers. II. Numerical simulations. *Journal de Physique II*, 4(4):561–566, 1994. doi:10.1051/jp2:1994141.
96. K. Zahn, R. Lenke, and G. Maret. Friction coefficient of rod-like chains of spheres at very low Reynolds numbers. I. Experiment. *Journal de Physique II*, 4(4):555–560, 1994. doi:10.1051/jp2:1994146.
97. A. Chakrabarty, A. Konya, F. Wang, J. V. Selinger, K. Sun, and Q. H. Wei. Brownian motion of arbitrarily shaped particles in two dimensions. *Langmuir*, 30(46):13844–13853, 2014. doi:10.1021/la5037053.
98. L. Koens, M. Lisicki, and E. Lauga. The non-Gaussian tops and tails of diffusing boomerangs. *Soft Matter*, 13(16):2977–2982, 2017. doi:10.1039/c6sm02649d.
99. A. V. Butenko, E. Mogilko, L. Amitai, B. Pokroy, and E. Sloutskin. Coiled to diffuse: Brownian motion of a helical bacterium. *Langmuir*, 28(36):12941–12947, 2012. doi:10.1021/la302056j.
100. I. Serdyuk, N. Zaccai, and J. Zaccai. *Methods in Molecular Biophysics: Structure, Dynamics, Function*. Cambridge University Press, 2007.

101. J. Garcia de la Torre. Hydrodynamics of segmentally flexible macromolecules. *Eur. Biophys. J.*, 5:307–322, 1994.
102. L. Gregory, K. G. Davis, B. Sheth, J. Boyd, R. Jefferis, C. Nave, and D. R. Burton. The solution conformations of the subclasses of human IgG deduced from sedimentation and small angle X-ray scattering studies. *Molecular Immunology*, 24(8):821–829, 1987. doi:10.1016/0161-5890(87)90184-2.
103. J. Yguerabide, H. F. Epstein, and L. Stryer. Segmental flexibility in an antibody molecule. *J. Mol. Biol.*, 51(3):573–590, 1970. doi:10.1016/0022-2836(70)90009-4.
104. P. Illien, T. Adeleke-Larodo, and R. Golestanian. Diffusion of an enzyme: The role of fluctuation-induced hydrodynamic coupling. *EPL*, 119(4):40002, 2017. doi:10.1209/0295-5075/119/40002.
105. W. A. Wegener. Center of Diffusion of Flexible Macromolecules. *Macromolecules*, 18(12): 2522–2530, 1985. doi:10.1021/ma00154a029.
106. W. A. Wegener. Bead models of segmentally flexible macromolecules. *J. Chem. Phys.*, 76 (12):6425–6430, 1982.
107. S. C. Harvey, P. Mellado, and J. G. De La Torre. Hydrodynamic resistance and diffusion coefficients of segmentally flexible macromolecules with two subunits. *J. Chem. Phys.*, 78 (4):2081–2090, 1983. doi:10.1063/1.444917.
108. S. C. Harvey. Transport properties of particles with segmental flexibility. I. Hydrodynamic resistance and diffusion coefficients of a freely hinged particle. *Biopolymers*, 18(5):1081–1104, 1979. doi:10.1002/bip.1979.360180506.
109. S. Mornet, O. Lambert, E. Duguet, and A. Brisson. The formation of supported lipid bilayers on silica nanoparticles revealed by cryoelectron microscopy. *Nano Lett.*, 5(2): 281–285, 2005.
110. S. A. Van Der Meulen and M. E. Leunissen. Solid colloids with surface-mobile DNA linkers. *J. Am. Chem. Soc.*, 135(40):15129–15134, 2013.
111. S. A. J. Van Der Meulen, G. V. Dubacheva, M. Dogterom, R. P. Richter, and M. E. Leunissen. Quartz crystal microbalance with dissipation monitoring and spectroscopic ellipsometry measurements of the phospholipid bilayer anchoring stability and kinetics of hydrophobically modified DNA oligonucleotides. *Langmuir*, 30(22):6525–6533, 2014.
112. S. A. J. Van der Meulen, G. Helms, and M. Dogterom. Solid colloids with surface-mobile linkers. *J. Phys.: Condens. Matter*, 27(23):233101, 2015.
113. A. L. Troutier and C. Ladavière. An overview of lipid membrane supported by colloidal particles. *Adv. Colloid Interface Sci.*, 133(1):1–21, 2007.
114. C. B. Carlson, P. Mowery, R. M. Owen, E. C. Dykhuizen, and L. L. Kiessling. Selective tumor cell targeting using low-affinity, multivalent interactions. *ACS chemical biology*, 2 (2):119–127, 2007.
115. D. Papakostas, F. Rancan, W. Sterry, U. Blume-Peytavi, and A. Vogt. Nanoparticles in dermatology. *Archives of dermatological research*, 303(8):533, 2011.
116. J. Li, X. Wang, T. Zhang, C. Wang, Z. Huang, X. Luo, and Y. Deng. A review on phospholipids and their main applications in drug delivery systems. *Asian J. Pharm. Sci.*, 10(2): 81–98, 2015.
117. S. Savarala, S. Ahmed, M. A. Ilies, and S. L. Wunder. Formation and Colloidal Stability of DMPC Supported Lipid Bilayers on SiO_2 Nanobeads. *Langmuir*, 26(14):12081–12088, 2010.
118. E. T. Castellana and P. S. Cremer. Solid supported lipid bilayers: From biophysical studies to sensor design. *Surf. Sci. Rep.*, 61(10):429–444, 2006.

119. F. Smallenburg, L. Filion, and F. Sciortino. Erasing no-man's land by thermodynamically stabilizing the liquid-liquid transition in tetrahedral particles. *Nat. Phys.*, 10(9):653–657, 2014.
120. H. Hu, P. S. Ruiz, and R. Ni. Entropy Stabilizes Floppy Crystals of Mobile DNA-Coated Colloids. *Phys. Rev. Lett.*, 120(4):048003, 2018.
121. S. M. Douglas, I. Bachelet, and G. M. Church. A logic-gated nanorobot for targeted transport of molecular payloads. *Science*, 335(6070):831–834, 2012.
122. A. E. Marras, L. Zhou, H.-J. Su, and C. E. Castro. Programmable motion of DNA origami mechanisms. *Proc. Natl. Acad. Sci. U.S.A.*, 112(3):713–718, 2015.
123. G. J. Lavella, A. D. Jadhav, and M. M. Maharbiz. A synthetic chemomechanical machine driven by ligand–receptor bonding. *Nano Lett.*, 12(9):4983–4987, 2012.
124. Y. Liu, J. Cheng, S. Fan, H. Ge, T. Luo, L. Tang, B. Ji, C. Zhang, D. Cui, Y. Ke, et al. Modular reconfigurable DNA origami: From two-dimensional to three-dimensional structures. *Angew. Chem.*, 59(51):23277–23282, 2020.
125. F. Wei, T. Zhong, Z. Zhan, and L. Yao. Self-assembled micro-nanorobots: From assembly mechanisms to applications. *ChemNanoMat*, 2020.
126. R. Lanfranco, P. K. Jana, L. Tunesi, P. Cicuta, B. M. Mognetti, L. Di Michele, and G. Bruylants. Kinetics of nanoparticlemembrane adhesion mediated by multivalent interactions. *Langmuir*, 35(6):2002–2012, 2019.
127. S.-H. Kim, J.-M. Lim, S.-K. Lee, C.-J. Heo, and S.-M. Yang. Biofunctional colloids and their assemblies. *Soft Matter*, 6(4):1092–1110, 2010. doi:10.1039/b920611f.
128. G. Wu, H. Cho, D. A. Wood, A. D. Dinsmore, and S. Yang. Confined assemblies of colloidal particles with soft repulsive interactions. *J. Am. Chem. Soc.*, 139(14):50955101, 2017. doi:10.1021/jacs.6b12975.
129. M. Han, J. K. Whitmer, and E. Luijten. Dynamics and structure of colloidal aggregates under microchannel flow. *Soft Matter*, 15(4):744–751, 2019. doi:10.1039/c8sm01451e.
130. E. Yildiz-Ozturk and O. Yesil-Celiktas. Diffusion phenomena of cells and biomolecules in microfluidic devices. *Biomicrofluidics*, 9(5):052606, 2015.
131. H. Serna, E. G. Noya, and W. T. Goźdź: The influence of confinement on the structure of colloidal systems with competing interactions. *Soft Matter*, 16:718, 2020.
132. P. Yang, A. H. Rizvi, B. Messer, B. F. Chmelka, G. M. Whitesides, and G. D. Stucky. Patterning porous oxides within microchannel networks. *Adv. Mat.*, 13(6):427–431, 2001.
133. R. Mondal and M. G. Basavaraj. Patterning of colloids into spirals via confined drying. *Soft Matter*, 15(16):3753–3761, 2020.
134. H.-J. Wu and M. A. Bevan. Direct measurement of single and ensemble average particle-surface potential energy profiles. *Langmuir*, 21(4):12441254, 2005.
135. H. Lorentz. *Adv. Theor. Phys.*, 1:23–33, 1907.
136. H. Faxen. Fredholm integral equations of hydrodynamics of liquids i. *Ark. Mat., Astron. Fys.* , 18:29–32, 1924.
137. H. Brenner. The slow motion of a sphere through a viscous fluid towards a plane surface. *Chem. Eng. Sci.*, 16:242–251, 1961.
138. A. J. Goldman, R. G. Cox, and H. Brenner. Slow viscous motion of a sphere parallel to a plane wall. I. Motion through a quiescent fluid. *Chem. Eng. Sci.*, 22:637–651, 1967.
139. N. A. Frej and D. C. Prieve. Hindered diffusion of a single sphere very near a wall in a nonuniform force field. *J. Chem. Phys.*, 98:7552, 1993. doi:10.1063/1.464695.
140. P. Sharma, S. Ghosh, and S. Bhattacharya. A high-precision study of hindered diffusion near a wall. *Appl. Phys. Lett.* , 97:104101, 2010. doi:10.1063/1.3486123.

141. S. A. Rogers, M. Lisicki, B. Cichocki, J. K. G. Dhont, and P. R. Lang. Rotational diffusion of spherical colloids close to a wall. *Phys. Rev. Lett.*, 109:098305, 2012. doi:10.1103/PhysRevLett.109.098305.
142. K. Huang and I. Szlufarska. Effect of interfaces on the nearby Brownian motion. *Nat. Commun.*, 6:8558, 2015. doi:10.1038/ncomms9558.
143. L. Lobry and N. Ostrowsky. Diffusion of Brownian particles trapped between two walls: Theory and dynamic-light-scattering measurements. *Phys. Rev. B*, 53:12050, 1996. doi:10.1103/PhysRevB.53.12050.
144. B. Lin, J. Yu, and S. A. Rice. Direct measurements of constrained Brownian motion of an isolated sphere between two walls. *Phys. Rev. E*, 62:3909, 2000. doi:10.1103/PhysRevE.62.3909.
145. E. R. Dufresne, D. Altman, and D. G. Grier. Brownian dynamics of a sphere between parallel walls. *Europhys. Lett.*, 53:264–270, 2001. doi:10.1209/epl/i2001-00147-6.
146. T. Benesch, S. Yiacoumi, and C. Tsouris. Brownian motion in confinement. *Phys. Rev. E*, 68:021401, 2003. doi:10.1103/PhysRevE.68.021401.
147. S. B. K Zembrzycki and T. A. Kowalewski. Analysis of wall effect on the process of diffusion of nanoparticles in a microchannel. *J. Phys.: Conf. Ser.* , 392:012014, 2012. doi:10.1088/1742-6596/392/1/012014.
148. S. L. Dettmer, S. Pagliara, K. Misiunas, and U. F. Keyser. Anisotropic diffusion of spherical particles in closely confining microchannels. *Phys. Rev. E*, 89:062305, 2014. doi:10.1103/PhysRevE.89.062305.
149. V. N. Michailidou, G. Petekidis, J. W. Swan, and J. F. Brady. Dynamics of concentrated hard-sphere colloids near a wall. *Phys. Rev. Lett.*, 102:068302, 2009. doi:10.1103/PhysRevLett.102.068302.
150. R. Pesché and G. Nägele. Stokesian dynamics study of quasi-two-dimensional suspensions confined between two parallel walls. *Phys. Rev. E* , 62:5432, 2000. doi:10.1103/PhysRevE.62.5432.
151. B. Eral, J. Oh, H. T. van den Ende, F. G. Mugele, and M. H. Duits. Anisotropic and hindered diffusion of colloidal particles in a closed cylinder. *Langmuir*, 22:16722–16729, 2010. doi:10.1021/la102273n.
152. B. Cui, H. Diamant, and B. Lin. Screened hydrodynamic interaction in a narrow channel. *Phys. Rev. Lett.*, 89:188302, 2002. doi:10.1103/PhysRevLett.89.188302.
153. J. Wang, C. F. Mbah, T. Przybilla, S. Englisch, E. Spiecker, M. Engel, and N. Vogel. Free energy landscape of colloidal clusters in spherical confinement. *ACS Nano*, 13:9005–9015, 2019. doi:10.1021/acsnano.9b03039.
154. J. T. Padding and W. J. Briels. Translational and rotational friction on a colloidal rod near a wall. *J. Chem. Phys.*, 132(5):054511, 2010. doi:10.1063/1.3308649.
155. T. Adeleke-Larodo, P. Illien, and R. Golestanian. Fluctuation-induced hydrodynamic coupling in an asymmetric, anisotropic dumbbell. *Eur. Phys. J. E*, 42(39):054511, 2019. doi:10.1140/epje/i2019-11799-5.
156. M. Haghighi, M. N. Tahir, W. Tremel, H.-J. Butt, and W. Steffen. Translational and rotational diffusion of gold nanorods near a wall. *J. Chem. Phys.*, 139:064710, 2013. doi:10.1063/1.4817405.
157. M. Lisicki, B. Cichocki, and E. Wajnryb. Near-wall diffusion tensor of an axisymmetric colloidal particle. *J. Chem. Phys.*, 145:034904, 2016. doi:10.1063/1.4958727.
158. S. Delong, F. B. Usabiaga, and A. Donev. Brownian dynamics of confined rigid bodies. *J. Chem. Phys.*, 143:144107, 2015. doi:10.1063/1.4932062.

159. M. X. Fernandes and J. G. de la Torre. Brownian dynamics simulation of rigid particles of arbitrary shape in external fields. *Biophys J*, 83(6):3039–3048, 2002. doi:10.1016/S0006-3495(02)75309-5.
160. M. D. Carbajal-Tinoco, R. Lopez-Fernandez, and J. L. Arauz-Lara. Asymmetry in colloidal diffusion near a rigid wall. *Phys. Rev. Lett.* , 99:138303, 2007. doi:10.1103/PhysRevLett.99.138303.
161. J. Leach, H. Mushfique, S. Keen, R. D. Leonardo, G. Ruocco, J. M. Cooper, and M. J. Padgett. Comparison of faxéns correction for a microsphere translating or rotating near a surface. *Phys. Rev. E*, 79:026301, 2009. doi:10.1103/PhysRevE.79.026301.
162. S. Jeney, B. Lukić, J. A. Kraus, T. Franosch, and L. Forró. Anisotropic memory effects in confined colloidal diffusion. *Phys. Rev. Lett.*, 100:240604, 2008. doi:10.1103/PhysRevLett.100.240604.
163. E. Schäffer, S. F. Nørrelykke, and J. Howard. Surface forces and drag coefficients of microspheres near a plane surface measured with optical tweezers. *Langmuir*, 23:3654, 2007. doi:10.1021/la0622368.
164. N. Garnier and N. Ostrowsky. Brownian dynamics in a confined geometry. experiments and numerical simulations. *J. Phys. II*, 1:1221–1232, 1991. doi:10.1051/jp2:1991129.
165. P. Holmqvist, J. K. G. Dhont, and P. R. Lang. Colloidal dynamics near a wall studied by evanescent wave light scattering: Experimental and theoretical improvements and methodological limitations. *J. Chem. Phys.*, 126:044707, 2007. doi:10.1063/1.2431175.
166. T. Watarai and T. Iwai. Direct observation of submicron Brownian particles at a solidliquid interface by extremely low coherence dynamic light scattering. *Appl. Phys. Express* , 7: 032502, 2014. doi:10.7567/APEX.7.032502.
167. M. I. M. Feitosa and O. N. Mesquita. Wall-drag effect on diffusion of colloidal particles near surfaces: A photon correlation study. *Phys. Rev. A* , 44:6677, 1991. doi:10.1103/PhysRevA.44.6677.
168. K. H. Lan, N. Ostrowsky, and D. Sornette. Brownian dynamics close to a wall studied by photon correlation spectroscopy from an evanescent wave. *Phys. Rev. Lett.*, 57:17, 1986. doi:10.1103/PhysRevLett.57.17.
169. P. Holmqvist, J. K. G. Dhont, and P. R. Lang. Anisotropy of Brownian motion caused only by hydrodynamic interaction with a wall. *Phys. Rev. E*, 74:021402, 2006. doi:10.1103/PhysRevE.74.021402.
170. M. Lisicki, B. Cichocki, S. A. Rogers, J. K. G. Dhont, and P. R. Lang. Translational and rotational near-wall diffusion of spherical colloids studied by evanescent wave scattering. *Soft Matter*, 10:4312–4323, 2014. doi:10.1039/C4SM00148F.
171. Y. Kazoe and M. Yoda. Measurements of the near-wall hindered diffusion of colloidal particles in the presence of an electric field. *Appl. Phys. Lett.*, 99:124104, 2011. doi:10.1063/1.3643136.
172. D. Prieve. Measurement of colloidal forces with TIRM. *Adv. Colloid Interface Sci.*, 82: 93–125, 1999. doi:10.1016/S0001-8686(99)00012-3.
173. G. Volpe, T. Brettschneider, L. Helden, and C. Bechinger. Novel perspectives for the application of total internal reflection microscopy. *Opt. Express*, 17:23975–23985, 2009. doi:10.1364/OE.17.023975.
174. L. Liu, A. Woolf, A. W. Rodriguez, and F. Capasso. Absolute position total internal reflection microscopy with an optical tweezer. *Proc. Natl. Acad. Sci. U.S.A.*, 111:E5609–E5615, 2014. doi:10.1073/pnas.1422178112.

175. S.-H. Lee, Y. Roichman, G.-R. Yi, S.-H. Kim, S.-M. Yang, A. van Blaaderen, P. van Oostrum, and D. G. Grier. Characterizing and tracking single colloidal particles with video holographic microscopy. *Opt. Express*, 15:18275–18282, 2007. doi:10.1364/OE.15.018275.
176. L. Dixon, F. C. Cheong, and D. G. Grier. Holographic deconvolution microscopy for high-resolution particle tracking. *Opt. Express*, 19:16410, 2011. doi:10.1364/OE.19.016410.
177. D. S. Bolintineanu, G. S. Grest, J. B. Lechman, F. Pierce, S. J. Plimpton, and P. R. Schunk. Particle dynamics modeling methods for colloid suspensions. *Comput. Part. Mech.*, 1: 321356, 2014.
178. C. Middleton, M. D. Hannel, A. D. Hollingsworth, D. J. Pine, and D. G. Grier. Optimizing the synthesis of monodisperse colloidal spheres using holographic particle characterization. *Langmuir*, 35:66026609, 2019. doi:10.1021/acs.langmuir.9b00012.
179. J. Garcia-Sucerquia, W. Xu, S. K. Jericho, P. Klages, M. H. Jericho, and H. J. Kreuzer. Digital in-line holographic microscopy. *Appl. Opt.*, 45:836, 2006. doi:10.1364/AO.45.000836.
180. P. Marquet, B. Rappaz, P. J. Magistretti, E. Cuche, Y. Emery, T. Colomb, and C. Depeursinge. Digital holographic microscopy: a noninvasive contrast imaging technique allowing quantitative visualization of living cells with subwavelength axial accuracy. *Opt. Lett.*, 30:468–470, 2005. doi:10.1364/OL.30.000468.
181. C. B. Giuliano, R. Zhang, and L. G. Wilson. Digital inline holographic microscopy (DIHM) of weakly-scattering subjects. *J. Vis. Exp.*, 84:e50488, 2014. doi:10.3791/50488.
182. W. Xu, M. H. Jericho, I. A. Meinertzhagen, and H. J. Kreuzer. Digital in-line holography for biological applications. *Proc. Natl. Acad. Sci. U.S.A.*, 98:11301–11305, 2001. doi:10.1073/pnas.191361398.
183. L. E. Altman and D. G. Grier. Catch: Characterizing and tracking colloids holographically using deep neural networks. *J. Phys. Chem. B*, 124:16021610, 2020. doi:10.1021/acs.jpcb.9b10463.
184. J. Zhang, P. Zhan, Z. Wang, W. Zhang, and N. Ming. Preparation of monodisperse silica particles with controllable size and shape. *J. Mater. Res.*, 18(3):649–653, 2003. doi:10.1557/JMR.2003.0085.
185. W. S. Rasband. ImageJ, 1997-2018. URL `imagej.nih.gov/ij/`.
186. S. Barkley, T. G. Dimiduk, J. Fung, D. M. Kaz, V. N. Manoharan, R. McGorty, R. W. Perry, and A. Wang. Holographic microscopy with Python and HoloPy, 2018.
187. D. W. Mackowski and M. I. Mishchenko. Calculation of the T matrix and the scattering matrix for ensembles of spheres. *J. Opt. Soc. Am. A*, 13(11):2266–2278, 1996.
188. D. Allan, C. van der Wel, N. Keim, T. A. Caswell, D. Wieker, R. W. Verweij, C. Reid, Thierry, L. Grueter, K. Ramos, apiszcz, zoeith, R. W. Perry, F. Boulogne, P. Sinha, pfigliozzi, N. Bruot, L. Uieda, J. Katins, H. Mary, and A. Ahmadia. soft-matter/trackpy: Trackpy v0.4.2, 2019. URL `doi.org/10.5281/zenodo.3492186`.
189. J. C. Crocker and D. G. Grier. Methods of digital video microscopy for colloidal studies. *J. Colloid Interface Sci.*, 179(1):298–310, 1996. doi:10.1006/jcis.1996.0217.
190. Y. Gu and D. Li. The zeta-potential of glass surface in contact with aqueous solutions. *J. Colloid Interface Sci.*, 226(2):328 – 339, 2000. doi:10.1006/jcis.2000.6827.
191. S. Ketzetzi, J. de Graaf, and D. J. Kraft. Diffusion-based height analysis reveals robust microswimmer-wall separation. *Phys. Rev. Lett.*, (125):238001, 2020. doi:10.1103/PhysRevLett.125.238001.
192. H. Faxén. *Einwirkung der Gefässwände auf den Widerstand gegen die Bewegung einer kleinen Kugel in einer zähen Flüssigkeit*. Uppsala Universitet, 1921.

193. I. Brouwer, A. Giniatullina, N. Laurens, J. R. T. V. Weering, D. Bald, G. J. L. Wuite, and A. J. Groffen. Direct quantitative detection of Doc2b-induced hemifusion in optically trapped membranes. *Nat. Commun.*, 6:8387, 2015.
194. A. McMullen, M. Holmes-Cerfon, F. Sciortino, A. Y. Grosberg, and J. Brujic. Freely Jointed Polymers Made of Droplets. *Phys. Rev. Lett.*, 121(13):138002, 2018. doi:10.1103/PhysRevLett.121.138002.
195. C. L. Phillips, E. Jankowski, B. J. Krishnatreya, K. V. Edmond, S. Sacanna, D. G. Grier, D. J. Pine, and S. C. Glotzer. Digital colloids: reconfigurable clusters as high information density elements. *Soft Matter*, 10(38):7468–7479, 2014.
196. N. B. Schade, M. C. Holmes-Cerfon, E. R. Chen, D. Aronzon, J. W. Collins, J. A. Fan, F. Capasso, and V. N. Manoharan. Tetrahedral Colloidal Clusters from Random Parking of Bidisperse Spheres. *Phys. Rev. Lett.*, 110(14):148303, 2013.
197. T. Sugimoto and K. Sakata. Preparation of monodisperse pseudocubic α-Fe2O3 particles from condensed ferric hydroxide gel. *J. Colloid Interface Sci.*, 152(2):587–590, 1992.
198. V. Meester and D. J. Kraft. Spherical, Dimpled, and Crumpled Hybrid Colloids with Tunable Surface Morphology. *Langmuir*, 32(41):10668–10677, 2016.
199. C. Van der Wel, R. K. Bhan, R. W. Verweij, H. C. Frijters, Z. Gong, A. D. Hollingsworth, S. Sacanna, and D. J. Kraft. Preparation of colloidal organosilica spheres through spontaneous emulsification. *Langmuir*, 33(33):8174–8180, 2017.
200. R. P. Doherty and D. J. Kraft. One-pot surfactant-free synthesis of organosilica colloids with various surface functional groups. In preparation.
201. J. Appel, S. Akerboom, R. G. Fokkink, and J. Sprakel. Facile One-Step Synthesis of Monodisperse Micron-Sized Latex Particles with Highly Carboxylated Surfaces. *Macromol. Rapid Commun.*, 34(16):1284–1288, 2013. doi:10.1002/marc.201300422.
202. C. Van Der Wel, A. Vahid, A. Šarić, T. Idema, D. Heinrich, and D. J. Kraft. Lipid membrane-mediated attraction between curvature inducing objects. *Sci. Rep.*, 6(1):1–10, 2016. doi:10.1038/srep32825.
203. D. Axelrod, D. Koppel, J. Schlessinger, E. Elson, and W. Webb. Mobility measurement by analysis of fluorescence photobleaching recovery kinetics. *Biophys. J.*, 16(9):1055–1069, 1976.
204. J. D. Hunter. Matplotlib: A 2D graphics environment. *Comput. Sci. Eng.*, 9(3):90–95, 2007. doi:10.1109/MCSE.2007.55.
205. C. M. Van der Wel. *Lipid Mediated Colloidal Interactions*. PhD thesis, Casimir PhD Series, 2017.
206. R. Sarfati, J. Bławzdziewicz, and E. R. Dufresne. Maximum likelihood estimations of force and mobility from single short Brownian trajectories. *Soft Matter*, 13(11):2174–2180, 2017.
207. D. Foreman-Mackey, D. W. Hogg, D. Lang, and J. Goodman. emcee : The MCMC Hammer. *Proc. Natl. Acad. Sci. U.S.A.*, 125(925):306–312, 2013. doi:10.1086/670067.
208. E. Sackmann. Supported Membranes: Scientific and Practical Applications. *Science*, 271 (5245):43–48, 1996. doi:10.1126/science.271.5245.43.
209. I. Gözen and A. Jesorka. Instrumental methods to characterize molecular phospholipid films on solid supports. *Anal. Chem.*, 84(2):822–838, 2012.
210. R. Machá and M. Hof. Lipid diffusion in planar membranes investigated by fluorescence correlation spectroscopy. *Biochim. Biophys. Acta*, 1798(7):1377–1391, 2010. doi:10.1016/j.bbamem.2010.02.014.

211. S. I. R. Castillo, S. Ouhajji, S. Fokker, B. H. Erné, C. T. W. M. Schneijdenberg, D. M. E. Thies-Weesie, and A. P. Philipse. Silica cubes with tunable coating thickness and porosity: From hematite filled silica boxes to hollow silica bubbles. *Microporous Mesoporous Mater.*, 195:75–86, 2014. doi:10.1016/j.micromeso.2014.03.047.
212. T. Cha, A. Guo, and X.-Y. Zhu. Formation of supported phospholipid bilayers on molecular surfaces: Role of surface charge density and electrostatic interaction. *Biophys. J.*, 90(4): 1270–1274, 2006.
213. P. G. De Gennes. Polymers at an interface; a simplified view. *Adv. Colloid Interface Sci.*, 27 (3-4):189–209, 1987.
214. S. Upadhyayula, T. Quinata, S. Bishop, S. Gupta, N. R. Johnson, B. Bahmani, K. Bozhilov, J. Stubbs, P. Jreij, P. Nallagatla, and V. I. Vullev. Coatings of polyethylene glycol for suppressing adhesion between solid microspheres and flat surfaces. *Langmuir*, 28(11): 5059–69, 2012.
215. C. Van der Wel, N. Bossert, Q. J. Mank, M. G. Winter, D. Heinrich, and D. J. Kraft. Surfactant-free colloidal particles with specific binding affinity. *Langmuir*, 33(38):9803–9810, 2017.
216. C. Van Der Wel, G. L. Van De Stolpe, R. W. Verweij, and D. J. Kraft. Micrometer-sized TPM emulsion droplets with surface-mobile binding groups. *J. Phys. Condens. Matter*, 30 (9), 2018.
217. C. A. Naumann, O. Prucker, T. Lehmann, J. Rühe, W. Knoll, and C. W. Frank. The polymer-supported phospholipid bilayer: Tethering as a new approach to substrate- membrane stabilization. *Biomacromolecules*, 3(1):27–35, 2002.
218. M. Tanaka and E. Sackmann. Polymer-supported membranes as models of the cell surface. *Nature*, 437(7059):656–663, 2005. doi:10.1038/nature04164.
219. M. Tanaka. Polymer-Supported Membranes: Physical Models of Cell Surfaces. *MRS Bulletin*, 31:513–520, 2006.
220. M. L. Wagner and L. K. Tamm. Tethered polymer-supported planar lipid bilayers for reconstitution of integral membrane proteins: silane-polyethyleneglycol-lipid as a cushion and covalent linker. *Biophys. J.*, 79(3):1400–1414, 2000. doi:10.1016/S0006-3495(00)76392-2.
221. M. A. Deverall, S. Garg, K. Ludtke, R. Jordan, J. Ruhe, and C. A. Naumann. Transbilayer coupling of obstructed lipid diffusion in polymer-tethered phospholipid bilayers. *Soft Matter*, 4:1899–1908, 2008.
222. R. Lipowsky. Bending of membranes by anchored polymers. *Europhys. Lett.*, 30(4):197, 1995.
223. P. L. Biancaniello, J. C. Crocker, D. A. Hammer, and V. T. Milam. DNA-mediated phase behavior of microsphere suspensions. *Langmuir*, 23(5):2688–2693, 2007.
224. G. Nordlund, R. Lonneborg, and P. Brzezinski. Formation of Supported Lipid Bilayers on Silica Particles Studied Using Flow Cytometry. *Langmuir*, 25(8):4601–4606, 2009.
225. A. Tan, A. Ziegler, B. Steinbauer, and J. Seelig. Thermodynamics of sodium dodecyl sulfate partitioning into lipid membranes. *Biophys. J.*, 83(3):1547–1556, 2002.
226. T. Drobek, N. D. Spencer, and M. Heuberger. Compressing PEG brushes. *Macromolecules*, 38(12):5254–5259, 2005.
227. F. Meng, G. H. M. Engbers, and J. Feijen. Polyethylene glycol-grafted polystyrene particles. *J. Biomed. Mater. Res. Part A*, 70(1):49–58, 2004.
228. O. Garbuzenko, Y. Barenholz, and A. Priev. Effect of grafted PEG on liposome size and on compressibility and packing of lipid bilayer. *Chem. Phys. Lipids*, 135(2):117–129, 2005.

229. S. Angioletti-Uberti, P. Varilly, B. M. Mognetti, and D. Frenkel. Mobile linkers on DNA-coated colloids: Valency without patches. *Phys. Rev. Lett.*, 113(12):128303, 2014.
230. R. Lipowsky. Spontaneous tubulation of membranes and vesicles reveals membrane tension generated by spontaneous curvature. *Faraday Discuss.*, 161:305–331, 2013.
231. S. I. Nakano, M. Fujimoto, H. Hara, and N. Sugimoto. Nucleic acid duplex stability: Influence of base composition on cation effects. *Nucleic Acids Res.*, 27(14):2957–2965, 1999.
232. M. Marsh and A. Helenius. Virus entry: open sesame. *Cell*, 124(4):729–740, 2006.
233. C.-H. Heldin. Dimerization of cell surface receptors in signal transduction. *Cell*, 80(2): 213–223, 1995.
234. M. Mammen, S.-K. Choi, and G. M. Whitesides. Polyvalent interactions in biological systems: implications for design and use of multivalent ligands and inhibitors. *Angew. Chem.*, 37(20):2754–2794, 1998.
235. L. L. Kiessling, J. E. Gestwicki, and L. E. Strong. Synthetic multivalent ligands as probes of signal transduction. *Angew. Chem.*, 45(15):2348–2368, 2006.
236. D. Nykypanchuk, M. M. Maye, D. Van Der Lelie, and O. Gang. DNA-based approach for interparticle interaction control. *Langmuir*, 23(11):6305–6314, 2007.
237. R. Dreyfus, M. E. Leunissen, R. Sha, A. V. Tkachenko, N. C. Seeman, D. J. Pine, and P. M. Chaikin. Simple quantitative model for the reversible association of DNA coated colloids. *Phys. Rev. Lett.*, 102(4):048301, 2009.
238. F. J. Martinez-Veracoechea and D. Frenkel. Designing super selectivity in multivalent nano-particle binding. *Proc. Natl. Acad. Sci. U.S.A.*, 108(27):10963–10968, 2011.
239. P. Varilly, S. Angioletti-Uberti, B. M. Mognetti, and D. Frenkel. A general theory of DNA-mediated and other valence-limited colloidal interactions. *J. Chem. Phys.*, 137(9):094108, 2012.
240. B. M. Mognetti, P. Cicuta, and L. Di Michele. Programmable interactions with biomimetic DNA linkers at fluid membranes and interfaces. *Rep. Prog. Phys.*, 82(11):116601, 2019.
241. J. S. Oh, M. He, G.-R. Yi, and D. J. Pine. High-density DNA coatings on carboxylated colloids by DMTMM- and azide-mediated coupling reactions. *Langmuir*, 36(13):3583–3589, 2020.
242. M. Rinaldin, R. W. Verweij, I. Chakraborty, and D. J. Kraft. Colloid supported lipid bilayers for self-assembly. *Soft Matter*, 15:1345–1360, 2019. doi:10.1039/C8SM01661E.
243. S. J. Bachmann, M. Petitzon, and B. M. Mognetti. Bond formation kinetics affects self-assembly directed by ligand–receptor interactions. *Soft Matter*, 12(47):9585–9592, 2016.
244. R. W. Verweij, P. G. Moerman, N. E. G. Ligthart, L. P. P. Huijnen, J. Groenewold, W. K. Kegel, A. van Blaaderen, and D. J. Kraft. Flexibility-induced effects in the Brownian motion of colloidal trimers. *Phys. Rev. Res.*, 2(3):033136, 2020. doi:10.1103/physrevresearch.2.033136.
245. E. B. Wilson. Probable inference, the law of succession, and statistical inference. *J. Am. Stat. Assoc.*, 22(158):209–212, 1927.
246. M. Newville, R. Otten, A. Nelson, A. Ingargiola, T. Stensitzki, D. Allan, A. Fox, et al. lmfit/lmfit-py 1.0.1, 2020.
247. P. Varilly, S. Angioletti-Uberti, et al. DNACC, 2015. URL `github.com/patvarilly/DNACC`.
248. S. Angioletti-Uberti, P. Varilly, B. M. Mognetti, A. V. Tkachenko, and D. Frenkel. Communication: a simple analytical formula for the free energy of ligandreceptor-mediated interactions. *J. Chem. Phys.*, (138):021102, 2013.
249. W. A. Kibbe. Oligocalc: an online oligonucleotide properties calculator. *Nucleic Acids Res.*, 35:W43–W46, 2007.

250. I. Chakraborty, D. J. Pearce, R. W. Verweij, S. C. Matysik, L. Giomi, and D. J. Kraft. Self-assembly dynamics of reconfigurable colloidal molecules. In preparation.
251. P. Mellado, A. Iniesta, F. Diaz, and J. Garcia de la Torre. Diffusion coefficients of segmentally flexible macromolecules with two subunits: A study of broken rods. *Biopolymers*, 27: 1771–1786, 1988.
252. S. Ishino, T. Yamagami, M. Kitamura, N. Kodera, T. Mori, S. Sugiyama, T. Ando, N. Goda, T. Tenno, H. Hiroaki, and Y. Ishino. Multiple interactions of the intrinsically disordered region between the helicase and nuclease domains of the archaeal Hef protein. *J. Biol. Chem.*, 289(31):21627–21639, 2014. doi:10.1074/jbc.M114.554998.
253. D. Burton. Structure and function of antibodies. *New Compr. Biochem.*, 17:1–50, 1987.
254. G. Barbato, M. Ikura, L. E. Kay, A. Bax, and R. W. Pastor. Backbone Dynamics of Calmodulin Studied by 15N Relaxation Using Inverse Detected Two-Dimensional NMR Spectroscopy: The Central Helix Is Flexible. *Biochemistry*, 31(23):5269–5278, 1992. doi:10.1021/bi00138a005.
255. D. E. Koshland. The KeyLock Theory and the Induced Fit Theory, 1995.
256. K. Nagasaka and H. Yamakawa. Dynamics of weakly bending rods: A trumbbell model. *J. Chem. Phys.*, 83(12):6480–6488, 1985. doi:10.1063/1.449548.
257. M. Fixman. Inclusion of Hydrodynamic Interaction in Polymer Dynamical Simulations. *Macromolecules*, 14(6):1710–1717, 1981. doi:10.1021/ma50007a019.
258. A. Z. Akcasu. Comments on the Diffusion Coefficient and First Cumulant. *Macromolecules*, 15(5):1321–1324, 1982. doi:10.1021/ma00233a021.
259. C. Riedel, R. Gabizon, C. A. Wilson, K. Hamadani, K. Tsekouras, S. Marqusee, S. Pressé, and C. Bustamante. The heat released during catalytic turnover enhances the diffusion of an enzyme. *Nature*, 517(7533):227–230, 2015. doi:10.1038/nature14043.
260. S. Sengupta, K. K. Dey, H. S. Muddana, T. Tabouillot, M. E. Ibele, P. J. Butler, and A. Sen. Enzyme molecules as nanomotors. *J. Am. Chem. Soc.*, 135(4):1406–1414, 2013. doi:10.1021/ja3091615.
261. L. Rundqvist, J. Ådén, T. Sparrman, M. Wallgren, U. Olsson, and M. Wolf-Watz. Noncooperative folding of subdomains in adenylate kinase. *Biochemistry*, 48(9):1911–1927, 2009. doi:10.1021/bi8018042.
262. D. Roitman. The elastic trumbbell model for dynamics of stiff chains. Rotational Dynamics of Small and Macromolecules. *Lecture Notes in Physics*, 293, 2005.
263. J. García de la Torre and B. Carrasco. Hydrodynamic properties of rigid macromolecules composed of ellipsoidal and cylindrical subunits. *Biopolymers*, 63(3):163–167, 2002. doi:10.1002/bip.10013.
264. A. Iniesta, F. G. Díaz, and J. García de la Torre. Transport properties of rigid bent-rod macromolecules and of semiflexible broken rods in the rigid-body treatment. Analysis of the flexibility of myosin rod. *Biophys. J.*, 54(2):269–275, 1988. doi:10.1016/S0006-3495(88)82956-4.
265. Y. Zhang, X. He, R. Zhuo, R. Sha, J. Brujic, N. C. Seeman, and P. M. Chaikin. Multivalent, multiflavored droplets by design. *Proc. Natl. Acad. Sci. U.S.A.*, 115(37):9086–9091, 2018. doi:10.1073/pnas.1718511115.
266. H. R. Vutukuri, A. F. Demirörs, B. Peng, P. D. Van Oostrum, A. Imhof, and A. Van Blaaderen. Colloidal analogues of charged and uncharged polymer chains with tunable stiffness. *Angew. Chem.*, 51(45):11249–11253, 2012. doi:10.1002/anie.201202592.
267. F. Montanarella, D. Urbonas, L. Chadwick, P. G. Moerman, P. J. Baesjou, R. F. Mahrt, A. Van Blaaderen, T. Stöferle, and D. Vanmaekelbergh. Lasing Supraparticles Self-Assembled from Nanocrystals. *ACS Nano*, 12(12):12788–12794, 2018. doi:10.1021/acsnano.8b07896.

268. F. G. Díaz and J. G. de la Torre. Viscoelastic properties of semiflexible macromolecules in solution: Brownian dynamics simulation of a trumbbell model. *Macromolecules*, 27(19): 5371–5376, 1994. doi:10.1021/ma00097a017.
269. B. Cichocki, M. Rubin, A. Niedzwiecka, and P. Szymczak. Diffusion coefficients of elastic macromolecules. *J. Fluid Mech.*, 878:R3, 2019. doi:10.1017/jfm.2019.652.
270. B. Carrasco and J. G. De La Torre. Improved hydrodynamic interaction in macromolecular bead models. *J. Chem. Phys.*, 111(10):4817–4826, 1999. doi:10.1063/1.479743.
271. V. Bloomfield, W. O. Dalton, and K. E. Van Holde. Frictional coefficients of multisubunit structures. I. Theory. *Biopolymers*, 5(2):135–148, 1967. doi:10.1002/bip.1967.360050202.
272. D. P. Filson and V. A. Bloomfield. Shell Model Calculations of Rotational Diffusion Coefficients. *Biochemistry*, 6(6):1650–1658, 1967. doi:10.1021/bi00858a011.
273. D. L. Ermak and J. A. McCammon. Brownian dynamics with hydrodynamic interactions. *J. Chem. Phys.*, 69(4):1352–1360, 1978. doi:10.1063/1.436761.
274. T. Lukka, J. Stewart, et al. FreeWRL: an X3D/VRML open source viewer for Windows, Linux, OSX and Android., 2017. URL `http://freewrl.sourceforge.net`.
275. H. Yamakawa. Transport properties of polymer chains in dilute solution: hydrodynamic interaction. *J. Chem. Phys.*, 53(1):436–443, 1970. doi:10.1063/1.1673799.
276. B. Carrasco and J. G. De La Torre. Improved hydrodynamic interaction in macromolecular bead models. *J. Chem. Phys.*, 111(10):4817–4826, 1999. doi:10.1063/1.479743.
277. G. D. Phillies. Translational drag coefficients of assemblies of spheres with higher-order hydrodynamic interactions. *J. Chem. Phys.*, 81(9):4046–4052, 1984. doi:10.1063/1.448148.
278. A. Ortega and J. García de la Torre. Equivalent radii and ratios of radii from solution properties as indicators of macromolecular conformation, shape, and flexibility. *Biomacromolecules*, 8(8):2464–2475, 2007. doi:10.1021/bm700473f.
279. P. Sharma, S. Ghosh, and S. Bhattacharya. *Nat. Phys.*, 4:960, 2008.
280. W. Weare, S. Reed, M. Warner, and J. Hutchison. Improved synthesis of small phosphine-stabilized gold nanoparticles. *J. Am. Chem. Soc.*, (122):12890–12891, 2000.
281. J. Piella, N. Bastús, and V. Puntes. Size-controlled synthesis of sub-10-nm citrate-stabilized gold nanoparticles and related optical properties. *Chem. Mater.*, (28):1066–1075, 2016.
282. H. J. Dyson and P. E. Wright. Intrinsically unstructured proteins and their functions. *Nat. Rev. Mol. Cell Biol.*, 6(3):197–208, 2005.
283. L. Makowski, D. J. Rodi, S. Mandava, D. D. Minh, D. B. Gore, and R. F. Fischetti. Molecular crowding inhibits intramolecular breathing motions in proteins. *J. Mol. Biol.*, 375(2):529–546, 2008.
284. A. Einstein. Über die von der molekularkinetischen Theorie der Wärme geforderte Bewegung von in ruhenden Flüssigkeiten suspendierten Teilchen. *Annalen der Physik*, 322(8): 549–560, 1905. doi:10.1002/andp.19053220806.
285. A. M. Mihut, B. Stenqvist, M. Lund, P. Schurtenberger, and J. J. Crassous. Assembling oppositely charged lock and key responsive colloids: A mesoscale analog of adaptive chemistry. *Sci. Adv.*, 3(9):e1700321, 2017.
286. J. Riseman and J. G. Kirkwood. The intrinsic viscosity, translational and rotatory diffusion constants of rod-like macromolecules in solution. *J. Chem. Phys.*, 18(4):512–516, 1950.
287. J. García De La Torre and B. Carrasco. Hydrodynamic properties of rigid macromolecules composed of ellipsoidal and cylindrical subunits. *Biopolymers*, 63(3):163–167, 2002. doi:10.1002/bip.10013.
288. R. R. Schmidt, J. H. Cifre, and J. G. de la Torre. Translational diffusion coefficients of macromolecules. *Eur. Phys. J. E*, 35(12):130, 2012.

289. T. Yamada, T. Yoshizaki, and H. Yamakawa. Transport coefficients of helical wormlike chains. 5. Translational diffusion coefficient of the touched-bead model and its application to oligo- and polystyrenes. *Macromolecules*, 25(1):377–383, 1992.
290. B. Sprinkle, E. B. van der Wee, Y. Luo, M. M. Driscoll, and A. Donev. Driven dynamics in dense suspensions of microrollers. *Soft Matter*, 16:7982–8001, 2020. doi:10.1039/D0SM00879F.
291. S. Delong, F. Balboa, B. Delmotte, B. Sprinkle, A. Donev, et al. Rigid Multiblobs in half-space (v. 427d241), 2020. URL `github.com/stochasticHydroTools/RigidMultiblobsWall`.
292. E. Wajnryb, K. A. Mizerski, P. J. Zuk, and P. Szymczak. Generalization of the Rotne-Prager-Yamakawa mobility and shear disturbance tensors. *J. Fluid Mech.*, 731:R3, 2013. doi:10.1017/jfm.2013.402.
293. F. Balboa Usabiaga, B. Delmotte, and A. Donev. Brownian dynamics of confined suspensions of active microrollers. *J. Chem. Phys.*, 146(13):134104, 2017. doi:10.1063/1.4979494.
294. P. A. Wiggins and P. C. Nelson. Generalized theory of semiflexible polymers. *Phys. Rev. E*, 73(3):031906, 2006.
295. P.-G. De Gennes and P.-G. Gennes. *Scaling concepts in polymer physics*. Cornell university press, 1979.
296. X. Wang and K. Wang. Calculation of the Flory exponent using the Renormalization theory. *Polym. J.*, 27:515518, 1995.
297. M. Doi, S. F. Edwards, and S. F. Edwards. *The theory of polymer dynamics*, volume 73. oxford university press, 1988.
298. J. P. Valleau. Distribution of end-to-end length of an excluded-volume chain. *J. Chem. Phys.*, 104(8):3071–3074, 1996.
299. M. Bishop and J. Clarke. Investigation of the end-to-end distance distribution function for random and self-avoiding walks in two and three dimensions. *J. Chem. Phys.*, 94(5): 3936–3942, 1991.
300. J. M. Victor and D. Lhuillier. The gyration radius distribution of twodimensional polymer chains in a good solvent. *J. Chem. Phys.*, 92(2):1362–1364, 1990. doi:10.1063/1.458147.
301. J. Agudo-Canalejo and R. Golestanian. Diffusion and steady state distributions of flexible chemotactic enzymes. *Eur. Phys. J. ST*, 229(17):2791–2806, 2020.
302. T. McLeish. Polymers without beginning or end. *Science*, 297(5589):2005–2006, 2002. doi:10.1126/science.1076810.
303. M. Kapnistos, M. Lang, D. Vlassopoulos, W. Pyckhout-Hintzen, D. Richter, D. Cho, T. Chang, and M. Rubinstein. Unexpected power-law stress relaxation of entangled ring polymers. *Nat. Mat.*, 7(12):997–1002, 2008.
304. S. Liu, S. Murata, and I. Kawamata. DNA ring motif with flexible joints. *Micromachines*, 11(11):987, 2020.
305. J. D. Halverson, G. S. Grest, A. Y. Grosberg, and K. Kremer. Rheology of ring polymer melts: From linear contaminants to ring-linear blends. *Phys. Rev. Lett.*, 108(3):038301, 2012.
306. J. D. Halverson, J. Smrek, K. Kremer, and A. Y. Grosberg. From a melt of rings to chromosome territories: the role of topological constraints in genome folding. *Rep. Prog. Phys.*, 77(2):022601, 2014. doi:10.1088/0034-4885/77/2/022601.
307. J. D. Halverson, W. B. Lee, G. S. Grest, A. Y. Grosberg, and K. Kremer. Molecular dynamics simulation study of nonconcatenated ring polymers in a melt. II. Dynamics. *J. Chem. Phys.*, 134(20):204905, 2011. doi:10.1063/1.3587138.

308. E. W. Weisstein. Domino graph. URL `mathworld.wolfram.com/DominoGraph.html`. Accessed Jan. 2020.
309. J. C. Maxwell. On the calculation of the equilibrium and stiffness of frames. *London Edinburgh Philos. Mag. J. Sci.*, 27(182):294–299, 1864.
310. Y. Han, A. Alsayed, M. Nobili, and A. G. Yodh. Quasi-two-dimensional diffusion of single ellipsoids: Aspect ratio and confinement effects. *Phys. Rev. E*, 80(1):011403, 2009.
311. Z. Zeravcic, V. N. Manoharan, and M. P. Brenner. Size limits of self-assembled colloidal structures made using specific interactions. *Proc. Natl. Acad. Sci. U.S.A.*, 111(45):15918–15923, 2014.
312. E. V. Shevchenko, D. V. Talapin, C. B. Murray, and S. O'Brien. Structural characterization of self-assembled multifunctional binary nanoparticle superlattices. *J. Am. Chem. Soc.*, 128(11):3620–3637, 2006.
313. J.-H. Lee, J. P. Singer, and E. L. Thomas. Micro-/nanostructured mechanical metamaterials. *Adv. Mater.*, 24(36):4782–4810, 2012.
314. Y.-S. Cho, G.-R. Yi, S.-H. Kim, D. J. Pine, and S.-M. Yang. Colloidal clusters of microspheres from water-in-oil emulsions. *Chem. Mater.*, 17(20):5006–5013, 2005.
315. D. J. Kraft, J. Groenewold, and W. K. Kegel. Colloidal molecules with well-controlled bond angles. *Soft Matter*, 5(20):3823–3826, 2009.
316. L. Feng, R. Dreyfus, R. Sha, N. C. Seeman, and P. M. Chaikin. DNA patchy particles. *Adv. Mater.*, 25(20):2779–2783, 2013.
317. V. Meester and D. J. Kraft. Spherical, dimpled, and crumpled hybrid colloids with tunable surface morphology. *Langmuir*, 32(41):10668–10677, 2016.
318. W. K. Kegel, D. Breed, M. Elsesser, and D. J. Pine. Formation of anisotropic polymer colloids by disparate relaxation times. *Langmuir*, 22(17):7135–7136, 2006.
319. M. Rinaldin. *On the geometry of demixing: A study of lipid phase separation on curved surfaces*. PhD thesis, Casimir PhD Series, 2019.
320. P. A. Beales, J. Nam, and T. K. Vanderlick. Specific adhesion between DNA-functionalized "Janus" vesicles: size-limited clusters. *Soft Matter*, 7(5):1747–1755, 2011.
321. M. Wang, Z. Liu, and W. Zhan. Janus liposomes: Gel-assisted formation and bioaffinity-directed clustering. *Langmuir*, 34(25):7509–7518, 2018.
322. P. Swinkels, S. Stuij, Z. Gong, H. Jonas, B. van der Linden, P. Bolhuis, S. Sacanna, S. Woutersen, and P. Schall. Revealing pseudorotation and ring-opening reactions in colloidal organic molecules. Under review, 2021.
323. S. Sacanna, W. T. Irvine, P. M. Chaikin, and D. J. Pine. Lock and key colloids. *Nature*, 464 (7288):575–578, 2010.
324. K. Braun, A. Hanewald, and T. A. Vilgis. Milk emulsions: Structure and stability. *Foods*, 8(10):483, 2019.
325. A. Papadopoulou, J. Laucks, and S. Tibbits. From self-assembly to evolutionary structures. *Architectural Design*, 87(4):28–37, 2017.
326. Trazyanderson. Velcro photomicrograph, 2018. URL `commons.wikimedia.org/wiki/File:Velcro_photomicrograph.jpg`.

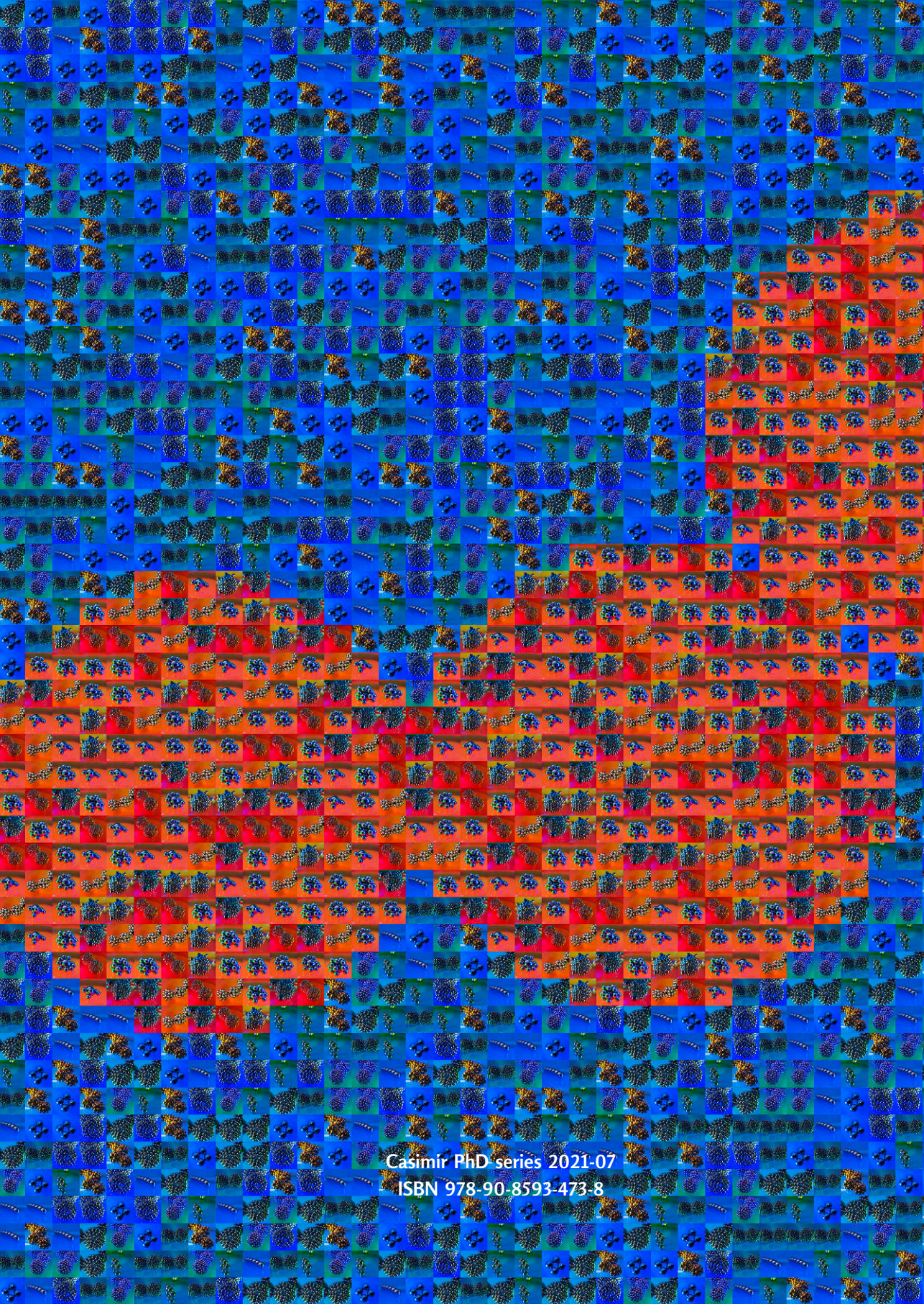

Casimir PhD series 2021-07
ISBN 978-90-8593-473-8